UAB
Universitat Autònoma de Barcelona

Advanced strategies for Solid Oxide Electrolysis cells

Simone Anelli

Tesi doctoral

Programa de doctorat en Ciència de Materials

Director/s: Prof. Albert Tarancón Rubio, Dr. Marc Torrell Faro, Dr. Federico Baiutti

Tutor/a: Prof. Eva Pellicer

Departament de Física

Facultat de Ciències

2020

El Prof. Albert Tarancón Rubio, el Dr. Marc Torrell Faro y el Dr. Federico Baiutti investigadors de l'Institut de Investigació en Energia de Catalunya (IREC), certifiquen:

Que la memòria titulada "Advanced strategies for Solid Oxide Electrolysis Cells" presentada per Simone Anelli per optar al grau de Doctor en el Programa de Ciència de Materials de la Universitat Autònoma de Barcelona ha estat realizada sota la seva direcció a l'Institut de Investigació en Energia de Catalunya (IREC).

Barcelona, a 16 de octubre de 2020

In mezô a stè crôze bagnëe daô sü	*Among these steep streets flooded by Sun*
Dôve anche ô tempô ô se ferma in pitin	*Where time is forced to stop a bit*
Gh'è n'ostaia de quelle de n'ota	*There is a tavern from the old times*
Dôve ghe canta di canterin	*Where the Canterini are singing*
A l'è gente allegra c'aô fä pë demôa	*They are cheerful people who sing for fun*
Streita in tô serciô dô cantô zeneize	*In the small circle of Genoese singing*
Man dërè a schenn'a pë due o tre ô-üe	*With their arms behind their backs for two or three ours*
Senti che canta	*Listen, they are singing*
Ô Sant'Orçeïse	*The Sant'Olcese*

E quande in giôrnô dôviemô parti	*And when will come the time for us to leave*
Nô vôemô fiôri pë chi se ne va	*We don't want flowers for those who left*
Se anche in tô sërciô ghe manca un	*If someone is missing from the circle*
Dôvunque ô segge sentine ô pôria	*Everywhere he will hear us.*
Ô trallallero cansôn de n'a vitta	*The trallalero is a song for life*
Nô ti ô capisci ma ô t'intra in tu chêu	*You don't understand it, but it enters in your heart*
Poche parolle cômmme dô restü	*Just a few words like*
Ô risô rëo	*the few laughs*
Da gente de chï	*Of the people from here*

Acknowledgments

This thesis was made thanks to the contribution of different people and entities which helped me during these three years. I would like to thank AMES group, that founded my PhD and allowed me to work at IREC.

I would like to thank my directors: Albert, Marc and Federico. Thank you, Albert, for offering me the PhD and making me stay after my internship. It has been one of the best choices that I could have never made without the opportunity that you gave to me. Marc, I would like to thank you because I think that you saw something in me that I never have been able to see in myself and you always managed to motivate me and to give me your best. Fede, there are many things to say. I would like to thank you because you always challenged me, you pushed me as hard as you could, and I really would like to thank you for this. I would also like to thank prof. Eva Pellicer, my tutor, who has always been available any time that I needed something, and you have been truly kind to me.

Thank you to prof. Vincenzo Esposito who hosted my stay in DTU, and of course thank you very much to all the people that made this time so special. Among many others: Massimo, Elena, Cate, Lars (and the hens) and Ale.

Of course I want to thank my colleagues, present and past, who really made me enjoy these years so much: Thank you to: Alex, Marc, Lucile, Arianna, Aitor, Inigo, Nerea, Marco, Merce, Gerard, Yunqing, Jose, Mari Carmen, Natalia, Maritta, Marina, Julián, Gotzon, Juande. I would like to specially thank Isabel, Elba, Miguel, Valerie, Fra and Fede.

Quiero agradecer a todos mis amigos de aquí, por el soporte que me habéis dado, tanto en las situaciones difíciles, como también por todas las

Abstract

Nowadays, the energy transition to a low carbon scenario is promoting the global installation of renewable energy sources, its deployment above 40% will need the use of efficient energy storage systems for covering the demand. Green hydrogen and power to gas routes has arisen as the best alternative for this storage while connecting the electric and gas grids. In this frame, Solid Oxide Electrolysis Cells (SOECs), which produce hydrogen and syngas (H_2+CO) from the electrolysis of water or the co-electrolysis of water and carbon dioxide, are the most efficient electrolysers for energy storage. SOECs possess high energy conversion rates ($\approx$80 %) granted by the operation temperature range (600-900 °C).

However, one of SOECs' main drawbacks is related to the manufacturing techniques, which involves many steps to produce complete devices. Furthermore, their performances and durability are still being investigated to increase the maturity of the technology and penetrate to the market competing with other electrolysis technologies that show lower efficiencies.

The present thesis is dedicated to the exploration of new concepts of SOECs. For this, three aspects are considered, which are: i) utilization of additive manufacturing (AM) techniques for reliable, automatic and tuneable fabrication of energy devices; ii) synthesis of mesoporous nanocomposites at the oxygen electrode to improve the general performances and durability of SOEC device; an finally iii) the production of syngas by co-electrolysis and partial oxidation of methane (POM) with the developed devices.

Advanced strategies for Solid Oxide Electrolysis Cells

Robocasting (RC) and Inkjet Printing (IJP) were used for the fabrication of hybrid 3D printed symmetrical cells, which were co-sintered at high temperatures and electrochemically tested. The feasibility of these two combined techniques for the fabrication of ceramic devices was demonstrated.

Mesoporous doped ceria (CGO) was synthesized and used as a scaffold for nanocomposite oxygen electrodes. An optimized route to improve the catalytic activity of the mesoporous based electrodes and to reduce the sintering temperature to maintain their nanostructure, is proposed after the study of their effects on the material. The improvement of the SOEC devices performance applying the developed synthesis and fabrication routes is demonstrated by the achievement of unprecedented results for this type of SOEC.

The performance of complete devices with mesoporous oxygen electrodes was tested at high temperatures. The optimized scaffold tested on a button test cell (diameter =2 cm) promoted the commented outstanding performances in both co-electrolysis and fuel cell conditions. Mesoporous CGO was also deposited on large area cells (25 cm^2) to demonstrate the scalability of the material, for devices of commercial interest. Both devices underwent a durability test, showing degradation rates in line with state-of-the-art literature.

Finally, the proof of concepts about electrochemically assisted partial oxidation of methane (POM) is shown. An SOEC with CGO scaffold infiltrated by Ni and Cu catalysers was produced and tested as POM device. Methane was supplied at the Ni-Cu-CGO electrode as fuel. The oxygen produced by the water electrolysis reaction at the Ni-YSZ electrode was used to produce syngas from CH_4 on an electrochemical assisted catalytic process. The working principles of the experiment were successfully demonstrated opening a new research line.

Advanced strategies for Solid Oxide Electrolysis Cells

As a summary the present document deals with the optimization of innovative high efficient electrochemical devices as SOEC, bringing a new step beyond the state of the art on the hydrogen production technologies due to the combination of innovative fabrication routes such as the additive manufacturing with advanced functional ceramic materials like mesoporous.

Advanced strategies for Solid Oxide Electrolysis Cells

Resum

Actualment, la transició energètica cap a un escenari baix en carboni està impulsant la instal·lació global de fonts d'energia renovables, el seu desplegament per sobre de l'40%, implicarà l'ús de sistemes eficients d'emmagatzematge d'energia per cobrir la demanda. Les rutes d'hidrogen verd i *power to gas* es presenten com la millor alternativa per a aquest emmagatzematge al connectar les xarxes elèctriques i de gas. En aquest marc, les cel·les d'electròlisi d'òxid sòlid (SOEC), que produeixen hidrogen i gas de síntesi ($H_2 + CO$) a partir de l'electròlisi de l'aigua o la co-electròlisi de l'aigua i el diòxid de carboni, són els electrolitzadors més eficients per a l'emmagatzematge d'energia. Les SOEC posseeixen altes taxes de conversió d'energia (≈80%) atorgades pel rang de temperatura d'operació (600-900 °C). No obstant, un dels principals inconvenients de les SOEC està relacionat amb les tècniques de fabricació, que impliquen molts passos per produir dispositius complets. A més, les seves prestacions i durabilitat encara s'estan investigant per augmentar la maduresa de la tecnologia i penetrar en el mercat competint amb altres tecnologies d'electròlisi que mostren menors eficiències.

La present tesi està dedicada a l'exploració de nous conceptes de SOEC. Per a això, es consideren tres aspectes, que són: i) utilització de tècniques de fabricació additiva per a la fabricació replicable, automàtica i customitzable de dispositius energètics; ii) síntesi de nanocompostos mesoporosos en l'elèctrode d'oxigen per millorar el rendiment general i la durabilitat del dispositiu SOEC; i finalment iii) la producció de gas de síntesi per co-electròlisi i oxidació parcial de metà (POM) amb els dispositius desenvolupats.

Advanced strategies for Solid Oxide Electrolysis Cells

Robocasting (RC) i InkJet printing (IJP) s'han utilitzat per a la fabricació de cel·les simètriques impreses per tecnologia híbrides d'impressió 3D, que van ser co-sinteritzades a altes temperatures i provades electroquímicament. S'ha demostrat la viabilitat d'aquestes dues tècniques combinades per a la fabricació de dispositius ceràmics.

S'ha sintetitzat ceria dopada mesoporosa (CGO) utilitzada com a suport per a elèctrodes d'oxigen nanocompostos. Per a això es proposa una ruta optimitzada per millorar l'activitat catalítica dels elèctrodes de base mesoporosa i per reduir la temperatura de sinterització mantenint la seva nanoestructura, i l'estudi dels seus efectes sobre el material. La millora del rendiment dels dispositius SOEC aplicant les rutes de síntesi i fabricació desenvolupades es demostra pels excel·lents resultats aconseguits, sense precedents per a aquest tipus de SOEC.

El rendiment de dispositius complets amb elèctrodes d'oxigen mesoporosos es va provar a altes temperatures. El suport nanoestructurat optimitzat ha estat provat en una cel·la de botó (diàmetre = 2 cm) mostrant excel·lents rendiments observats en condicions de co-electròlisi i pila de combustible. També es va dipositar CGO mesoporós en cel·les d'àrea gran (25 cm^2) per demostrar l'escalabilitat del material, per a dispositius d'interès comercial. Com a resum, el document presentat tracta de l'optimització de dispositius electroquímics innovadors d'alta eficiència com les SOEC, donant un nou pas més enllà de l'estat de l'art en les tecnologies de producció d'hidrogen a causa de la combinació de rutes de fabricació innovadores com la fabricació additiva de materials ceràmics amb funcionalitats avançades com els mesoporosos.

Advanced strategies for Solid Oxide Electrolysis Cells

Index

Advanced strategies for Solid Oxide Electrolysis Cells

Advanced strategies for Solid Oxide Electrolysis Cells

Advanced strategies for Solid Oxide Electrolysis Cells

Advanced strategies for Solid Oxide Electrolysis Cells

Acronym list

ABS	Acrylonitrile Butadiene Styrene
ADF	Annular Dark-Field
AECs	Alkaline Electrolysis Cells
AIBN	Azobisisobutyronitrile
AM	Additive manufacturing
ASR	Area Specific Resistance
BET	Brunauer–Emmett–Teller theory
BF	Bright-Field
BSE	Backscattered Electrons
CAD	Computer Aided Design
CapEx	Capital Expenditures
CGO	Gadolinium doped Ceria
CIJ	Continuous Inkjet
CPE	Constant Phase Element
CTE	Coefficient of Thermal Expansion
DIW	Direct Ink Writing
DOD	Drop-On-Demand
DPG	Dipropylene Glycol
DRT	Distribution of Relaxation Times
EDX	Energy Dispersive X-Ray spectroscopy
EFF	Extrusion Free-Forming
EELS	Electron Energy Loss Spectroscopy
EIS	Electrochemical Impedance Spectroscopy
ET	Electron Tomography

FDM	Fuse Deposition Modelling
GB	Grain Boundary
GHE	Greenhouse Effect
GR	Graphite
HAADF	High-Angle Annular Dark-Field
HF	Hydrofluoric acid
HRTEM	High Resolution Transmission Electron Microscopy
ICP-MS	Inductively Coupled Plasma Mass Spectrometry
IJP	Inkjet Printing
I-V	Galvanostatic polarization current-voltage curve
LSC	$La_{1-x}Sr_xCoO_{3-\delta}$
LSCF	$La_{1-x}Sr_xCo_{1-y}Fe_yO_{3-\delta}$
LSM	$La_{1-x}Sr_xMnO_3$
MDR	Methane Dry Reforming
MIEC	Mixed Ionic Electronic Conductor
MSEC	Molten Salt Electrolysis Cell
MSR	Methane Steam Reforming
OCV	Open Circuit Voltage
OER	Oxygen Evolution Reaction
OpEx	Operating Expenses
ORR	Oxygen Reduction Reaction
PEGDA	Poly(Ethylene Glycol) Diacrylate
PEMECs	Proton Exchange Membrane Electrolysis Cells
P2G	Power to Gas routes
PG	Propylene Glycol
PLA	Polylactic Acid
PLD	Pulsed Laser Deposition
PMMA	Poly(Methyl Methacrylate)

Advanced strategies for Solid Oxide Electrolysis Cells

POM	Partial Oxidation of Methane
PVP	Polyvinylpyrrolidone
RC	Robocasting
RWGS	Reverse Water-Gas Shift
SAXS	Small-angle X-ray Scattering
S/C	Steam to Carbon ratio
SE	Secondary Electron
SEM	Scanning Electron Microscopy
SLA	Stereolithography
SLS/SLM	Selective Laser Sintering/Selective Laser Melting
SO41K	SOLSPERSE 41000
SOEC	Solid Oxide Electrolysis Cell
STEM	Scanning Transmission Electron Microscopy
TEM	Transmission Electron Microscopy
TPB	Triple Phase Boundary
TPR	Thermal Programmed Reduction
TWM3D	Tomography 3D Reconstruction
TPR	Thermal Programmed Reduction
WGS	Water-Gas Shift
XRD	X-ray Diffraction
YSZ	Yttria stabilized zirconia
μGC	Micro Gas chromatographer

Advanced strategies for Solid Oxide Electrolysis Cells

Chapter I

Introduction

1.1 General Introduction

There is a clear and global concern to limit the global warming by decreasing the CO_2 emission in the next years, as the main responsible for the greenhouse effect (GHE). Considering a recent report from the EU commission,[*] the amount of carbon dioxide emitted in Europe is around 70 to 100 million tonnes CO_2 annually.[1,2]

Decarbonisation is an unprecedented challenge that will require the efforts of all the society sectors. The use of hydrogen, the lightest and more abundant element in the universe, as energy vector for energy storage and distribution, is considered as one of the best routes in consideration of the potential absence of C-based by-products and of the superior energy storage capacity. It has been calculated that from 1 kg of H_2 is possible to produce ≈120 MJ (33.33 kWh),[3] while from the same amount of petroleum the energy obtained is ≈46 MJ.[4]

Nowadays, hydrogen is still mainly produced by fossil fuels – coal or natural gas (so-called "grey" hydrogen) – with a consistent emission of CO_2 in the environment.[5] In some cases, carbon sequestration technologies are coupled with grey production process, in order to compensate for the CO_2 emission (Figure 1.1). The hydrogen produced by fossil fuels but with controlled CO_2 emission is called "blue" hydrogen.[6]

---

[*] EUROPEAN COMMISSION Brussels, 8.7.2020. COM(2020) 301 final

Advanced strategies for Solid Oxide Electrolysis Cells
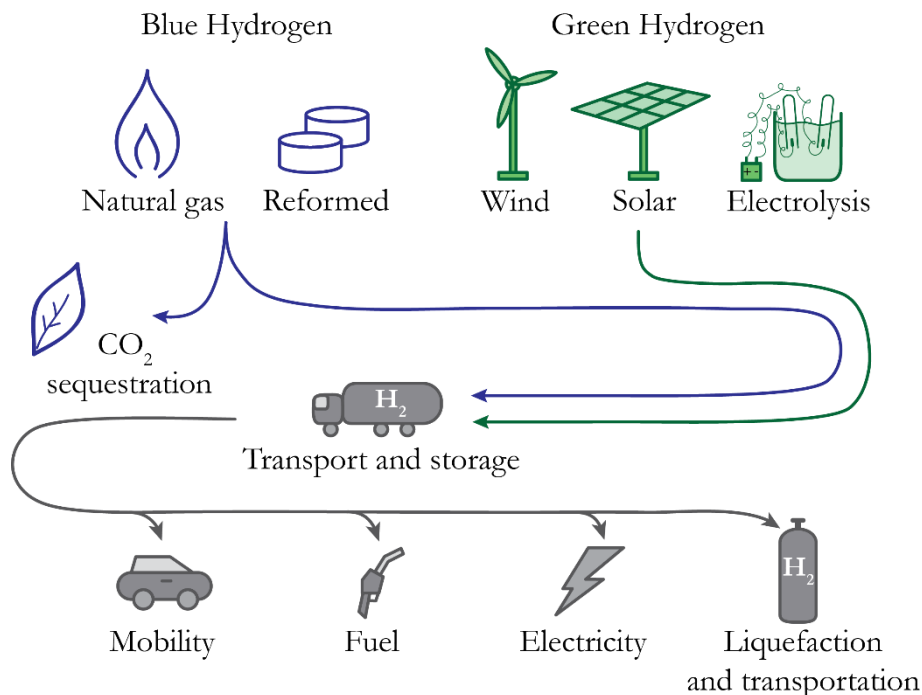
Figure 1.1: Scheme of Blue and Green H_2 production routes. Blue H_2 is produced from natural gas but with controlled CO_2 emission, green H_2 is obtained from electrolysis. Hydrogen can be stored and used in different applications which are mobility, fuel production and direct production of electricity. H_2 can be easily transported to the final user after is liquefaction.

Conversely, hydrogen production through renewable energy sources (green hydrogen) can smartly couple the two biggest energy infrastructures of our society, gas and electric networks, through the so-called Power to Gas routes (P2G). P2G routes (Figure 1.2) are based on the use of systems for the generation of green hydrogen and its electrification. In the P2G scenario, using hydrogen as an energy vector for the storage of renewables, such solar or wind energy,[7] would allow overcoming one of the main limitations of these sources, i.e. their intermittent nature.[8]

Advanced strategies for Solid Oxide Electrolysis Cells
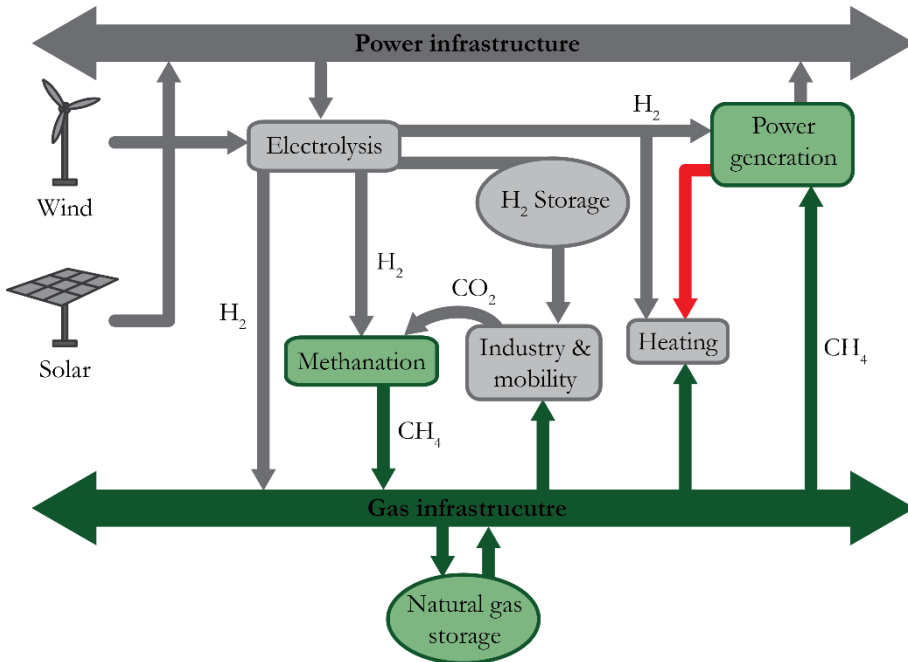
Figure 1.2: Flowsheet diagram of P2G system, representing the role of hydrogen in the storage of energy from renewable sources.

Methods for green hydrogen production comprise thermochemical water splitting, photocatalytic water splitting and water electrolysis.[9] The latter in particular is characterized by higher current efficiency and can be also used for the syngas production by co-electrolysis of steam and carbon dioxide. Such products are the basis for obtaining synthetic fuels through Fischer-Tropsch reaction[10,11] or methane by the Sabatier reaction.[12,13]

1.2   Types of electrolysis cells

An electrolysis cell is a device, which uses electrical energy to promote a non-spontaneous reaction. Hydrogen can be produced, together with oxygen, by the electrochemical separation of water as schematically sketched in Figure 1.3.
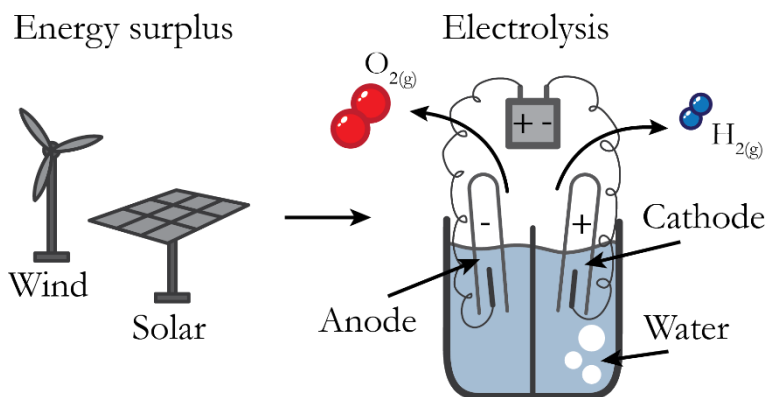
Figure 1.3: Scheme of the electrolysis of water by injecting electrical current. The energy necessary to promote the non-spontaneous reaction can be obtained from renewable sources.

There are four different types of electrolysers depending on the nature of the electrolyte: proton exchange membrane electrolysis cells (PEMECs), alkaline electrolysis cells (AECs), molten salt electrolysis cells (MSEC) and solid oxide electrolysis cells (SOECs).[14–16] Table 1.1 summarizes the main characteristics of the four types of electrolysis cells. PEMECs split water into oxygen, protons and electrons at the anode. Protons pass through the polymer electrolyte membrane and they combine with electrons to form hydrogen on the cathode side.[17] PEMECs are usually composed by metallic components (porous structures, flow fields and separator plates). They used typically platinum or platinum alloys with other metals as catalysts.[17]

In AECs, the water is split into oxygen and OH⁻ at the cathode, which is the charge carrier. The hydroxide ions travel through the liquid electrolyte and reach the anode, where oxygen and water are formed.[18,19] Platinum and nickel are typical materials for the cathode, while the anode is generally composed by metals (e.g. nickel) or oxides (e. g. PtO, Pyrochlore oxides).[19] The liquid electrolyte is in general KOH, even if recent efforts have been done to replace it with other kind of materials, such as polymeric membranes.[19]

Advanced strategies for Solid Oxide Electrolysis Cells

MSECs use molten carbonates as electrolytes, because of their low cost and their high ionic conductivity. The species which moves through the molten electrolyte is CO_3^{2-}. Such electrolysers are mainly used for the carbon dioxide reduction.[20–22] CO_2 is electro-reduced to solid carbonaceous species such as carbon spheres, carbon nanotubes, and carbon flakes on the surface of the cathode. This makes the reaction discontinuous because the cathode should be replaced frequently.[16]

Table 1.1: Summary of the main characteristics of the different types of electrolysis cells. Usually electrolysis cells are identified by the material constituting the electrolyte and the charge carrier. Here are reported proton exchange membrane electrolysis cells (PEMECs), alkaline electrolysis cells (AECs), molten salt electrolysis cells (MSEC) and solid oxide electrolysis cells (SOECs).

	PEMEC	AEC	MSEC	SOEC
Electrolyte	Polymer membrane	Liquid KOH	Molten salt	Ceramic
Charge carrier	H^+	OH^-	CO_3^{2-}	O^{2-}
Operating temperature	60-80 °C	60-80 °C	400-800 °C	600-900 °C
Pressure	30-80 atm	1-30 atm	1-6 atm	1 atm
Catalyst	Platinum	Platinum, Nickel	Ni	Nickel
Cell components	Carbon based	Carbon based	Metal-based, oxides	Ceramic based
Fuel compatibility	H_2O	H_2O	CO_2	H_2O, CH_4, CO_2
Degradation % kh^{-1}	0,25	0,13	0.25	1

Among these devices, SOECs have gained much interest in the recent years. This is because of their high efficiency, which is around the 80 %, granted by the high working temperature (600-900 °C).[23,24] Even considering other low-temperature devices with similar catalytic activity, such high-temperature cells present lower internal resistance due to their kinetic and

Advanced strategies for Solid Oxide Electrolysis Cells

thermodynamic advantages. Furthermore, chemical reactions are thermally activated, therefore higher conversion rates can be achieved.[25] The differences between low and high temperature electrolysis cells using steam and CO_2 are illustrated in Figure 1.4. One can notice that SOECs have a much higher efficiency with respect to AECs and PEMECs.

Recently, SOECs have also awaken interest on the research community due to their utilisation in co-electrolysis mode to reduce mixtures of steam and carbon dioxide and produce syngas as a feedstock for synthetic fuels.[23,26–28]
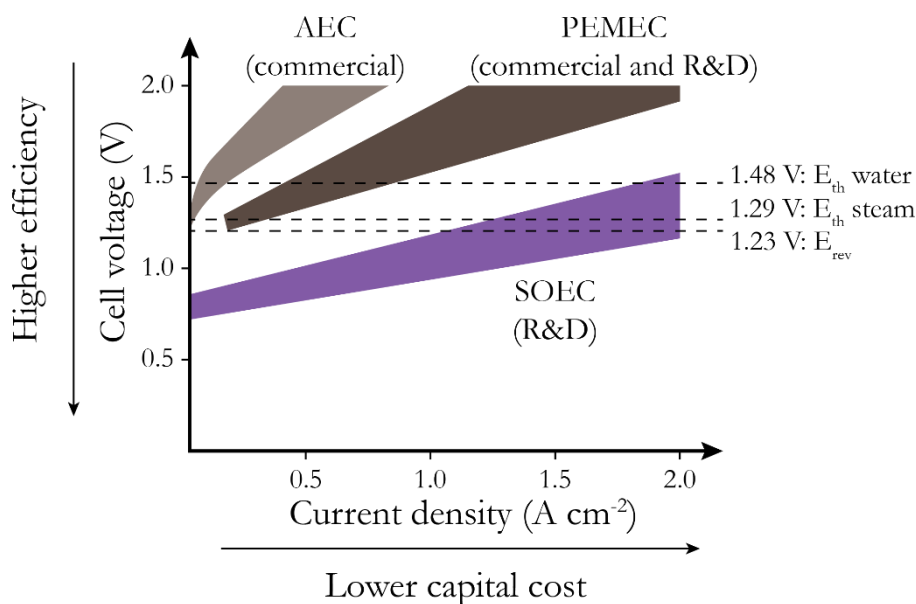
Figure 1.4: Ranges of polarization curves for different types of electrolysers. E_{th} water and E_{th} steam indicate the thermoneutral voltages for water and steam, while E_{rev} is the reversible potential for water electrolysis. Figure reproduced with the permission from Elsevier.[25]

Regarding the capital cost of PEMEC, AEC and SOEC, Table 1.2 shows their Capital Expenditures (CapEx) and the Operating Expenses (OpEx) today and the expectations for the 2030. CapEx are defined as the funds used by a company to acquire, upgrade, and maintain physical assets such as property, plants, buildings, technology, or equipment. OpEx are the

Advanced strategies for Solid Oxide Electrolysis Cells

costs of the normal business operation. They involve rent, equipment, inventory costs, marketing, payroll, insurance, step costs, and funds allocated for research and development. The CapEx and OpEx previsions for 2030 highlight a reduction of capital cost for SOEC technology which is approaching the path for commercialization. However, many efforts should be made to increase the performance and the durability of these devices. Moreover, scale-up and manufacturing process should be further improved.

Table 1.2: CapEx and OpEx index of AEC, PEMEC and SOEC today and the expectation for the 2030.[29,30]

	AEC		PEMEC		SOEC	
	Today	2030	Today	2030	Today	2030
CapEx ($/kWe)	500-1400	400-900	1100-1800	650-1500	2800-3500	800-2800
OpEx (%Capex)	4	3	4	3	-	<2

It is apparent that the development and optimisation of SOEC systems, as targeted by the present thesis, are crucial for the roll out of green hydrogen and their associated technologies. Particularly, focus will be put on the long-term stability of the system and on the simplification of the fabrication process, which arguably represent the main drawbacks for SOEC stable utilization in the market. In particular, the performance improvement by the utilization of nanocomposite electrodes and the fabrication process with the implementation of Additive Manufacturing techniques have been extensively studied.

1.3   Design of an SOEC

An SOEC is constituted by two porous ceramic electrodes in which the chemical reactions take place and by a dense ceramic electrolyte as an ionic conductor. Figure 1.5a shows the scheme of a simple steam electrolysis cell. The cathode (or fuel electrode) is the place where steam is reduced to release oxygen ions and hydrogen. The oxygen ions move inside the dense electrolyte and reach the oxygen electrode, which is the anode of the cell. Here the oxygen evolution reactions (OERs) generate molecular oxygen.

Solid oxides electrolysers cells have been historically developed after SOFCs (Figure 1.5b). SOFC utilizes hydrogen as a fuel for electricity production: Here, the oxygen electrode is the cathode, where the oxygen reduction reactions (ORRs) take place. The oxygen ions move through the electrolyte in the opposite direction compared to SOEC until the fuel electrode, which in this configuration is the anode. Oxygen ions react with the hydrogen that is supplied at the fuel electrode, forming water and releasing electrons.

In the general case of co-electrolysis in an SOEC, splitting of steam and carbon dioxide is described by the global reactions (1.1) and (1.2):

$$H_2O \rightleftarrows H_2 + \frac{1}{2}O_2 \qquad (1.1)$$

$$CO_2 \rightleftarrows CO + \frac{1}{2}O_2 \qquad (1.2)$$

These can be broken down in partial reactions for the separation of H_2O (1.3) and CO_2 (1.4) at the fuel electrode:

$$H_2O + 2\,\bar{e} \rightleftarrows H_2 + O^{2-} \qquad (1.3)$$

Advanced strategies for Solid Oxide Electrolysis Cells

$$CO_2 + 2\,e^- \rightleftarrows CO + O^{2-} \tag{1.4}$$

While at the oxygen electrode there is the formation of molecular oxygen and the release of electrons (1.5):

$$O^{2-} \rightleftarrows \frac{1}{2}O_2 + 2\,e^- \tag{1.5}$$
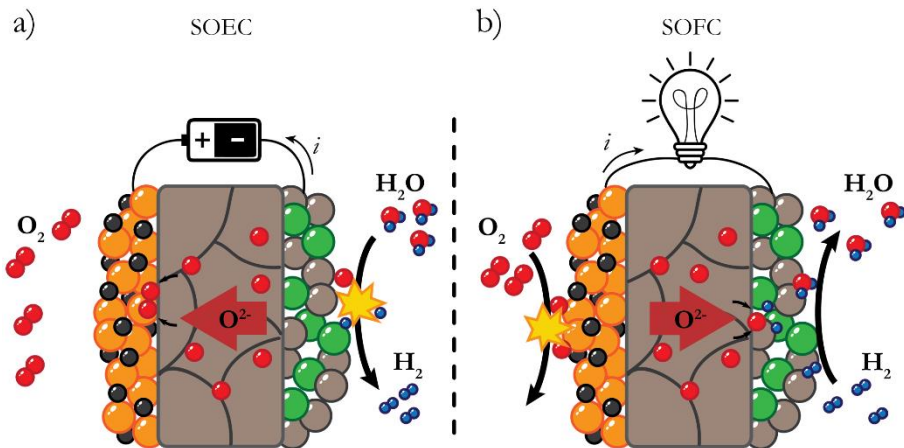
Figure 1.5: Schematic representation of an SOEC (a) and of an SOFC (b). In the figure is possible to notice the porous oxygen electrode (orange and black), the dense electrolyte (grey) where the oxygen ions move and the fuel electrode (green and grey).

1.3.1 SOEC for methane conversion

Beside the conversion reactions described above, SOEC systems have also been employed in the present thesis for syngas production by methane conversion.

One of the most used methane reforming processes is methane steam reforming (MSR):[31–33] In MSR the methane reacts with steam to produce hydrogen and carbon monoxide as is shown in equation (1.6):[31]

$$CH_4 + H_2O \rightleftarrows 3H_2 + CO \tag{1.6}$$

1. Introduction

MSR is widely used in SOFC systems in the so-called direct internal reforming. Here, the heat generated by fuel cell exothermic reaction and the steam produced can be directly used for the reforming of methane.[33] Although characterized by high thermal efficiency, MSR provides syngas with a ratio (H_2/CO) of ≈ 3, while the optimal required for Fischer-Tropsch reactions is ≈ 2.[34] Therefore, MSR requires a gas composition with a high H_2O/CH_4 ratio during operation, making the process energetically unfavourable and accelerating the deactivation of the catalysts.[35,36]

Methane Dry Reforming (MDR)[36–39] (1.7) and Partial Oxidation of Methane (POM) (1.8) reactions are possible alternatives to MSR:[40–42]

$$CH_4 + CO_2 \rightleftarrows 2CO + 2H_2 \tag{1.7}$$

$$CH_4 + \frac{1}{2}O_2 \rightleftarrows CO + 2H_2 \tag{1.8}$$
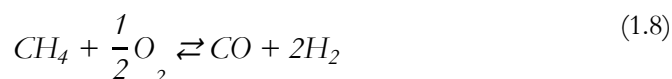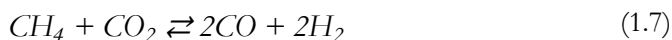
MDR produces a syngas mixture with ratio $H_2/CO \approx 1$; Moreover, the final outcome is often influenced by the occurrence of Reverse Water-Gas Shift (RWGS) reactions (1.9), so that part of the hydrogen is consumed to produce water.[43] The final H_2/CO ratio coming from MDR is often below the unity.[38]

$$CO + H_2O \underset{RWGS}{\overset{WGS}{\rightleftarrows}} CO_2 + H_2 \tag{1.9}$$
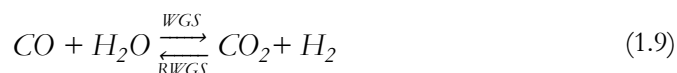
Compared with MSR and MDR, POM possesses the unique advantage of producing H_2/CO mixture with ideal ratio ≈ 2[44] and has therefore been considered in this thesis for the direct production of syngas through an electrochemically assisted process using SOECs devices.

Particularly, the potential coupling of POM on the same cell than the co-electrolysis processes takes place has been evaluated in this work. The motivation for this innovative studies is that a COSOEC+POM device could

Advanced strategies for Solid Oxide Electrolysis Cells

be extremely advantageous because of the moderately exothermic nature of the POM reaction (ΔH^o_{298K} = -802 kJ mol^{-1}), which can compensate the energetic demand of co-electrolysis.[45–47]

It should be noted that quite large number of reactions compete during syngas production through MSR, MDR and POM. The preferential route will depend on the selected operation parameters (e. g. temperature, type of catalyst, etc.). For a correct operation of the system it is crucial to find the correct thermodynamic window. Side reactions such as Boudouard reaction (1.10) and methane decomposition (1.11) can be extremely deleterious for the electrode because of the carbon deposition.

$$2CO \rightarrow C_{(s)} + CO_2 \qquad\qquad (1.10)$$

$$CH_4 \rightarrow C_{(s)} + 2H_2 \qquad\qquad (1.11)$$

Coke deposition is a well-known issue that deactivate the catalyser active points by the deposition of solid carbon on top of them.[48] This is due to both thermodynamics and kinetics contributions. Temperature, gas composition and steam to carbon (S/C) ratio are all parameters which influence this phenomenon. High temperatures, the presence of H_2 in the gas mixture and high S/C ratios can effectively prevent carbon deposition.[49] It has also been demonstrated that the utilization of high current densities during operation can further mitigate this effect.[50]

Carbon deposition can still be caused by kinetic reasons, some catalysts, widely utilize in SOC field, are prone to such an effect (e.g. nickel).[48,51] The role of the catalysts it will be further discussed below in a dedicated section.

1.3.2 Thermodynamic of SOEC

The energy demand required for the electrolysis process is given by the Gibbs free energy (1.12):

$$\varDelta G = \varDelta H - T \varDelta S \qquad (1.12)$$

Where ΔH is the enthalpy change, T is the temperature and ΔS is the entropy change. Figure 1.6 shows how the electrical energy demand of the steam electrolysis reaction decreases with the increase of temperature.[23,52] One can notice that the total energy demand of the reaction is slightly growing, anyway heat can provide part of the energy necessary for the reaction.[52]
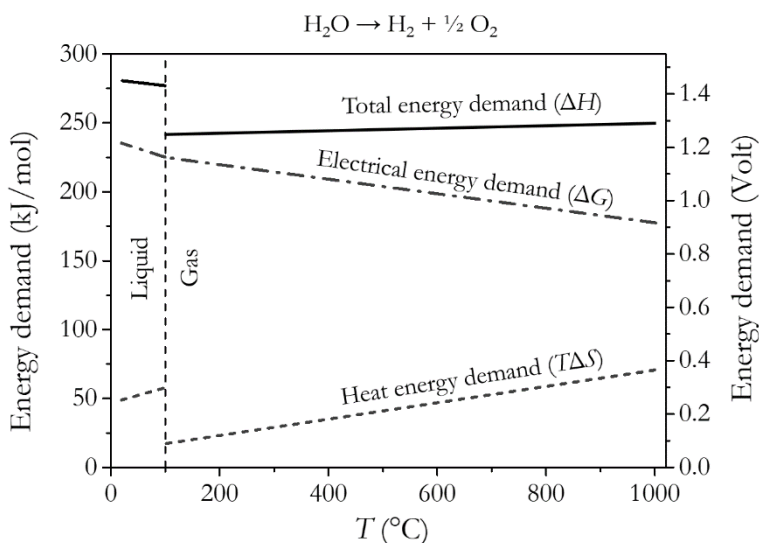
Figure 1.6: Thermodynamic of steam electrolysis. In figure are indicated the total energy demand (ΔH), the electric energy demand (ΔG) and the heat demand ($T\Delta S$) for SOEC operation. Adapted with permission from (Chem. Rev. 2014, 114, 21, 10697–10734). Copyright (2014) American Chemical Society.[52]

Similar consideration could be done for the energy demand in the case of carbon dioxide electrolysis reported in Figure 1.7. One can notice that

Advanced strategies for Solid Oxide Electrolysis Cells

in this case the total energy demand remains almost constant form 300 °C to 1000 °C degrees.
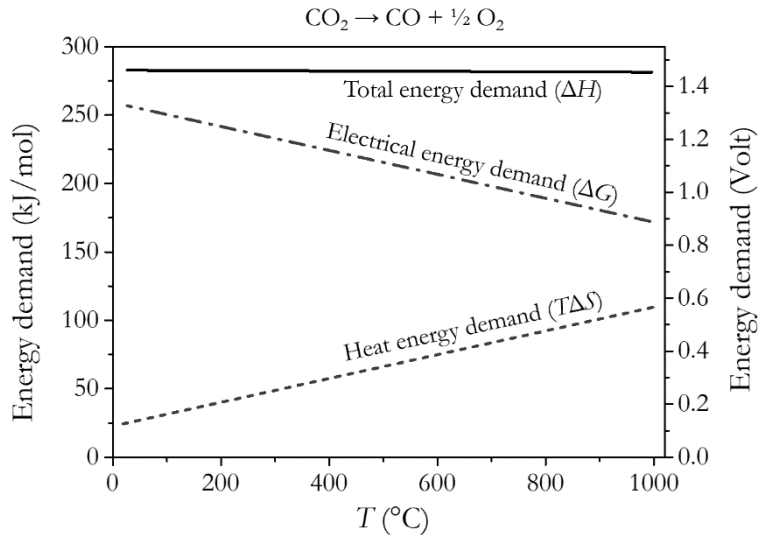
Figure 1.7: Thermodynamic of carbon dioxide electrolysis. In figure are indicated the total energy demand (ΔH), the electric energy demand (ΔG) and the heat demand ($T\Delta S$). Adapted with permission from (Chem. Rev. 2014, 114, 21, 10697–10734). Copyright (2014) American Chemical Society.[52]

The consequence of the endothermic nature of both reactions is that they require a constant supply of heat to work.

In the ideal case of a perfectly insulated electrolyser, with no inflow or outflow of heat, it is possible to define the thermoneutral voltage (E_{tn}), which is the minimum thermodynamic voltage of operation (1.13).[52]

$$E_{tn} = \frac{1}{nF}\Delta H \qquad (1.13)$$

With ΔH the reaction molar enthalpy of formation, F the Faraday's constant and n the number of electrons involved in the reaction. E_{tn} is function of the operating conditions (e. g. temperature, pressure, etc.) and of the species which participate in the reaction.[52]

1.3.3 SOCs under operation (non-ideal SOCs)

SOC operation can be conveniently represented by polarization curves (i-V), in which the measured voltage of the cell is expressed as a function of the current density applied to the device (Figure 1.8).[53] The operation voltage of an SOEC can be expressed as (1.14):[54]

$$V_{op} = V_{eq} + \eta_{act} + \eta_{Ohmic} + \eta_{conc} \tag{1.14}$$

V_{op} is the measured voltage and V_{eq} is the equilibrium voltage also called open circuit voltage (OCV). η_{act} is the overpotential due to the reaction activation processes, η_{Ohmic} is the overpotential due to all the ohmic contributions (e.g. ionic conductivity through the electrolyte)[55] and η_{conc} is the overpotential caused by mass transport. The performance representation by galvanostatic polarization curve is showed in Figure 1.8, where activation, ohmic and mass transport regions of equation (1.14) are highlighted.

Considering the example of steam electrolysis, V_{eq} can be calculated from Nernst equation (1.15):

$$V_{eq} = V^0 + \frac{RT}{2F} ln \left(\frac{p_{H_2} p_{O_2}^{1/2}}{p_{H_2O}} \right) \tag{1.15}$$

Where V^0 the standard reversible cell potential, R the ideal gas constant (R = 8.314 J mol^{-1} K^{-1}), T the temperature in K, F the Faraday constant, and p the gas partial pressure.
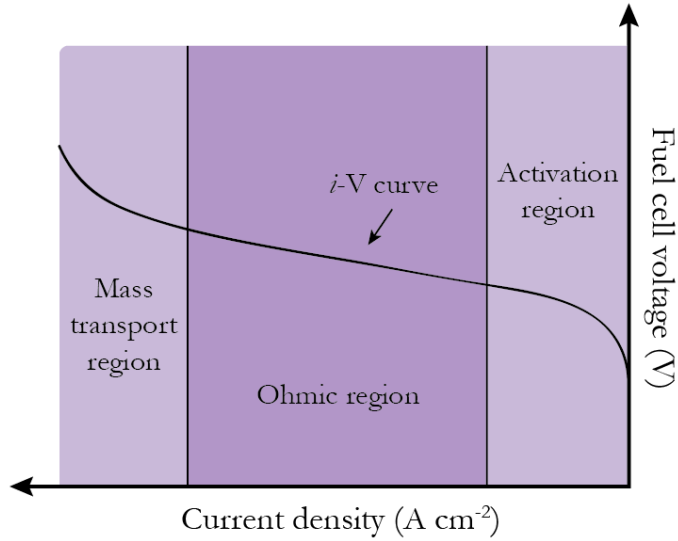
Figure 1.8: *i*-V curve of an electrolysis cell in which are highlight the activation, the ohmic and the mass transport region.

The hydrogen produced by an electrolysis device considering only steam at the fuel electrode and therefore only one chemical reaction, can be simply calculated dividing the injected current *i* by the *n* number of electros and the faraday constant F (1.16):

$$x_{produced} = \frac{|i|}{nF} \tag{1.16}$$

However, the same approach cannot be used for co-electrolysis, where two reactions are operating simultaneously. Therefore, unless a gas chromatography analysis is provided, the percentages of steam and carbon monoxide produced cannot be directly correlated to the current.

Furthermore, the simultaneous reaction of steam and carbon dioxide co-electrolysis can be complicated Water-Gas-Shift (WGS) (1.9). WGS reaction involves steam and the carbon monoxide produced by the co-electrolysis process.

Zheng *et al.* report that for WGS ΔG is zero at ≈816 °C.[47] This means that it is spontaneous only for temperatures below such threshold, while for

Advanced strategies for Solid Oxide Electrolysis Cells

T >816 °C the equilibrium moves to the reactants. In this case the carbon dioxide is reduced and RWGS occurs.[47]

Nevertheless, the conversion rate of reactants in products can be calculated by the current even for a cell which is operating in co-electrolysis mode (1.17):

$$conversion\ rate = \frac{\frac{|i|}{nF}}{x_{H_2O} + x_{CO_2}} \tag{1.17}$$

Where x_{H_2O} and x_{CO_2} are the mol min^{-1} of reactants. In this case the number of electrons $n = 2$ for both H_2 and CO produced.

Polarization curves are also common for studying the performance of SOFC devices Figure 1.9. In this case the V_{op} is given by (1.18):

$$V_{op} = V_{eq} - \eta_{act} - \eta_{Ohmic} - \eta_{conc} \tag{1.18}$$

From an SOFC i-V curve it is possible to calculate the generated power of the cell, just multiplying the measured voltage with the applied current density.[53]

Advanced strategies for Solid Oxide Electrolysis Cells
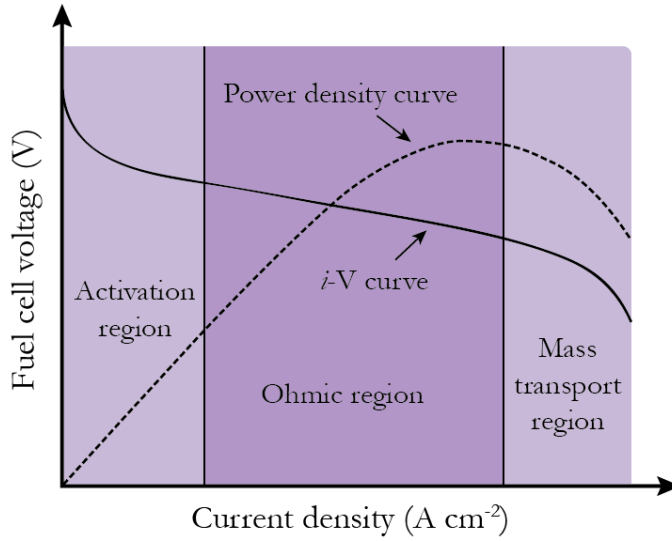
Figure 1.9: *i*-V curve of a Fuel cell in which are highlight the activation, the ohmic and the mass transport region. The power density curve is here represented with a dashed line.

Advanced strategies for Solid Oxide Electrolysis Cells

1.4 State of the art materials for SOEC

During the years, a lot of different materials were developed for the utilization in SOC applications. Figure 1.10 presents a comprehensive list of materials classified for the different applications: electrolytes, fuel electrodes and oxygen electrodes.
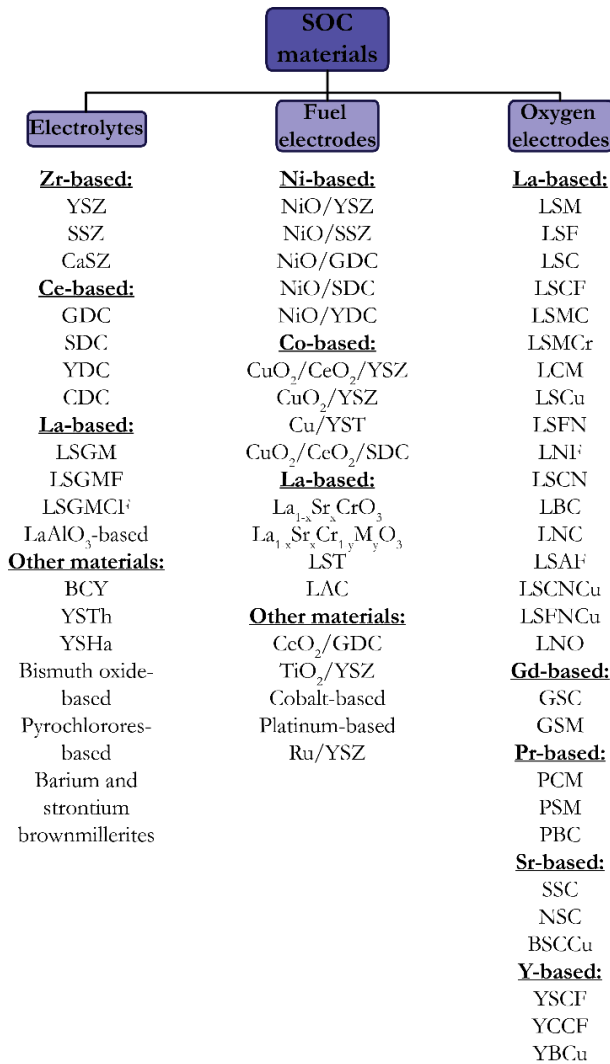
Figure 1.10: List of different SOFC/SOEC materials adapted from Wincewicz *et al.* with the permission from Elsevier.[56]

Advanced strategies for Solid Oxide Electrolysis Cells

1.4.1 Electrolyte materials

Electrolyte materials for SOEC applications should satisfy some characteristics. First of all, they should present good ionic conductivity and electronic insulation, to allow the oxygen mobility and avoid short circuits between the electrodes. The electrolyte should be chemically stable in both oxidizing and reducing environments, gastight and dense. Furthermore, the different elements of the cell should be chemically compatible among them and present a similar thermal expansion coefficients (TEC) with respect to the supporting element (e.g. YSZ in the case of an electrolyte-supported cell).[57]

Figure 1.11 shows the ionic conductivity as a function of temperature for the state-of-the-art electrolyte materials from Wincewicz *et al*.[56] Even not showing the highest conductivity, the most common materials used as electrolytes are zirconia-based and ceria-based oxides. In particular, considering zirconia, the doping with yttria $(ZrO_2)_{1-x}(Y_2O_3)_x$ (x $\approx$ 0.08–0.1) is very common and leads to ionic conductivity $\approx 2 \cdot 10^{-2}$ S cm^{-1} at 800 °C.[56] Due to its good chemical stability respect both oxidizing at reducing atmospheres YSZ, remains a reference electrolyte material for SOEC application. Among the rest of materials Gadolinium doped Ceria $(Ce_{1-x}Gd_xO_{2-\delta}$ - CGO) is worth to be mentioned. CGO has an ionic conductivity which is almost two order of magnitude larger than the one of YSZ. Despite the greater values in term of conductivity, CGO and other electrolytes present drawbacks, such electronic conductivity in reducing condition, high cost, poor stability at high temperatures and difficult in processing, which limit their technological implementation.[58]
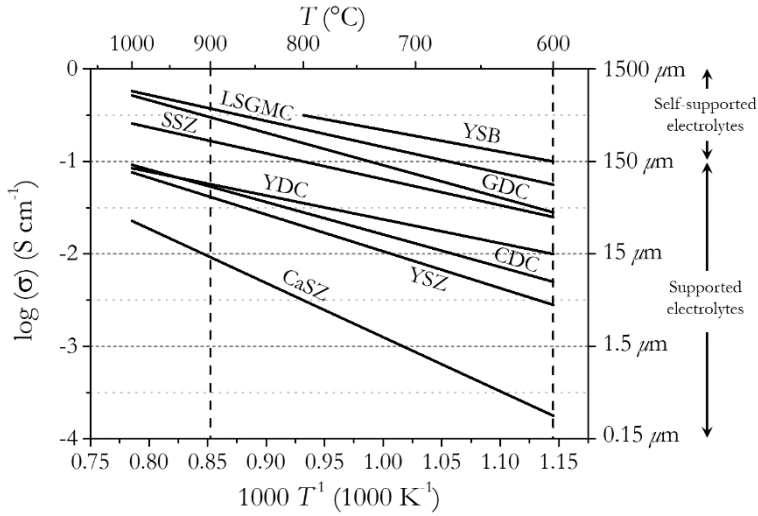
Figure 1.11: Ionic conductivity data of the main electrolyte materials for SOFC applications. Conductivity data from K. Wincewicz *et al.*[56] YSB [(Bi$_2$O$_3$)$_{0.75}$(Y$_2$O$_3$)$_{0.25}$]; LSGMC (La$_x$Sr$_{1-x}$Ga$_y$Mg$_{1-y-z}$Co$_z$O$_3$; x ≈0.8, y ≈0.8, z ≈0.085); CGO (Ce$_{0.9}$Gd$_{0.1}$O$_{1.95}$); SSZ [(ZrO2)$_{0.8}$(Sc$_2$O$_3$)$_{0.2}$]; YDC (Ce0.8Y0.2O$_{1.96}$); CDC (Ce$_{0.9}$Ca$_{0.1}$O$_{1.8}$); YSZ [(ZrO$_2$)$_{0.92}$(Y$_2$O$_3$)$_{0.08}$]; CaSZ (Zr$_{0.85}$Ca$_{0.15}$O$_{1.85}$).

1.4.2   Electrode materials

The electrodes are the part of the cell where the electrochemical reactions take place. The necessary features of a good performing electrode are:[57,59]

- Interconnected porosity to allow the diffusion of gas (fuel or oxygen) while ensuring the percolation of the electronic and ionic paths
- Good catalytic activity and high ionic and electronic conductivity
- Chemical and thermal stability under operating conditions.

The active region in which the reactions take place in an electrode is the area in which electrons, oxide ions and oxygen gas are available together.

Advanced strategies for Solid Oxide Electrolysis Cells

For electrodes characterized by poor ionic conductivity, this area is confined at the triple phase boundary gas/electrode/electrolyte (TPB).

In the case of fuel electrodes materials, electrodes are exposed to reducing conditions. They are generally formed by an ensemble of ceramic and metallic phases which is called "cermet". The reference material for fuel electrodes is NiO-YSZ, with YSZ which offers an outstanding stability in reducing conditions and has the function of providing the ionic pathway. After reduction, metallic nickel has the twofold function to provide electronic percolation to the electrode and to catalyze the reduction of hydrogen or the reforming of hydrocarbon fuels.[60]

As far as oxygen electrodes are concerned, strategies for extending the reaction area led to the introduction of materials characterized by high ionic and electronic conductivity at the same time (so-called MIEC, mixed ionic electronic conductors).[53]

In a MIEC electrode all the surface can potentially be active toward chemical reactions (two-phase boundary between solid and gas)[61]. State-of-the-art oxygen electrodes are commonly based on MIEC perovskites. In particular, $La_{1-x}Sr_xMnO_3$ (LSM) was extensively utilized for its good matching with the other elements of the cell in terms of thermal expansion coefficient, chemical compatibility and good electronic conductivity.[60] In the last decades LSM has been substituted by other perovskite able to provide a mixed ionic/electronic conductivity (MIEC) like $La_{1-x}Sr_xCoO_{3-\delta}$ (LSC) and $La_{1-x}Sr_xCo_{1-y}Fe_yO_{3-\delta}$ (LSCF).[57]

1.4.2.1 *Composite electrodes*

A major drawback for single phase MIEC is the low thermochemical stability for long-term operation at high temperatures, together with limited ionic conductivity.[61] A good strategy to stabilized the electrode performance is the formulation of composite materials coupling the MIECs with good

Advanced strategies for Solid Oxide Electrolysis Cells

ionic conductors such YSZ and particularly CGO.[57,59,61,62] The use of CGO in particular is becoming more common because of the high reactivity of the zirconia with Sr-rich oxides, which causes the formation of insulating phases during fabrication.[63,64] Fabrication of composite oxygen electrode demonstrated to be a highly promising approach to maximize the active area.[59,61,65–68] Figure 1.12 presents a sketch of a composite electrode formed by pure electronic and ionic conductive species (Figure 1.12a), formed by a MIEC (Figure 1.12b) and by an ionic conductor infiltrated by a MIEC (Figure 1.12c). One can notice that in the first case the chemical reactions are localized only at the contact points between the two phases with the gas. In the composite electrode with MIEC, all the surface of the perovskite can in principle be active towards chemical reactions, with a tremendous increase of the electrode performance. However, this consideration is intimately related to the fundamental properties of the considered MIEC and to the microstructure of the electrode. In some cases, MIECs characterized by poor ionic conductivity (e.g. LSM) are active for reactions only in the region of the TPB.[69]

Different is the case of the ionic conducting scaffold infiltrated by MIEC's nanoparticles; in this case there are much more contact points between the two phases and this mean a consistent extension of the TPB region.
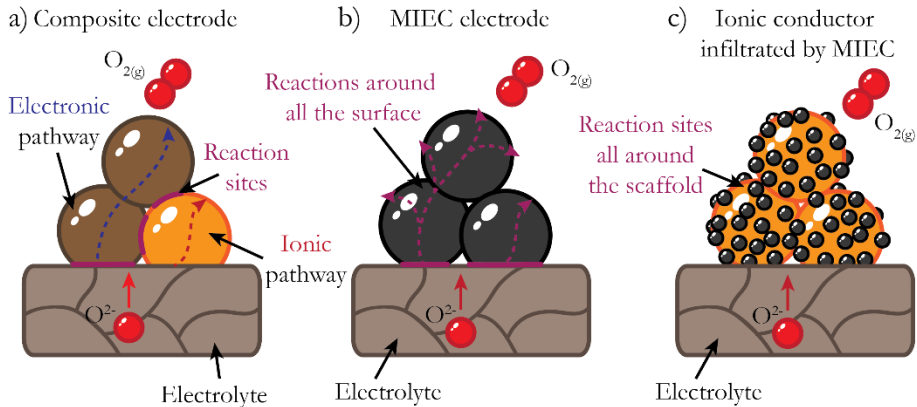
Figure 1.12: Schematic representation of three different strategies for TPB extension. Composite electrode formed by electric conductive and ionic conductive species (a), where the reactive zones are limited to the contact points (in purple). Composite electrode formed by MIEC (b) where part of the surface could be available for chemical reactions. Ionic conducting phase infiltrated by MIEC (c) where the TPB is extended because of the numerous contact point between the two phases.

Finally, Figure 1.13 shows a schematic representation of two composite electrodes in an SOEC. The fuel electrode scheme of Figure 1.13a is a cermet of metallic Ni and YSZ. In the case of the oxygen electrode (Figure 1.13b) an ionic conductor scaffold (e.g. rare earth doped ceria) infiltrated by a MIEC perovskite (e.g., LSC, LSCF, etc.), with the aim to increase the TPB of the electrode, is represented. Such strategy is also necessary to mitigate one of the main causes of failure for SOEC, which is the delamination caused by high oxygen pressure at the oxygen electrode. This is an issue especially for high current densities.[47] In the present thesis, a detailed dedicated study on composite electrodes, which specific focus on composite based on mesoporous backbones, has been carried out. In the following section (1.4.3), the fundamental aspects related to mesoporous materials are presented.
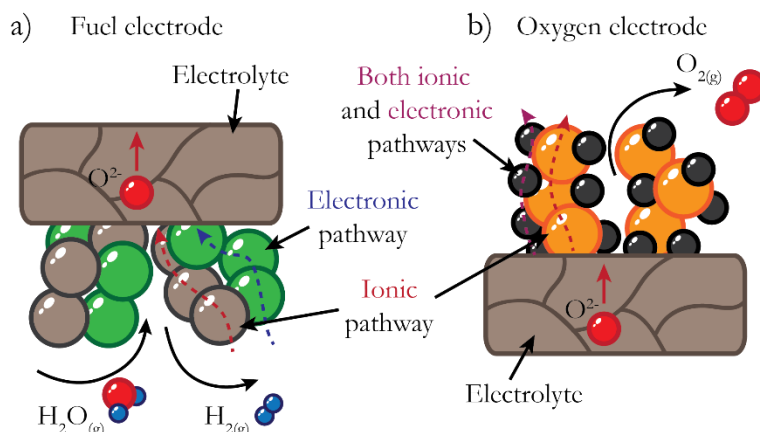
Figure 1.13: Schematic representation of the electrodes in an SOEC. The fuel electrode in figure (a) represents the typical situation where the ionic pathway is provided by YSZ and the electronic percolation by metallic Ni. The oxygen electrode (b) shows an ionic conductor scaffold (e.g. CGO) infiltrated by a MIEC perovskite (e.g. LSC or LSCF)

1.4.3   Mesoporous structures for electrode application

The use of nanostructured materials has been adopted in many fields such chemistry, physics and medicine. In particular, mesoporous materials (pores diameter 2-50 nm) can offer new opportunities for advanced energy storage and conversion technologies. They are used in supercapacitors,[70] batteries[71] and SOC devices.[72–74]

In particular, ordered mesoporous materials became an interesting research topic in 1992 when Mobil Oil Corporation (Mobil) scientists first reported the M41S series of mesoporous silica materials.[75] They are used for the fabrication of different micro and macro devices, due to the high surface area available (in the order of hundreds of $m^2 g^{-1}$), pore tunability and the high catalytic activity.[76] This periodicity of the structure makes them suitable for a wide range of application in the energy production and storage field.[75]

Mesoporous materials can present different ordered structures: two-dimensional (2D) hexagonal, space group *p6mm*, three-dimensional (3D)

Advanced strategies for Solid Oxide Electrolysis Cells

hexagonal $P6_3/mmc$, 3D cubic $Pm\overline{3}m$, $Pm\overline{3}n$, $Fd\overline{3}m$, $Fm\overline{3}m$, $Im\overline{3}m$, bicontinuous cubic $Ia\overline{3}d$, etc.[75,77]

Silica and carbon were the first materials being synthesized to obtain mesoporous structures. Among different materials, the ones presenting the $Ia\overline{3}d$ symmetry have been object of particular interest due to their bicontinuous structure (e.g. MCM-48, KIT-6 and FDU-5). As shown in Figure 1.14, such materials are characterized by two sets of helical channels separated between them.[75]
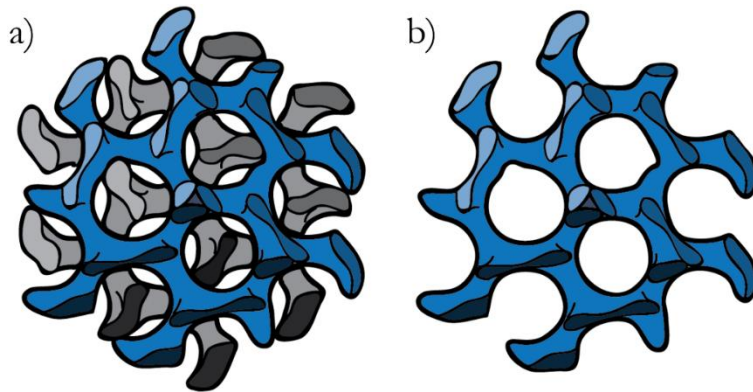
Figure 1.14: Schematic representation of mesoporous with cubic bi-continuous $Ia\overline{3}d$ geometry (a). Representation of one of the channels (b).

According to literature, the strategies to produce ordered mesoporous materials could be divided into two major groups, which are *soft* and *hard* template methods.[78–80] Soft template method consists on the utilization of surfactants or co-block polymers, and involves complex wet chemistry processes and requires a very high control of the synthesis parameters (temperature, pH, etc.). The hard-template method is a very feasible technique which consents the production of mesoporous materials with higher degree of crystallinity.[78,81] The latter has been used to obtain the materials studied in the present work.

1.4.3.1   Hard template method: The nano-casting process

The *hard template method* can be considered a real casting process, as the ones used at the macroscopic scale. For this reason, it is often called *nano-casting*, highlighting that the process is referred to the fabrication of nanometric structures.[78] It consists on an impregnation of the pre-existent mould (silica or carbon).[82] The chosen template is infiltrated at controlled temperature by a precursor solution of the desired cations in stochiometric proportions, which, after its gelification, is possible to calcinate. Lastly, the template is removed by chemical etching [83]releasing the desired mesostructured synthetized material as a replica of the removed hard template.

Figure 1.15 shows the case of the KIT-6, used in this thesis, for the synthesis of mesoporous CGO. After the template removal, the replica could present a displacement of the structure compared to the original KIT-6 symmetries. In other cases, with a careful control of the synthesis parameters (especially temperature), it is possible to fill one or both the bi-continuous channels, leading to pores around 10 or 3 nm respectively.[83,84] The most common situation is to obtain a replica that presents the combination of the three phenomena: dislocation, partial and complete filling.[75]
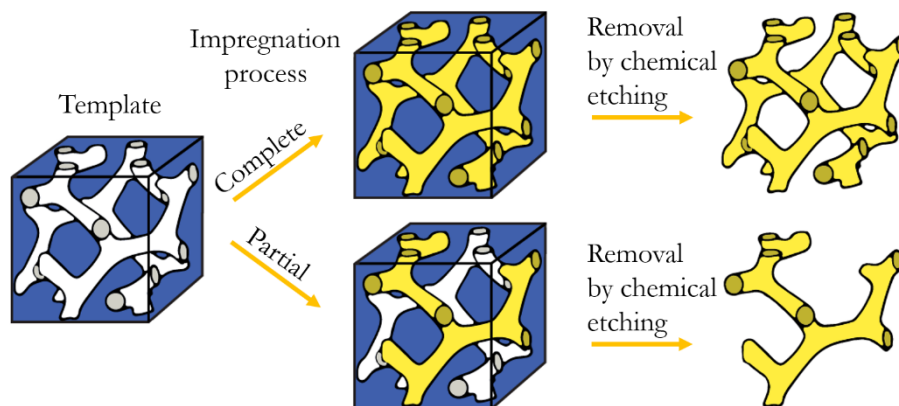
Figure 1.15: Scheme of the KIT6 nanocasting process: the control of the synthesis parameters makes possible to tune the final porosity.[83]

Advanced strategies for Solid Oxide Electrolysis Cells

An interesting characteristic of the complete filling of the mesoporous KIT-6 template is the presence of small interconnected pores (average diameter ≈2 nm) between the two bi-continuous channels in the replica.[75] This means a more interconnected porosity of the structure.

Ceria-based nanostructured backbones have been studied in the past as part of functional layers, revealing excellent mass transport and high catalytic properties.[85–89] Particularly, their utilization as scaffold for electrode application in SOC allows the fabrication of complex architecture characterized by very high porosity. The fabrication of composite layers by infiltration with MIECs can generate highly percolating networks.[90–93]

However, despite the great advantages that mesoporous materials can provide, there are still unresolved issues which limit their application at the industrial scale. First, the complete removal of the silica template is problematic. Very often the chemical etching by alkaline or acid solution is not completely effective, leading to the presence of appreciable amount of SiO_2. Another unresolved drawback is their thermal stability, especially important for high temperature applications and for high temperature steps during the fabrication of functional ceramic devices. A great variety of such materials, including most silica-based mesoporous materials or metal oxides, are not stable above 500 °C.[77] The production of mesoporous metal oxides by nano-casting pushed this thermal limit to higher temperatures. Almar *et al.* studied the stability of nanocasted mesoporous ceria upon 24 h of exposition at different temperatures, demonstrating high stability of the nanostructured architecture for temperatures in the range 600-1000 °C.[73] These results demonstrate the applicability of CGO mesoporous materials as scaffold for SOC application.[94,95]

The present work is focused on the improvement of such mesoporous materials for application in SOEC devices. The synthesis process was modified to ensure a more effective removal of the silica

contamination and to lower the sintering temperature of the material. The fundamental properties of mesoporous CGO and its structure have been deeply studied together with its electrochemical performance.

The powders obtained for the optimized route were utilized in a real SOEC device in order to test the performance in a real device showing outstanding results.

1.4.4 Catalyst materials for POM

Since the present work also deals with the application of the developed devices as POM cells, the role of the catalyst materials for the POM reaction is also presented and discussed. A fundamental role during POM processes is played by the catalyst because it can reduce the activation barrier E_a and accelerate the reaction rate. The utilization of a catalyst allows therefore to increase the methane conversion rate and to select the final product promoting the formation of syngas.[96]

The most common catalysts used for H_2 and CO production are transition metals such Ni, Co, Cu and Fe;[97–100] noble metals like Pt, Pd, Rh, Ru and Ir[35,101] and metal oxides, such Ce_2O_3, Al_2O_3.[102–104] In most cases, different catalysts are used together in order to combine different effects and maximize the advantages.[103,104]

Among the different catalysts one with the best balance between effectiveness on methane consumption and general cost is metallic Ni. Unfortunately, nickel is prone to coke deposition which could cause a fast deactivation of the device.[105] Some strategies have been studied to overcome this problem and in most of the cases they consist in the combination of Ni with other catalysts able to reduce the carbon deposition on the electrode.[105] In particular the coupling of Ni with catalytic oxides or the formation of bimetallic systems is very common.

Advanced strategies for Solid Oxide Electrolysis Cells

The main advantage of the utilization of catalytic oxides is that they can store oxygen in the lattice and due to the tolerance of their anion sublattice with respect to nonstoichiometry, they can consistently help on preventing carbon deposition.[46] However, such oxides do not have a catalytic activity strong enough to break the C-H bonds of methane and promote its reactions. They are mainly utilized to mitigate the carbon deposition effect. A widely utilized example is cerium oxide inserted as nanoparticle in an already existing scaffold or (doped by gadolinium or samarium oxides) used to fabricate the backbone for the electrode.[103,104,106]

The formation of bimetallic systems formed by Ni together with other metals such K, Au or Cu can effectively reduce carbon deposition.[107] In particular, copper has been largely used together or in substitution of nickel for SOC applications.[108] The poor catalytic activity of copper and its merely function as electronic conductor in cermet electrodes make the presence of an active species, such as Ni, essential.[104]

1.5 Additive manufacturing for SOEC fabrication

1.5.1 Additive Manufacturing principles

Additive manufacturing (AM), also called 3D printing, rapid prototyping or layer manufacturing is defined as a process able to produce a 3D object, previously designed from a three-dimensional Computer Aided Design (CAD), by the addition of material layer by layer.[109,110] The irruption of the 3D printing in the last decades, and especially with its rollout in the last years, has led to a breakthrough on the field of the materials processing. The additive manufacturing has embedded all types of materials and has been adopted at industrial and domestic level. AM technologies are substituting, in some cases, the traditional manufacturing routes based on subtractive material, machining or moulding. In particular, they can be particularly effective for the fabrication of structural and functional ceramics materials.

AM techniques was firstly developed and commercialized for polymeric materials and was lately also developed for metallic structural parts at industrial level. Due to the nature of the ceramic materials, these have been processed by additive manufacturing technologies only in the last decades. However, their application on different AM techniques awoke a great interest for the scientific community. AM fabrication ceramic materials for energy devices is part of the motivation of the present thesis.

Figure 1.16 shows a schematic representation of AM existing technologies, dividing the processing techniques by the dimensional order of the printing process. In the following paragraphs a brief description of the main AM techniques used for functional ceramic processing is reported.

Advanced strategies for Solid Oxide Electrolysis Cells
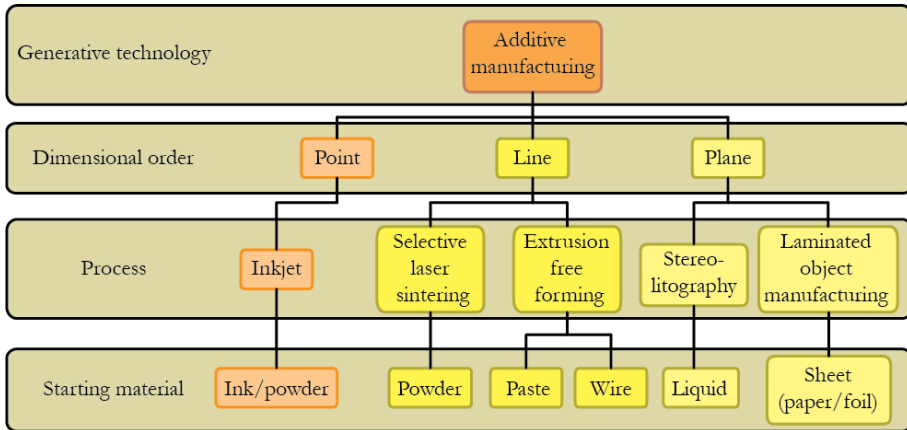
Figure 1.16: Hierarchical representation of AM techniques classified by their dimensional order: point, line and plane. Figure represented with the permission from Energy Environ. Sci., 2017,10, 846-859 - Published by The Royal Society of Chemistry.[111]

Stereolithography (SLA) is characterized by the conversion of a liquid photosensitive resin to a solid state by selective exposure of a resin vat to ultraviolet light.[112] Furthermore, SLA can be used with a large amount of pastes also loaded by ceramics materials.[113] SLA can print high-dense pieces with good surface definition.

One of the most known filament-based technique is the Extrusion Free-Forming (EFF) also called Fuse Deposition Modelling (FDM). In FDM a thermoplastic material, such as Acrylonitrile Butadiene Styrene (ABS) and PolyLactic Acid (PLA), is extruded through a nozzle, which moves along three axes by a computer-controlled mechanism. The materials is melted inside a liquefier and pushed out by the solid upstream filament.[114] FDM has been used also for the deposition of metallic filaments and viscous slurries with load by ceramic oxide materials.[111] FDM is economic, fast and large size capability techniques, which drawbacks are the surface finishing of the final piece and the limited amount of materials which can be used.[111]

Selective Laser Sintering/Selective Laser Melting (SLS/SLM) technology uses metals, ceramics, plastics as starting material. This makes it

possible to fabricate fully functional parts without using any intermediate binders.[115] In SLS/SLM a laser beam scans over the surface of a thin powder layer previously deposited on a substrate. Each layer is formed by sintered/melted lines of the starting material.[115] The main drawback of this technique is the surface finishing of the final piece. When applied to metals or ceramics, materials with high melting points, other limitations are present. The thermal shock due the printing process could lead to poor mechanic stability or crack formation.[111]

InkJet printing (IJP) is a precise printing technique characterized by high resolution, in which droplets of ink (1 nL - 1 pL) are deposited on a substrate directed by electrostatic forces. The domestic IJP application is printing black ink on paper, but in the recent decades the technology gained new attentions becoming a very versatile technique. In fact, IJP is used for the deposition of sub microparticles (e.g. precious metal and ceramic materials) for different kind of applications:[116–118] electronics,[119] rapid prototyping,[120] ceramic based components[116,117] and sensors.[121] In IJP the viscosity range for ceramics-based inks is 1-20 mPa s and thickness ranging goes from below 100 nm to 100 μm.[122,123] The low solid loading of the inks (1-10 %vol) make IJP very time consuming.

Robocasting (RC), also known as direct ink writing (DIW), is an AM process in which a filament of extruded viscous slurry is deposit layer by layer though a nozzle controlled by a computerized system to reproduce a CAD designed object. The nozzle diameter usually below 1 mm defines the filament dimension. In recent years, it has become a very utilized technique to produce components and devices like biocompatible scaffold for medical applications,[124] catalyst support materials for power generation[125] and ceramics structures for energy storage and environmental applications.[126–128] In the case of ceramic slurries, the average thickness of a layer is 100-200 μm.[129] RC is faster than other 3D printing techniques but is characterized

Advanced strategies for Solid Oxide Electrolysis Cells

by less resolution. RC allows the multi-material printing, which is an interesting feature for energy devices 3D printing. However, co-sintering of different materials is still an issue.[129]

1.5.1.1   *AM for functional ceramics*

Because of their fundamental properties (e.g. high melting point, great hardness and strength) ceramics materials have been traditionally limited in their forming process to very simple shapes (i.e. square sheets, cylindrical tubes, etc.). In SOC field the most used techniques for producing substrates materials are tape casting and tape calendaring. In tape casting a layer of ceramic liquid paste is spread on a temporary support with a doctor blade. The film is subsequently dried and separated from the temporary support to be fired at high temperature.[58] Tape calendaring consists in a viscous paste which is squeezed between two rolls obtaining a continuous sheet of tape. The thickness is adjusted by regulating the distance between the rolls. Afterwards the tape is fired at high temperature.[58]

The most common deposition techniques, used in SOC processing need a pre-existing substrate (e.g. screen printing, sputtering, dip coating, spin coating, spray pyrolysis, electrophoretic deposition, etc.),[58] limiting the designs.

Therefore, additive manufacturing, with its capacity to easily produce pieces with more complex shapes, opened a new perspective in the field of the solid-state devices.[130,131] In thesis Inkjet printing and Robocasting were used for the fabrication of devices. Their main principles and application on the generation of functional ceramic devices will be extensively discussed in the following sections. Such techniques are generically considered *slurry-based* technologies, because they involve ceramic particles dispersed in liquid or semi-liquid systems. Very liquid inks or viscous pastes can be formed depending on the solid load and the addition of different additives.[109,132] The

formulation of the ink/slurry is of great importance for the final result of the printing process.

1.5.2   Inkjet printing process

There are basically two strategies for the generation of the stream of droplets necessary for the deposition, which are the continuous inkjet (CIJ)[116,133,134] printing and the drop-on-demand (DOD)[116,135,136] inkjet printing. CIJ was the first type of printers to be developed. It consists of a pressurized flow of ink which generates a continuous stream of drops through a micro-scaled nozzle. When the printing is not required, the stream is just deflected to a gutter for being recycled.[116] This fact exposes the ink to possible contamination. CIJ produces a great volume of ink per minute but it is limited in terms of placement accuracy and it is mainly used for marking and coding.[117]

DOD-IJP is based on a different strategy, a stream of droplets is generated only when is required for the printing avoiding unnecessary waste of material.[117,136] Naturally, the strategy for generating the drop is different and consists in a pressurized liquid which generates droplets driven by Ryleigh instability., The so called *compressive element* which is usually constituted by a small heater has the function to generate the force necessary to overcome the surface tension of the liquid (Figure 1.17a). Such heater generates a steam bubble inside the ink chamber forcing the liquid out. Another type of compressive element quite used is constituted by a piezoelectric piece, that contracts by the simply application of a voltage and *pushes* the ink out (Figure 1.17b).[116,117]

Advanced strategies for Solid Oxide Electrolysis Cells
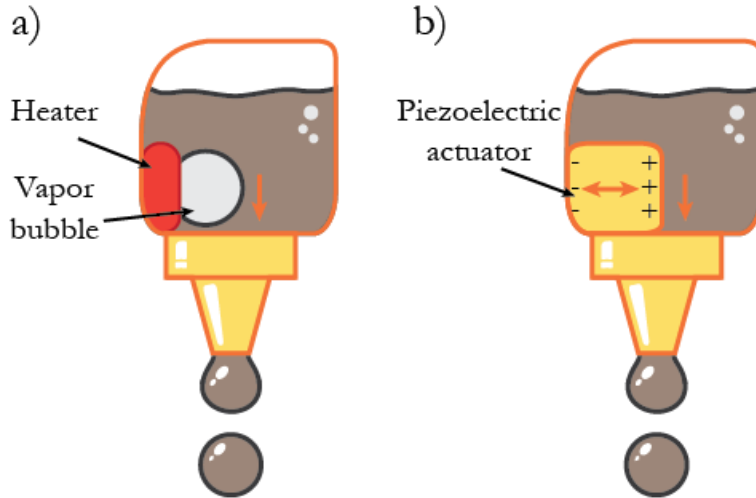
Figure 1.17: Schematic representation of the two strategies to generate a droplet in a DOD inkjet printer, which consist a) in a small heater which generates a vapor bubble (a) or a piezoelectric element (b) which contracts by the application of a voltage. In both cases the ink is pushed out overcoming its own surface tension.

DOD-IJP has been used in the field of SOCs to produce different components, from dense electrolytes[137] to the functionalization of composite electrodes by infiltration increasing the TPB.[138–140]

DOD-JIP grants a great customization of the printing object with limited waste of the produced ink. It allows the multi-material printing with the utilization of different printheads. Furthermore, the printing process is characterized by high resolution due to the small dimension of the droplets.

The volume range of a single drop is 1 pL - 1nL, which approximately corresponds to a diameter of 10-100 μm in flight. Droplets deposited on a substrate tend to coalesce in a single object, driven by capillary forces. This process is influenced by the interaction with the substrate and can lead to some printing limitations. After the deposition the layer shrinks because of the evaporation of the solvent.[117] The printing of dense films with thicknesses < 10 μm by means of DOD-IJP was demonstrated by different publications.[137,141–143]

In Table 1.3 are reported the main works that used DOD-IJP to produce SOFC components using state-of-the-art materials.

Table 1.3: Main references about YSZ and LSCF inks for inkjet printing.

Material	Solvent	Z number	Reference
NiO-YSZ	α-terpineol	-	Sukeshini et al.[144]
NiO-YSZ	α-terpineol	-	Sukeshini et al.[145]
LSCF	Water	-	Yashiro et al.[146]
YSZ	Water	7	Li et al.[142]
LSCF	α-terpineol	2.5-25	Hill et al.[147]
YSZ	Water	6-3	Esposito et al.[143]
YSZ	Water	4-9	Farandos et al.[137]
LSCF	Water	-	Han et al.[148]
YSZ	α-terpineol	-	Tomov et al.[149]
YSZ	Water/ethanol	1-3	Gadea et al.[150]
LSCF	Hydroxypropyl cellulose	-	Tomov et al.[151]
YSZ	Water	1.6-25	Rosa et al.[152]
YSZ	Water	8	Farandos et al.[123]
LSCF	Water	4-7	Chen et al.[153]
YSZ	TMPTA	6.7-9.2	Rosa et al.[154]
LSCF	hydroxypropyl cellulose	-	Venezia et al.[155]
NiO-YSZ	Isopropanol	4.3-11.3	Rosa et al.[156]
YSZ	Isopropanol	2-4	Salari et al.[157]
YSZ	Water/ethanol	6-9	Han et al.[158]

DOD-IJP has also been used for automatic infiltration on pre-existent scaffolds. Infiltration is one of the largely used method for the production of composite materials.[159–161] It allows to process potentially highly reactive materials at low temperature and takes advantage of the mechanical stability provided by backbones which are usually already sintered at high temperature.[59] Infiltration process can be done with the utilization of metal-salt solutions,[159] nanoparticles in suspension[162] and molten salt.[163]

Advanced strategies for Solid Oxide Electrolysis Cells

In particular infiltration by metal-salt solution is the most widely utilized, because of its feasibility and the larger abundancy of materials.[59] It involves the utilization of different additives to ensure a proper dispersion such urea, citric acid, glycine, ethylene glycol, etc.[159]

1.5.3 Robocasting process

RC can print self-sustained pieces, with minimum waste of ink compared to other slurry-based technology. It allows the utilization of pastes with high solid loading, reducing the risk of cracks formation during shrinkage. Multi-material printing of objects is also a possible feature for RC processing

RC does not rely on solidification for the printing of self-sustainable structures, but rather in rheology. This means that during the printing process no thermal gradients, which could lead to the cracking of the layer, are expected.[164] However, the main challenge of RC as deposition technique is related to the multi-material deposition. Shrinkage mismatch between different materials during the co-sintering process can lead to the cracking of the final piece.[129]

Figure 1.18 shows the schematic representation of the robocasting printing process. During the printing, a piston driven by pneumonic or a mechanic force, pushes the slurry out a conical nozzle.[129] The dimension of the nozzle determines the final diameter of the filament. The nozzle can move in the horizontal plane building layer by layer the 3D object.
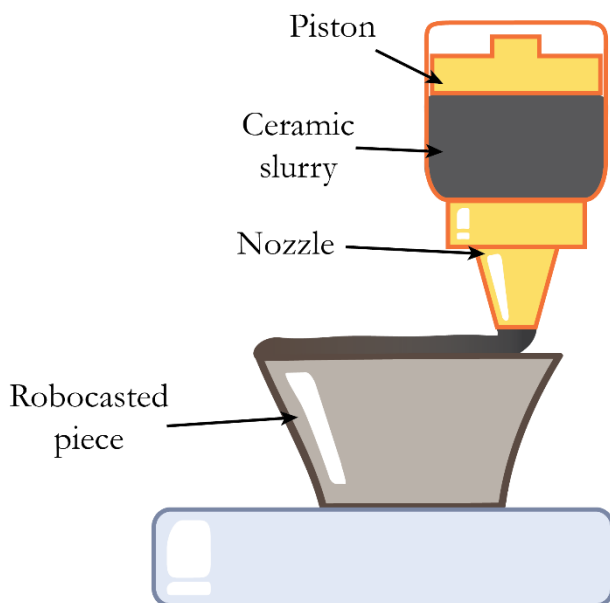
Figure 1.18: Schematic representation the robocasting printing process. One can notice the piston which presses the ink out of the nozzle. The piece is printed layer by layer with the nozzle which moves in the x, y plane.

1.5.3.1 *Robocasting applied to ceramic materials*

The RC technique was firstly patent by Ceserano's group for colloidal systems, opening to the possibility of print ceramic materials[165] and therefore to the possibility of the application of 3D printed energy devices. RC became a common technique for the deposition of different oxides (e.g. ZnO, Al_2O_3, etc.).[129] In the present thesis, RC technology has been used for printing doped zirconia and LSM. Table 1.4 reports the main contributions found in literature related to the use of RC for SOC materials

Table 1.4: Main references about YSZ and LSM slurries for robocasting.

Material	Solvent	Application	Reference
YSZ	Stearic acid + wax	-	Grida et al.[166]
NiO-YSZ, YSZ, LSM	Terpineol	Fuel cells	Khun et al.[167]
YSZ	Poly(ethylenimine)	-	Kondo et al.[168]
NiO-YSZ, YSZ, LSM	α-terpineol	Fuel cells	Desai et al.[169]

Advanced strategies for Solid Oxide Electrolysis Cells

YSZ	Ammonium polyacrylate	-	Liao et al.[170]
ZrO$_2$	Water based	-	Shao et al.[171]
YSZ	Pluronic F-127®	Fuel cells	Cabezas y Peñalva[172]
YSZ	Water based	-	Peng et al.[173]
YSZ	Pluronic F-127®	Fuel cells	Claude[174]
NiO-YSZ, YSZ, LSM	DPG, Acrylic monomer	Fuel cells	Rosa[175]

1.5.4 Inks formulation

In both DOD-IJP and RC there are several characteristics which an ink should satisfy to ensure a good printing. The ceramic suspension should be stable over a long period of time. It is also important that no significant segregation or agglomeration are formed during the process. Additionally, the ink must have fluid and rheological properties which allows the reproducibility of the deposited layer.

In AM processing based on ink/slurry, the principles which can lead to solidification of the printed liquid ink can be different. Solidification can be obtained by crystallisation, liquid to glass transition, gelation, polymerisation, dilatant transition or solvent evaporation.[176] FDM of thermoplastic materials is a typical example of liquid to glass transition. For ceramics material this is not a viable option and therefore the inks/slurries produced rely generally on gelification, polymerization or solvent evaporation.[176]

1.5.4.1 *Rheological requirements of inkjet printing inks*

DOD-IJP typical inks for printing of ceramic materials are colloidal suspension and sol-gel solutions. Such inks are usually characterized by density ≈1 g cm^{-3}, viscosity in the range 1-30 mPa s and surface tension 35-70 mN m^{-1}.[177] Colloidal suspensions can be prepared using both aqueous or

non-aqueous mediums, granting different properties in terms of rheological properties of the ink. Sol-gel solutions realized by the utilization of organometallic compounds or more frequently by metal salt precursors and additives. The salts can be dissolved in both aqueous and non-aqueous solvents.

In order to ensure a good final result of the deposition process in DOD-IJP deposition a good knowledge of the rheological properties is necessary. Without a deep control of such properties the deposition process could be characterized by the clogging of the nozzles, the formation of satellite drops[178] or also of the *splashing*[118] of the liquid on the substrate.

In literature, Reynolds (*Re*) (1.19) and Weber (*We*) (1.20) numbers are often used to describe the properties of inks:[116,179]

$$Re = \frac{v \varrho a}{\eta} \tag{1.19}$$

$$We = \frac{v^2 \varrho a}{\gamma} \tag{1.20}$$

Where v is the velocity of the droplet, a is its average diameter (which correspond to the nozzle diameter), ϱ, η and γ are density, dynamic viscosity, and surface tension of the ink. *Re* and *We* numbers are often combined to give the Ohnesorge (*Oh*) number (1.21)(1.21):[116]

$$Oh = \frac{\sqrt{We}}{Re} = \frac{\eta}{\sqrt{\gamma \varrho a}} \tag{1.21}$$

Although in literature the utilization of the parameter Z, which is the inverse of the *Oh* number (1.22), is quite common:[136]

$$Z = Ob^{-1} = \frac{Re}{\sqrt{We}} = \frac{\sqrt{\gamma \rho a}}{\eta} \qquad (1.22)$$

The reason of the success of Z as parameter to investigate the printability come from its independence form the jetting speed of the ink and by the fact that is determine only by parameters which are quite simpler to measure, like the diameter of the nozzle and the rheological properties of the inks. Common printability ranges for the Z number are $1 \leq Z \leq 10$[180,181] and $4 \leq Z \leq 14$.[182] Recently Z range was modified to $1 \leq Z \leq 20$.[136]

1.5.4.2 *Rheological requirements of robocasting inks*

For RC application are mostly used water-based or organic-based slurries. The water-based slurries grant lower toxicity and slower drying, while the utilization of organic-based slurries which allows fast born-out and high densities.[164]

Considering organic-based slurries, the polymeric matrix is charged with micrometric or submicrometric powders of the desired ceramic load and other additives to tune the final structure of the piece (e.g. pore formers).[164] The matrix is usually a monomer mixed with another component which can trig the polymerization of the solvent and is usually activated by heat or light. Eventually the polymer is burnt in furnace together with eventual additives and the piece is sintered at high temperature.[183]

To ensure a good printability the viscous ceramic slurry should comply with the characteristics described by the Herschel-Bulkley model (1.23):[129,184]

$$\tau = \tau_y + K\dot{\gamma}^n \qquad (1.23)$$

Where τ is the shear stress, K is the viscosity parameter, $\dot{\gamma}$ is the share stress, n is the shear thinning exponent (<1) and τ_y is the yield stress beyond which the slurry starts to present a shear-thinning flow behaviour.

The viscoelastic modulus of the slurry does not change until the yield stress (τ_y) is reached, breaking the bonds of the colloidal suspension and letting the slurry flow through the nozzle.[165] When the filament is deposited and the stress goes below the yield value, the viscoelastic modulus goes back to its starting condition; this guarantees enough mechanical stability to the printed piece before the curing of the polymeric matrix.[165,184]

The slurry should generally satisfy the characteristics of a reversible shear-thinning behaviour. In order to facilitate material extrusion and to retain the shape afterward, viscosity should be around 10–100 Pa s at high shear rate. Furthermore, the slurry should be free of particle agglomerates to avoid clogging the nozzle. Lastly, the elastic modulus G' should be > 200 Pa to allow structural self-support.[129]

1.5.4.3 Principles of colloidal suspensions

In chemistry a suspension is a heterogeneous mixture in which solid particles are not dissolved in a liquid medium. Suspensions are generally classified as *colloidal* when the average diameter of the powders constituting the solid loading is in the range of 10^{-3}-1 μm, therefore when the energy associated to the surface area of the powders could play an active role with respect to the stability of the suspension itself.[185–187]

Van der Waals forces on dry particles can drive to agglomeration or to aggregation, in the first case the particles are joined by their corners giving low density structures, while in the second case they have their faces touching, leading to high density structures. This is schematically represented in Figure 1.19. When powders are mixed in a liquid medium a good wettability is necessary in order to ensure a proper stability of the

Advanced strategies for Solid Oxide Electrolysis Cells

suspension.[188] To make that possible one simple approach could be the application of some mechanical stimulation to break these agglomerates/aggregates and the utilization of wettability agents. This depends on the nature of the interaction between the particle and the liquid medium (e.g. carbon black owes its poor wettability in water to its low surface energy in aqueous mediums).[188]
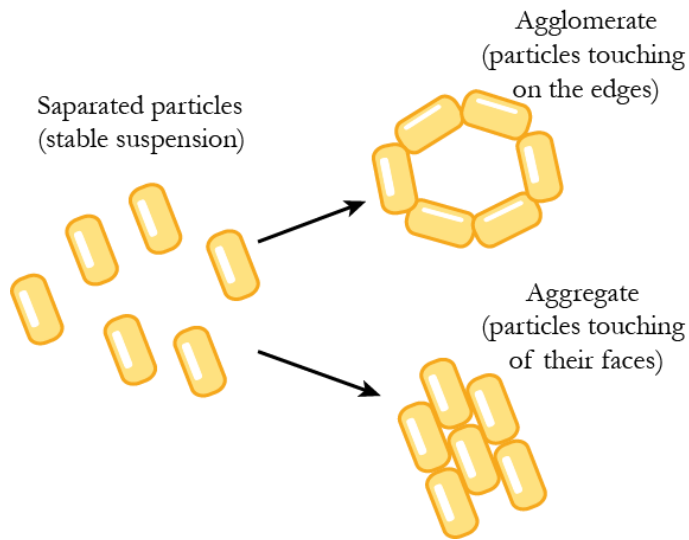
Figure 1.19: Schematic representation of the difference between a stable suspension, in which the particles are not in contact and when agglomerates and aggregates are present. Agglomerates are formed by particles which are in contact by the corners, leading to weak interactions. Aggregates are constituted by particles touching on their faces and they are more difficult to break.

However, agglomerates driven by Van der Waals Forces could also be formed once the solid load is dispersed in the liquid. It is necessary to overcome the magnitude of such interactions to prevent an unwanted destabilization of the colloidal suspension. In general, additives to keep separated the particles by *electrostatic* and/or *steric* repulsive forces are utilized (see Figure 1.20).[189] Its amount should be calculated considering the surface area of the particles to guarantee a proper steric stabilization.[188,190,191]
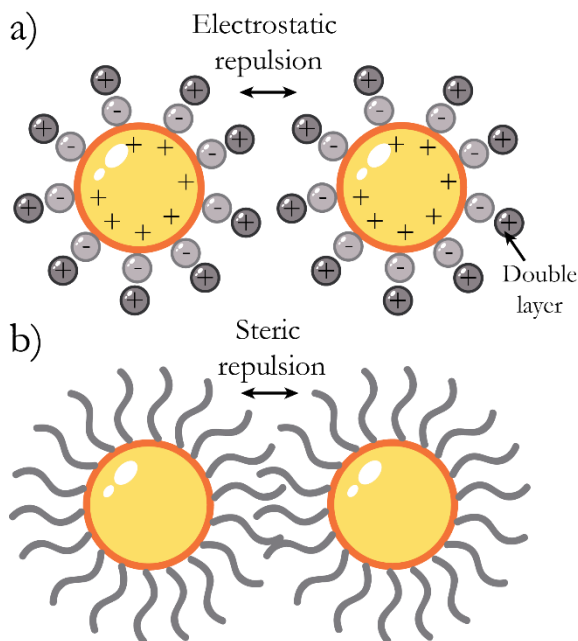
Figure 1.20: Schematic representation of the two different mechanisms to avoid particle agglomeration: a) electrostatic and b) steric repulsion.

1.5.4.4 Principles of sol-gel chemistry

Sol-gels are colloidal suspensions in which metal alkoxide (M-OR) or metal salts together with complexing agents (e.g. citric acid, Ethylenediaminetetraacetic acid, amino acids, etc.), dispersed in a liquid medium (*sol*), form complex 3D networks (*gel*) characterized by high degree of purity through hydrolysis and condensation reactions.[192,193] Sol-gels are widely used in the field of ceramic materials and allowed for the production of high purity ceramics,[194,195] ultrafine powders[196,197] and also thin films,[198–200] coatings[201–203] and dense bulk materials.[192]

Sol-gel has been also used in recent years for the formulation of inks for additive manufacturing deposition, in particular for DOD-IJP.[133,150] With respect to colloidal inks, sol-gels do not need steps such as sintering at high temperatures to become dense. The only thermal treatment that they need is a calcination process to remove the organic part of the solution.[150] In recent

Advanced strategies for Solid Oxide Electrolysis Cells

years, DOD-IJP sol-gel inks for printing different kind of ceramic oxides such TiO_2,[204] Al_2O_3,[133,205] CGO,[206] YSZ have been prepared.[150]

Hydrolysis and condensation are two competitive processes which affect the nucleation and growth evolution during the formation of the network and therefore are directly correlated to the final structure of the gel. The pH of the solution greatly influences the growth process (Figure 1.21). Generally, in literature, there are two different mechanisms to consider: the first one is the *monomer-cluster*, which is predominant when the pH is around 7. Here the hydrolysis is the limiting reaction generating a highly ramification of the cluster. The second one is the *cluster-cluster* mechanism for very acid solutions, where the condensation limits the process and the hydrolysis reactions are finished long before the gelification of the colloidal suspension, producing long chain clusters.[207,208]
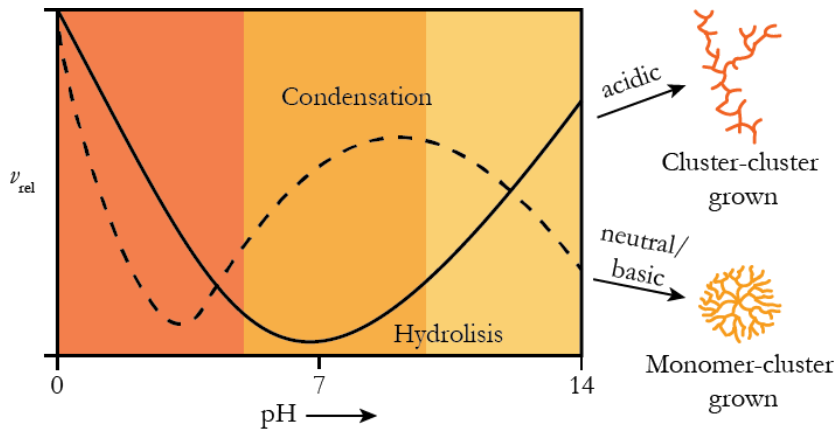
Figure 1.21: pH dependence of the hydrolysis and condensation process, which determine the growth mechanism of the clusters. For low pH values long chain cluster are promoted, while when pH is close to neutrality or slightly alkaline the cluster is characterized by high ramification.

In addition, the final results of the synthesis could be defined by the controlled removal of the liquid substituted by the vapor phase, maintaining the pre-existent structure and generate a so called *aerogel*.[209,210] On the contrary, if the gel is dried in air or in an oven, the network shrinks and

Advanced strategies for Solid Oxide Electrolysis Cells

eventually collapses forming a *xerogel*, which could be subsequently converted in a dense or porous coating with a proper thermal treatment.[193,211,212]

As it has been already mentioned, the gelification of a colloidal suspension using metals salts and complexing agents can also take place. Complexing (or chelating) agents are compounds which react with metal ions to form a stable and soluble complex. This is the case of the well-known Pechini method to produce alkaline earth titanites, developed by Maggio Pechini in 1967.[213]

In Pechini's method, citric acid is used as chelating agent because of its high stability due to the strong coordination to metal cations. The addition of ethylene glycol promotes the formation of an ester and then the formation of the network though condensation.[214] Another useful, and very well know approach, similar to Pechini's is the so called *glycine combustion method*. The utilization of glycine (amino acid) as chelating agent is particularly effective due to its ability to operate with metal cations with different ionic sizes and it is therefore quite advantageous for the production of complex oxides, such perovskites, constituted by multiple cations (e.g. LSM, LSC, LSCF).[215,216]

1.6   Scope of the thesis

The scope of this thesis is to explore advanced materials and manufacturing concepts for the next generation of Solid Oxide Electrolysis Cells. In this regard, additive manufacturing is evaluated here as a potential key enabling technology for the fabrication of enhanced layers for SOC cells that will facilitate the future implementation of high materials complexity. Complementary, advanced nanocomposites for electrodes are proposed in this thesis with the main goal of improving the performance and durability of currently existing SOECs by taking advantage of an intimate intermixing of their parent compounds. Finally, the previous advances will be employed in this thesis to evaluate a novel concept such as the use of SOEC cells for the electrochemical conversion of methane into hydrogen.

According to this, the thesis is focused on the following aspects:

- Development of AM techniques such as inkjet printing or robocasting to fabricate enhanced SOC layers.

- Introduction of improvements in mesoporous CGO for application as scaffold for oxygen electrodes in real devices. Particularly this work developed a strategy to enhance the material's chemical homogeneity and the attachment to the electrolyte

- Study of the performance of full devices based on enhanced mesoporous CGO as oxygen electrode backbone. The performance of SOC cells was studied together with its long-term stability. Mesoporous CGO was also deposited on large area cells ($\approx$25 cm^2) to prove its scalability. The large area device was electrochemically tested and a durability test was made

- Exploration of strategies for syngas production through the utilization of SOC devices. In particular, the electrochemically assisted partial oxidation of methane was simulated and tested in a real device.

1.6.1 Organization of the thesis

Figure 1.22 presents a scheme showing the main topic of the thesis associated to the different chapters.
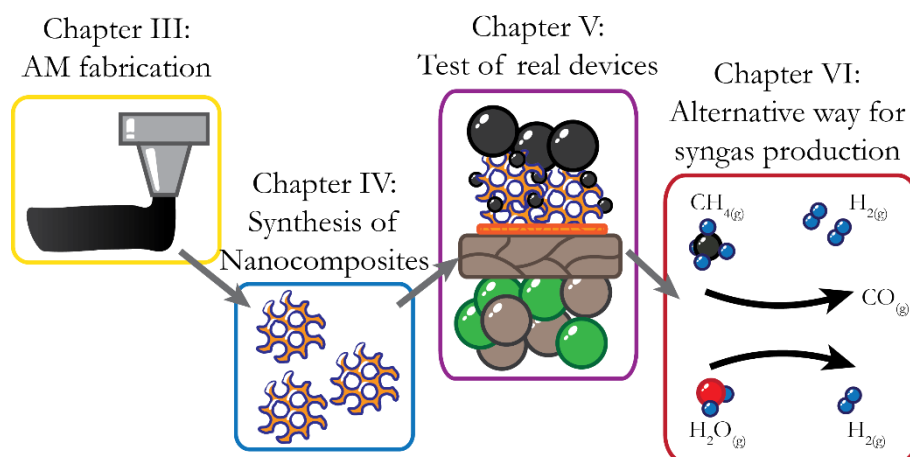
Figure 1.22: Concepts scheme of the organization of the thesis.

Chapter 2: shows the experimental method used in this work. The fabrication of the mesoporous powders, the formulation of the inks for inkjet and robocasting, the fabrication of the devices and the characterization techniques are extensively described in this chapter.

Chapter 3: reports all the results related to the devices produced by AM processes. The first part is dedicated to the automatic infiltration of functional perovskites by inkjet printing. The second part is focused on the hybrid printing of symmetrical cells (LSM-YSZ/YSZ) by robocasting and inkjet printing.

Advanced strategies for Solid Oxide Electrolysis Cells

Chapter 4: shows the results on the properties of mesoporous CGO and the optimization made on the material. The first part is dedicated to the description of the optimized route for the synthesis of the nanostructured powders and the results of their characterization. Afterwards the chapter moves to the electrochemical characterization of symmetrical cells produced using the nanostructured powder.

Chapter 5: presents the results of complete devices with oxygen electrode composed by mesoporous CGO. The first part is dedicated to the measurements of a cell with mesoporous scaffold produced with the optimized route formulated in Chapter 4. The second part is dedicated to the measurements of large area cells (5×5 cm^2) with mesoporous CGO scaffold at the oxygen electrode, as a scale up of the optimised SOEC cells fabrication.

Chapter 6: shows the preliminary result of the proof of concept for the application of the developed devices as electrochemical assisted POM reactors. The chapter starts with the fabrication of the specific devices, followed by a theoretical study based on the simulation of the main possible reactions at different temperature. Finally, the electrochemical characterisation of the produced devices is discussed together with the compositional produced gas analysis by gas chromatography.

The conclusions are summarized in **Chapter 7**

1.7 Bibliography

1   Intergovernmental Panel on Climate Change, Ed., *Communication from the Commission to the European Parliament, the Council, the European Economic and Social Committee and the Committee of the Regions*, Brussels, 2020.

2   N. S. Lewis, G. Crabtree, A. J. Nozik, M. R. Wasielewski, P. Alivisatos, H. Kung, J. Tsao, E. Chandler, W. Walukiewicz, M. Spitler, R. Ellingson, R. Overend, J. Mazer, M. Gress, J. Horwitz, C. Ashton, B. Herndon, L. Shapard and R. M. Nault, *Basic Research Needs for Solar Energy Utilization. Report of the Basic Energy Sciences Workshop on Solar Energy Utilization, April 18-21, 2005*, 2005.

3   J. O. Abe, A. P. I. Popoola, E. Ajenifuja and O. M. Popoola, *Int. J. Hydrogen Energy*, 2019, **44**, 15072–15086.

4   Heat values of gases, https://www.world-nuclear.org/information-library/facts-and-figures/heat-values-of-various-fuels.aspx.

5   C. M. Stoots, J. E. O'Brien, J. S. Herring and J. J. Hartvigsen, *J. Fuel Cell Sci. Technol.*, 2009, **6**, 0110141–01101412.

6   J. R. Mrorante, T. Andreu, G. Garcia, J. Guilera, A. Tarancón and M. Torrell, *Hidrógeno Vector energético de una economía descarbonizada*, 2020.

7   S. S. Penner, *Energy*, 2006, **31**, 33–43.

8   I. Staffell, D. Scamman, A. Velazquez Abad, P. Balcombe, P. E. Dodds, P. Ekins, N. Shah and K. R. Ward, *Energy Environ. Sci.*, 2019, **12**, 463–491.

9   M. Ni, M. K. H. Leung and D. Y. C. Leung, *Int. J. Hydrogen Energy*, 2008, **33**, 2337–2354.

10   J. R. Rostrup-Nielsen, *Catal. Today*, 2002, **71**, 243–247.

11   W. L. L. Becker, R. J. J. Braun, M. Penev and M. Melaina, *Energy*, 2012, **47**, 99–115.

12   L. Chen, F. Chen and C. Xia, *Energy Environ. Sci.*, 2014, **7**, 4018–4022.

13   S. D. Ebbesen, C. Graves and M. Mogensen, *Int. J. Green Energy*, 2009, **6**, 646–660.

14   A. Mohammadi and M. Mehrpooya, *Energy*, 2018, **158**, 632–655.

15   A. Keçebaş, M. Kayfeci and M. Bayat, in *Solar Hydrogen Production: Processes, Systems and Technologies*, 2019, pp. 299–317.

16   Y. Song, X. Zhang, K. Xie, G. Wang and X. Bao, *Adv. Mater.*, 2019, **31**, 1–18.

17   F. Barbir, *Sol. Energy*, 2005, **78**, 661–669.

18   S. Marini, P. Salvi, P. Nelli, R. Pesenti, M. Villa, M. Berrettoni, G. Zangari and Y. Kiros, *Electrochim. Acta*, 2012, **82**, 384–391.

19   M. Bodner, A. Hofer and V. Hacker, *Wiley Interdiscip. Rev. Energy Environ.*, 2015, **4**, 365–381.

20   H. Morita, M. Kawase, Y. Mugikura and K. Asano, *J. Power Sources*, 2010, **195**, 6988–6996.

21   H. Yin, X. Mao, D. Tang, W. Xiao, L. Xing, H. Zhu, D. Wang and D. R. Sadoway, *Energy Environ. Sci.*, 2013, **6**, 1538–1545.

22   W. Weng, L. Tang and W. Xiao, *J. Energy Chem.*, 2019, **28**, 128–143.

Advanced strategies for Solid Oxide Electrolysis Cells

23   M. A. Laguna-Bercero, *J. Power Sources*, 2012, **203**, 4–16.

24   M. Reytier, S. Di Iorio, A. Chatroux, M. Petitjean, J. Cren, M. De Saint Jean, J. Aicart and J. Mougin, *Int. J. Hydrogen Energy*, 2015, **40**, 11370–11377.

25   C. Graves, S. D. Ebbesen, M. Mogensen and K. S. Lackner, *Renew. Sustain. Energy Rev.*, 2011, **15**, 1–23.

26   Z. Zhan, W. Kobsiriphat, J. R. Wilson, M. Pillai, I. Kim and S. A. Barnett, *Energy and Fuels*, 2009, **23**, 3089–3096.

27   S. D. Ebbesen, J. Høgh, K. A. Nielsen, J. U. Nielsen and M. Mogensen, *Int. J. Hydrogen Energy*, 2011, **36**, 7363–7373.

28   L. Kleiminger, T. Li, K. Li and G. H. Kelsall, *Electrochim. Acta*, 2015, **179**, 565–577.

29   D. Ferrero, M. Gamba, A. Lanzini and M. Santarelli, *Energy Procedia*, 2016, **101**, 50–57.

30   G. Matute, J. M. Yusta and L. C. Correas, *Int. J. Hydrogen Energy*, 2019, **44**, 17431–17442.

31   E. Achenbach and E. Riensche, *J. Power Sources*, 1994, **52**, 283–288.

32   Y. Wang, F. Yoshiba, M. Kawase and T. Watanabe, *Int. J. Hydrogen Energy*, 2009, **34**, 3885–3893.

33   L. van Biert, K. Visser and P. V. Aravind, *Appl. Energy*, 2020, **264**, 114748.

34   P. Gangadharan, K. C. Kanchi and H. H. Lou, *Chem. Eng. Res. Des.*, 2012, **90**, 1956–1968.

35   L. S. Carvalho, A. R. Martins, P. Reyes, M. Oportus, A. Albonoz, V. Vicentini and M. do C. Rangel, *Catal. Today*, 2009, **142**, 52–60.

36   B. Abdullah, N. A. Abd Ghani and D. V. N. Vo, *J. Clean. Prod.*, 2017, **162**, 170–185.

37   J. Guo, H. Lou, H. Zhao, D. Chai and X. Zheng, *Appl. Catal. A Gen.*, 2004, **273**, 75–82.

38   M. Usman, W. M. A. Wan Daud and H. F. Abbas, *Renew. Sustain. Energy Rev.*, 2015, **45**, 710–744.

39   R. Singh, A. Dhir, S. K. Mohapatra and S. K. Mahla, *Biomass Convers. Biorefinery*, , DOI:10.1007/s13399-019-00417-1.

40   R. Pitchai and K. Klier, *Catal. Rev.*, 1986, **28**, 13–88.

41   P. D. F. Vernon, M. L. H. Green, A. K. Cheetham and A. T. Ashcroft, *Catal. Letters*, 1990, **6**, 181–186.

42   D. Dissanayake, M. P. Rosynek, K. C. C. Kharas and J. H. Lunsford, *J. Catal.*, 1991, **132**, 117–127.

43   S. T. Oyama, P. Hacarlioglu, Y. Gu and D. Lee, *Int. J. Hydrogen Energy*, 2012, **37**, 10444–10450.

44   K. Otsuka, Y. Wang, E. Sunada and I. Yamanaka, *J. Catal.*, 1998, **175**, 152–160.

45   Y. Wang, T. Liu, S. Fang, G. Xiao, H. Wang and F. Chen, *J. Power Sources*, 2015, **277**, 261–267.

46   T. M. Gür, *Prog. Energy Combust. Sci.*, 2016, **54**, 1–64.

47   Y. Zheng, J. Wang, B. Yu, W. Zhang, J. Chen, J. Qiao and J. Zhang, *Chem. Soc. Rev.*, 2017, **46**, 1427–1463.

48   C. M. Finnerty, N. J. Coe, R. H. Cunningham and R. M. Ormerod, *Catal. Today*, 1998, **46**, 137–145.

49   K. Sasaki and Y. Teraoka, *J. Electrochem. Soc.*, 2003, **150**, A885.

50   J.-H. Koh, B.-S. Kang, H. C. Lim and Y.-S. Yoo, *Electrochem. Solid-State Lett.*, 2002, **4**, A12–A15.

51   T. Takeguchi, R. Kikuchi, T. Yano, K. Eguchi and K. Murata, *Catal. Today*, 2003, **84**, 217–222.

52   S. D. Ebbesen, S. H. Jensen, A. Hauch and M. B. Mogensen, *Chem. Rev.*, 2014, **114**, 10697–10734.

53   R. O'Hayre, S.-W. Cha, W. Colella and F. B. Prinz, *Fuel Cell Fundamentals*, John Wiley & Sons, Inc, Hoboken, NJ, USA, 2016.

54   M. Ni, *Chem. Eng. J.*, 2010, **164**, 246–254.

55   H. Fan, M. Keane, N. Li, D. Tang, P. Singh and M. Han, *Int. J. Hydrogen Energy*, 2014, **39**, 14071–14078.

56   K. C. Wincewicz and J. S. Cooper, *J. Power Sources*, 2005, **140**, 280–296.

57   N. Mahato, A. Banerjee, A. Gupta, S. Omar and K. Balani, *Prog. Mater. Sci.*, 2015, **72**, 141–337.

58   S. C. Singhal, *Solid oxide fuel cells*, 2007, vol. 16.

59   P. A. Connor, X. Yue, C. D. Savaniu, R. Price, G. Triantafyllou, M. Cassidy, G. Kerherve, D. J. Payne, R. C. Maher, L. F. Cohen, R. I. Tomov, B. A. Glowacki, R. V. Kumar and J. T. S. Irvine, *Adv. Energy Mater.*, 2018, **8**, 1–20.

60   S. C. Singhal and K. K., *High Temperature and Solid Oxide Fuel Cells*, Elsevier, 2003.

61   J. T. S. S. Irvine, D. Neagu, M. C. Verbraeken, C. Chatzichristodoulou, C. Graves and M. B. Mogensen, *Nat. Energy*, 2016, **1**, 1–13.

62   K. J. Yoon, M. Biswas, H. H. Kim, M. Park, J. Hong, H. H. Kim, J. Son, J. Lee, B. Kim and H. Lee, *Nano Energy*, 2017, **36**, 9–20.

63   H. Zhang, F. Zhao, F. Chen and C. Xia, in *Solid State Ionics*, 2011, vol. 192, pp. 591–594.

64   F. Wang, D. Chen and Z. Shao, *J. Power Sources*, 2012, **216**, 208–215.

65   W. X. Kao, M. C. Lee, Y. C. Chang, T. N. Lin, C. H. Wang and J. C. Chang, *J. Power Sources*, 2010, **195**, 6468–6472.

66   J. M. Vohs and R. J. Gorte, *Adv. Mater.*, 2009, **21**, 943–956.

67   C. Sun, R. Hui and J. Roller, *J. Solid State Electrochem.*, 2010, **14**, 1125–1144.

68   T. B. Mitchell-Williams, R. I. Tomov, S. A. Saadabadi, M. Krauz, P. V. Aravind, B. A. Glowacki and R. V. Kumar, *Mater. Renew. Sustain. Energy*, 2017, **6**, 1–9.

69   S. B. Adler, *J. Electrochem. Soc.*, 1996, **143**, 3554.

70   X. He, R. Li, J. Qiu, K. Xie, P. Ling, M. Yu, X. Zhang and M. Zheng, *Carbon N. Y.*, 2012, **50**, 4911–4921.

71   A. Eftekhari, *Microporous Mesoporous Mater.*, 2017, **243**, 355–369.

72   J. M. Serra, S. Uhlenbruck, W. A. Meulenberg, H. P. Buchkremer and D. Stöver, *Top. Catal.*, 2006, **40**, 123–131.

73   L. Almar, T. Andreu, A. Morata, M. Torrell, L. Yedra, S. Estradé, F. Peiró and A. Tarancón, *J. Mater. Chem. A*, 2014, **2**, 3134–3141.

74   Y. Chen, K. Gerdes and X. Song, *Sci. Rep.*, 2016, **6**, 1–8.

75   D. Zhao, Y. Wan and W. Zhou, *Ordered Mesoporous Materials*, Wiley-VCH Verlag GmbH & Co. KGaA, Weinheim, Germany, 2013.

76   L. Peng, J. Zhang, Z. Xue, B. Han, X. Sang, C. Liu and G. Yang, *Nat.*

Advanced strategies for Solid Oxide Electrolysis Cells

Commun., 2014, **5**, 1–7.

77 J. S. Ping and J. Liu, *Mesoporous Materials for Advanced Energy Storage and Conversion Technologies*, 2017.

78 X. Deng, K. Chen and H. Tü̈Ysü̈, *Chem. Mater*, 2017, **29**, 40–52.

79 Y. Wan and D. Zhao, *Chem. Rev.*, 2007, **107**, 2821–2860.

80 N. Hedayat, Y. Du and H. Ilkhani, *Renew. Sustain. Energy Rev.*, 2017, **77**, 1221–1239.

81 Y. Ren, P. G. Bruce and Z. Ma, *J. Mater. Chem.*, 2011, **21**, 9312–9318.

82 A. H. Lu and F. Schüth, *Adv. Mater.*, 2006, **18**, 1793–1805.

83 Y. Ye, C. Jo, I. Jeong and J. Lee, *Nanoscale*, 2013, **5**, 4584–4605.

84 L. Zhang, L. Jin, B. Liu and J. He, *Front. Chem.*, 2019, **7**, 1–13.

85 C. Sun, H. Li and L. Chen, *Energy Environ. Sci.*, 2012, **5**, 8475–8505.

86 C. Sun, J. Sun, G. Xiao, H. Zhang, X. Qiu, H. Li and L. Chen, *J. Phys. Chem. B*, 2006, **110**, 13445–13452.

87 C. Sun, H. Li and L. Chen, *J. Phys. Chem. Solids*, 2007, **68**, 1785–1790.

88 C. Sun, Z. Xie, C. Xia, H. Li and L. Chen, *Electrochem. commun.*, 2006, **8**, 833–838.

89 S. C. Laha and R. Ryoo, *Chem. Commun.*, 2003, 2138–2139.

90 L. Almar, T. Andreu, A. Morata and A. Tarancón, 2011, pp. 1647–1654.

91 L. Almar, A. Morata, M. Torrell, M. Gong, T. Andreu, M. Liu and A. Tarancón, *Electrochim. Acta*, 2017, **235**, 646–653.

92 L. Almar, A. Morata, M. Torrell, M. Gong, M. Liu, T. Andreu and A. Tarancón, *J. Mater. Chem. A*, 2016, **4**, 7650–7657.

93 H. Yang and D. Zhao, *J. Mater. Chem.*, 2005, **15**, 1217–1231.

94 M. Torrell, L. Almar, A. Morata and A. Tarancón, *Faraday Discuss.*, 2015, **182**, 423–435.

95 E. Hernández, F. Baiutti, A. Morata, M. Torrell and A. Tarancón, *J. Mater. Chem. A*, 2018, **6**, 9699–9707.

96 A. S. Larimi and S. M. Alavi, *Fuel*, 2012, **102**, 366–371.

97 J. Zhang, H. Wang and A. K. Dalai, *J. Catal.*, 2007, **249**, 300–310.

98 V. V. Chesnokov and A. S. Chichkan, *Int. J. Hydrogen Energy*, 2009, **34**, 2979–2985.

99 A. Hornés, M. J. Escudero, L. Daza and A. Martínez-Arias, *J. Power Sources*, 2014, **249**, 520–526.

100 Z. Bian, S. Das, M. H. Wai, P. Hongmanorom and S. Kawi, *ChemPhysChem*, 2017, **18**, 3117–3134.

101 A. I. Tsyganok, M. Inaba, T. Tsunoda, S. Hamakawa, K. Suzuki and T. Hayakawa, *Catal. Commun.*, 2003, **4**, 493–498.

102 S. Wang and G. Q. Lu, *Appl. Catal. B Environ.*, 1998, **19**, 267–277.

103 A. Hornés, D. Gamarra, G. Munuera, J. C. Conesa and A. Martínez-Arias, *J. Power Sources*, 2007, **169**, 9–16.

104 A. Hornés, P. Bera, M. Fernández-García, A. Guerrero-Ruiz and A. Martínez-Arias, *Appl. Catal. B Environ.*, 2012, **111–112**, 96–105.

105 W. Wang, C. Su, Y. Wu, R. Ran and Z. Shao, *Chem. Rev.*, 2013, **113**, 8104–8151.

106 Z. Liu, D. C. Grinter, P. G. Lustemberg, T. D. Nguyen-Phan, Y. Zhou, S. Luo, I. Waluyo, E. J. Crumlin, D. J. Stacchiola, J. Zhou, J. Carrasco, H. F.

Busnengo, M. V. Ganduglia-Pirovano, S. D. Senanayake and J. A. Rodriguez, *Angew. Chemie - Int. Ed.*, 2016, **55**, 7455–7459.

107   S. De, J. Zhang, R. Luque and N. Yan, *Energy Environ. Sci.*, 2016, **9**, 3314–3347.

108   R. J. J. Gorte, H. Kim and J. M. M. Vohs, *J. Power Sources*, 2002, **106**, 10–15.

109   I. Gibson, D. Rosen and B. Stucker, *Additive Manufacturing Technologies*, Springer US, 2015.

110   S. Mellor, L. Hao and D. Zhang, *Int. J. Prod. Econ.*, 2014, **149**, 194–201.

111   J. C. Ruiz-Morales, A. Tarancón, J. Canales-Vázquez, J. Méndez-Ramos, L. Hernández-Afonso, P. Acosta-Mora, J. R. Marín Rueda and R. Fernández-González, *Energy Environ. Sci.*, 2017, **10**, 846–859.

112   N. Guo and M. C. Leu, *Front. Mech. Eng.*, 2013, **8**, 215–243.

113   L. Wei, J. Zhang, F. Yu, W. Zhang, X. Meng, N. Yang and S. Liu, *Int. J. Hydrogen Energy*, 2019, **44**, 6182–6191.

114   O. S. Carneiro, A. F. Silva and R. Gomes, *Mater. Des.*, 2015, **83**, 768–776.

115   I. Yadroitsev, P. Bertrand and I. Smurov, *Appl. Surf. Sci.*, 2007, **253**, 8064–8069.

116   B. Derby, *Annu. Rev. Mater. Res.*, 2010, **40**, 395–414.

117   B. Derby, *Engineering*, 2015, **1**, 113–123.

118   S. D. Hoath, *Fundamentals of Inkjet Printing*, Wiley-VCH Verlag GmbH & Co. KGaA, Weinheim, Germany, 2016, vol. 1.

119   Z. P. Yin, Y. A. Huang, N. Bin Bu, X. M. Wang and Y. L. Xiong, *Chinese Sci. Bull.*, 2010, **55**, 3383–3407.

120   E. Sachs, M. Cima, P. Williams, D. Brancazio and J. Cornie, *J. Manuf. Sci. Eng. Trans. ASME*, 1992, **114**, 481–488.

121   A. Bietsch, J. Zhang, M. Hegner, H. P. Lang and C. Gerber, *Nanotechnology*, 2004, **15**, 873–880.

122   I. Fasaki, K. Siamos, M. Arin, P. Lommens, I. Van Driessche, S. C. Hopkins, B. Glowacki and I. Arabatzis, *Appl. Catal. A Gen.*, 2012, **411–412**, 60–69.

123   N. M. Farandos, T. Li and G. H. Kelsall, *Electrochim. Acta*, 2018, **270**, 264–273.

124   M. Li, M. J. Mondrinos, X. Chen, M. R. Gandhi, F. K. Ko and P. I. Lelkes, *J. Biomed. Mater. Res. Part A*, 2006, **79**, 963–73.

125   J. N. Stuecker, J. E. Miller, R. E. Ferrizz, J. E. Mudd and J. Cesarano, *Ind. Eng. Chem. Res.*, 2004, **43**, 51–55.

126   A. Vlad, N. Singh, C. Galande and P. M. Ajayan, *Adv. Energy Mater.*, 2015, **5**, 1–53.

127   C. Zhu, T. Liu, F. Qian, W. Chen, S. Chandrasekaran, B. Yao, Y. Song, E. B. Duoss, J. D. Kuntz, C. M. Spadaccini, M. A. Worsley and Y. Li, *Nano Today*, 2017, **15**, 107–120.

128   O. Santoliquido, G. Bianchi, P. Dimopoulos Eggenschwiler and A. Ortona, *Int. J. Appl. Ceram. Technol.*, 2017, **14**, 1164–1173.

129   E. Peng, D. Zhang and J. Ding, *Adv. Mater.*, 2018, **30**, 1–14.

130   J. Deckers, J. Vleugels and J. P. Kruth, *J. Ceram. Sci. Technol.*, 2014, **5**, 245–260.

131   A. Hagen and H. L. Frandsen, *ECS Trans.*, 2019, **91**, 235–245.

132   Z. Chen, Z. Li, J. Li, C. Liu, C. Lao, Y. Fu, C. Liu, Y. Li, P. Wang and Y. He,

J. Eur. Ceram. Soc., 2019, **39**, 661–687.

133   A. Atkinson, J. Doorbar, A. Hudd, D. L. Segal and P. J. White, *J. Sol-Gel Sci. Technol.*, 1997, **8**, 1093–1097.

134   W. D. Teng and M. J. Edirisinghe, *J. Am. Ceram. Soc.*, 2005, **81**, 1033–1036.

135   R. I. Tomov, M. Krauz, J. Jewulski, S. C. Hopkins, J. R. Kluczowski, D. M. Glowacka and B. A. Glowacki, *J. Power Sources*, 2010, **195**, 7160–7167.

136   Y. Liu and B. Derby, *Phys. Fluids*, , DOI:10.1063/1.5085868.

137   N. M. M. Farandos, L. Kleiminger, T. Li, A. Hankin and G. H. H. Kelsall, *Electrochim. Acta*, 2016, **213**, 324–331.

138   C. Wang, R. I. Tomov, T. B. Mitchell-Williams, R. V. Kumar and B. A. Glowacki, *J. Appl. Electrochem.*, 2017, **47**, 1227–1238.

139   R. I. Tomov, T. B. Mitchel-Williams, R. Maher, G. Kerherve, L. Cohen, D. J. Payne, R. V. Kumar and B. A. Glowacki, *J. Mater. Chem. A*, 2018, **6**, 5071–5081.

140   S. B. Adler, *Chem. Rev.*, 2004, **104**, 4791–4843.

141   C. Wang, S. C. Hopkins, R. I. Tomov, R. V. Kumar and B. A. Glowacki, *J. Eur. Ceram. Soc.*, 2012, **32**, 2317–2324.

142   C. Li, H. Shi, R. Ran, C. Su and Z. Shao, *Int. J. Hydrogen Energy*, 2013, **38**, 9310–9319.

143   V. Esposito, C. Gadea, J. Hjelm, D. Marani, Q. Hu, K. Agersted, S. Ramousse and S. H. Jensen, *J. Power Sources*, 2015, **273**, 89–95.

144   A. M. Sukeshini, R. Cummins, T. L. Reitz and R. M. Miller, *Electrochem. Solid-State Lett.*, , DOI:10.1149/1.3243468.

145   M. A. Sukeshini, R. Cummins, T. L. Reitz and R. M. Miller, *J. Am. Ceram. Soc.*, 2009, **92**, 2913–2919.

146   N. Yashiro, T. Usui and K. Kikuta, *J. Eur. Ceram. Soc.*, 2010, **30**, 2093–2098.

147   T. Y. Hill, T. L. Reitz, M. A. Rottmayer and H. Huang, *ECS J. Solid State Sci. Technol.*, 2015, **4**, P3015–P3019.

148   G. D. Han, H. R. H. J. Choi, K. Bae, H. R. H. J. Choi, D. Y. Jang, J. H. Shim, K. C. Neoh, K. Bae, H. R. H. J. Choi, S. W. Park, J. W. Son and J. H. Shim, *J. Power Sources*, 2016, **306**, 503–509.

149   R. I. Tomov, R. Duncan, M. Krauz, R. V. Kumar and B. A. Glowacki, *E3S Web Conf. SEED 2016*, 2016, **10**, 000098.

150   C. Gadea, Q. Hanniet, A. Lesch, D. Marani, S. H. Jensen and V. Esposito, *J. Mater. Chem. C*, 2017, **5**, 6021–6029.

151   R. I. Tomov, T. Mitchell-Williams, C. Gao, R. V. Kumar and B. A. Glowacki, *J. Appl. Electrochem.*, 2017, **47**, 641–651.

152   M. Rosa, P. N. Gooden, S. Butterworth, P. Zielke, R. Kiebach, Y. Xu, C. Gadea and V. Esposito, *J. Eur. Ceram. Soc.*, 2017, 0–6.

153   Z. Chen, J. Ouyang, W. Liang, Z. chao Yan, F. Stadler and C. Lao, *Ceram. Int.*, 2018, **44**, 13381–13388.

154   M. Rosa, C. Barou and V. Esposito, *Mater. Lett.*, 2018, **215**, 214–217.

155   E. Venezia, M. Viviani, S. Presto, V. Kumar and R. I. Tomov, *Nanomaterials*, 2019, **9**, 1–16.

156   M. Rosa, P. Zielke, R. Kiebach, V. Costa Bassetto, A. Lesch and V. Esposito, *J. Eur. Ceram. Soc.*, 2019, **39**, 1279–1286.

157   F. Salari, A. Badihi Najafabadi, M. Ghatee and M. Golmohammad, *Int. J.*

Appl. Ceram. Technol., 2020, 1–8.

158   G. D. Han, K. Bae, E. H. Kang, H. J. Choi and J. H. Shim, *ACS Energy Lett.*, 2020, 1586–1592.

159   M. Shah and S. A. Barnett, *Solid State Ionics*, 2008, **179**, 2059–2064.

160   H. Fan, Y. Zhang and M. Han, *J. Alloys Compd.*, 2017, **723**, 620–626.

161   T. L. Skafte, J. Hjelm, P. Blennow and C. Graves, *J. Power Sources*, 2018, **378**, 685–690.

162   S. P. Jiang, *Int. J. Hydrogen Energy*, 2012, **37**, 449–470.

163   T. Z. Sholklapper, C. P. Jacobson, S. J. Visco and L. C. Dejonghe, *Fuel Cells*, 2008, 303–312.

164   E. Feilden, E. G. T. Blanca, F. Giuliani, E. Saiz and L. Vandeperre, *J. Eur. Ceram. Soc.*, 2016, **36**, 2525–2533.

165   J. E. Smay, J. Cesarano and J. A. Lewis, *Langmuir*, 2002, **18**, 5429–5437.

166   I. Grida and J. R. G. Evans, *J. Eur. Ceram. Soc.*, 2003, **23**, 629–635.

167   M. Kuhn, T. Napporn, M. Meunier, S. Vengallatore and D. Therriault, *J. Micromechanics Microengineering*, , DOI:10.1088/0960-1317/18/1/015005.

168   A. Kondo, H. Abe and M. Naito, *Trans. JWRI.*, 2010, **39**, 81–83.

169   S. Desai, M. Yang, Z. Xu and J. Sankar, *J. Environ. Res. Dev.*, 2014, **8**, 477–483.

170   J. Liao, H. Chen, H. Luo, X. Wang, K. Zhou and D. Zhang, *J. Mater. Chem. C*, 2017, **5**, 5867–5871.

171   H. Shao, D. Zhao, T. Lin, J. He and J. Wu, *Ceram. Int.*, 2017, **43**, 13938–13942.

172   L. Cabezas i Peñalva, 2018.

173   E. Peng, X. Wei, U. Garbe, D. Yu, B. Edouard, A. Liu and J. Ding, *J. Mater. Sci.*, 2018, **53**, 247–273.

174   P. Claude, 2019.

175   M. Rosa, 2019.

176   X. Lu, Y. Lee, S. Yang, Y. Hao, J. R. G. Evans and C. G. Parini, *J. Eur. Ceram. Soc.*, 2010, **30**, 1–10.

177   X. Liu, T. J. Tarn, F. Huang and J. Fan, *Particuology*, 2015, **19**, 1–13.

178   Y. Zhong, H. Fang, Q. Ma and X. Dong, *J. Fluid Mech.*, 2018, **845**, 378–391.

179   G. D. Martin, S. D. Hoath and I. M. Hutchings, *J. Phys. Conf. Ser.*, , DOI:10.1088/1742-6596/105/1/012001.

180   N. Reis and B. Derby, *MRS Proc.*, 2000, **625**, 117.

181   B. Derby, *J. Eur. Ceram. Soc.*, 2011, **31**, 2543–2550.

182   D. Jang, D. Kim and J. Moon, *Langmuir*, 2009, **25**, 2629–2635.

183   C. Parra-Cabrera, C. Achille, S. Kuhn and R. Ameloot, *Chem. Soc. Rev.*, 2018, **47**, 209–230.

184   J. E. Smay, G. M. Gratson, R. F. Shepherd, J. Cesarano and J. A. Lewis, *Adv. Mater.*, 2002, **14**, 1279–1283.

185   J. Mewis and N. J. Wagner, *Colloidal Suspension Rheology*, Cambridge University Press, Cambridge, 2011.

186   R. Moreno, *Adv. Appl. Ceram.*, 2012, **111**, 246–253.

187   F. Babick, *Suspensions of Colloidal Particles and Aggregates*, Springer International Publishing, Cham, 2016, vol. 20.

188   T. F. Tadros, *Dispersion of Powders in Liquids and Stabilization of Suspensions*,

Wiley-VCH Verlag GmbH & Co. KGaA, Weinheim, Germany, 2012.

189   E. M. Hotze, T. Phenrat and G. V. Lowry, *J. Environ. Qual.*, 2010, **39**, 1909–1924.

190   M. J. López-Robledo, J. Silva-Treviño, T. Molina and R. Moreno, *J. Eur. Ceram. Soc.*, 2013, **33**, 297–303.

191   T. Phenrat, N. Saleh, K. Sirk, H. J. Kim, R. D. Tilton and G. V. Lowry, *J. Nanoparticle Res.*, 2008, **10**, 795–814.

192   R. ROY, *Science (80-.).*, 1987, **238**, 1664–1669.

193   L. L. Hench and J. K. West, *Chem. Rev.*, 1990, **90**, 33–72.

194   D. Avnir, *Acc. Chem. Res.*, 1995, **28**, 328–334.

195   M.-F. Hsieh, L.-H. Perng, T.-S. Chin and H.-G. Perng, *Biomaterials*, 2001, **22**, 2601–2607.

196   Q. Z. Chen, Y. Li, L. Y. Jin, J. M. W. Quinn and P. A. Komesaroff, *Acta Biomater.*, 2010, **6**, 4143–4153.

197   J. Li, J. Tian and L. Dong, *J. Eur. Ceram. Soc.*, 2000, **20**, 1853–1857.

198   M. Garcia-Heras, A. Jimenez-Morales, B. Casal, J. C. Galvan, S. Radzki and M. A. Villegas, *J. Alloys Compd.*, 2004, **380**, 219–224.

199   C. J. Brinker, A. J. Hurd, P. R. Schunk, G. C. Frye and C. S. Ashley, *J. Non. Cryst. Solids*, 1992, **147–148**, 424–436.

200   G. Bahuguna, N. K. Mishra, P. Chaudhary, A. Kumar and R. Singh, *Res. J. Chem. Sci.*, 2016, **6**, 65–72.

201   C. J. Brinker, G. C. Frye, A. J. Hurd and C. S. Ashley, *Thin Solid Films*, 1991, **201**, 97–108.

202   Y. Lu, R. Ganguli, C. A. Drewien, M. T. Anderson, C. Jeffrey Brinker, W. Gong, Y. Guo, H. Soyez, B. Dunn, M. H. Huang and J. I. Zink, *Nature*, 1997, **389**, 364–368.

203   R. A. Caruso, J. H. Schattka and A. Greiner, *Adv. Mater.*, 2001, **13**, 1577–1579.

204   M. Morozova, P. Kluson, J. Krysa, P. Dzik, M. Vesely and O. Solcova, *Sensors Actuators, B Chem.*, 2011, **160**, 371–378.

205   B. E. Yoldas, *J. sol-gel Sci. Technol.*, 1998, **13**, 147–152.

206   C. Wang, R. I. Tomov, R. V. Kumar and B. A. Glowacki, *J. Mater. Sci.*, 2011, **46**, 6889–6896.

207   C. J. Brinker, *J. Non. Cryst. Solids*, 1988, **100**, 31–50.

208   C. J. Brinker and G. W. Scherer, *Sol-Gel Science*, Elsevier, 1990.

209   M. Moner-Girona, A. Roig, E. Molins and J. Llibre, *J. Sol-Gel Sci. Technol.*, 2003, **26**, 645–649.

210   R. Sui, A. S. Rizkalla and P. A. Charpentier, *J. Phys. Chem. B*, 2004, **108**, 11886–11892.

211   F. Li, Y. Xing and X. Ding, *Surf. Coatings Technol.*, 2008, **202**, 4721–4727.

212   P. Karasiński, J. Jaglarz, M. Reben, E. Skoczek and J. Mazur, *Opt. Mater. (Amst).*, 2011, **33**, 1989–1994.

213   M. P. Pechini, *US Pat. 3,330,697*.

214   S. Sakka and H. Kozuka, *Handbook of Sol-Gel Science and Technology: Processing, Characterization and Applications*, 2005, vol. 1.

215   L. A. Chick, L. R. Pederson, G. D. Maupin, J. L. Bates, L. E. Thomas and G. J. Exarhos, *Mater. Lett.*, 1990, **10**, 6–12.

216   M. Shi, N. Liu, Y. Xu, Y. Yuan, P. Majewski and F. Aldinger, *J. Alloys Compd.*, 2006, **425**, 348–352.

Advanced strategies for Solid Oxide Electrolysis Cells

Chapter II

Experimental methods

2.1 Chapter overview

The aim of this chapter is to provide a general overview of the experimental techniques and methods used in this thesis.

i.   Synthesis of mesoporous CGO is explained in detail, including the etching process for silica template removal and Co oxide decoration to reduce the sintering temperature (section 2.2).

ii. Synthesis and formulation of the different inks (sol-gels and colloidal suspensions) used in this thesis for the fabrication of the difference devices are presented (section 2.3).

iii. The fabrication techniques used in this thesis are described. The fabricated devices are shown and their composition together with their main characteristics are illustrated (section 2.4).

iv. The characterization techniques used are shown and commented. Such techniques were grouped in four categories:

   a.   Printability characterization of inks and slurries: viscosity, surface tension, particle size and roughness measurements (section 2.5).

   b.   Electrochemical impedance spectroscopy (section 2.6).

   c.   Microstructural characterization techniques: XRD, SAXS, SEM and TEM (section 2.7).

   d.   Other characterization techniques: μGC, BET, TPR and ICP-MS (section 2.8).

2.2 Synthesis of mesoporous CGO

The *hard template method*, already presented in the introduction, consists on the impregnation of a pre-existent silica mould for their final removal after the desired phase consolidation.[1,2] The infiltration of the template is done, under controlled temperature, by a precursor solution containing the desired cations in stochiometric proportions. After the gelification of the suspension, the obtained gel is calcinated and the template is removed by chemical etching.[3]

Mesoporous $Ce_{0.8}Gd_{0.2}O_{1.9}$ powder was synthetized by impregnation of a KIT-6 template (ACS material) to replicate its characteristic $Ia\overline{3}d$ periodic structure. Figure 2.1 shows the scheme of the described process. The precursors used for the impregnation were nitrates salts of the desired elements, which were dissolved into ethanol in stoichiometric proportion under constant stirring at 37 °C. Once that $Ce(NO_3)_3 \cdot 6H_2O$ and $Gd(NO_3)_3 \cdot 6H_2O$, were completely dissolved, the KIT-6 silica template was added to the solution. The mixture remained at the same temperature and in constant stirring for two hours, ensuring the impregnation of the template by the precursors. Afterwards, the temperature of the solution was raised up to 60 °C and kept in stirring overnight to obtain the gel. Once the synthesis process was finished, the dense gel was put in a furnace for 5 h at 600 °C and calcinated in air. Eventually, the silica template was removed by stirring of the powders in an alkaline water solution (NaOH, 2M), which was renewed several times and kept at constant temperature (≈70 °C), followed by washing with pure water. Between the different washing steps the washing solution was separated from the cleaned powder by centrifugation (10000 rpm-10 min).[4,5]
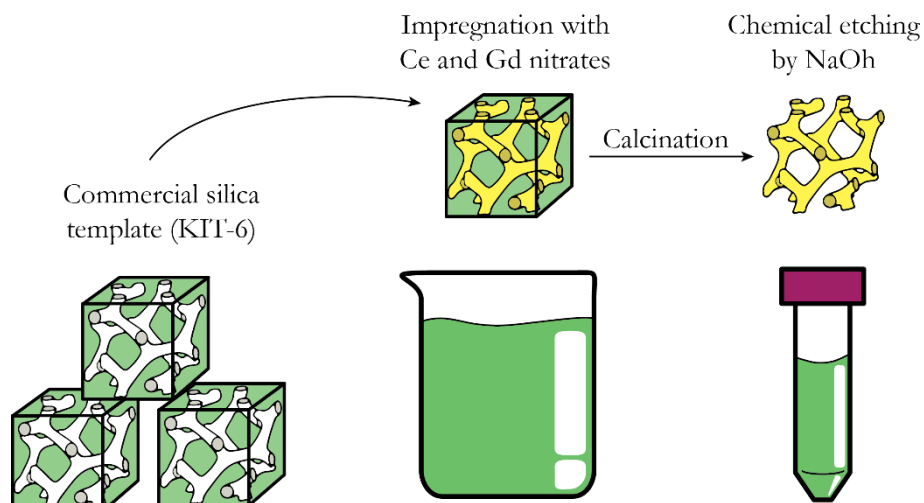
Figure 2.1: Scheme of the mesoporous productions steps. The commercial KIT-6 template is impregnated by Ce and Gd nitrates. After the calcination process the chemical etching by NaOH removes the silica template.

2.2.1 Existing and developed strategies for efficient silica removal

The standard method for the removal of the SiO_2 template by the use of NaOH water-based solution has been proven to be chemically compatible with ceria, but leads to the presence of a highly electrically insulating siliceous phase (≈ 1 %wt. Si) at the end of the process.[6–8] An additional cleaning step using hydrofluoric acid (HF) was developed, proved and optimized with the aim of reducing the final Si content (and other impurities). The process also ensured good chemical compatibility with ceria,[9] taking advantage of the ability of HF to dissolve silica[10–12] and its slow etching rate for rare heart materials.[13] The mesoporous powder was exposed to HF solution (2.5 %v/v) for 1, 5 and 10 minutes at room temperature, followed by washing with water and drying in oven at 60 °C overnight. Detailed results on this strategy are extensively described in Chapter IV.

2.2.2   Co oxide decoration as sintering aid

Co oxide decorated CGO powders were prepared with the aim of improving the inter-particle sintering of the mesoporous scaffold and the attachment to the other elements of the cells at lower firing temperatures.

Chapter IV describes extensively the results of this approach to improve the attachment of mesoporous CGO. Pursuing this objective the powders were mixed in ethanol with 1 %mol of $Co(NO_3)_2 \cdot 6H_2O$; the suspension was subjected to ultrasonication at room temperature for 30 min and then dried in oven at 120 °C overnight. Afterwards, the decorated powders were ground in a mortar and calcined in air at 400 °C for two hours.[14]

> **In this thesis** the study of the structural and electrochemical properties of mesoporous CGO is the main topic of Chapter IV. The nanostructured powder was used to fabricate oxygen electrodes for button (d ≈2 cm) and large area (5×5 cm²) cells, as described in Chapter V.

2.3   Inks and slurries for SOC fabrication

This section reports all the formulation of the inks and slurries used during this thesis. Table 2.1 shows an overview of the different materials according to the employed solvent and the deposition method used in this work. The following sections are devoted to detail the formulation process of the different inks and slurries listed in Table 2.1, as well as the topics of this thesis for which they were developed.

Table 2.1: Summary of the materials and the liquid medium used coupled with the corresponding techniques.

	Used materials	Deposition technique	Part of the device
Ethanol/water Sol-gel inks	LSCF, Ni and Cu precursors	IJP, micropipette	Oxygen electrode
Ethanol based inks	CGO_{meso}, CGO, LSCF	Airbrush	Oxygen electrode
Water based inks	YSZ	Inkjet printing	Electrolyte
DPG and PEGDA slurries	YSZ, NiO-YSZ, LSM	Robocasting	Fuel electrode, Oxygen electrode

2.3.1 Sol gel inks for functionalization via infiltration

Sol gel inks, based on LSCF, were prepared to functionalize by infiltration the CGO backbones of the SOC devices. Specifically, the mesoporous functional layers of the SOFC/SOEC devices were infiltrated by a nitrate precursor solution with the aim to obtain a $La_{0.6}Sr_{0.4}Co_{0.2}Fe_{0.8}O_3$ (LSCF) perovskite, while the scaffolds made of commercial CGO deposited for the partial oxidation of methane (POM) were infiltrated with a precursor solution of Cu and Ni nitrates to use as metallic catalysts after the reduction of the electrode.

2.3.1.1 *Sol-gel of functional perovskites*

To obtain a LSCF perovskite, a solution 0.1 M of lanthanum, strontium, cobalt and iron nitrates (all from Sigma-Aldrich) was prepared in stochiometric proportion. Polyvinylpyrrolidone (PVP, Sigma-Aldrich) dispersant and glycine ($C_2H_5NO_2$, Sigma-Aldrich) as complexing agent, were dissolved in an ethanol/water (70/30 %v/v) medium during continuous stirring at room temperature. After the complete dissolution of PVP and

glycine the precursors were added one by one keeping the continuous stirring. The proportions are reported in Table 2.2.

Table 2.2: Recipe for the LSCF infiltration solution.

	Compounds	Recipe 0.1 M
Metal salts	$La(NO_3)_3 \cdot 6H_2O$	2.7 %wt.
	$Sr(NO_3)_3$	0.9 %wt.
	$Co(NO_3)_3 \cdot 6H_2O$	0.6 %wt.
	$Fe(NO_3)_3 \cdot 9H_2O$	3.4 %wt.
Complexing agent	Glycine $(C_2H_5NO_2)$	2.4 %wt.
Dispersant	PVP $(C_6H_9NO)_n$	0.5 %wt.

2.3.1.2 Sol-gel of catalysts for POM studies

Sol-gel solutions of Ni and Cu nitrates (Sigma-Aldrich) based on Pechini method[15] were prepared in an ethanol/water (30/70 %v/v) solvent using citric acid (Sigma-Aldrich) as complexing agent and ethylene glycol (Sigma-Aldrich) to enhance the polymerization.[16]

In order to guarantee a proper distribution of the cations in the solution the citric acid and the ethylene glycol were the first components added to the liquid medium. During the process the solution was kept in constant stirring and at room temperature. The used ratio between the salts and the complexing/polymerizing agents is reported in Table 2.3.

Table 2.3: Amounts in %wt. of the two recipes used for the infiltration of Cu and Ni sol-gel solutions.

	Compounds	Recipe 0.1 M	Recipe 1.3 M
Metal salts	$Cu(NO_3)_2 \cdot 6H_2O$	1.4 %wt.	10.3 %wt.
	$Ni(NO_3)_2 \cdot 3H_2O$	1.2 %wt.	8.6 %wt.
Complexing agent	Citric acid $(C_6H_8O_7)$	1.9 %wt.	13.6 %wt.
Polymerizing agent	Ethylene Glycol $(C_2H_6O_2)$	1.2 %wt.	8.8 %wt.

In this thesis, the infiltration by LSCF were used for the symmetrical cells of Chapter III and for the functionalization of the SOC scaffolds of Chapter V. Cu and Ni nitrates were infiltrated inside CGO scaffolds to promote POM reaction, as presented in Chapter VI.

2.3.2 Ethanol based inks

Ethanol based inks were prepared to deposit commercial and synthetized mesoporous powders as scaffold for oxygen electrode of SOC. Such inks (Table 2.4) were optimized for the deposition by airbrush spray coating with a solid load concentration ≈1 %v/v and using commercial PVP with low molar weight (≈10000 Mw, Sigma-Aldrich) as dispersant. The amount of PVP was 1 % with respect to the solid load in the case of the commercial powders (CGO, LSCF) and 2 % in the case of mesoporous CGO, because of the higher surface area of the nano-powders.

Firstly, the PVP was dissolved in ethanol during continuous stirring, then the ceramic load was added step by step. Before the deposition, the ink was ultrasonicated for 1 h in order to avoid agglomeration.

Table 2.4: List of compounds used to produce the ethanol-based inks for airbrush.

	Compounds	LSCF	CGO	CGO$_{meso}$
Solid loading	LSCF	9 %wt.	-	-
	CGO	-	9 %wt.	-
	CGO$_{meso}$	-	-	9 %wt.
Dispersant	PVP $C_3H_8O(C_6H_9NO)_n$	0.1 %wt.	0.1 %wt.	0.2 %wt.

In this thesis, ethanol-based inks for airbrushing were used for the processing of the cells measured in Chapter III, IV, V and VI.

2.3.3 Water-based inks

The good dispersion of the YSZ ink, which is necessary in order to avoid a possible clogging of the cartridge nozzles and therefore compromise the final result of the deposition, was achieved by the utilization of an electro-steric dispersant.

Agglomerates driven by Van der Waals Forces can be formed once the solid load is dispersed in the liquid. Therefore, it is necessary to overcome the magnitude of such interactions to prevent an unwanted destabilization of the colloidal suspension. In general, additives to keep separated the particles by *electrostatic* and/or *steric* repulsive forces are utilized.[17] In the electrostatic case of the addition of additives and the tuning of the pH conditions promote the extension of the electrical double layer. This double layer is formed between the particle surface and the ions of opposite charge which are electrostatically attract on the surface.[17,18] The larger is the double layer the more effective is the repulsion among particles which present similar surface charge. In the steric case, which is the case of DURAMAX™ D-3005, the addition of polymeric molecule adsorbed on the particle surfaces builds a steric barrier which keeps them separated. It is evident that, the surface agent should be chosen considering its affinity with the solid load and the liquid medium of the suspension. Its amount should be calculated considering the surface area of the particles to guarantee a proper steric stabilization.[19–21]

Water-based inks were produced to print YSZ electrolytes by inkjet printing. The ceramic loading (Tosoh) of these inks was calculated to obtain ≈2 %v/v with 2 %wt (respect to the YSZ) of DURAMAX™ D-3005 (Rohm-Haas) as dispersant. Several steps were necessary to obtain a stable suspension with fine particle size to avoid the clogging of the cartridge nozzles. First the dispersant was mixed with the deionized water at room temperature and subsequently the ceramic load was added step by step in

Advanced strategies for Solid Oxide Electrolysis Cells

constant stirring. Afterwards, the mixture was put in ultrasound for few minutes. The average particle size of the particles was measured by laser scattering analysis to identify possible agglomerates/aggregates. Such clusters, difficult to break by ultrasound, were removed by centrifugation. The suspension was filtered to ensure the removal of any possible large particle remaining agglomerate and then put again in ultrasound. The new concentration of the mixture (≈1 %v/v) was verified every time by drying and weight of a knew small volume.

In order to produce the ink, the water-based mixture was diluted by isopropanol and propylene glycol (from Sigma Aldrich) with proportion 3:1:1 %v/v. The additive addition was made to satisfy the printability requirements in terms of viscosity and surface tension. The concentration of each component of the ink is reported in Table 2.5.

Table 2.5: List of compounds used to produce the YSZ water-based inks for inkjet printing with the relative concentrations.

	Compounds	Concentration
YSZ	$(Y_2O_3)_{0.08}(ZrO_2)_{0.92}$	3.6 %wt.
Duramax	DURAMAX™ D-3005	0.1 %wt.
Isopropanol	C_3H_8O	15.5 %wt.
Propylene Glycol	$CH_3CH(OH)CH_2OH$	21.8 %wt.

In this thesis, water-based and DPG/PEGDA inks for inkjet printing and robocasting were used to fabricate the symmetrical cells of Chapter III and for the interlayer of Appendix I.

2.3.4   Formulation of slurries for robocasting processing

Viscous inks based on dipropylene glycol (DPG) and poly(ethylene glycol) diacrylate (PEGDA) were prepared for printing electrodes by robocasting.

2.3.4.1 Acrylate-based slurries

With the aim to produce slurries presenting high solid loadings, PEGDA (from Sigma-Aldrich with molecular weight 250 g mol^{-1} and viscosity 25 mPa s) was chosen as monomer due to its relative low viscosity and mixed with a standard thermal initiator (azobisisobutyronitrile - AIBN, $[(CH_3)_2C(CN)]_2N_2$, from Sigma-Aldrich) to trigger the polymerization reaction. The solid load of the prepared slurries was 72 %wt. using YSZ $((Y_2O_3)_{0.08}(ZrO_2)_{0.92}$ from Tosoh with a particle size around ≈40 nm and a surface area of ≈16 m^2 g^{-1}) and LSM commercial powders ($La_{0.8}Sr_{0.2}MnO_3$, from H.C. Stark with a particle size <500 nm and calcinated for 2 h in air at 800 °C.) as ceramic load. Polymethylmethacrylate (PMMA, from Esprix Technologies; spheres with an average diameter ≈1.5 µm) and graphite (GR, platelets from Graphit Kropfmuhl AG with a lateral particle size ≈20 µm) were used as pore formers (Table 2.6).

Firstly, the dispersant (SOLSPERSE 41000 - SO41K, from Lubrizol) was dissolved in the PEGDA-AIBN mixture and, after several minutes of stirring, the solid load was added step by step. The slurry was mixed for 10 minutes in a planetary mill after the addition of each component. Then, the final viscous slurry was kept 2 h more in the planetary mill, to ensure a good dispersion of the solid loading.

Table 2.6: List of compounds for the PEGDA-based slurries with the relative concentrations.

Components	P1	P2
YSZ	21.0 %wt.	25.5 %wt.
LSM	21.0 %wt.	25.5 %wt.
GR	18.5 %wt.	13.9 %wt.
PMMA	9.0 %wt.	7.4 %wt.
PEGDA	27.8 %wt.	24.8 %wt.
SO41K	2.4 %wt.	2.6 %wt.
AIBN	0.3 %wt.	0.3 %wt.

2.3.4.2 Di-propylene glycol (DPG) based slurries

DPG-based (Sigma-Aldrich, molecular weight 134 kg mol^{-1}) slurries were formulated to print YSZ and NiO-YSZ (NiO and $(Y2O_3)_{0.08}(ZrO_2)_{0.92}$ from Kceracell, with proportion 60:40 by weight. Surface area ≈6 m^2 g^{-1}) on metals substrates by robocasting as described in Appendix I. Polyvinylpyrrolidone K30, (PVP K30, from Applichem, with molecular weight ≈67 kg mol^{-1}) was used as dispersant, while PVP K90 (from Applichem, with molecular weight ≈1600 kg mol^{-1}.) due to its higher molecular mass was used as plasticizer. Dispersions at 5 %wt. and 15 %wt. with DPG of PVP K30 and PVP K90 respectively were previously prepared and mixed for few days to ensure a good homogeneity of both dispersant and binder. The PVP mixtures were diluted by other DPG to obtain the desired concertation and then the rest of the components was added gradually and mixed with a planetary mill for 10 minutes before every step. Lastly, the slurries were mixed by planetary mill for two hours. The recipes of the different slurries are reported in Table 2.7.

Table 2.7: concentrations of the different components of the DPG-based slurries.

	DPG 1 (%wt.)	DPG 2 (%wt.)	DPG 3 (%wt.)	DPG 4 (%wt.)	DPG 5 (%wt.)
YSZ	30.6	22.1	30.3	18.9	69.1
NiO	80.8	33.3	20.2	28.4	-
GR	-	9.6	8.7	8.2	-
PMMA	-	5.2	4.7	4.4	-
DPG	3.0	4.6	17.2	18.6	14.3
DPG+PVP K30 (5%wt.)	11.9	18.5	16.1	15.8	12.2
DPG+PVP K90 (15%wt.)	4.3	6.6	5.7	5.6	4.3

2.4 Fabrication of SOC devices

Several cells were produced to test the electrochemical properties of the advanced layers and materials (e.g. mesoporous functional layer, backbones infiltrated by catalysts or 3D printed layers). In the following section, first an account of the techniques is given, followed by the description of the specific procedure for each processed device.

2.4.1 Techniques

2.4.1.1 *Automatic airbrushing for electrode deposition*

Airbrush is a tool usually used for spraying paint. It can be also used for depositing inks with different solid loading, including ceramic materials. In the SOFC field, airbrush is used for depositing porous electrodes on top of pre-existing substrates.[22,23] It uses pressurize air to nebulize the ink which is sprayed through a nozzle.

In this project, a 3-axis automated airbrushing (Print3D Solutions, Spain) was used to deposit different layers of the final cells. These layers were the attachment roughness layer, the mesoporous CGO scaffold and the LSCF current collector (Figure 2.2). The nozzle used for printing had a diameter of ≈0.6 mm. The most important parameters were the pressure of the compressed air that drives the ink (pressure used ≈2.5 bar) and the distance to the target substrate (≈8.5 cm). In order to obtain reproducible layers, the thickness of the layer was controlled by weight. PVP was used as dispersant to avoid particles agglomeration and ensure the homogeneity of the inks.

The software of the printer can follow the instruction of a designed CAD file, like in a standard 3D printing process. Therefore, a uniform deposition on large substrates can be granted.
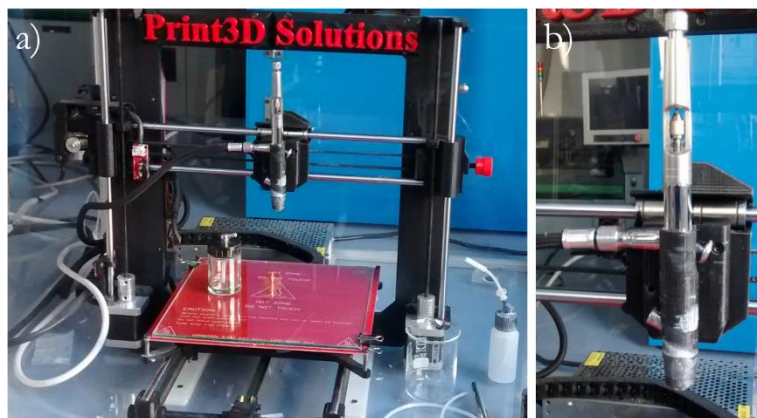
Advanced strategies for Solid Oxide Electrolysis Cells

Figure 2.2: Automatic airbrushing machine from Print3d Solution used for the deposition of the CGO, CGO$_{meso}$ and LSCF backbones.

> **In this thesis**, air brushing was routinely used to fabricate porous layers as electrodes for SOCs in Chapter III, IV, V and VI. In the case of the large area cell of Chapter V, a CAD object was design to control the movements for the deposition on a ≈25 cm^2 area.

2.4.1.2 *Robocasting*

Robocasting (RC), is an AM technique where a filament of dense ceramic ink is extruded through a conical/cylindrical nozzle usually driven by a pneumonic or a mechanic force.[24] The dimension of the nozzle determines the final diameter of the filament.

In AM techniques the control system of the equipment follows the CAD model and can print layer by layer the designed piece. RC allows a certain control of some parameters: print speed, infill % of the piece, print pressure and filament diameter (determine by the nozzle). The printing principles of RC are quite similar to the ones of the more known Fuse Deposition Modelling (FDM). However, in RC the paste is not heated. The viscous slurry rely on rheological properties, to build a monolithic piece.[25]

The robocasting used in this work was a BioX (Figure 2.3), produced by CellInk. The machine is able to print with one or up to three cartridges at

the same time, has a pressure range from 5 up to 200 kPa and a positioning accuracy around 1 μm. Moreover, the BioX has the possibility to warm up the cartridge up to 65 °C and a printing bed which can reach 60 °C. The BioX RC used belongs to the Department of Energy Conversion and Storage (Risø Campus) of the Technical University of Denmark (DTU).

Figure 2.3: Image of the BioX robocasting machine form CellInk used for this thesis.

> **In this thesis**, robocasting was used in Chapter III for printing the YSZ-LSM electrodes of the hybrid 3D printed symmetrical cells. Robocasting was used in Appendix I for depositing porous YSZ on top of metal substrates.

2.4.1.3 *Inkjet printing*

Inkjet printing (IJP) is a well know technology for printing different types of ink drop by drop, on a substrate (classically paper or plastic). It has been extensively developed in the second part of the 20th Century and in the last decades has been object of new attention. Nowadays is also used for the

Advanced strategies for Solid Oxide Electrolysis Cells

printing of ceramic oxides or metal particles dispersed in low viscous medium for microfabrication, electronics and powder bed technology.

In Drop on Demand (DOD) IJP a stream of individual droplets is produced only when is necessary for the printing.[26] The drop is generated by a pressure pulse which must overcome the surface tension of the ink and push it out of the nozzle.[27] Such pressure is usually generated by a piezoelectric actuator or by a small heater which warm up the ink until a small pressure bubble is created.[27]

Two inkjet printers were used during this work: a Pixdro LP50 from Meyer-Burger used at the DTU facilities in Risø (Denmark) and a custom-made inkjet printing at the IREC facilities produced by Print3d Solutions, using a commercial Hawlett-Packard cartridge.

The PixDro (Figure 2.4) has a heated printing bed (up to 50°C) of $22.7\times32.7\times2.5$ cm^3 and an automatic cleaning system for removing the excess of ink from the nozzles. For a better control of the printing process there are also two cameras: one observing the jetting of the cartridge and another pointing the substrate to allow the positioning. The PixDro allows the assembly of numerous types of cartridges, the one used in this work was the Dimatix DMC 2810. The spatial resolution between the nozzle and the substrate was ≈10 μm.

The software which controls the process, produced by Meyer-Burger, allows to measure the volume of the drops and their printing speed.

Figure 2.4: PixDro inkjet printer used at the DTU facilities (Risø campus) to print YSZ electrolytes.

The inkjet printer produced by Print3d Solutions (Figure 2.5) has an 8×8 cm^2 printing bed, which can warm up until 50 °C. The movements of the 3-axis system are controlled by Arduino (https://www.arduino.cc/) and the printing process (with the HP C6602A cartridge) by Processing© software.
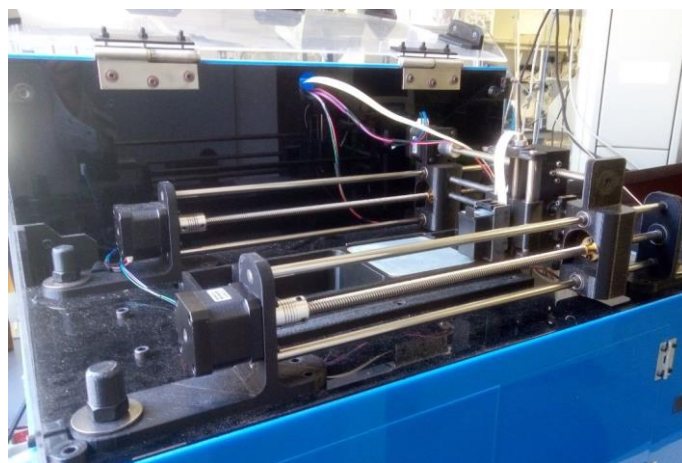
Figure 2.5: Inkjet printer produced by Print3d Solutions ate the IREC facilities, used for infiltration of CGO scaffolds.

Advanced strategies for Solid Oxide Electrolysis Cells

> **In this thesis**, inkjet printing is one of the main deposition techniques used in Chapter III. The custom-made IJP from Print3d Solutions was used for the automatic infiltration of LSCF precursor on symmetrical cells with CGO scaffolds.
>
> The Pixdro LP50 was utilized for the deposition of dense layers by means of YSZ suspension. The layers were electrochemically studied as electrolyte in a fully 3D printed devices.

2.4.1.4   *Screen printing for porous layer deposition*

Screen printing, also known as *serigraphy,* is a very well-known technique where an ink is transferred on a substrate through a mesh with the desired pattern. In an industrial screen printer usually, an automatic system moves one or two blades which apply a certain pressure on the mesh were the ink is deposit, the blade spreads the slurry ensuring a homogeneous deposition. Lastly the resulting layer is dried and subsequentially sintered at high temperature.[28]

This technique is widely used for solid oxide fuel cells industrial production allowing to fabricate layers of many different ceramic materials including YSZ, NiO-YSZ, CGO with a controlled thickness range ≈10-100 μm.[28,29]

The Sony SI-P850 industrial screen printer (Figure 2.6) at the IREC facilities has a PWB support dimension from 50mm×50mm×0.4mm to 410mm×460mm×3mm. Screen dimension: 750mm×750mm×30-40mm. Printing speed from 10 mm s^{-1} up to 200 mm s^{-1}, printing pressure from 10 N to 200 N.

> **In this thesis**, the Sony SI-P850 industrial screen printer was used to deposit intermediate YSZ layers on top of the metallic substrates (Appendix I).

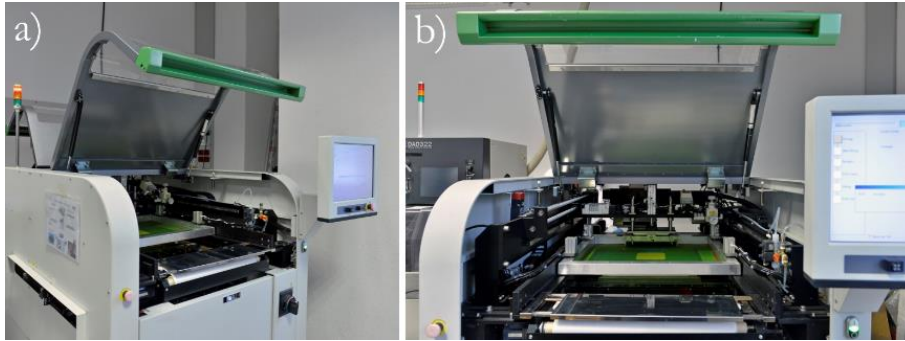Advanced strategies for Solid Oxide Electrolysis Cell

Figure 2.6: Image of the screen printer Sony SI-P850 at the IREC facilities a) later and b) frontal view.

2.4.1.5 Pulsed laser deposition (PLD)

Pulsed laser deposition (PLD) is a technique for depositing high quality thin film on top of pre-existent substrates. PLD uses, as indicated by its name, laser pulses to evaporate and ionize material from a target. The process generates a plasma plume of ions, which condensed on top of the substrate. PLD can generate very thin films, with thicknesses from tens of nanometres to few microns. The deposition parameters (e.g. temperature, pO_2, etc…) influence the final microstructure of the film, i.e. its density.[30]

The deposition chamber is maintained under high vacuum condition, in order to reduce possible contaminations. The oxygen flow during the deposition is usually in the range $10^{-3} – 10^{-1}$ mbar. Infrared lamps are used to heat up the target and the substrate at the desired temperature for the deposition. Furthermore, the target is maintained in constant rotation to homogenize its surface and avoid the presence of defects in the deposited layer.[30]

Figure 2.7: Image of the PLD-5000 from PVD® at the IREC facilities.

In this thesis, a large area PLD-5000 from PVD® (Figure 2.7) located at IREC facilities was used in Chapter V for depositing of CGO dense barrier layer. The ≈1 μm barrier layer was deposited on top of commercial fuel electrode based half-cells (Chapter V). The depositions were conducted by other researchers of the group.

2.4.2 Symmetrical cells with mesoporous CGO scaffold

Symmetrical electrolyte supported cells were prepared using ≈160 μm thick tape-casted YSZ film (FAE S.A.U.) as electrolyte. A roughness layer was deposited by 3-axis automated airbrushing (Print3D Solutions) using an ethanol-based ink with commercial CGO powder (Kceracell). The coating was deposited on both sides of the YSZ electrolyte and sintered at 1250 °C for 3 h. This layer was deposited to improve the attachment of the electrodes with the electrolyte ensuring minimum contact resistance of the interfaces. The mesoporous CGO scaffold layers (thickness ≈90 μm) were deposited by the same method (Figure 2.8). The optimization of the final mesoporous attachment temperature (850 °C) is described in Chapter IV. Gold paste was hand brushed and cured at 800 °C to ensure the current collection.
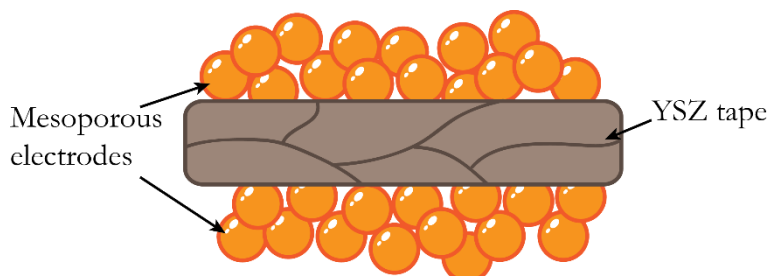
Figure 2.8: Schematic representation of the YSZ/CGO symmetrical test cells used to study the electrochemical properties of the mesoporous CGO.

2.4.2.1   *Symmetrical cells with CGO scaffold infiltrated by IJP*

Some symmetrical cells with mesoporous scaffold were infiltrated with LSCF perovskite by means of IJP.

To prevent the potential formation of insulating Sr-rich phases due to the reactivity between YSZ and LSCF at high temperature, a barrier layer was airbrushed on both faces of the tapes ($\approx$15 μm). Airbrush ethanol-based ink for barrier layer deposition was made mixing commercial $Ce_{0.8}Gd_{0.2}O_{2.9}$ powder (KCeracell), $Co(NO_3)_2 \cdot 6H_2O$ and PVP with proportion 10:2:0.2 %wt. respectively. The barrier layer was sintered at 1275 ºC. Ceramic scaffolds were deposited on top of the YSZ tapes, made of commercial CGO ($\approx$60 μm) sintered at 1200 °C or of mesoporous CGO ($\approx$60 μm) sintered at 900 °C.

After sintering, the cells were infiltrated by inkjet printing with ethanol-based sol gel inks of LSCF precursors. The infiltration was carried out in three different steps, with drying at 500 °C after each. At the end of the process the solution was calcinated at 800 °C for 2 h.

Lastly a layer of commercial LSCF ($\approx$15 μm) was airbrushed on top of the CGO-LSCF electrodes to ensure the current collection. This last layer was sintered using the same parameters of the CGO scaffold. Figure 2.9 shows a schematic representation of the structure of such cells.
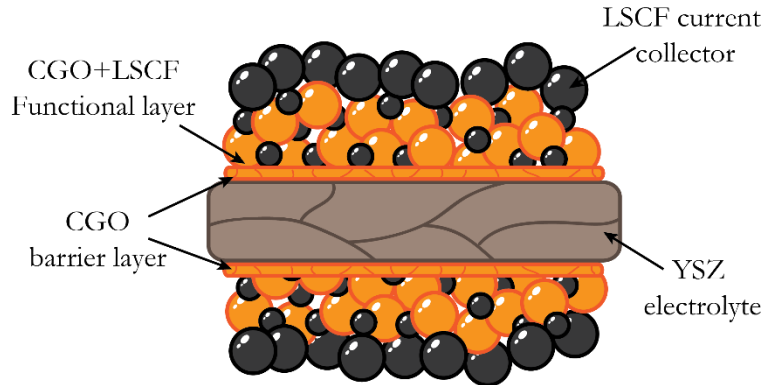
Advanced strategies for Solid Oxide Electrolysis Cells

Figure 2.9: Schematic representation of the YSZ/CGO/CGO-LSCF/LSCF symmetrical cells infiltrated by inkjet printing.

2.4.3 Symmetrical fully 3D printed cells

Symmetrical fully 3D printed fuel cells with configuration LSM+8YSZ/8YSZ had been fabricated at the DTU facilities (Risø Campus, Roskilde, Denmark) by robocasting and inkjet printing and afterwards co-sintered up to 1295 °C in a muffle furnace. Few cells had been fabricated to optimize the process (e.g. rheological properties of the inks/slurries, printing parameters, optimal thickness of the electrolyte). Electrochemical properties of the cells were studied by impedance spectroscopy.

The electrodes made of LSM+8YSZ were deposited by robocasting (≈250 μm). The first layer made of thermal curable ink was put in an oven at 90°C to initiate the polymerization process and to allow the deposition of the 8YSZ electrolyte (≈3 μm) by inkjet printing. After drying in air of the electrolyte a second electrode was deposited (Figure 2.10) and polymerized in oven. The symmetrical cell was co-sintered at 1295 °C for 2 h.
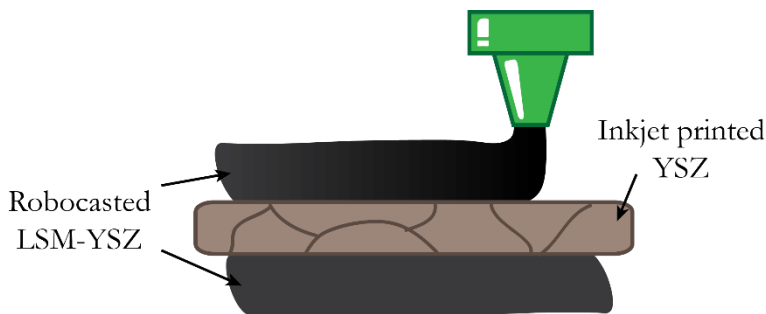
Figure 2.10: Scheme representing the YSZ/YSZ-LSM symmetrical cells printed by Robocasting and Inkjet printing.

2.4.4 Fuel electrode-supported cells

2.4.4.1 *Deposition and functionalization of the mesoporous functional layer*

The oxygen electrode with mesoporous CGO infiltrated by LSCF solution was deposited on top of commercial half-cells to produce complete SOC devices (Figure 2.11). The mesoporous CGO etched by HF and decorated with Co oxide was deposited on commercial fuel electrode-supported half-cells (diameter ≈2 cm) from SOLIDpower, SPA with a NiO-YSZ fuel electrode (≈300 μm thick) and YSZ electrolyte (≈7 μm thick). A CGO barrier layer (≈1 μm thick) was deposited by PLD on top of the electrolyte and sintered at a temperature of 1200 °C before the deposition of the oxygen-electrode.[31]

Mesoporous CGO etched only by NaOH and without Co oxide decoration was deposited on commercial electrode supported substrate from HT Ceramics with large area (5×5 cm^2). The half-cells were composed by tape casted NiO-YSZ fuel electrode (≈300 μm thick) and YSZ electrolyte (≈7 μm thick). Screen-printed CGO barrier layer (≈3 μm thick) was deposited on top of the electrolyte by the producer. These commercial NiO-YSZ/YSZ half-cells are usually co-sintered at ≈1400 °C, while the screen-printed barrier layer at ≈1200 °C.[31]

CGO roughness layers were fabricated under the same conditions as the symmetrical test cells (see above) to improve the attachment between the scaffold and the barrier layer. Mesoporous CGO layers were deposited by airbrushing (thickness ≈10–15 μm) and sintered at 850 °C, in the case of the button cell, and 900 °C, in the case of the large area cell. The scaffolds were subsequently infiltrated using a 0.1 M sol-gel solution of LSCF precursors (total volume in the button cell ≈30 μL, while in the large area cell ≈240 μL), followed by thermal treatment at 800 °C for 3 hours, to obtain the LSCF phase.[32]

An additional LSCF current collector layer (thickness ≈20–25 μm) was deposited by airbrushing on top of the functional layer. An ethanol-based ink was used for the deposition. LSCF layers were sintered at the same condition of the corresponding mesoporous backbones in a different step. LSCF commercial powders were provided by Kceracell.
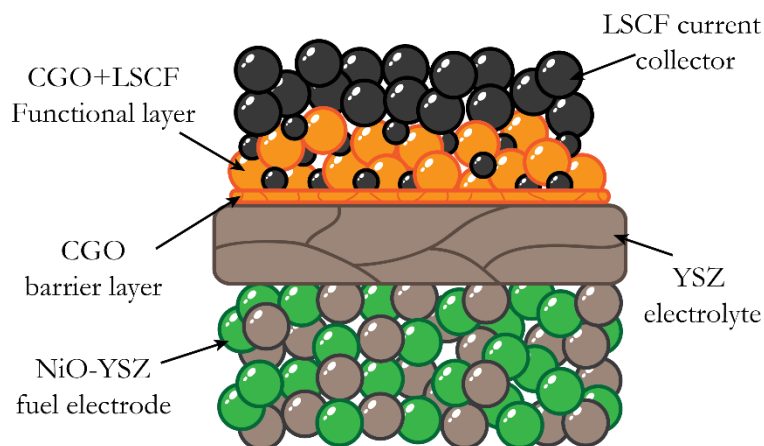

Figure 2.11: Schematic view of an anode-based cell with mesoporous CGO infiltrated by LSCF perovskite.

2.4.4.2 *Ni-Cu infiltration for POM application*

Complete cells were fabricated for producing syngas through the electrochemically assisted partial oxidation of methane (POM). Commercial fuel electrode supported half-cells made by tape casting (SOLIDpower, SPA)

were used. The half-cells were airbrushed by an ethanol solution of commercial CGO powder (from Kceracell). The layers were sintered at 1250 °C for 3 h. CGO scaffolds were infiltrated by a Ni-Cu Pechini solution to enhance the catalytic properties of the electrode, and then cured at 500 °C. Gold paste was brushed by hand as current collector on top of the cells and cured at 500 °C. In Figure 2.12 the structure of an infiltrated complete cell is shown, highlighting the porous Ni-YSZ fuel electrode, the dense YSZ layer and the porous CGO scaffold infiltrated by Ni and Cu.
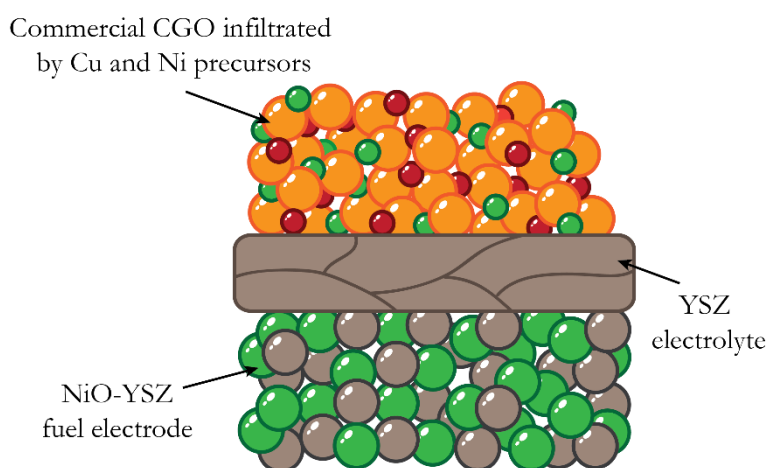

Figure 2.12: Scheme of the Ni-YSZ/YSZ/CGO-Ni-Cu cell produced for the electrochemical assisted partial oxidation of methane.

In this thesis, the characterization of symmetrical cells with mesoporous CGO electrodes is showed in Chapter IV. The characterization of symmetrical cells with CGO-LSCF electrodes infiltrated by IJP and of LSM-YSZ/YSZ symmetrical cells printed by IJP and RC is discussed in Chapter III. Electrochemical and microstructural analysis of complete devices with mesoporous HF-Co-CGO+LSCF and with mesoporous CGO+LSCF functional layers are tested in Chapter V. The results of the analysis of cells with Ni-Cu-CGO electrodes for electrochemically assisted POM can be found in Chapter VI.

2.5 Rheological characterisation for printability evaluation

This section briefly describes the equipment and the techniques used to measure the rheological properties of the inks/slurries produced.

2.5.1 Viscosity measurement

A DV3T Rheometer (Brookfield Engineering Labs., Inc.) was used to measure the viscosity of the produced inks. The instrument can measure the viscosity of a liquid medium at given share rates (Figure 2.13). It has a speed rate which goes from 0.01 to 250 RPM, a viscosity accuracy ±1.0 % and a viscosity repeatability around ±0.2 %. All the measurements were carried out at the IREC facilities.

Figure 2.13: DV3T Rheometer used to measure the viscosity of the sol gel inks for inkjet printing.

In this thesis, viscosity measurements were used in Chapter III for characterizing the LSCF sol gel and the YSZ water-based suspension inks for inkjet printing.

2.5.2   Surface tension measurement by pendant drop method

Surface tension measurement of the inks were made by an OCA20 optical contact angle and contour analysis system, using the pendant drop method. This method can determine the surface tension of a liquid medium from Young-Laplace equation (2.1).

$$\Delta p = \sigma \left(\frac{1}{r_1} + \frac{1}{r_2} \right) \tag{2.1}$$

Figure 2.14a shows a liquid drop which is characterized by two different curvature radii (r_1, and r_2) because of the slight elongation due to gravity. The difference in pressure between the inside and the outside of the curved surface (Δp), known as Laplace pressure, is proportional to the surface tension (σ) of the liquid, multiplied by the sum of the radii reciprocals.
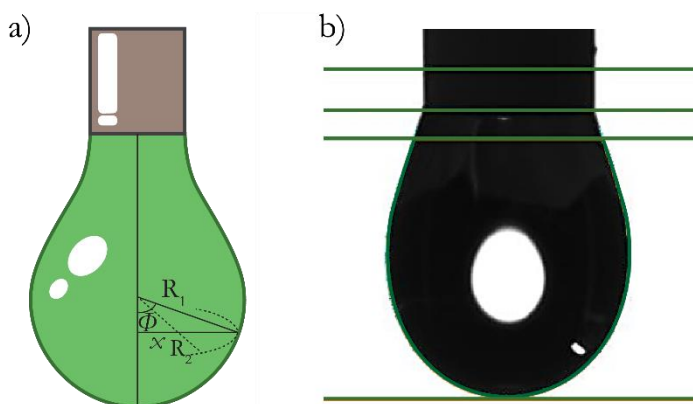

Figure 2.14: Schematic representation of the pendant drop method (a) and picture of a drop during a measurement (b).

The ratio between the weight and the surface tension of the drop determines its deviation from the spherical shape. If the difference in density between the two phases is known, it is possible to calculate the surface tension from the shape of the drop. Figure 2.14b is a representative picture of an ink drop measured by the OCA20.

Advanced strategies for Solid Oxide Electrolysis Cells

OCA20 is an optical contact angle and contour analysis systems of the OCA series which can also provide surface tension measurements of a liquid medium (Figure 2.15). In particular, the OCA20 model has a video camera with a resolution of 768×576 pixels (up to 50 images per second), a micro-controller module for control of the electronic syringe units and an electronic multiple dosing system. The instrument has the possibility to make:

- Static and dynamic contact angle measurement according to the Sessile and Captive Drop method.

- Calculation of the surface and interfacial tension from the contours of pendant and sessile drops.

- Calculation of the surface free energy of solids and their components.
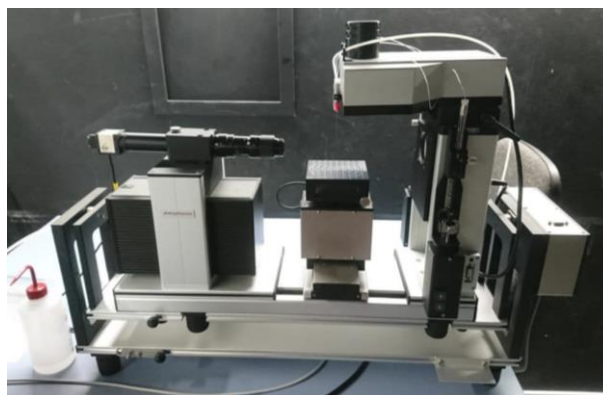

Figure 2.15: Contact angle and surface tension device used for the characterization of the inkjet printed sol-gel inks.

All the measurements have been carried out in the IREC facilities.

In this thesis, Surface tension measurements were conducted on IJP inks for depositing LSCF sol-gel solution and water-based suspension of YSZ. The results of such characterization can be found in Chapter III.

2.5.3   Particle size analysis

The analysis of particle size in a dispersed medium is crucial to have information about inks and slurries. It can provide information about the presence of agglomerates, which can strongly influence the stability of the ink. This can affect the quality of the final piece.[33] Particle size analysis is usually made by a laser scattering equipment, where a sample of powder, very dispersed in a known medium (e.g. water, ethanol, etc.), is passing through a set of optical cells (Figure 2.16). The laser invests from different angles the cell and the intensity and the angle of the beam after the collision with the particles are revealed. From these data, the software can calculate the average particle size distribution. In the case of the present study, the Mie Scattering theory method, based on a great number of data about known materials and their interaction with the light of the laser (refractive index and absorption) has been used.

In this work a Mastersized 2000 (IREC facilities) and a Beckman Coulter LS (DTU, Risø campus, Denmark) laser diffraction analysers had been used to characterize the particle size of the inks used for inkjet printing, robocasting and Airbrushing
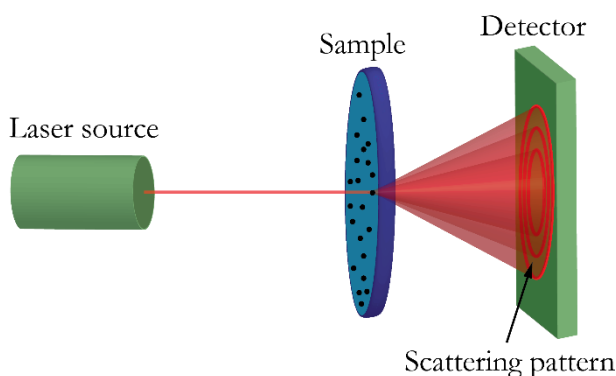

Figure 2.16: Schematic representation of laser scattering analysis.

Advanced strategies for Solid Oxide Electrolysis Cells

> **In this thesis**, particle size analysis was used in Chapter III for the characterization of the YSZ water-based suspensions. The suspensions were used to deposit dense YSZ layers by means of inkjet printing.

2.5.4 Non-contact surface roughness measurements

Measure the surface roughness of a printed piece could be of extreme importance to evaluate the quality of the printing. High resolution 3D profilometer allows to measure the roughness of a surface with the utilization of a laser and a confocal system, coupled with a base unit with an in integrated translation stage. In this work a Cyberscan Vantage, coupled with a LT9010 detector was used.

> **In this thesis**, the Cyberscan profilometer was used in Chapter III to determine the robocasting printing parameters.

2.6 Electrochemical characterization of cell performances

The devices produced were electrochemical characterized at the typical operating temperature (700-900 °C). This section presents the experimental setups used for the characterization. Afterwards, Electrochemical Impedance Spectroscopy (EIS) principles are reported.

2.6.1 Experimental setup

2.6.1.1 *Button cell characterization*

Figure 2.17 shows the experimental setup used in this thesis for testing button cells (diameter ≈2 cm). The setup consists in a cell holder sample (ProboStat™ station form NorECS AS), a furnace with a thermal

control system (Lenton), a gas flow system with a water vaporization, a power supply, a Potentiostat/galvanostat to measure the performance of the measured cell and a impedance analyser (Parstat and novocontrol).
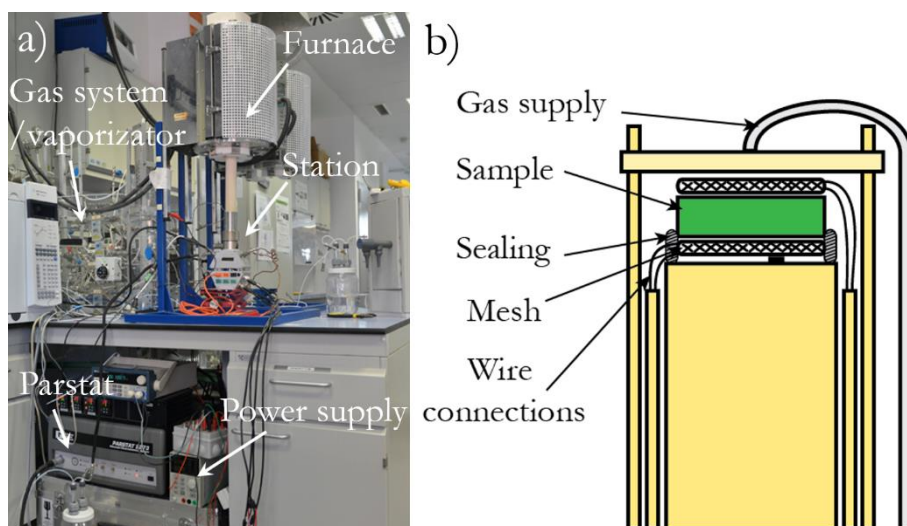

Figure 2.17: Picture of the ProboStat station used for the measurements of the button cells (a) and schematic representation of the cell assemble inside the chamber (b).

Figure 2.17a shows the measurement station already mounted inside the furnace, while Figure 2.17b displays a schematic view of the system. The scheme shows the two meshes (area ≈1.54 cm²), placed on the two faces of a sample to ensure proper current collection. The meshes were made of gold and platinum for oxygen and hydrogen sides, respectively. Gold wires (diameter ≈0.5 mm) were used for the electrical connections of the system. In Figure 2.17b the sealing for separating the atmosphere between the inner and the outer chambers (Ceramabond™) and the gas supply tubes are also represented.

2.6.1.2 *Hybrid 3D printed symmetrical cells characterization*

The Hybrid 3D printed cells fabricated by Robocasting and Inkjet printing were characterized at the Technical University of Denmark facilities.

Advanced strategies for Solid Oxide Electrolysis Cells

Gold paste and gold wires were used to ensure the electrical contact. The cells were measured inside a quartz tube in air. A tubular furnace was used for heating up the system (W. C. Heraeus Hanau). The cells were electrochemically characterized by from 800 °C to 550 °C using a Solartron 1260 for data acquisition. Impedance measurements were taken every 50 °C in potentiostatic mode with 200 mV of amplitude.

2.6.1.3   *Large area cell characterization*

The 5×5 cm^2 cells were characterized at the Technical University of Denmark facilities. They were placed between two alumina blocks which had gas supply channels, cavities to include Pt foils (4×4 cm^2) as current collectors and holes with Pt wires (1 mm diameter) for current pick-up and voltage probing. A Ni mesh (4×4 cm^2) was placed on top of the Pt current collector on the fuel electrode side and a gold ring was used as a sealant to ensure the gas tightness of both chambers at the working temperature. The measurement station was placed inside an electrically heated tubular furnace.[34,35]

Composition of the water content in fuel gas inlet mixture was controlled by a steam generator and mass flow controllers (Brooks 5850S). A gas flow inlet system allows for mixing steam with the other gases (H_2 and CO_2). The cells have been electrochemically characterized by i-V measurement and EIS in galvanostatic mode, using a Keithley 2000 multimeter and Solartron 1260 for data acquisition.[34,35] EIS measurements were carried out at OCV in a frequency range from 0.1 MHz to 100 mHz by applying an AC signal of 3.75 mA cm^{-2} of amplitude.[34,35]

> **In this thesis**, ProboStat setup was used in Chapter III, IV, V and VI for the characterization of all the button cells (diameter ≈2 cm) produced. The electrochemical characterization of the hybrid 3D printed cells of LSM+YSZ is presented in Chapter III.
>
> The large area cell system was used for the electrochemical characterization of ≈25 cm² cells. The results are showed in Chapter V.

2.6.2   Impedance spectroscopy characterisation

Electrochemical impedance spectroscopy (EIS) is a powerful tool to investigate the properties of power sources devices (e.g. batteries, fuel cells, supercapacitors, membranes). Impedance spectroscopy can separate the phenomena that take place in these complex systems in individual processes by the characteristic frequency related to their time responses.[36]

Impedance is defined as (2.2):[37]

$$Z = \frac{\Delta V}{\Delta I} = \frac{|V|}{|I|} \frac{e^{j\omega t}}{e^{j(\omega t + \phi)}} = |Z| e^{j\phi} \tag{2.2}$$

Where **ΔV** is a periodic potential perturbation applied to a circuit, which in case of a periodic sinusoidal signal (ω angular velocity) is equal to (2.3):

$$\Delta V = |V| e^{j\omega t} \tag{2.3}$$

Impedance **Z** determines an angular shift ϕ in the current response. The current **ΔI** is (2.4):

$$\Delta I = |I| e^{j\omega t + \phi} \tag{2.4}$$

The application of a mathematical model is often required to analyse an impedance measurement. The interpretation of the measurements can be

Advanced strategies for Solid Oxide Electrolysis Cells

done with the application of equivalent circuits with a limited number of parameters, which could fit the experimental data. This means that the physicochemical significance of the obtained parameters is not always clear.

The measurement is made varying the frequency of the signal in a wide range (several orders of magnitude). The data acquired during the measurements are usually in terms of Z' and Z", which are respectively the real and imaginary parts of the impedance (2.5):

$$Z(j\omega) = Z' + iZ'' \tag{2.5}$$

The obtained data can be plotted in complex plots called Argand diagram (also known as Nyquist plot). A typical representation is the one showed in Figure 2.18.
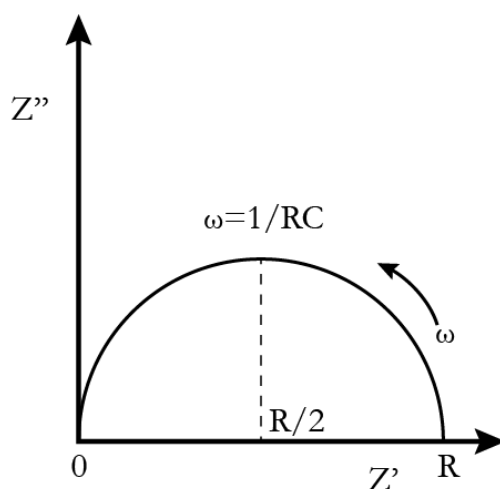

Figure 2.18: Nyquist plot of an RC element with angular frequency 1/RC at R/2.

The figure shows the specific impedance response in a circuit made of a resistance in parallel with a capacitor (*RC*) with impedance equation (2.5):

$$Z(j\omega) = \left(\frac{1}{R} + j\omega C\right)^{-1} \tag{2.6}$$

Where the serial resistance (which corresponds to the first intersection of the spectrum with the real axe) is in this case equal to zero. Notably, *RC* circuits are often used for the modellization of electrochemical phenomena, which are then described in terms of polarization resistance *R* and capacitance *C* to the associated phenomena. The characteristic angular frequency at $R/2$ is equal to $1/RC$.

In a real system the relaxation time of the process is often distributed, therefore the substitution of the pure capacitor with a Constant Phase Element (CPE) could be useful. CPE presents capacitance with a certain time dispersion. Its impedance is (2.7):

$$Z(j\omega) = \left[\frac{1}{R} + (j\omega)^n Q\right]^{-1} \tag{2.7}$$

Where *Q* is a parameter related to the true capacitance *C* of the element, and *n* is the constant phase exponent $0 < n < 1$, which is related to the deviation from the 90° of an ideal capacitor in the Argand diagram: $\alpha = 90°(1-n)$. Such variable exponent partially reflects the nature of the phenomenon described by the CPE. It is usually between 0.8 and 1 when the CPE approaches the behaviour of an ideal capacitor (e.g. chemical reaction), while it is around 0.5 for other types of phenomena such mass transport.[37]

In this thesis, impedance spectroscopy was used to study the performances of the devices fabricated in chapter III, chapter IV and chapter V. The equipment used for the measurement were alternatively impedance Frequency Response Analysers (Novocontrol Alpha and Solartron 1260) and potentiostats (Parstat 2273)

2.6.2.1   *Distribution of relaxation times (DRT)*

Distribution of relaxation times (DRT) is an alternative way to analyse impedance spectra, which separates the processes characterized by different

Advanced strategies for Solid Oxide Electrolysis Cells

time constantans.[36,38] In DRT the experimental data is fitted by the following expression (2.8):[38]

$$Z_{DRT}(f) = R_\infty + \int_0^{+\infty} \frac{G(\tau)}{1+i2\pi f\tau}\, d\tau \qquad (2.8)$$

Where R_∞ is the serial resistance and $G(\tau)$ is the distribution or relaxation times. Such an expression corresponds to an equivalent circuit composed by a serial resistance R_∞ followed by an infinite succession of *RC* elements (for $f \rightarrow \infty$). Frequency data are usually collected in logarithmic scale. Equation (2.8) can be rewritten as follows (2.9):[38]

$$Z_{DRT}(f) = R_\infty + \int_{-\infty}^{+\infty} \frac{\lambda(ln\tau)}{1+i2\pi f\tau}\, dln\tau \qquad (2.9)$$

$\lambda(ln\tau)$ is the regularization parameter and its determination is of great importance to reduce the error of the DRT fitting and it should be carefully chosen. High regularization parameter means poor fitting of the impedance spectra, while a too low $\lambda(ln\tau)$ can lead to overfit the experimental data.

> **In this thesis**, The DRT analysis was carried out using the open source software *DRTtools*.[38] DRT was used in Chapter V to fit the impedance spectra obtained measuring the large are cells.

2.7   Microstructural characterization

In the following section a brief description of the structural characterization techniques used for this project and their basic principles is reported.

2.7.1 X-ray diffraction (XRD)

X-rays have a wavelength (0.01 - 10 nm) which is comparable with the dimension of the internal planes of a crystal, therefore they can provide a great number of information about the inner structure of a material.[39]

During the analysis, a coherent beam with fix wavelength hits a sample generating coherent and uncoherent scattering phenomena that happen in all directions. If a plane is part of a family with same orientation, the constructive interactions between the reflections of each plane will generate a diffraction peak for a determined angle. This constructive interaction take place when Bragg law conditions are satisfied (2.10):[39]

$$2dsin\theta = n\lambda \qquad (2.10)$$

Where θ is the incident angle, λ is the wavelength of the beam, d is the interplanar distance and n is the order of reflection and is equal to the number of wavelengths in the path (Figure 2.19a). In a structure analysis by X-ray, 2θ is the angle considered and is the sum of the angles of incident and reflected beams (Figure 2.19a).

X-ray diffraction analysis was conducted using a Bruker-D8 Advance with copper K_α radiation (λ = 1.54060 Å), a nickel filter and Lynxeye 1D detector, with 2θ between 20° and 90° (Figure 2.19b).

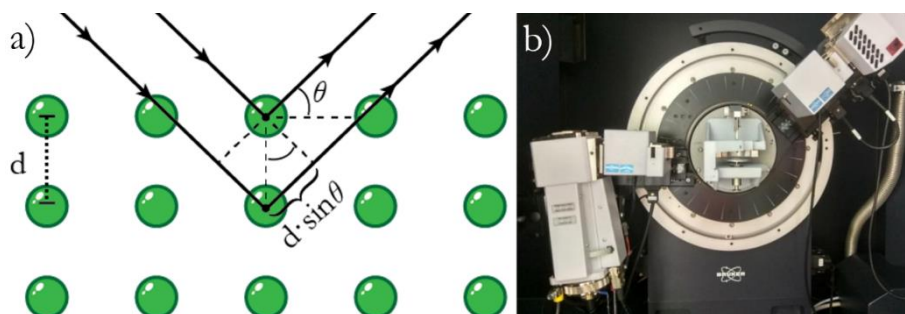**Figure 2.19:** Schematic representation of the Bragg Law (a), Bruker-D8 Advance diffractometer at the IREC facilities (b).

Advanced strategies for Solid Oxide Electrolysis Cells

> **In this thesis** XRD analysis was used in Chapter III for the characterization of the 3D printed cells produced. In Chapter IV the XRD analysis of the mesoporous powders after etching by HF are reported.

2.7.2 Small-angle X-ray scattering (SAXS)

Small angle X-ray scattering is based on the same principles of regular X-ray diffraction and relies on the reciprocal relation between the dimension of the object and the amplitude of the angle of the incident beam. In particular, objects with average diameter of tens on nanometers can be measured for angle $\theta < 1°$ and small wavelength (0.1 nm $< \lambda <$ 10 nm).[40] In SAXS analysis the diffraction patterns is usually represented as function of the *scattering vector* **q**, which is defined as the difference between the $\mathbf{k_0}$ vector of the scattered beam and the **k** vector of the incident one.[40] Bragg law can be rewritten as (2.11):

$$|\boldsymbol{q}| = |\boldsymbol{k_0} - \boldsymbol{k}| = 4\pi sin\theta\lambda^{-1} \tag{2.11}$$

SAXS data were obtained on the NCD-SWEET beamline at the synchrotron ALBA (Cerdanyola del Vallés, Barcelona, Spain) at 12.4 KeV. The data were collected on a Pilatus 1M detector (with a pixel size of 172.0 × 172.0 mm^2) for the SAXS data and on an LX255-HS Rayonix detector. The distance between the sample and detector was 6660.00 mm for the SAXS detector. The exposure time was 1 s. The temperature of the sample was controlled using a Linkam hot stage.

> **In this thesis**, SAXS measurements were employed in Chapter IV to verify the presence of the $Ia\overline{3}d$ structure and investigate any possible variation of the meso-structure which may be caused by HF etching. The analysis was conducted by other researchers of the group.

2.7.3 Scanning electron microscopy (SEM)

Scanning electron microscopy (SEM) is a very common analysis technique in which an electrode beam generated from an electron gun is focused by magnetic lenses on a sample in high vacuum conditions (Figure 2.21a). When electrons hit the surface of the specimen, they can be scattered away from the sample (backscattered electrons - BSEs), or they can induce the emission of secondary electrons (SEs), X-rays or Auger electrons (Figure 2.21b).[41]

BSE are elastically reflected from the samples after collision with the atoms. BSE can provide information about specimen composition, topography, mass thickness, and crystallography. The number of backscattered electrons is proportional to the atomic number of the atoms composing the specimen. This means that with BSE imaging is easier to differentiate between different phases.[41]

SEs consist in electrons ejected from the atoms of the specimen because of the interaction with the electron beam. A small fraction of all the SEs generated by the interaction beam/specimen can escape from the sample with enough energy to be detected. This means that SEs detected during SEM analysis are coming mainly from the surface of the specimen. For this reason, SEs provide information about the topography of sample's surface.[41]

X-ray emitted due to the interaction beam/specimen are sharply characteristic of each atom species. Energy Dispersive X-Ray spectroscopy

Advanced strategies for Solid Oxide Electrolysis Cells

(EDX) can identify the presence of elements in a certain area and quantify their amount.
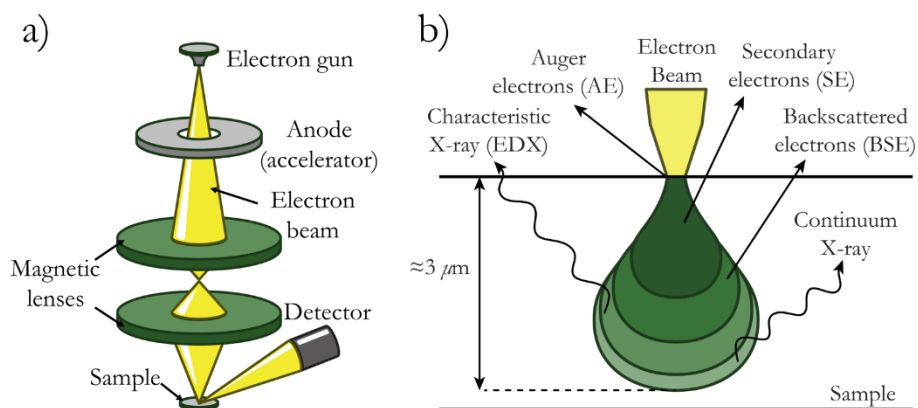

Figure 2.20: Schematic representation of the working principles of an SEM (a). Signals generated from the electron-matter interaction and typical interaction volume (b).

SEM and Auriga scanning electron microscope with an EDX spectroscope (Figure 2.21) at the IREC facilities was used for the microstructural analysis of synthetized powders or cell.

Figure 2.21: Auriga SEM at the IREC facilities.

In this thesis, SEM-EDX was used in all the chapter of the present thesis, for the characterization of the synthesized powders (Chapter IV) and the produced devices (Chapter III, Chapter V and Chapter VI).

2.7.4 Transmission electron microscopy (TEM)

Transmission electron microscopy (TEM) is a technique in which a high energy electron beam is passing through an ultrathin sample. The beam is accelerated at high voltage (200-300 kV). TEM allows the analysis of very small objects. The resolution limits of high resolution TEM (HRTEM) is below 0.1 nm.[42] Regular TEM uses a parallel beam, while scanning TEM (STEM) analysis uses a convergent beam which moves along the sample.

As already mentioned for SEM, the interaction of the electron beam with the specimen could lead to different events. Some of the electrons can be backscattered, others can present different kind of interactions with the atoms of the specimen. These interactions can involve the emission of secondary electrons, X-ray and Auger electrons. Specimens for TEM analysis are usually very thin (<100 nm), therefore most of the electrons are transmitted through the sample. Some of the electrons of the beam do not have any interaction with the samples, while the majority is scattered forward (elastically and inelastically). Those elastic scattering events that occur at relative low angles (>10°) are usually coherent. (S)TEM imaging consists of the generation of contrast images from these electrons.[42]

In STEM imaging the signal from the scattered electron on axis using a bright-field (BF) detector is usually utilized. Also, electrons scattered through small angles (>3°) or through higher angles, using annular dark-field

Advanced strategies for Solid Oxide Electrolysis Cells

(ADF) and high-angle annular dark-field (HAADF) detectors, respectively can be analysed for imaging.

Inelastic scattering takes place for very small angles ($<1°$) and is always incoherent. These electrons lose part or their energy and the analysis of their energy distribution is called electron energy-loss spectroscopy (EELS).[42] EELS provides information about the electronic structure of the specimen, including the valence state of the atoms.

Similarly, EDX analysis can be employed to obtain information about the chemical properties of the specimen through the analysis of the X-ray emitted.

> **In this thesis** TEM analysis have been done from the University of Barcelona (UB) to study the mesoporous CGO powders synthetized during this study. The results are shown in Chapter IV.

2.8   Other characterization techniques

2.8.1   Micro Gas Chromatographer (μGC)

Gas chromatography is a quite common analytical technique to quantify the amount of the different components of a gas mixture. The sample gas is drive through a column by a carrier gas, which is generally helium or other inert gases, such nitrogen and argon. Inside the column, covering its walls, there is the *stationary phase*. The stationary phase forces the gases to elute at different times allowing their identification (Figure 2.22a).

Figure 2.22b shows the Agilent 490 Micro Gas Chromatographer (μGC) utilized during this work at the IREC facilities. The μGC has three columns for the separation of the gaseous species (calibrated to measure H_2,

Ar, N_2, O_2, CO, CH_4, CO_2). The carrier gases used are helium and argon (Molsieve 0.5 nm with Ar, Molsieve 0.5 nm with He and PoraPLOT Q).
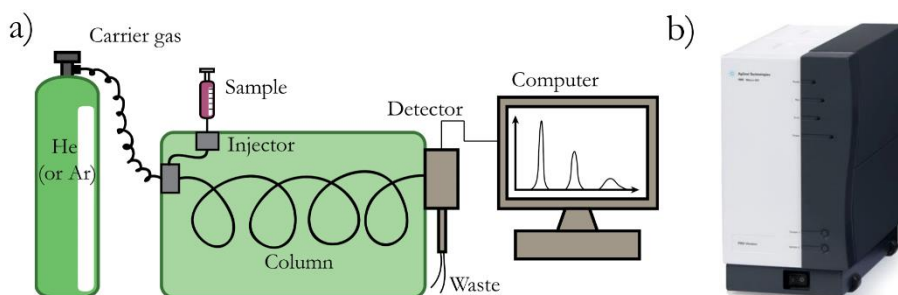

Figure 2.22: Schematic representation of a gas chromatographer (a). Agilent 490 μGC (b).

In this thesis, μGC analysis were conducted in Chapter VI to determine the amount of H_2, CO and CO_2 produced by the partial oxidation of methane.

2.8.2 Nitrogen physisorption measurements (BET)

Brunauer–Emmett–Teller (BET) theory uses the physical adsorption of a gas on a sample to determine its surface area. The analysis derived by this theory is generally undertaken at constant temperature and with the utilization of an inert gas in order to avoid chemical adsorption and keep the process only driven by Van der Waals forces.[43] Accepted standard procedure utilizes nitrogen at its boiling temperature, 77.350 K (−195.795 °C) at 1 atm. Since the analysis is conducted at constant temperature an adsorption isothermal curve can be determine (2.12):[44]

$$n_a = f(p/p_o)_{T,gas,solid} \tag{2.12}$$

The amount of gas adsorbed (n_a) is expressed as a function of the equilibrium relative pressure, p/p_o. At low partial pressures nitrogen forms a

Advanced strategies for Solid Oxide Electrolysis Cells

monolayer of adsorbed molecules increasing p/p_o. The first stage is followed by the formation of an adsorbed multilayer which leads to the complete filling of the porosity by capillarity condensation (Figure 2.23).
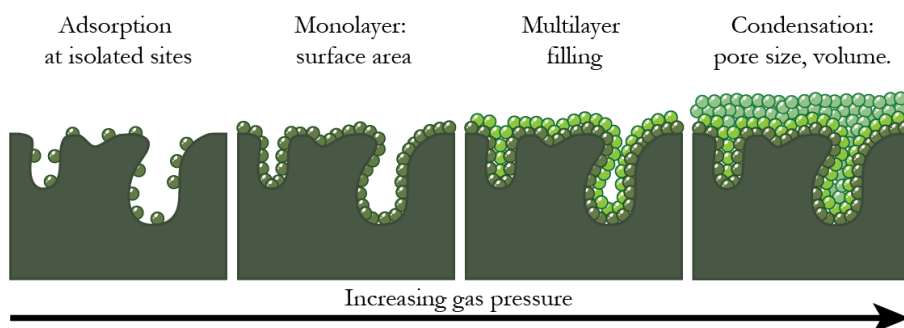

Figure 2.23: Schematic representation of the different stages of an inert gas surface adsorption, starting from isolated sites to the formation of the first monolayer, followed by the formation of different layers up to the complete filling of the porosity.

A Micromeritics TriStar II 3020 surface analyser (with liquid nitrogen, 77 K) was used at the IREC facilities for the analysis.

In this thesis, BET analysis was used to measure the surface area of CGO mesoporous powders synthetized by nanocasting. The results of this analysis are presented in Chapter IV.

2.8.3 Thermal programmed reduction (TPR)

Thermal programmed reduction (TPR) is a technique largely used for the study of redox properties of oxide materials and effectiveness of certain catalysts. In TPR a constant flux of reducing gas (e.g. 5% H_2 / 95% N_2) passes through a chamber in which a known amount of oxide is placed and at the starting point the temperature should be low enough to avoid premature reduction of the catalyst. The temperature is risen with a constant rate and

Advanced strategies for Solid Oxide Electrolysis Cell

the difference of gas amount before and after the reduction process is measured by the difference in the thermal conductivity. TPR determines the number of reducible species present on the surface of a material and the temperature at which the reduction process take place.

> **In this thesis**, TPR was used to characterize the redox activity of mesoporous powders before and after etching by HF as reported in Chapter IV and also using methane instead of hydrogen, to determine the effectiveness of metallic Ni and Cu as catalyst for methane partial oxidation.

2.8.4   Inductively coupled plasma mass spectrometry (ICP-MS)

ICP-MS is a quite common and precise techniques to analyse inorganic elements dispersed into aqueous solutions with a precision up to parts per billion. An electromagnetic coil inductively heats the steam until an ionized gas is generated forming the plasma. The plasma is then analysed by the mass spectrometer giving the precise amount of species present.

> **In this thesis**, ICP-MS was used in Chapter IV to determine the amount of SiO_2 present in the mesoporous CGO before and after the etching by HF.

2.9   Bibliography

1   X. Deng, K. Chen and H. Tü˙Ysü˙, *Chem. Mater*, 2017, **29**, 40–52.
2   A. H. Lu and F. Schüth, *Adv. Mater.*, 2006, **18**, 1793–1805.
3   Y. Ye, C. Jo, I. Jeong and J. Lee, *Nanoscale*, 2013, **5**, 4584–4605.
4   M. Torrell, L. Almar, A. Morata and A. Tarancón, *Faraday Discuss.*, 2015, **182**, 423–435.
5   L. Almar, T. Andreu, A. Morata, M. Torrell, L. Yedra, S. Estradé, F. Peiró and A. Tarancón, *J. Mater. Chem. A*, 2014, **2**, 3134–3141.
6   S. C. Laha and R. Ryoo, *Chem. Commun.*, 2003, 2138–2139.

Advanced strategies for Solid Oxide Electrolysis Cells

7   S. A. Ghom, C. Zamani, S. Nazarpour, T. Andreu and J. R. Morante, *Sensors Actuators, B Chem.*, 2009, **140**, 216–221.

8   W. Yue and W. Zhou, *Chem. Mater.*, 2007, **19**, 2359–2363.

9   J. W. Kury, Z. Z. Hugus and W. M. Latimer, *J. Phys. Chem.*, 1957, **61**, 1021–1021.

10   J. Bae, *Solid State Ionics*, 1998, **106**, 247–253.

11   J. S. Judge, *J. Electrochem. Soc.*, 1971, **118**, 1772.

12   P. A. M. van der Heide, M. J. Baan Hofman and H. J. Ronde, *J. Vac. Sci. Technol. A Vacuum, Surfaces, Film.*, 1989, **7**, 1719–1723.

13   J. L. M. Rupp, U. P. Muecke, P. C. Nalam and L. J. Gauckler, *J. Power Sources*, 2010, **195**, 2669–2676.

14   E. Jud, C. B. Huwiler and L. J. Gauckler, *J. Am. Ceram. Soc.*, 2005, **88**, 3013–3019.

15   M. P. Pechini, *US Pat. 3,330,697*.

16   M. Liu and D. Wang, *J. Mater. Res.*, 1995, **10**, 3210–3221.

17   E. M. Hotze, T. Phenrat and G. V. Lowry, *J. Environ. Qual.*, 2010, **39**, 1909–1924.

18   R. Moreno, *Adv. Appl. Ceram.*, 2012, **111**, 246–253.

19   T. F. Tadros, *Dispersion of Powders in Liquids and Stabilization of Suspensions*, Wiley-VCH Verlag GmbH & Co. KGaA, Weinheim, Germany, 2012.

20   M. J. López-Robledo, J. Silva-Treviño, T. Molina and R. Moreno, *J. Eur. Ceram. Soc.*, 2013, **33**, 297–303.

21   T. Phenrat, N. Saleh, K. Sirk, H. J. Kim, R. D. Tilton and G. V. Lowry, *J. Nanoparticle Res.*, 2008, **10**, 795–814.

22   D. Stöver, H. P. Buchkremer and S. Uhlenbruck, *Ceram. Int.*, 2004, **30**, 1107–1113.

23   T. Ishihara, J. Tabuchi, S. Ishikawa, J. Yan, M. Enoki and H. Matsumoto, *Solid State Ionics*, 2006, **177**, 1949–1953.

24   E. Peng, D. Zhang and J. Ding, *Adv. Mater.*, 2018, **30**, 1–14.

25   E. Feilden, E. G. T. Blanca, F. Giuliani, E. Saiz and L. Vandeperre, *J. Eur. Ceram. Soc.*, 2016, **36**, 2525–2533.

26   B. Derby, *Annu. Rev. Mater. Res.*, 2010, **40**, 395–414.

27   B. Derby, *Engineering*, 2015, **1**, 113–123.

28   M. R. Somalu, A. Muchtar, W. R. W. Daud and N. P. Brandon, *Renew. Sustain. Energy Rev.*, 2017, **75**, 426–439.

29   X. Ge, X. Huang, Y. Zhang, Z. Lu, J. Xu, K. Chen, D. Dong, Z. Liu, J. Miao and W. Su, *J. Power Sources*, 2006, **159**, 1048–1050.

30   R. Eason, *Pulsed Laser Deposition of Thin Films*, John Wiley & Sons, Inc., Hoboken, NJ, USA, 2006.

31   M. Morales, V. Miguel-Pérez, A. Tarancón, A. Slodczyk, M. Torrell, B. Ballesteros, J. P. Ouweltjes, J. M. Bassat, D. Montinaro and A. Morata, *J. Power Sources*, 2017, **344**, 141–151.

32   E. Hernández, F. Baiutti, A. Morata, M. Torrell and A. Tarancón, *J. Mater. Chem. A*, 2018, **6**, 9699–9707.

33   N. M. M. Farandos, L. Kleiminger, T. Li, A. Hankin and G. H. H. Kelsall, *Electrochim. Acta*, 2016, **213**, 324–331.

34   S. H. Jensen, A. Hauch, P. V. Hendriksen and M. Mogensen, *J. Electrochem.*

Soc., 2009, **156**, B757.

35   E. M. Hernández Rodríguez, University of Barcelona, 2018.

36   E. Barsoukov and J. R. Macdonald, *Impedance Spectroscopy: Theory, Experiment, and Applications, 2nd Edition*, John Wiley & Sons, Inc., 2005.

37   A. Lasia, *Electrochemical impedance spectroscopy and its applications*, Springer New York, New York, NY, 2014, vol. 9781461489.

38   M. Saccoccio, T. H. Wan, C. Chen and F. Ciucci, *Electrochim. Acta*, 2014, **147**, 470–482.

39   B. D. (Associate P. of M. of N. D. CULLITY, , DOI:10.1017/CBO9781107415324.004.

40   A. Hofmann, *Synchrotron radiation*, 2008.

41   J. I. Goldstein, D. E. Newbury, J. R. Michael, N. W. M. Ritchie, J. H. J. Scott and D. C. Joy, *Scanning Electron Microscopy and X-Ray Microanalysis*, Springer New York, New York, NY, 2018.

42   D. B. Williams and C. B. Carter, *Transmission electron microscopy: A textbook for materials science*, 2009.

43   F. Ambroz, T. J. Macdonald, V. Martis and I. P. Parkin, *Small Methods*, 2018, **2**, 1800173.

44   K. S. W. Sing, *J. Porous Mater.*, 1995, **2**, 5–8.

Advanced strategies for Solid Oxide Electrolysis Cells

Chapter III

Advanced Solid Oxide Cells from additive manufacturing: from the powder to the printing optimisation

3.1   Chapter overview

The aim of this chapter is to discuss the results regarding the optimization of the Additive Manufacturing (AM) techniques used for the fabrication of Solid Oxide Cells (SOC) devices.

i. Symmetrical cells with CGO scaffolds automatically infiltrated by inkjet printing with sol gel solution of La, Sr, Mn and Fe nitrates were fabricated (section 3.2)

    a. Rheological characterization of the inks is presented, followed by microstructural characterization of the symmetrical YSZ/CGO+LSCF cells (sections 3.2.1, 3.2.2 and 3.2.3).

    b. Electrochemical characterization of the cells is shown and the effect of the infiltration to the measured *ASR* is discussed (section 3.2.4).

ii. Hybrid 3D-printed symmetrical cells with composition YSZ/YSZ+LSM were produced by means of Inkjet printing and Robocasting (section 3.3).

    a. Printing process is presented, followed by the rheological characterization of the inks/slurries. Results of the microstructural characterization of the cells are shown (sections 3.3.1, 3.3.2 and 3.3.3).

    b. The cells were electrochemical analysed. The discussion was rationalized with the results obtained from the microstructure (section 3.3.4).

Hybrid 3D-printed cells were produced and characterized at the DTU facilities in Denmark, where the printability of the slurries was tested and the cells were electrochemical and microstructural characterized after fabrication.

3.2   Inkjet printing for the infiltration of SOC electrodes

With the goal of obtaining an optimised composite for SOC oxygen electrodes, the inkjet printing process was optimized for wet infiltration of a MIEC material (LSCF) in an ionic conductor scaffold (CGO). For this purpose, electrolyte-supported symmetric cells were employed using 8YSZ tapes (thickness ≈150 μm; FAE S.A.U.) as an electrolyte. Infiltration of LSCF was carried out using a sol-gel ink.

3.2.1   Choice of the ink for LSCF infiltration

Three types of ink were produced using different amounts of glycine respect the total molar cations (cations:glycine were 1:3, 1:6 and 1:9 respectively). Viscosity and surface tension measurements were conducted to characterize the inks, calculating the Z number to determine their printing feasibility.[1,2]

Viscosity measurements of the three different inks are shown in Figure 3.1a together with the surface tension measurements (Figure 3.1b). The inks are here compared to the commercial HP black ink.

Advanced strategies for Solid Oxide Electrolysis Cells
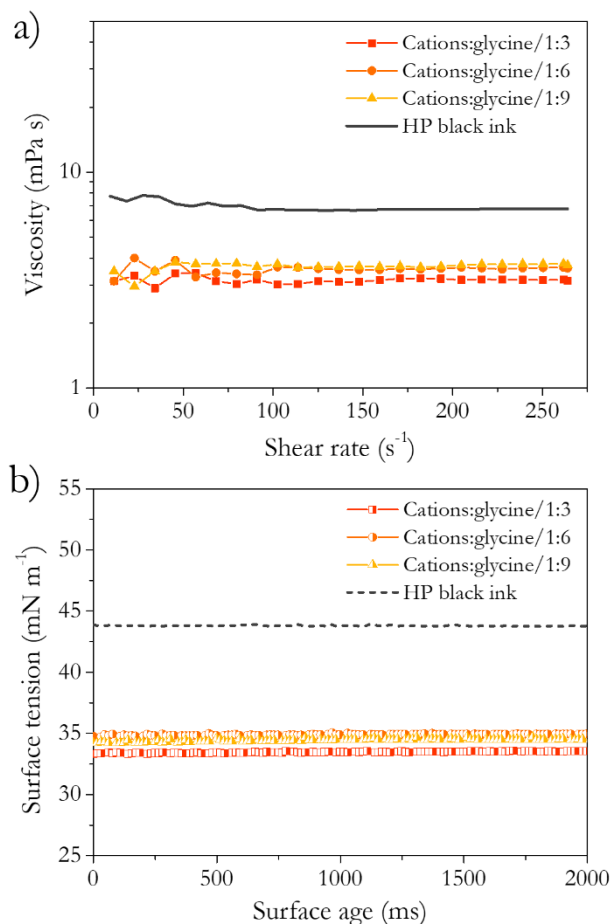
Figure 3.1: Viscosity (a) and surface tension (b) measurements of the sol gel inks compared with the HP ink inside the cartridges.

On Table 3.1 the average values of viscosity and surface tension of the inks are reported, together with the respective densities and the calculated Z numbers.

Table 3.1: Properties of the sol-gel inks used for the functionalization of the CGO scaffolds.

Ink	Density (g cm⁻³)	Viscosity (cP)	Surface tension (mN m⁻¹)	Z number
EtOH 1:3	0.9	3.2 ± 0.1	33.1 ± 0.3	17.9 ± 0.4
EtOH 1:6	1.0	3.5 ± 0.1	35.2 ± 0.5	16.8 ± 0.6
EtOH 1:9	1.0	3.6 ± 0.1	34.6 ± 0.5	16.3 ± 0.7

3. Advanced Solid Oxide Cells from additive manufacturing

The printability range given by Z changes a little depending on the authors, Reis and Derby put it between 1 and 10^{3},[4] while Jang et al. move it between 4 and 14.[5] Nowadays the Z range of printability has changed and in different paper has been demonstrated feasible prints from Z number far above 10 (e.g. Delort *at al.* which show $0.5 < Z < 100$,[6] Choi *et al.* which report $0.23 < Z < 84.77$,[7]). Despite the advantages provided by the utilization of such parameter, it is generally accepted that Z by itself cannot provide detailed indications about the printability of an ink. Indeed, Z contains all together the three most important parameters governing the wettability (inertial force, viscosity and surface tension). This means that inks that possess very different characteristics one to the other could give the same Z number. For these reasons Nallan *et al.* suggested instead to plot *We* with the capillarity (*Ca*) of the suspension[8] and Derby already in 2010 proposed a representation on the *Re-We* space.[1] In a more recent work from Liu and Derby himself, the Z range was readjusted. In this work the authors considered a good printability feasible for $1 < Z < 20$. Additionally, a representation in the *Z-We* space was proposed to provide a more precise indication about the final result of the jetting, which bounded the printability also to the $2 < We < 25$ range.[2]

Unfortunately, regarding the formulated sol-gel inks, the volume and the jetting speed of the droplets produced by the HP C66002 could not be measured. However, We and Ca number ranges were estimated considering a reasonable speed range of 1-10 m s^{-1}. Figure 3.2 shows the printability range notations from Derby (Figure 3.2a) and Nallan (Figure 3.2b), including an estimation of the printability zones of the produced inks. It can be observed that the inks are comprised, in both cases, between the printable area and the satellite drops formation. The formation of satellite drops is not considered an issue for infiltration and, during the printing process, no jetting issues were observed.
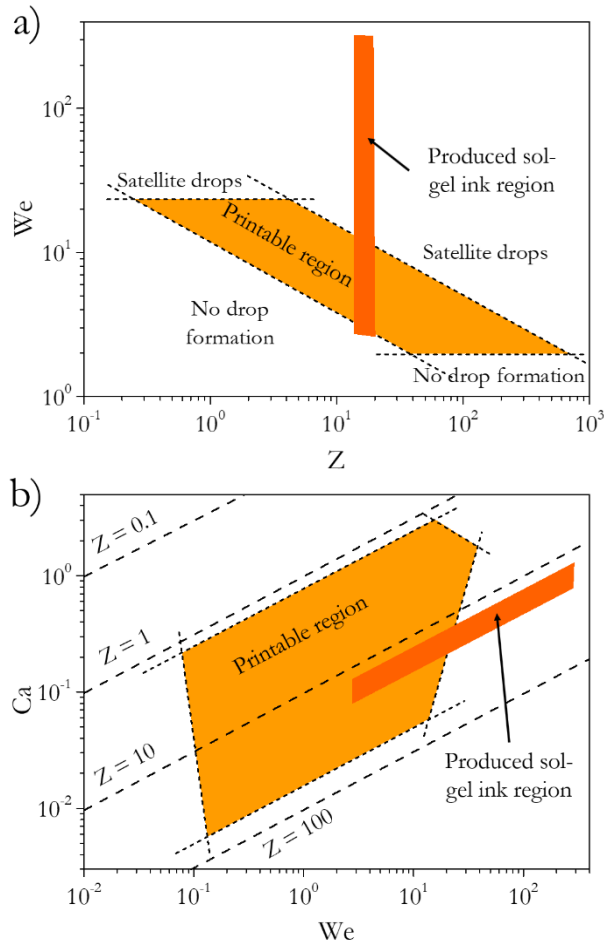
Advanced strategies for Solid Oxide Electrolysis Cells

Figure 3.2: Derby[2] (a) and Nallan[8] (b) printable regions, considering the velocity range of the drops $(1 - 10 \text{ m s}^{-1})$ the inks are comprise between the preferable region for jetting and the satellite drop region.

Since the three inks had very similar rheological properties the one with the higher ratio cations:glycine (1:3) was the final choice to infiltrate the samples. A higher ratio means larger amount of cations inside the CGO backbones for the same volume of infiltration solution. This is expected to improve the functionalization of the backbone.

3.2.2 Symmetrical cell infiltration by Inkjet printing

3.2.2.1 Calibration of the printing process

For the automatic infiltration, a Custom-made inkjet printer produced by Print3d Solutions equipped with a commercial HP cartridge (HP C6602A) was used. This kind of cartridge allow to select a "saturation" parameter (from 0 to 20) for determining the amount of jetted ink during the deposition.
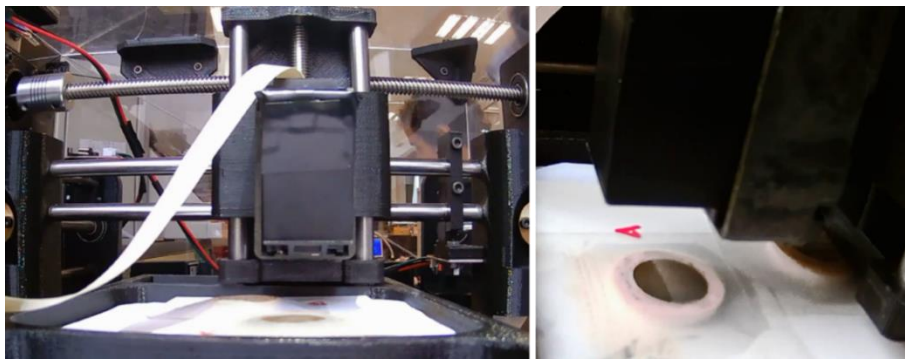
Figure 3.3: Custom-made Inkjet printer produced by Print3d Solutions used for the automatic infiltration of CGO scaffolds by sol gel inks.

With the aim to calibrate the automatic infiltration process, which is influenced by the saturation number, a test symmetrical cell with two commercial CGO scaffolds was prepared. The backbones were infiltrated with saturation 5 in three steps. For each one the cartridge injected LSCF ink three times on top of the scaffold. Therefore, IJP deposited the ink nine times in total for each side. After each step, the ink was left to dry at room temperature and the cell was weighted (Figure 3.4).

The results presented in Figure 3.4 are compared to a reference cell with commercial CGO scaffold which was infiltrated by hand in three steps for an overall volume of 120 μL (after every 30 μL the cell was left drying at room temperature)

Advanced strategies for Solid Oxide Electrolysis Cells
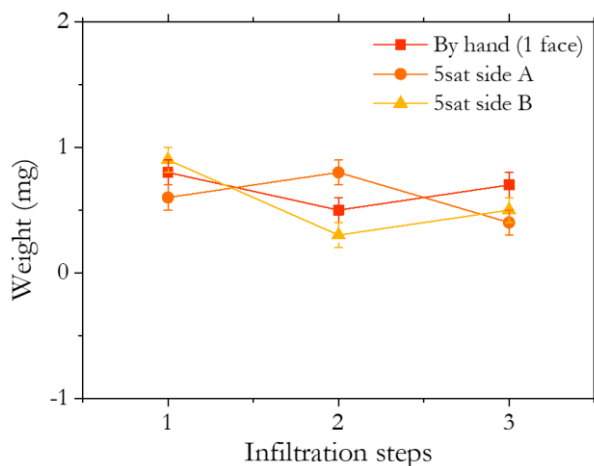
Figure 3.4: Comparison between manually and automatic inkjet infiltration. Weight difference before and after the infiltration of the cells after each step.

The weights of the three scaffolds are quite similar. Therefore, the volume of ink jetted three times by the IJP with saturation 5 can be considered close to the 30 μL infiltrated by hand for the same area. With the aim of reducing the printing steps during the deposition, saturation was also kept at 10 during the fabrication of the symmetrical cells described below. The amount of solution infiltrated in the scaffold was controlled by weight and the effectiveness of the two saturation values during infiltration was discussed with the electrochemical characterization of the cells.

3.2.2.2 *Infiltration of the cells*

One test half-cell for a preliminary printability test was produced followed by four symmetrical cells. In Table 3.2 the main characteristics of the cells are presented.

Table 3.2: Characteristics of the cells produced. Commercial YSZ tape (160 μm) was used for all the fabricated cells. A barrier layer made of commercial CGO decorated by Co oxide was deposited and sintered at 1275 °C. Commercial CGO scaffolds were sintered at 1250 °C and the mesoporous CGO at 900 °C.

CELL	Scaffold	Infiltration	Saturation
Preliminary test	Commercial CGO	Yes	10
CGO	Commercial CGO	No	-
5-CGO	Commercial CGO	Yes	5
10-CGO	Commercial CGO	Yes	10
10-CGO$_{meso}$	Mesoporous CGO	Yes	10

The three symmetrical test cells fabricated by airbrushing with commercial CGO scaffolds (thickness ≈60 μm) were produced and analysed to evaluate the effectiveness of the automatic infiltration. They were processed in three different ways: one cell was measured without any infiltration (CGO) and the other two (see Figure 3.5) were infiltrated respectively keeping the ink saturation at 5 (5-CGO, Figure 3.5a) and 10 (10-CGO, Figure 3.5b). The mesoporous CGO symmetrical cell (sintered at 900 °C for 5 h) was infiltrated with saturation at 10 (10-CGO$_{meso}$). In order to deposit a similar amount of solution inside each scaffold, the 5-CGO cell was infiltrated with more deposition steps than the 10-CGO and the 10-CGO$_{meso}$ cells. This was made to compensate the different saturations used for printing. After the infiltration process each cell was weighted, showing a total increment of 25 ± 2 mg.
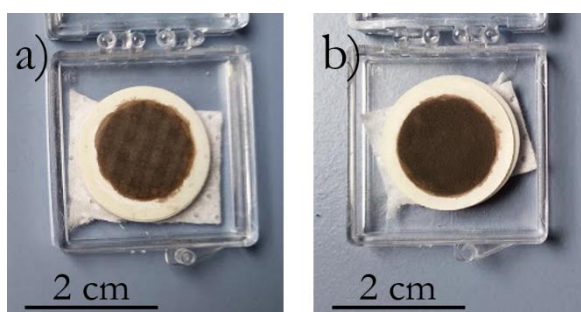
Figure 3.5: Two of the produced cells, with commercial CGO scaffold and infiltrated using saturation parameter 5 (a) and 10 (b) respectively.

3.2.3 Microstructural characterization of the infiltrated cells

3.2.3.1 *Preliminary printability test*

Microstructural characterization was carried out on a commercial CGO backbone upon automatic infiltration by LSCF (preliminary test cell). Saturation value used for the infiltration: 10.

XRD analysis was carried out to investigate the formation of the LSCF perovskite after the calcination process (2 h at 800°C). In Figure 3.6 the XRD pattern of the cell is presented, showing the characteristic peaks of YSZ (electrolyte support), CGO and LSCF. No secondary phases were detected.
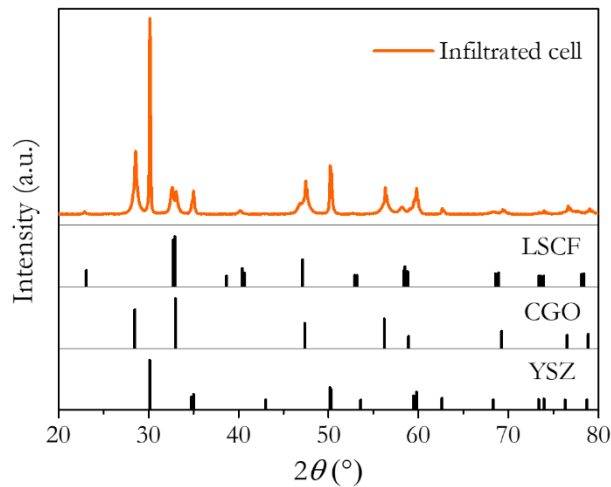
Figure 3.6: XRD made on the preliminary test cell. The presence of the LSCF characteristic peaks confirms the formation of the perovskite after the calcination process.

SEM micrographs (Figure 3.7) were also obtained to investigate the homogeneity of the infiltration process. The airbrushed electrode shows, in the representative Figure 3.7a, that the infiltration reached the YSZ electrolyte. The LSCF phase infiltrated and calcinated at 800 °C partially covers the CGO backbone (Figure 3.7b). An open porosity is a fundamental aspect to allow the diffusion flow of the air during cell operation.
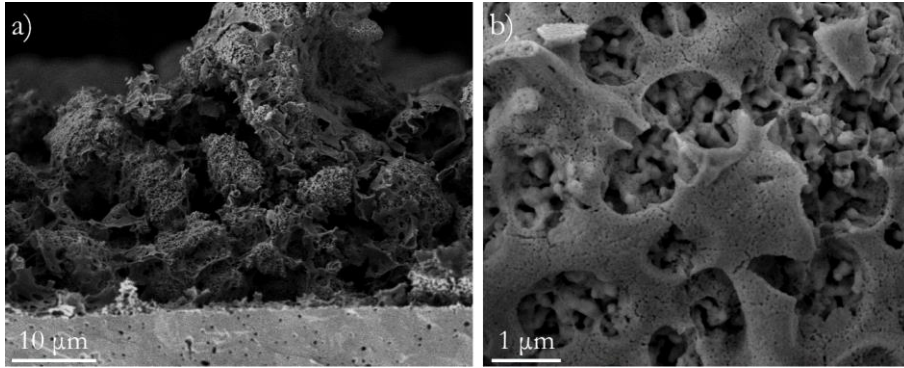
Figure 3.7: Cross section micrographs of the scaffold of the preliminary test cell. In the micrograph is possible to see both the CGO scaffold and the LSCF infiltrated by inkjet printing (a). High magnification micrograph of the infiltrated scaffold (b).

Figure 3.8 shows an SEM-EDX map made on a representative region (Figure 3.8a) of the infiltrated CGO scaffold. Zr, Ce and La were chosen as marker elements of the main phases (YSZ, CGO and LSCF, Figure 3.8b). The elemental mapping shows that the perovskite is homogeneously distributed all along the airbrushed backbone. This confirmed the success of the infiltration process and the functionalization of the oxygen electrode for SOC application.
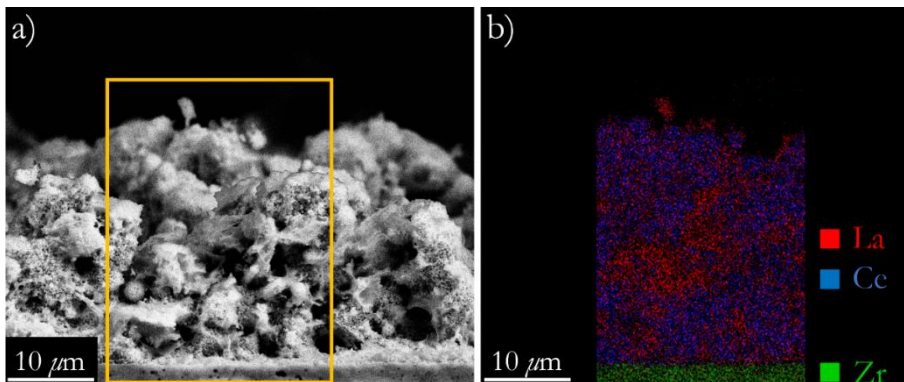
Figure 3.8: Representative region of the infiltrated scaffold (a) and EDX map (b) where Zr (green), Ce (blue) and La (red) show the presence of YSZ, CGO and LSCF respectively.

3.2.3.2   Microstructural characterization of the symmetrical cells

The 5-CGO and the 10-CGO cells were observed by SEM and EDX maps to evaluate the result of the infiltration process as showed in Figure 3.9. Observing the 5-CGO samples, in Figure 3.9a, one can distinguish the YSZ electrolyte, the CGO barrier layer and the infiltrated CGO scaffold. On the SEM-EDX maps of Figure 3.9b, the YSZ electrolyte (marked by the Zr signal, green), the CGO barrier layer and the airbrushed backbone (Ce signal, blue) infiltrated by LSCF (La signal, red) are presented. The LSCF seemed well distributed inside the scaffold as highlighted by Figure 3.9b, where La and Ce signals are clearly overlapped in the zone corresponding to the CGO scaffold. Figure 3.9c shows a representative area of the 10-CGO cell, where is highlighted with a yellow square the zone where the SEM-EDX map (Figure 3.9d) was conducted. Such an analysis shows the YSZ electrolyte, the CGO barrier layer and the CGO backbone (Zr in green, Ce in blue). As in the 5-CGO case, La and Ce signals are clearly overlapped in the zone of the CGO scaffold. This proves the success of the automatic infiltration process and the desired functionalization of the oxygen electrode.
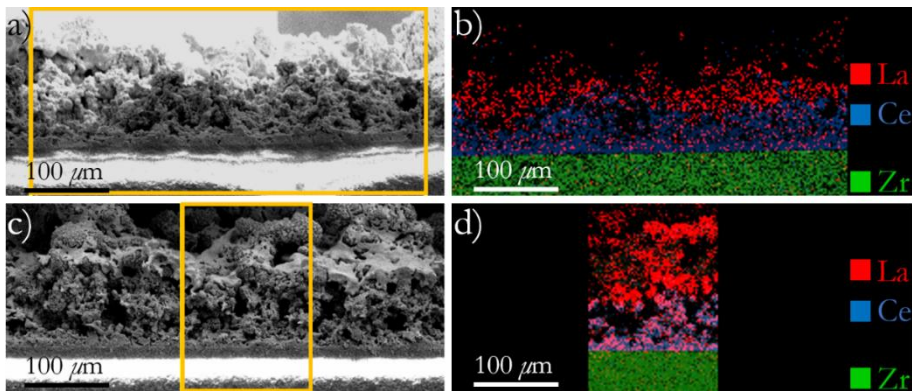

Figure 3.9: SEM micrographs of a) cell 5-CGO, with the corresponding b) EDX map and of the c) cell 10-CGO and its d) elemental distribution.

3.2.4 Electrochemical characterization of the infiltrated cells

CGO, 5-CGO, 10-CGO and 10-CGO$_{meso}$ were characterized by electrochemical impedance spectroscopy. The symmetrical cells were analysed under OCV conditions, air atmosphere and temperature range from 900 to 600 °C, with measurements taken every 50 °C. Figure 3.10a shows the impedance spectra at three different temperature (700 °C, 750 °C and 800 °C) of the 5-CGO cell, while Figure 3.10b presents the impedance spectra of all the symmetrical cells taken at 700 °C. Each impedance spectrum was fitted by Zview software applying the reciprocal circuit showed as inset of Figure 3.10a and Figure 3.10b. This circuit is characterized by an inductance L, a serial resistance R_s and two ZARC elements. The selected equivalent circuit was the simplest circuit able to fit the experimental data and for this reason it was considered the most appropriate choice for the fitting.
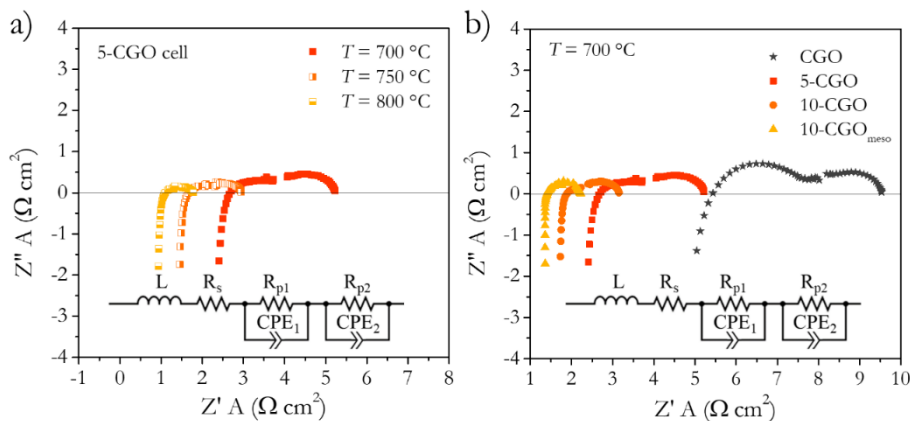
Figure 3.10: EIS spectra of the 5-CGO cell at 700 °C, 750 °C and 800 °C (a). EIS spectra of the four measured cells at 700°C (b). The equivalent circuit used for the fitting ins presented as inset of (a) and (b).

Arrhenius plots of the serial and polarization ASR are reported in Figure 3.12 and Figure 3.12 respectively. The calculated activation energies related to the serial resistance of all the four cells were quite similar ($\approx$0.9 eV) and are in agreement with the reported values for YSZ.[9]

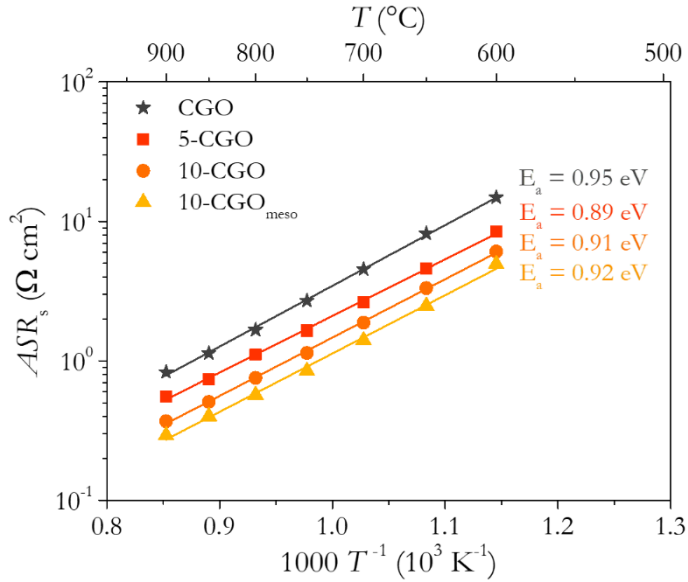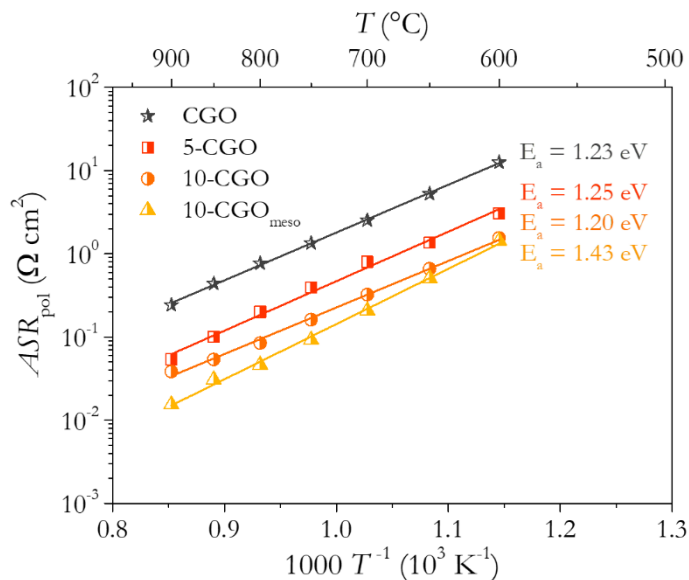Advanced strategies for Solid Oxide Electrolysis Cells

Figure 3.11: Arrhenius plots with serial ASR contributions of CGO, 5-CGO, 10-CGO and 10-CGO$_{meso}$ cells. The values were obtained by the fitting with the equivalent circuit showed in Figure 3.10.

Regarding the polarization resistance (Figure 3.12), the relatives activation energies are in the range 1.2 - 1.4 eV, which are typical values for the CGO-LSCF composites reported in literature.[10]

In particular, the cells with commercial CGO scaffold presented similar values (1.23 ±0.01 eV, 1.25 ±0.03 eV and 1.20 ±0.02 eV for CGO, 5-CGO and 10-CGO cells respectively). One can notice that the 10-CGO$_{meso}$ showed a slight E_a increment (1.4 ±0.02 eV). This difference could be caused by the presence of silica contamination due to the incomplete removal of the template by NaOH washing.[11]

Figure 3.12: Arrhenius plots with polarization ASR contributions of CGO, 5-CGO, 10-CGO and 10-CGO$_{meso}$ cells. The values were obtained by the fitting with the equivalent circuit showed in Figure 3.10.

Figure 3.13 and Figure 3.14 show a final comparison of the serial and polarization resistances at 700, 750 and 800 °C of the four cells. The beneficial effect of the infiltration process was improved by the adjustment of the deposition parameters (saturation which passes from 5 to 10) and by the combination with mesoporous CGO. The ASR_s values (Figure 3.13) decreased for the infiltrated cells, passing from 2.7 Ω cm^2 (CGO cell) to 1.6 Ω cm^2 (5-CGO cell), 1.1 Ω cm^2 (10-CGO) and 0.8 Ω cm^2 (10-CGO$_{meso}$) at 750 °C. Serial resistance includes ohmic resistance of the electrolyte and current collection contributions.[12,13] Its decrease is justified by the improvement of the electronic percolation, due to the infiltration of the LSCF phase. The MIEC increased the current collection points of the system.

As mentioned before 5-CGO and 10-CGO were infiltrated with the same amount of solution. Therefore, the better results of the 10-CGO are explained by a better general electronic percolation. This effect could correspond to a more uniform distribution of LSCF inside the scaffold. Note

that 10-CGO needed less deposition steps with respect to the 5-CGO cell. The advantage of an infiltration process with saturation at 10 was twofold: less time-consuming and better final result.

The mesoporous cell was infiltrated with saturation 10, and the scaffold was sintered at 900 °C, while the commercial CGO scaffold were sintered at 1250 °C. Nevertheless 10-CGO$_{meso}$ cell showed the lowest serial resistance of the four. This was assigned to the positive effect of the open porosity of the mesoporous scaffold for the infiltration process. Mesoporous CGO surface was ≈100 m^2 g^{-1} while for the commercial CGO powder was around 10-15 m^2 g^{-1}.[14,15] These values controlled the catalytic activity once the scaffold was functionalised by the developed process.

The polarization resistance, presented in Figure 3.14, showed also a quite evident improvement as consequence of the infiltration. At 750 °C ASR_{pol} passes from 1.3 Ω cm^2 (CGO cell) to 0.4 Ω cm^2, 0.2 Ω cm^2 and 0.1 Ω cm^2 for the 5-CGO, 10-CGO and 10-CGO$_{meso}$ respectively. The beneficial effect of the impregnation by the MIEC and the consequent extension of the TPB region can explain such a decrease.
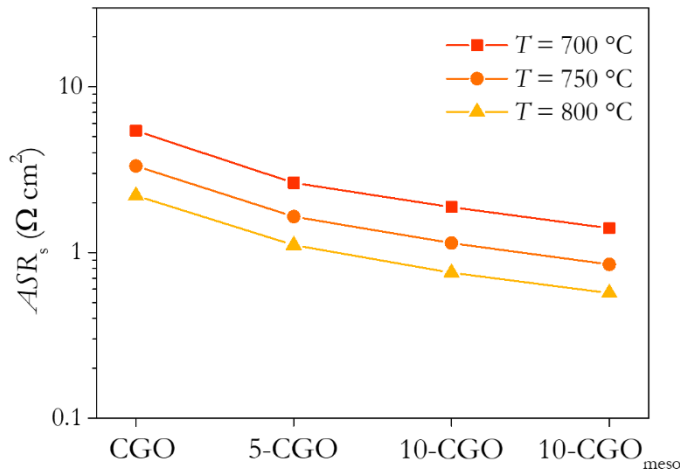

Figure 3.13: ASR_s of CGO, 5-CGO, 10-CGO and 10-CGO$_{meso}$ cells at 700, 750 and 800 °C.
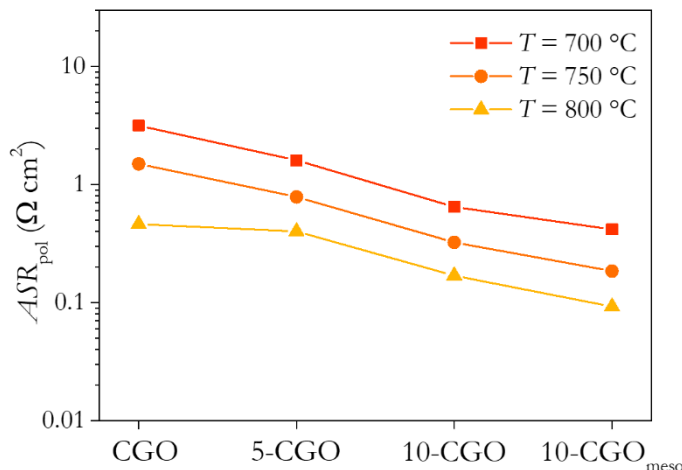
Figure 3.14: ASR_{pol} of CGO, 5-CGO, 10-CGO and 10-CGO$_{meso}$ cells at 700, 750 and 800 °C.

Figure 3.15 shows the capacitance values (C_1 vs. T and C_2 vs. T showed in Figure 3.15a and Figure 3.15b) of the two contribution. Figure 3.16 presents the relative resistance contributions (R_1 vs. T and R_2 vs. T in Figure 3.16a and Figure 3.16b respectively). The capacitance values of the $R_{p1}C_1$ element (with a frequency range between 10^4-10^2 Hz) were comprised between $1 \cdot 10^{-6}$-$5 \cdot 10^{-3}$ F cm^{-2}. In literature similar contributions for CGO/LSCF electrodes are consistent with charge transfer phenomena.[16–19] The $R_{p2}C_2$ element (10^1-10^0 Hz), was characterized by larger capacitance values $5 \cdot 10^{-4}$-$5 \cdot 10^{-2}$ F cm^{-2}. These frequency and capacitance values are identified in literature with surface exchange reaction like dissociation and adsorption of oxygen molecules.[18,20,21]

Dos Santos Gomez *et al.* highlights that electrode functionalization through infiltration can increase capacitance values for both processes due to the increment of contact points between CGO and LSCF.[18] This was revealed in the case of the present study for the high frequency contribution ($R_{p1}C_1$). Considering $R_{p2}C_2$ this increment of the capacitance value was not observed for the 10-CGO$_{meso}$ cell (Figure 3.15b). This effect was probably correlated to the aforementioned SiO$_2$ contamination which is due to the synthesis

process.[22] The contamination played a role reducing the contact point between CGO and infiltrated LSCF.[23]

This interpretation is supported by the ASR_{pol} plots of the two contributions presented in Figure 3.16a and Figure 3.16b. The $R_{p1}C_1$ resistance decreased while the saturation number increased. One can notice that the two cells infiltrated with saturation parameter at 10 presented similar resistance values. The infiltration volume was the same for 5-CGO and for 10-CGO and 10-CGO$_{meso}$ cells, but the infiltration process for the last two cells was characterized by a better distribution. This better distribution generated more contact points between the two phases improving charge transfer reactions.

In the case of the $R_{p2}C_2$, CGO and 5-CGO cell presented similar resistance values. The 10-CGO$_{meso}$ cell presented the best performance for this contribution. This was surely due to the larger surface area provided by the nanostructured architecture. The cell showed a higher activation energy with respect to the ones fabricated with commercial CGO scaffold, because surface exchange reactions were partially blocked by the silica contamination.[11]
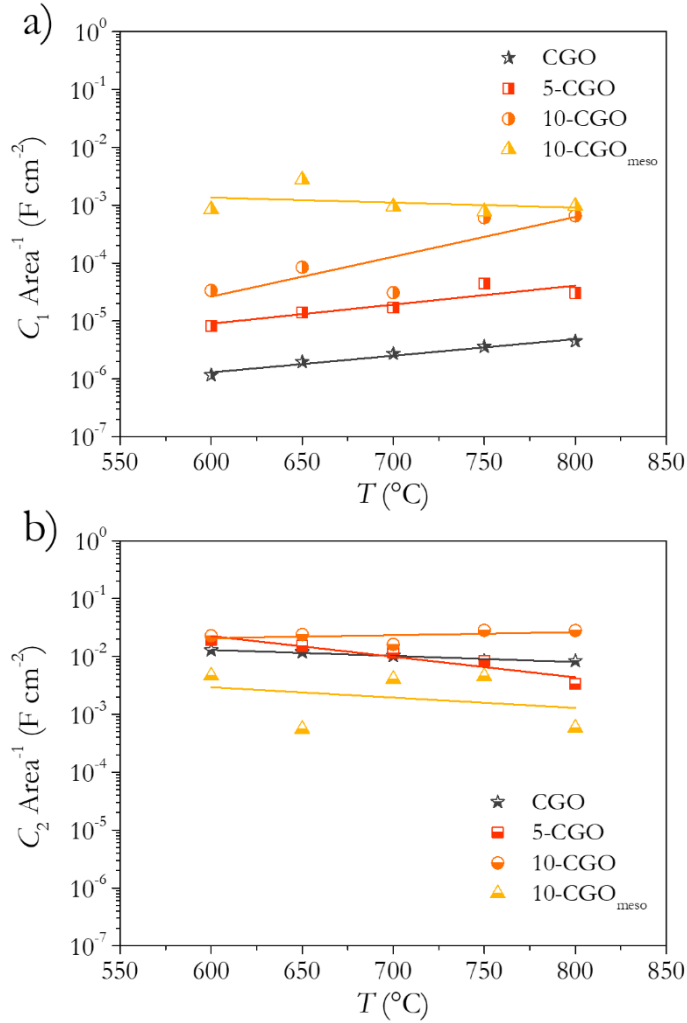
Figure 3.15: EIS measurements of CGO, 5-CGO, 10-CGO and 10-CGO$_{meso}$ cells. Capacitance values of the two ZARC elements used for the fitting of the EIS spectra. C_1 (a) and C_2 (b) values are represented as function of temperature.
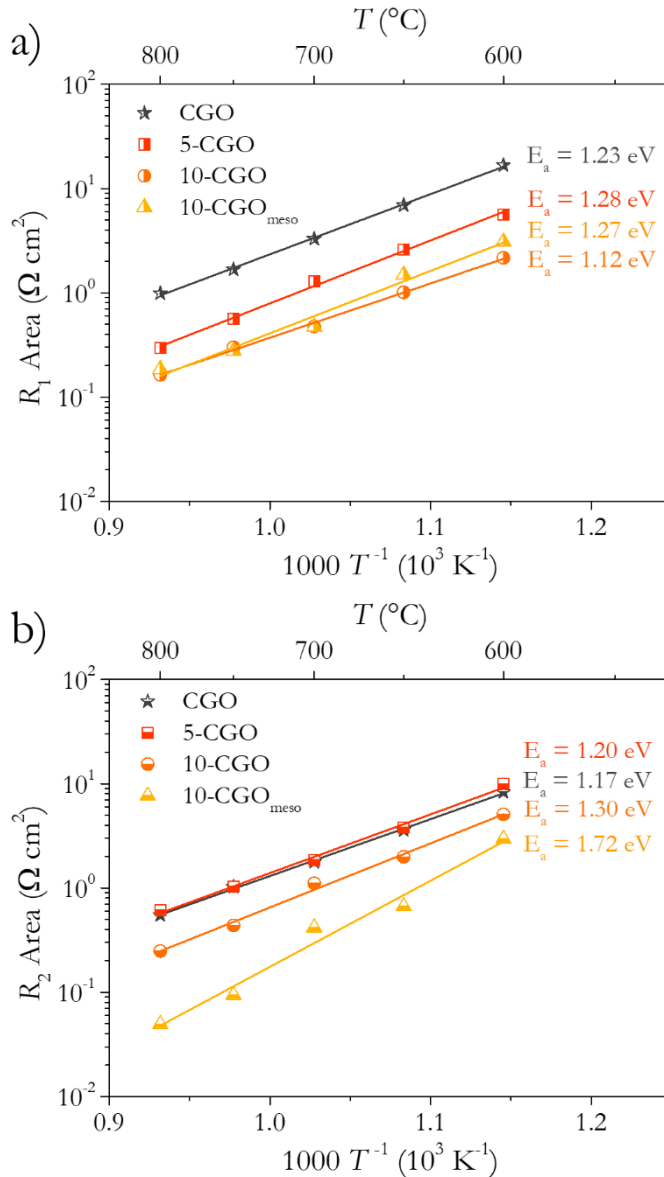
Advanced strategies for Solid Oxide Electrolysis Cells

Figure 3.16: EIS measurements of CGO, 5-CGO, 10-CGO and 10-CGOmeso cells. R_1 (a) and R_2 (b) Arrhenius plots from the two ZARC elements used for the fitting of the EIS spectra.

Automatic infiltration of LSCF perovskites inside CGO scaffold was demonstrated. Scaffolds infiltrated with saturation parameter at 10 presented the best results in terms of polarization resistance. The combination with

mesoporous CGO further reduced the ASR_{pol} and better results can be expected for such nanocomposite scaffold after removal of SiO_2 remains.

3.3 Hybrid 3D-printed cells

Fully 3D printed symmetrical cells were produced with LSM+YSZ/YSZ/LSM+YSZ composition. The composite electrodes were deposited using the BioX robocasting produced by cell inks and the dense electrolyte by the Pixdro LP50 inkjet printer. Part of these results were done in collaboration with DTU Energy (Denmark) researchers in a research stay carried out in Copenhagen and they are also reported as part of the thesis work of M. Rosa.[24][†]

3.3.1 Development of hybrid printing process

The printing process of the symmetrical cells was divided into three steps as schematically represented in Figure 3.17. The composite electrode of LSM+YSZ was deposited on top of a glass support and cured at 90°C for 15 min (Figure 3.17a). The temperature triggered the polymerization reaction to obtain a dense piece to make feasible the deposition of the inkjet-printed electrolyte. PMMA and graphite were dispersed in the slurry with the ceramic load to ensure the presence of an open and interconnected porosity of the electrode after sintering. The YSZ electrolyte was deposited by inkjet printing (Figure 3.17b) using a water based colloidal suspension charged by sub-micrometrical particles of 8YSZ. The moving platform of the inkjet printer was kept at 50 °C to promote the drying of the ink. Finally, the second

---

[†]Characterization of the inks, printability tests, fabrication of the cells, electrochemical characterization and fitting of the obtained spectra were carried out by the author.

Advanced strategies for Solid Oxide Electrolysis Cells

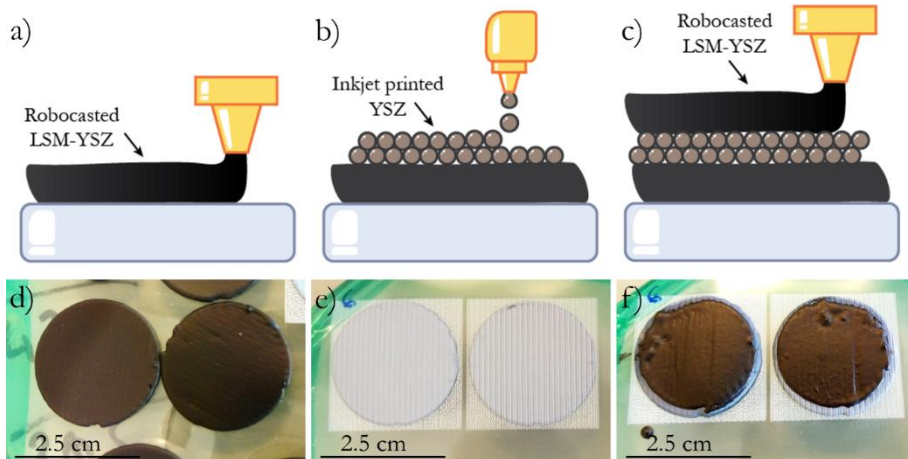electrode (Figure 3.17c) was deposited on top of the YSZ layer using the same conditions of the first one.

Figure 3.17: Schematic representation of the hybrid printing process to produce the symmetrical cells. The first robocasted layer of LSM+YSZ wass deposited on a support and cured in oven (a), YSZ was deposited by inkjet printing using a water-based ink (b). The second electrode was deposited maintaining the same conditions with respect to the first one and cured in oven (c). Pictures of two symmetrical cells during the three production steps are shown (d), (f) and (g).

Figure 3.17d, Figure 3.17e and Figure 3.17f show the processing of two symmetrical cells at the different stages. The cells were co-sintered at 1200 °C with heating rate of ≈15 °C h^{-1} to allow a correct debinding process and burning of the pore formers.

3.3.2 Characteristics of robocasting slurries and inkjet inks

3.3.2.1 *Acrylic-based slurries for robocasting of porous electrodes*

Acrylic-based slurries were formulated and produced at the DTU facilities, using PEGDA as a solvent. In order to find the best combination between print speed and applied pressure, some printability tests were made with the produced slurries. As showed in Figure 3.18 some stripes were deposited at different velocity and pressures: a preliminary test was made

(Figure 3.18a) with relative slow printing speed (5 mm s^{-1}) and applying six different pressures (from 20 to 45 kPa). Subsequently a new test was conducted (Figure 3.18b) selecting three different pressures (25, 30 and 35 kPa) and speed rates (5, 10 and 20 mm s^{-1}).
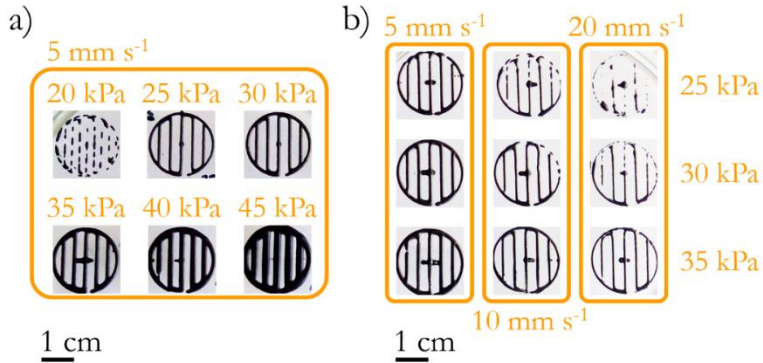

Figure 3.18: Printability test of the robocasting slurry with constant speed (5 mm s^{-1}) and different hydrostatic pressures (from 20 to 45 kPa) (a) and stripes deposited using 5, 10 and 20 mm s^{-1} and 25, 30 and 35 kPa (b).

With the utilization of a Cyberscan profilometer the thicknesses of the printed stripes were measured in different position of the samples. Figure 3.19 shows some representative measurements of the different specimens divided by their printing speed rates.
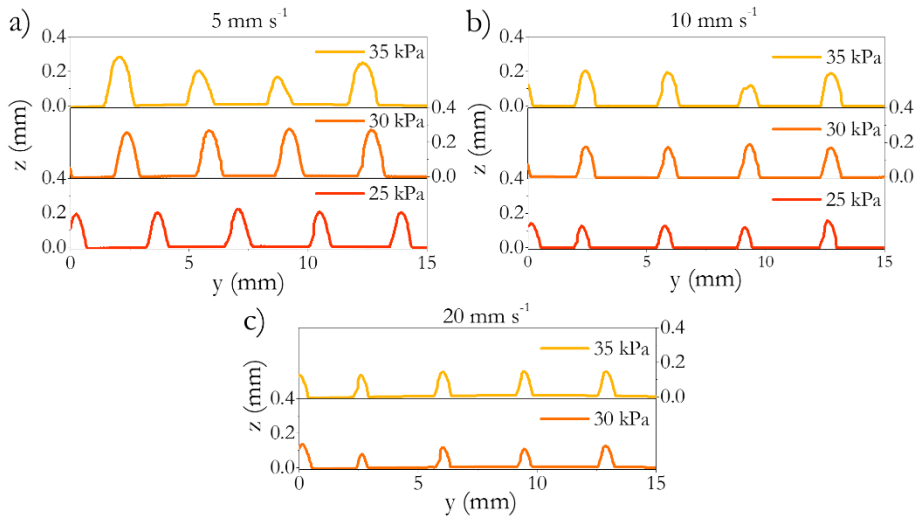
Figure 3.19: Profilometer measurements after printability test showed in Figure 3.18b at 25, 30 and 35 kPa with printing speed 5 mm s^{-1} (a), 10 mm s^{-1} (b) and 20 mm s^{-1} (c).

From this analysis the best candidates to obtain a uniform print were identified with 5 mm s^{-1}/25 kPa, 5 mm s^{-1}/30 kPa and 10 mm s^{-1}/35 kPa. These pairs showed uniformity of the layers deposited and thicknesses ≈250 μm, enough for providing mechanical support to the cell. Eventually, the combination 5 mm s^{-1}/25 kPa was chosen to maintain a better control of the printing process due to the low printing speed.

To produce symmetrical 3D printed cells by robocasting, two different slurries were formulated based on the PEGDA acrylate monomer. On Table 3.3 one can find the values in % of shrinkage, solid loading and ratio between ceramic load and pore formers of the two different slurries. The difference of pore former amount in the slurries determines the final porosity of the electrodes, therefore the two composition were named P1 and P2 (porosity 1 and 2).

Table 3.3: Shrinkage, solid loading and ceramic loading/solid loading ratio of the P1 and P2 (porosity 1 and 2) slurries.

Slurries	Shrinkage	Solid loading	Ceramic/solid loading
P1	22 %	46 %v/v	0.29
P2	26 %	45 %v/v	0.40

3.3.2.2   *YSZ water-based ink for inkjet of dense electrolyte*

YSZ water-based ink using commercial powders was formulated at the DTU facilities. This ink was deposited by inkjet printing to produce dense electrolytes for hybrid 3D-printed symmetrical cells. Further information about the production and characterization of similar inks could be found elsewhere.[24]

The water suspension was firstly kept in ultrasound, then centrifugated to remove the remaining agglomerates and finally passed through a filter with a pore size around 0.7 μm. Figure 3.20 shows a representative particle size analysis, made before each printing to keep the stability of the dispersion under control. A SEM micrograph of the powders is showed as inset of Figure 3.20 in order to clarify the results of the laser scattering analysis.
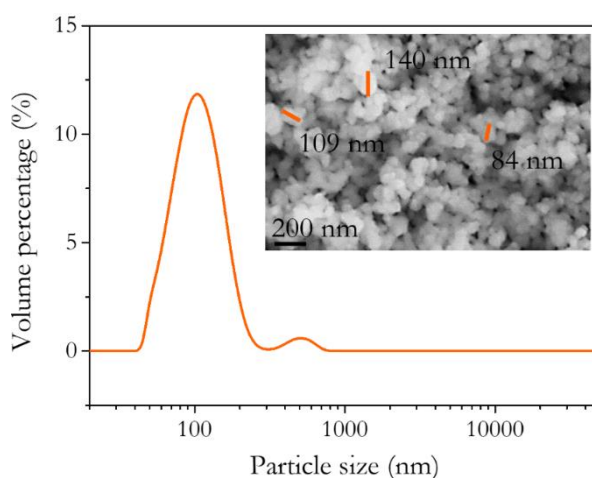

Figure 3.20: Laser scattering measurement of the YSZ colloidal dispersion in water and inset showing a SEM micrograph of the used powders.

Advanced strategies for Solid Oxide Electrolysis Cells

To produce the YSZ inks isopropanol and propylene glycol were added to the water suspension in order to adjust the viscosity and the surface tension. Viscosity and surface tension measurements are presented in Figure 3.21a and Figure 3.21b respectively. The results are compared with the optimum values provided by Meyer-Burger[25] for the printing with the Pixdro LP50 and a reference form DTU about the characterization of a similar ink.[24] The calculated Z number for this ink is ≈5.7, therefore in the range proposed by Derby for a good jettability.[2]
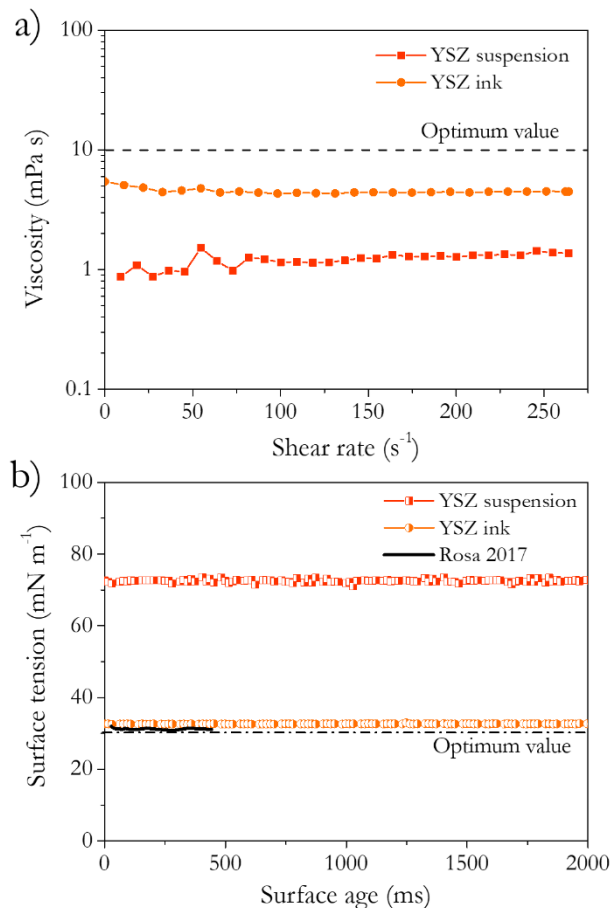

Figure 3.21: Characterization of the YSZ water suspension and of the ink: viscosity (a) and surface tension (b) measurements. The optimum values for the printing with the Pixdro LP50 are reported in the graph together with a reference of a similar ink printed by the same inkjet.[25]

The YSZ inks were deposited on previously deposited support electrodes by robocasting substrates and then sintered at 1200 °C to evaluate the densification of the layers at such temperatures. Figure 3.22 presents the SEM image of the deposited layer after the sintering process, showing a very dense microstructure with only few small pores with no interconnection among them.
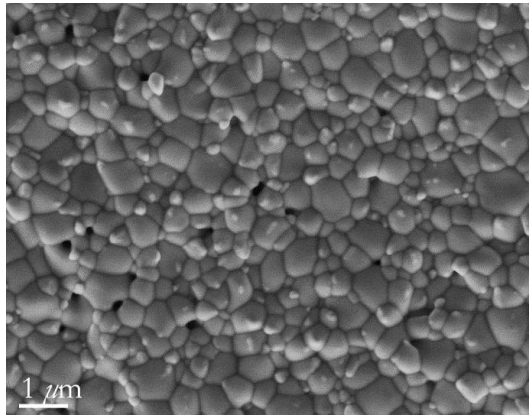

Figure 3.22: SEM micrograph representing the YSZ layer deposited by IJP and sintered at 1200 °C for 1 h.

3.3.2.3   *Fabrication of the symmetrical cells*

Two symmetrical cells were fabricated using the same YSZ colloidal dispersion for the deposition of the electrolytes and the two robocasted slurries to form the electrodes. These slurries were characterized by different ratio ceramic loading/solid loading (0.29 for P1 and 0.4 for P2). The two cells were therefore named following the name of the slurries presented in Table 3.3 P1 (Figure 3.23a) and P2 (Figure 3.23b).
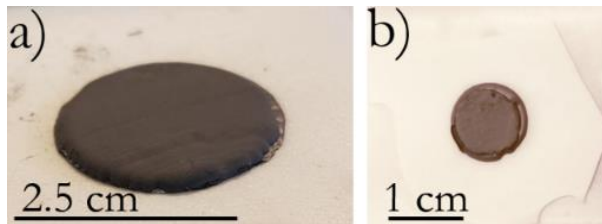

Figure 3.23: Cells produced with the a) P1 and with b) P2 slurries

Advanced strategies for Solid Oxide Electrolysis Cells

3.3.3 Microstructural characterization of hybrid 3D-printed cells

The microstructural properties of the P1 and P2 cells were characterized by XRD and SEM-EDX.

XRD analysis were made at the DTU facilities to investigate the presence of possible secondary phases between Zirconia and Strontium, which are typical for sintering temperature above 1300 °C. Such secondary phases could be detrimental for the cells performances blocking the electrochemical kinetic processes, which usually are occurring at the interface.[26,27] Figure 3.24 shows the patterns of the two cells compared with reference patterns of YSZ, LSM and Au (which was used as current collector during the electrochemical measurements).
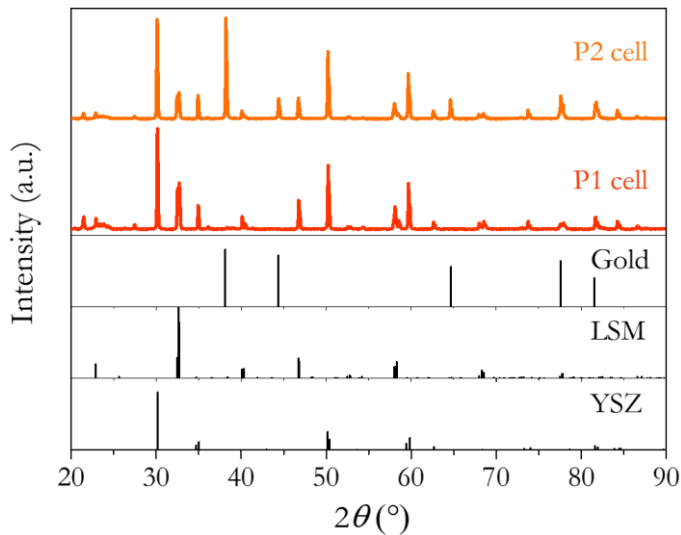

Figure 3.24: XRD pattern of the P1 and P2 cells in comparation with reference patterns of YSZ and LSM.

Some peaks which apparently do not correspond to any of the reference patterns reported in Figure 3.24 are present at the 2θ positions 21.5°, 23.6°, 27.5, 36.1°. These peaks remained unidentified, but their position seems not to fit any of the typical secondary phases which are formed for this kind of electrodes (e.g. $La_2Sr_2ZrO_7$ and $SrZrO_3$).[28] These

secondary phases were formed despite the firing temperature used for the co-sintering of the cells was below 1200°C and the good stability of the LSM perovskite should have prevented the formation of secondary phases with YSZ.[28]

SEM-EDX characterization was made on the two printed cells to investigate the role of the microstructure on the electrochemical performances of section 3.3.4.

Figure 3.25a shows the general microstructure of the P1 cell which presented a quite high relative porosity of the electrodes. A dense electrolyte with a thickness ≈2.8 μm can be observed in Figure 3.25b.

Figure 3.25c shows some cracks present along the electrolyte, probably caused by differences in the shrinkage rate with the layers. The tension carried out by the LSM+YSZ robocasted layers broke the YSZ electrolyte in different zone during the firing process. This last consideration made this formulation not suitable for the production of a complete SOC, in which the electrolyte should ensure the separation of the different gases during operation.

Lastly, Figure 3.25d shows the EDX maps made on the P1 cell, demonstrating the good distribution of the YSZ and of LSM (represented respectively by Zr signal, green pixels and La signal, red pixels in the figure).
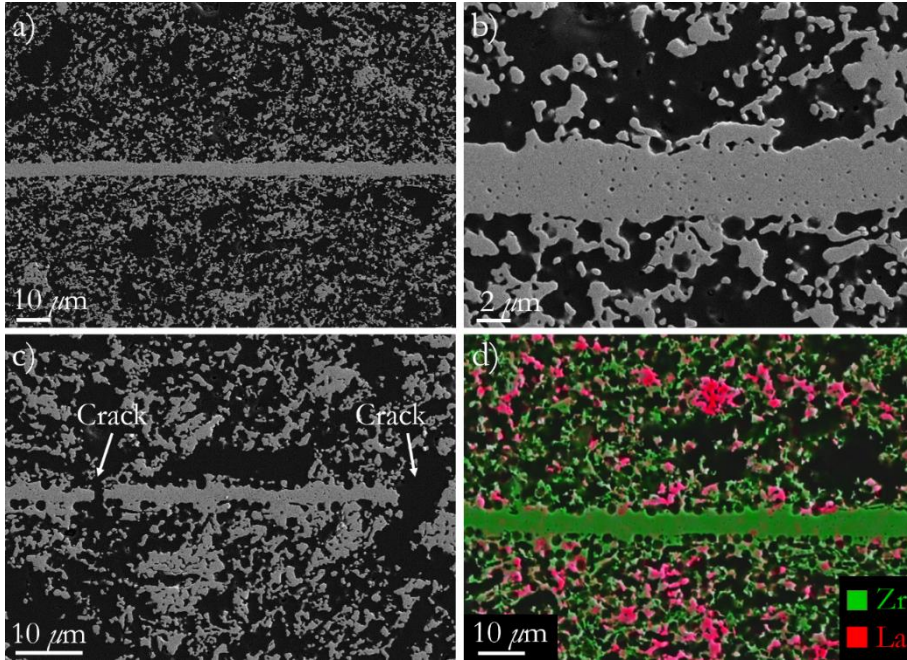
Advanced strategies for Solid Oxide Electrolysis Cells

Figure 3.25: SEM micrographs of the P1 cell with a general view of the cross-section of the cell (a), a high magnification micrographs showing the dense YSZ electrolyte (b), detail of cracks present alongside the electrolyte (c) and element distribution of the cell (d).

Figure 3.26a shows the SEM micrograph of the P2 cell, which presented a relative low porosity. As expected, the increased ratio between ceramic load and pore formers respect the P1 promoted such a result. The electrolyte of Figure 3.26b presents a very dense structure with a thickness ≈2.8 μm. No cracks were found, demonstrating a good match between the layers. Nevertheless Figure 3.26c shows an area where the two electrodes seem to be in contact. These contact point could affect the electrochemical properties of the device. Their formation was probably due to the presence of some voids on the electrolyte layer during the deposition. The voids were probably caused by presence of dust particles on the surface of the first electrode or de-wetting during the drying of the YSZ coating. Such imperfections of the printed YSZ layer can be avoided with a more effective

control of the printing conditions since they are not structural defects as in the case of the cracks present in the P1 cell.

Figure 3.26d presents the elemental distribution of Zr and La, considered as marker elements for LSM and YSZ. From Figure 3.26d it can be seen that the composition of the electrode is generally uniform. Notably, the electrode is supposed to be characterized by an enhanced percolation due to its denser microstructure.
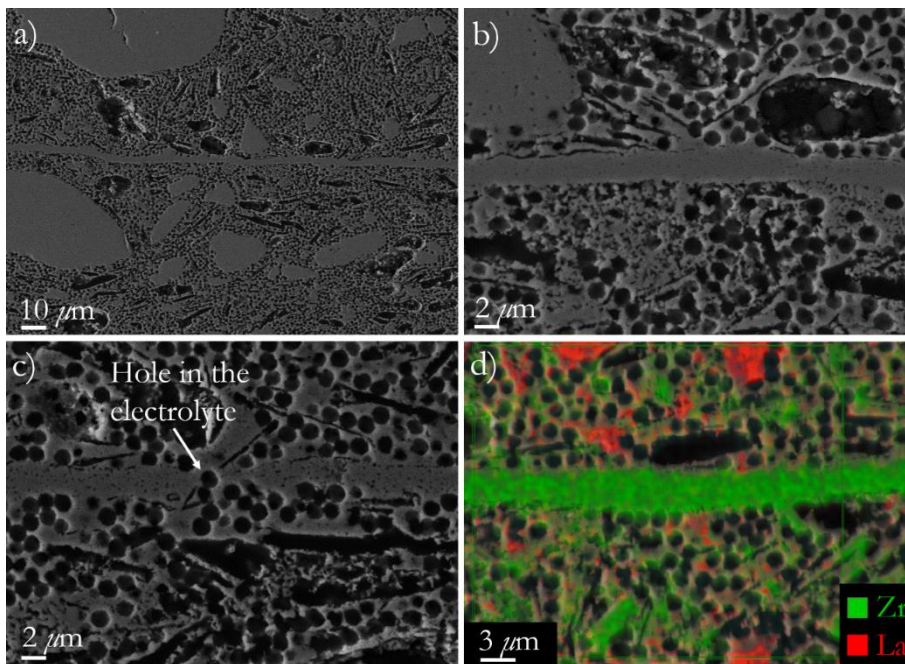

Figure 3.26: SEM micrographs of the P2 cell with a general view of the cross-section of the cell (a), high magnification particular of the YSZ layer (b), representative micrograph of a contact point between the two electrodes (c) and element distribution of the cell (d).

3.3.4 Electrochemical characterization of hybrid 3D-printed cells

The two type of cells were electrochemically characterized at the DTU facilities. The measurements were conducted painting gold as current collector layer and using gold wires which were applied in contact with the two faces of the cells (as showed in Figure 3.27a and Figure 3.27b).

Advanced strategies for Solid Oxide Electrolysis Cells

The measurements were conducted in air from 800 °C to 550 °C and the spectra were fitted with the equivalent circuit which is shown as inset of Figure 3.27c. For the fitting the simplest circuit able to fit the EIS spectra was chosen. It is constituted by an inductive element (L), a serial resistance (R_s) and three ZARC elements.
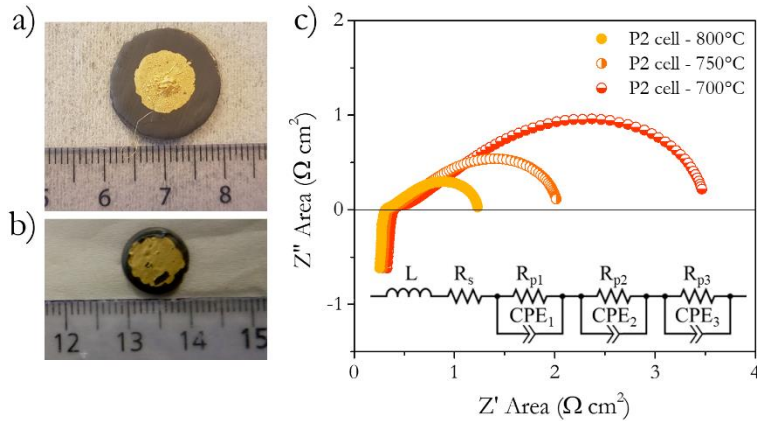

Figure 3.27: Measured cells with electrodes made of P1 (a) and P2 slurries (b). Representative Nyquist plot of the P2 cell measured at 700, 750 and 800 °C (c), in the inset of the figure the equivalent circuit of the measurement is reported.

Figure 3.28 shows the Arrhenius plots of the serial resistances for the measured cells. The activation energy of the P1 cell (0.93 ±0.01 eV) was very close to the typical one for YSZ reported in literature (≈0.8 eV).[29] Conversely P2 cell presented a first value for low temperatures (from 550 °C to 650 °C) which was 0.63 ±0.06 eV and an unusual lower value (0.31 ±0.04 eV) for higher temperatures. This could be explained either by the contact points between the two electrodes highlighted by the microstructural characterization, which induced some electronic conductivity across the electrodes or by the saturation of the resistance after 700 °C caused by contribution from the setup. Because of the small thickness of the layer, it is possible that the resistance from the setup became dominant at higher temperatures.

141

At 750 °C P1 and P2 cells showed a larger serial resistance compared to the typical values for YSZ electrolytes. Wincewicz *et al.* report a conductivity of $1.3 \cdot 10^{-2}$ Ω^{-1} cm^{-1} for a YSZ film at 750 °C.[30] Normalizing this value for the thickness of the YSZ layer deposited by IJP (≈2.8 μm), ASR_s ≈0.02 Ω cm^2. However, it should be noticed that the ASR_s for both cells passed from ≈7.0 Ω cm^2 (P1) to ≈0.27 Ω cm^2 (P2). Furthermore, taking into consideration the possible contribution from the setup, one can extrapolate the value depending to this contribution for lower temperatures, from the fitting line indicated in Figure 3.28 by light orange dots. At 600 °C the value of the resistance from the setup should be ≈0.44 Ω cm^2. Subtracting this value to the measured one at 600 °C (≈0.54 Ω cm^2) the resistance become ≈0.1 Ω cm^2. One can notice that this is the same value of the predicted ASR value from YSZ (black line in Figure 3.28).[30] Between the two cells the only difference was related to the formulation of the LSM/YSZ electrodes. More specifically the difference was the ratio between ceramic load and pore formers, which as a consequence affected the shrinkage during the co-sintering process. This microstructural difference, which consisted in poorer attachment and lower percolation, caused a higher resistance value for the P1, which did not present a similar behaviour. The P2 cell, which was characterized by a higher ceramic load/pore former ratio, showed a lower ASR_s value. The denser constitution of the porous electrode played a key role in improving the percolation and the contact points with the electrolyte.
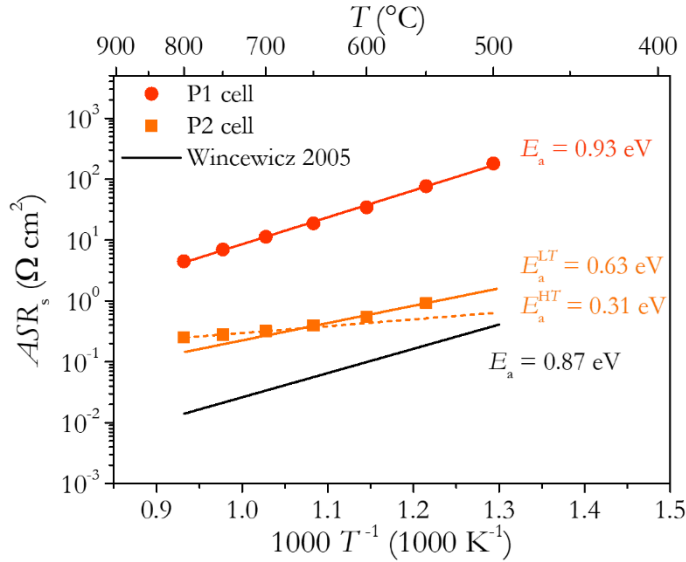
Figure 3.28: Arrhenius plots serial ASR of the P1 and P2 cells. For the P2 cell two activation energies are reported: one for the points at lower temperatures (550-650 °C), indicated by a light orange line and one for the points at higher temperatures (700-800 °C), indicated by a dotted light orange line. In the plots are reported reference values taken from literature.[30]

In the case of the activation energy of the polarization resistance, presented in Figure 3.29, the values are comparable, showing 1.14 ±0.02 eV and 1.01 ±0.04 eV for P1 and P2, respectively. They are in accordance with the typical range for LSM+YSZ electrodes, as the activation energy values for electrodes with similar composition are usually ≥1 eV.[31,32]

The ASR_{pol} of the P1 cell showed a quite large resistance (≈57 Ω cm² at 750°C) while for P2 the values are similar to the typical values from literature. The ASR_{pol} for the P2 cell at 750 °C was ≈0.9 Ω cm², while Murray *et al.* report ≈1.3 Ω cm² at the same temperature for a LSM/YSZ composite electrode.[31]

High polarization resistance of the P1 cell could be explained by the lack of percolation of the electrodes, involving both paths, ionic and electronic conductivity. In the case of the P2 cell the higher density of the electrode promoted a better percolation. Optimised conduction paths extend

the TPB area of the cell, lowering the polarization resistance of more than one order of magnitude.
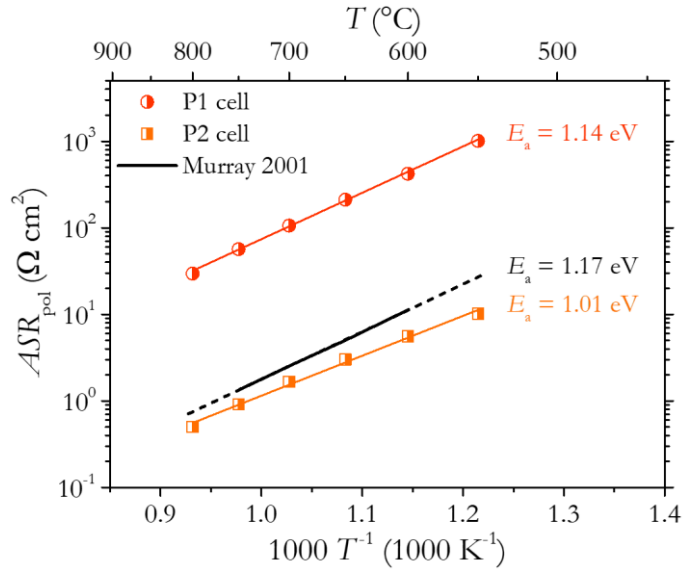

Figure 3.29: Arrhenius plots of polarization ASR of the P1 and P2 cells, measured in air. Reference values taken from literature are reported in the plot.[31]

Figure 3.30 shows the capacitance and the polarization resistance contributions of the three ZARC elements obtained by the fitting.

A displacement for the capacitance values was detected for P1 and P2. As showed in Figure 3.30a, the $(R_{p1}Q_1)$, $(R_{p2}Q_2)$ and $(R_{p3}Q_3)$ elements presented respectively capacitance values around $\approx 10^{-7}$ F cm^{-2}, $\approx 10^{-5}$ F cm^{-2} and $\approx 10^{-4}$ F cm^{-2} (P1) and $\approx 10^{-6}$ F cm^{-2}, $\approx 10^{-3}$-10^{-2} F cm^{-2} and $\approx 10^{-2}$ F cm^{-2} (P2). The frequency of the ZARC elements between the two cells were of the same order: 10^4 Hz $(R_{p1}Q_1)$, 10^1-10^0 Hz $(R_{p2}Q_2)$ and 10^0-10^{-1} Hz $(R_{p3}Q_3)$.

Regarding the $(R_{p3}Q_3)$ element, which was the limiting step of the process as highlighted by Figure 3.30b, its attribution can be safely addressed to oxygen reduction reaction at the MIEC's surface.[32–34] In particular, for LSM the mechanism considered is dissociative adsorption of oxygen molecules on the surface.[32]

Murray *et al.* highlight also that these kind of processes present generally high activation energies (≈1.4 eV).[32] This is also what highlighted by Figure 3.30b where $(R_{p3}Q_3)$ activation energies were quite larger (1.4 eV and 1.1 eV for P1 and P2 respectively) compared to the ones of the other ZARC elements (around >1 eV).

A unique interpretation of the $(R_{p1}Q_1)$ and $(R_{p2}Q_2)$ arcs and their attribution to specific physicochemical phenomena could be difficult. The $LR_s(R_{p1}Q_1)(R_{p2}Q_2)(R_{p3}Q_3)$ equivalent circuit was chosen to minimize the number of ZARC elements. However, the shape of the impedance spectra shown in Figure 3.27 recall the one of a finite-length-Warburg element, which is associated to diffusion followed by reaction.[27,35] During the EIS fitting the *n* parameters of $(R_{p1}Q_1)$ and $(R_{p2}Q_2)$ were maintained ≈0.5 during the fitting. It is known that in a CPE *n* values around 0.5 described a Warburg-type diffusion phenomenon.[36] After these consideration, diffusion seems to be the more plausible interpretation for such elements.

It is worth to be mentioned the interpretation provided by Kim *et al.* which studied LSM+YSZ composites electrodes and modelled the obtained impedance spectra with the same equivalent circuit.[33] In their work they attribute the $R_{p1}Q_1$ either to oxygen ion transfer from the TPB to the YSZ electrolyte or to grain boundary resistance in YSZ.[32,33] $R_{p2}Q_2$ is assigned in the same study to diffusion of O^- species along the LSM surface to the TPB.[33]
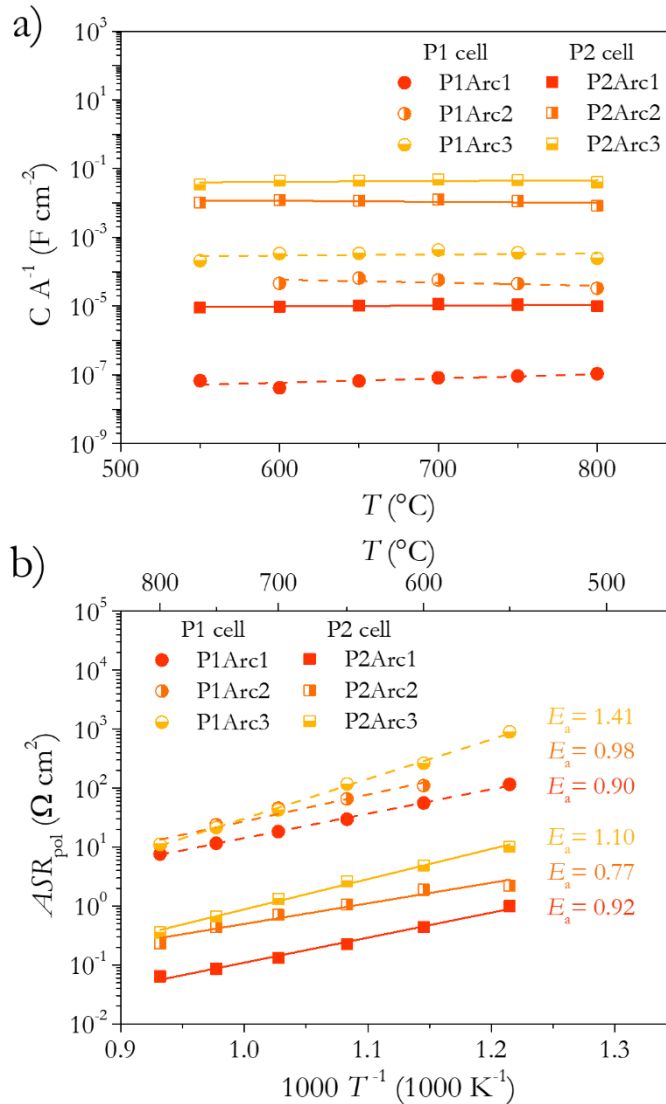
Figure 3.30: EIS measurements of the P1 and P2 cells. Capacitance values vs temperature (a) and Arrhenius plot of the polarization resistances (b) of the three ZARC elements used for the fitting are plotted.

As a summary, it can be stated that the robocasted 3D printed electrodes presented typical performances for LSM+YSZ electrodes demonstrating RC's feasibility as deposition techniques for electrodes fabrication in SOC application. Furthermore, IJP has demonstrated its potential for the processing of dense and thin electrolytes.

Advanced strategies for Solid Oxide Electrolysis Cells

3.4   Conclusion

In this chapter the results about the implementation of additive manufacturing techniques (inkjet printing and robocasting) for the processing of energy devices are presented. Regarding the symmetrical cells (YSZ/CGO+LSCF) automatically infiltrated by IJP, the percolation of the cell improved because of the infiltration process. The serial resistance measured at 750 °C on a symmetrical cell without infiltration was ≈2.7 Ω cm^2. After automatic infiltration by means of IJP, ASR_s passed to ≈1.6 Ω cm^2 and ≈1.1 Ω cm^2 for increasing saturation parameter of IJP. Symmetrical cell with mesoporous CGO-based scaffold infiltrated by IJP with saturation at 10, showed the best results (0.8 Ω cm^2). Mesoporous nanostructured architecture, characterized by large open porosity, demonstrated to effectively promote a better distribution of the infiltrating solution and consequently the percolation of the cell. The electrode performance was improved as demonstrated by the reduction of the polarization resistance upon infiltration. At 750 °C the cell without infiltration presented an ASR_{pol} ≈1.3 Ω cm^2. The infiltrated cells showed ≈0.4 Ω cm^2 (infiltration with saturation =5), ≈0.2 Ω cm^2 (infiltration with saturation =10) and ≈0.1 Ω cm^2 (mesoporous CGO scaffold infiltrated with saturation =10). Two different processes contributed to the overall polarization, which were identified as charge transfer[18,19] and surface exchange reactions.[18,20,21]

The two symmetrical YSZ/LSM+YSZ cells 3D-printed by robocasting and inkjet printing, characterized by different ceramic loading/solid loading ratio in the electrode composition, showed ASR_s values at 750 °C ≈7.0 Ω cm^2 (0.29 ceramic loading/solid loading) and ≈0.27 Ω cm^2 (0.40 ceramic loading/solid loading). The enhanced electronic percolation provided by the higher ceramic loading/solid loading ratio improved the current collection of the cell and lowered the serial resistance contribution.

However, the serial resistance of the cell with higher ceramic loading was influenced by the setup, which lowered the activation energy at high temperature up to ≈0.31 eV. Therefore, the contribution to the serial resistance of this cell was probably lower with respect to the measured values.

The microstructure analysis highlighted some contact points between the two electrode which could also had played a role. In any case the ability of IJP to fabricated dense electrolyte was demonstrated. Contact point formation between the electrodes during the deposition of the layer will be easily avoided in the future with a better control of the fabrication conditions.

Regarding the performance of the electrodes, lower polarization resistance was measured because of the increasing of the ceramic loading/solid loading ratio. The formulation with less pore formers determined a microstructure characterized by better percolation which extended the TPB. ASR_{pol} passed from ≈57 Ω cm^2 to ≈0.9 Ω cm^2 at 750°C.

From EIS analysis three different contributions to the polarization resistance were identified at 10^4, 10^1-10^0 Hz and 10^0-10^{-1} Hz, respectively.

The high frequency and middle frequency contribution were identified with mass diffusion phenomena. The third contribution, which was the limiting step of the cell performance, was attributed to ORR reactions at the MIEC's surface.

3D-hybrid printing of symmetrical cells by Robocasting and Inkjet printing was successfully demonstrated. These AM techniques proved to be advantageous alternatives to classical fabrication techniques.

Advanced strategies for Solid Oxide Electrolysis Cells

3.5 Bibliography

1   B. Derby, *Annu. Rev. Mater. Res.*, 2010, **40**, 395–414.
2   Y. Liu and B. Derby, *Phys. Fluids*, , DOI:10.1063/1.5085868.
3   N. Reis and B. Derby, *MRS Proc.*, 2000, **625**, 117.
4   B. Derby, *J. Eur. Ceram. Soc.*, 2011, **31**, 2543–2550.
5   D. Jang, D. Kim and J. Moon, *Langmuir*, 2009, **25**, 2629–2635.
6   P. Delrot, M. A. Modestino, F. Gallaire, D. Psaltis and C. Moser, *Phys. Rev. Appl.*, 2016, **6**, 1–8.
7   I. H. Choi, Y. K. Kim, S. Lee, S. H. Lee and J. Kim, *J. Microelectromechanical Syst.*, 2015, **24**, 768–770.
8   H. C. Nallan, J. A. Sadie, R. Kitsomboonloha, S. K. Volkman and V. Subramanian, *Langmuir*, 2014, **30**, 13470–13477.
9   M. Ghatee, M. H. Shariat and J. T. S. Irvine, *Solid State Ionics*, 2009, **180**, 57–62.
10   R. I. Tomov, T. Mitchell-Williams, C. Gao, R. V. Kumar and B. A. Glowacki, *J. Appl. Electrochem.*, 2017, **47**, 641–651.
11   S. Anelli, F. Baiutti, A. Hornés, L. Bernadet, M. Torrell and A. Tarancón, *J. Mater. Chem. A*, 2019, **3**, 10031–10037.
12   H. Fan, M. Keane, N. Li, D. Tang, P. Singh and M. Han, *Int. J. Hydrogen Energy*, 2014, **39**, 14071–14078.
13   A. Nechache, M. Cassir and A. Ringuedé, *J. Power Sources*, 2014, **258**, 164–181.
14   L. Almar, T. Andreu, A. Morata, M. Torrell, L. Yedra, S. Estradé, F. Peiró and A. Tarancón, *J. Mater. Chem. A*, 2014, **2**, 3134–3141.
15   Kceracell Co., Ltd - SOFC materials, www.kceracell.com.
16   F. S. Baumann, J. Fleig, H. U. Habermeier and J. Maier, *Solid State Ionics*, 2006, **177**, 1071–1081.
17   T. E. Burye and J. D. Nicholas, *J. Power Sources*, 2015, **300**, 402–412.
18   L. dos Santos.Gómez, J. M. Porras-Vázquez, E. . Losilla, F. Martín, J. R. Ramos-Barrado and D. Marrero-López, *J. Power Sources*, 2017, **347**, 178–185.
19   R. I. Tomov, T. B. Mitchel-Williams, R. Maher, G. Kerherve, L. Cohen, D. J. Payne, R. V. Kumar and B. A. Glowacki, *J. Mater. Chem. A*, 2018, **6**, 5071–5081.
20   X. Xu, Z. Jiang, X. Fan and C. Xia, *Solid State Ionics*, 2006, **177**, 2113–2117.
21   L. Nie, M. Liu, Y. Zhang and M. Liu, *J. Power Sources*, 2010, **195**, 4704–4708.
22   S. A. Ghom, C. Zamani, S. Nazarpour, T. Andreu and J. R. Morante, *Sensors Actuators, B Chem.*, 2009, **140**, 216–221.
23   J. Druce and J. A. Kilner, *J. Electrochem. Soc.*, 2014, **161**, F99–F104.
24   M. Rosa, 2019.
25   M. Rosa, P. N. Gooden, S. Butterworth, P. Zielke, R. Kiebach, Y. Xu, C. Gadea and V. Esposito, *J. Eur. Ceram. Soc.*, 2017, 0–6.
26   S. B. Adler, *Chem. Rev.*, 2004, **104**, 4791–4843.
27   J. Nielsen and J. Hjelm, *Electrochim. Acta*, 2014, **115**, 31–45.
28   S. P. Jiang, *J. Mater. Sci.*, 2008, **43**, 6799–6833.
29   O. H. Kwon and G. M. Choi, *Solid State Ionics*, 2006, **177**, 3057–3062.

30   K. C. Wincewicz and J. S. Cooper, *J. Power Sources*, 2005, **140**, 280–296.

31   E. Perry Murray, *Solid State Ionics*, 2001, **143**, 265–273.

32   E. P. Murray, T. Tsai and S. A. Barnett, *Solid State Ionics*, 1998, **110**, 235–243.

33   J. D. Kim, G. D. Kim, J. W. Moon, Y. il Park, W. H. Lee, K. Kobayashi, M. Nagai and C. E. Kim, *Solid State Ionics*, 2001, **143**, 379–389.

34   E. Lee, H. Jeong, T. H. Shin and J. ha Myung, *Ceram. Int.*, 2020, 1–6.

35   S. B. Adler, *J. Electrochem. Soc.*, 1996, **143**, 3554.

36   D. E. Vladikova, Z. B. Stoynov, A. Barbucci, M. Viviani, P. Carpanese, J. A. Kilner, S. J. Skinner and R. Rudkin, *Electrochim. Acta*, 2008, **53**, 7491–7499.

Advanced strategies for Solid Oxide Electrolysis Cells

Chapter IV

Improved mesoporous CGO for application in SOCs

4.1 Chapter overview

The aim of this chapter is to show the results of an improved route for the preparation of ordered mesoporous ceria-based materials (BET areas > 100 m^2 g^{-1}) for the application in SOCs and to overcome some issues that such nanostructured powders observed in the seminal works of our research group.[1–5] The properties of ceria-based nanostructured backbones have been studied, revealing excellent mass transport and high catalytic properties.[6–14]

i. Results about silica removal from the mesoporous structure are presented (section 4.2).

    a. To demonstrate the effectiveness of the silica removal treatment and the effect on the structure, characterization by complementary techniques (SEM, XRD, SAXS, ICP-MS, BET, TPR) is provided.

    b. Mesoporous structure was characterized by TEM analysis. Annular Dark-Field (ADF) and electron tomography 3D reconstruction (TWM3D) were used for the reconstruction of the mesoporous bi-continuous channel. EELS analysis and clustering tomography were used for the characterization of the material (section 4.3).

ii. Results on Co oxide decoration for the reduction of the sintering temperature are presented (section 4.4).[9,18]

iii. Electrochemical characterization of symmetrical cells with CGO mesoporous scaffold is presented. CGO scaffolds were deposited on top of YSZ tapes and the electrochemical properties were studied by means of impedance spectroscopy (section 4.5).

4.2 Etching strategies for nanocasting template removal

4.2.1 Implementation of the cleaning process

An important process in the fabrication of rare-earth mesoporous materials is the removal of the sacrificial template. For application as a functional layer in an SOC the replica needs a high surface to promote the gas permeation.[15–18] The etching of the SiO_2 template needs to be particularly effective and selective, to not compromise the ordered mesoporous structure or result in deleterious effects in the final application. The standard method for the removal of the SiO_2 template involves the use of NaOH water-based solution which had been shown to be chemically compatible with ceria. Because of its effectiveness, sodium hydroxide had been largely used for the removal of silica templates in nano-casting fabrication.[1,9,19–21]

Unfortunately, the presence of a highly electrically insulating and catalyst inhibitor siliceous phase ($\approx$ 1 wt % Si) at the end of the washing process by NaOH has been demonstrated.[3,22,23] Therefore, an additional cleaning step had been optimized with the aim to reduce the SiO_2 content while ensuring a good chemical compatibility with ceria,[24] taking advantage of the ability of hydrofluoric acid (HF) to dissolve silica[25–27] and of the slow etching rates of CGO by HF.[28]

Figure 4.1 presents the process used for the complete removal of the silica contamination after the NaOH etching. The powder was etched by HF, then water was added to stop the reaction. Finally, the mixture was filtered with a paper filter in an Erlenmeyer flask and was washed several times with water (Figure 4.1).
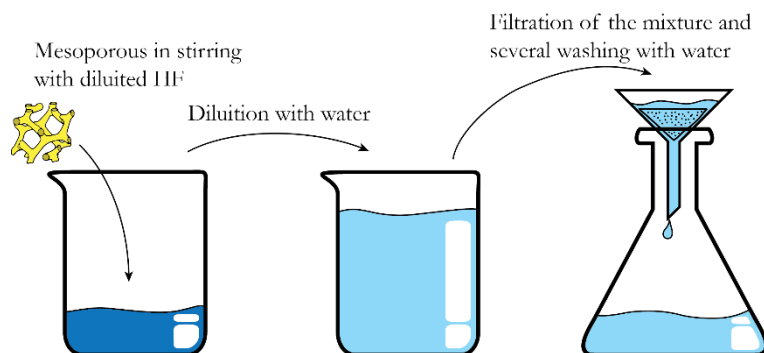
154

Figure 4.1: Scheme of the etching by HF divided by the three foundamental steps: i) mixing of the mesoporous powders with the diluited solution of HF for 1, 5 or 10 minutes; ii) diluition by water to stop the reaction; iii) filtering of the mixture and washing by water to recover the particles.

The poweders were analyzed by ICP-MS to determine the silica contamination remaining from the template. Figure 4.2 highlights the significant decrease of the silica content that was measured on the powders after the NaOH etching and after the additional etching of 1, 5 and 10 minutes of HF, resulting in 0.88 wt%, 0.26 wt%, 0.22 wt% and 0.14 wt%, respectively.
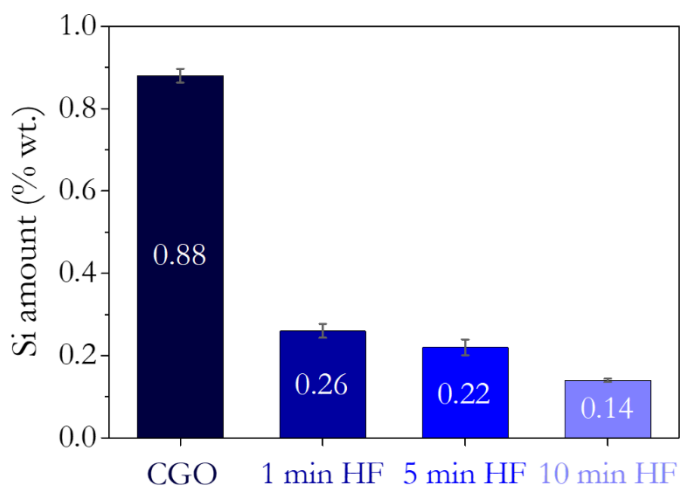

Figure 4.2: ICP-MS analysis of CGO powders before and after silica removal etching by NaOH and NaOH+HF (1, 5, 10 mins) exposure. The figure highlights the decrease of Si content with increased etching time.

4.2.1.1 Etching mechanisms of silicon dioxide by HF

The utilization of HF to etch silicon dioxide had been object of a certain interest in the microfabrication field due to its selectivity. This is because the etching rate of SiO_2 is much faster than for Silicon when they are exposed to hydrofluoric acid.[29] Besides, the hydrofluoric acid seems to work much better with rough surfaces.[29] Different mechanism are proposed in literature e.g. chemical replacement of the hydroxyl groups with the fluorine anion or hydrogen bonding of HF to the silanol groups. Monk *et al.* pointed out that nucleophilic chemisorption of HF to the silicon (Figure 4.3) is most plausible mechanism, because it can explain the need of an open surface for the oxide to work.[29]
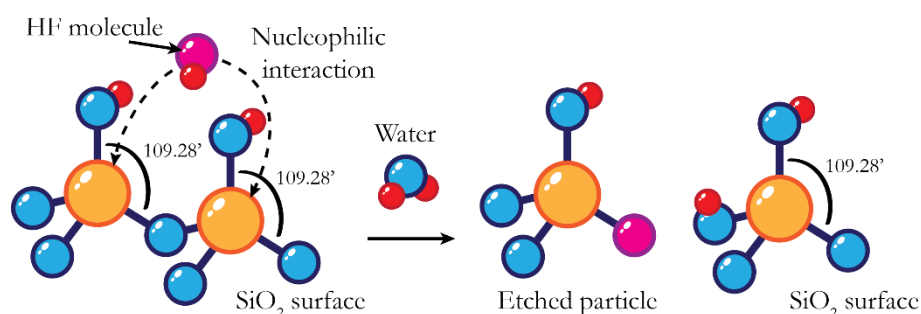

Figure 4.3: Schematic rapresentation of the nucleophilic chemisorption of HF to the silicon.

4.2.2 Effect of the etching processes on the structure

The cleaning process NaOH + HF demonstrated to be particularly effective for the removal of the silica contamination on the CGO mesoporous powders. However, a series of complementary analysis were conducted on the powders in order to better understand the effect of such process on the properties of the nanostructured material.

Figure 4.4 shows the structural analysis of mesoporous cerium oxide after washing by NaOH (CGO) to eliminate the main amount of SiO_2,

Advanced strategies for Solid Oxide Electrolysis Cells

proving that single phase ordered mesoporous powder was obtained. Together are presented the results on the investigation of the structural effects of a second etching process by HF to eliminate the SiO_2 remaining particles. With reference to the CGO powders, the XRD analysis in Figure 4.4 confirmed the desired formation of the $Ce_{0.8}Gd_{0.2}O_{1.9}$ phase.

The analysis of the ceria stability upon HF treatment, as carried out by XRD (Figure 4.4), highlighted that, for increasing etching times, secondary phases appeared. This is particularly evident for the longest treatment (10 min), although some secondary phase peaks were already visible after 1 min and 5 min exposure. The detected peaks suggested the presence of $(Gd,Ce)F_x$ mixtures as a consequence of a certain reactivity of ceria and gadolinium towards HF.[24] Such reactivity is expected to lead to a partial etching of the CGO phase[28] present at the grain boundary (GB) and surfaces as previously reported by the author hosting research group.[9]
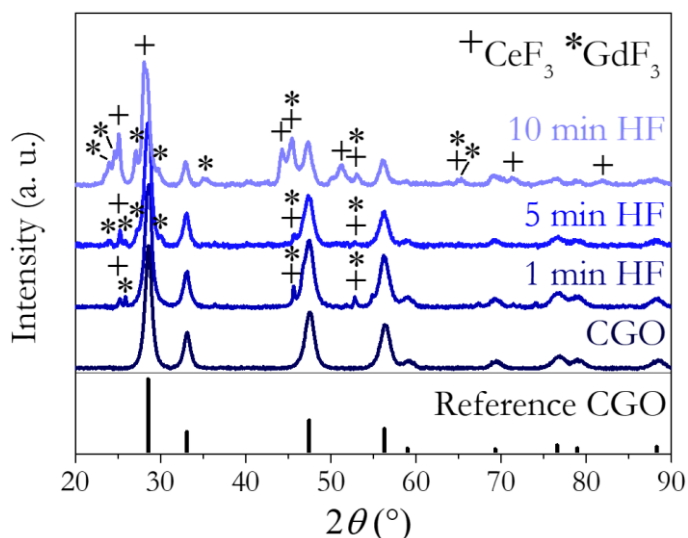

Figure 4.4: XRD analysis of CGO powders after silica removal etching by NaOH and NaOH+HF (1, 5, 10 mins). Results of theta-two theta XRD scans are shown, in which the presence of the CGO phase after the synthesis is confirmed. Secondary phase precipitates, in the form of fluorine-based compounds, (CeF_3 and GdF_3, indicated by the symbols (+) and (*), respectively), are formed upon HF exposure.

Advanced strategies for Solid Oxide Electrolysis Cells

4. Improved mesoporous CGO for application in SOCs

SAXS of Figure 4.5 clearly showed the presence of the characteristic peaks related to the *Ia3d* symmetry of the mesoporous periodic structure. The measurements performed at ALBA synchrotron (this analysis was carried out by collaborators to the present work) revealed a certain evolution of the CGO scaffold structure upon HF treatment. The peaks indexed as 211 and 220 planes of the cubic structure of the mesoporous with *Ia3d* symmetry[30–33] were still present after up to 5 min of HF treatment although a certain broadening and flattening of the peaks were observed. The intensities of the SAXS patterns were reported as function of the magnitude of the scattering vector q and the values of two peaks are 0.72 nm^{-1} and 0.83 nm^{-1}, respectively. After the 10 min treatment, no peaks were observed at low angles indicating the collapse of the mesoporous structure (likely due to the slow but continuous etching of the CGO phase through the grain boundaries).[28] This confirmed that after 1 and 5 min of exposure to HF the mesoporous structure is stable and could be effectively used as scaffold for SOC applications.

Please note here that a slight shift (0.03 nm^{-1}) with respect to the KIT-6 reference (whose peak positions are indicated by the black bars at the bottom of Figure 4.5) was detected. Such a shift was correlated to the shrinkage of the periodic structure and it was already observed in previous works of Almar *et al.*[34] and Hernandez *et al.*[35] The cell parameter a presented a variation from 22.4 nm (KIT-6) to 21.4 nm (Δa = -1 nm). The analysis also revealed another contribution at lower values of scattering vector q, which corresponds to the position of the (110) reflection of an $I4_132$ structure with lower symmetry. Notably, such a reflection is not allowed for the *Ia3d* system[30,31] and should be ascribed to the partial filling of the KIT-6 during the ceria hydrothermal synthesis. This means that one of the two sets of channels was preferred for the filling respect to the other.[31] Doi *et al.* suggest the utilization of synthesis temperatures above 100 °C to achieve an improved replica.[30]

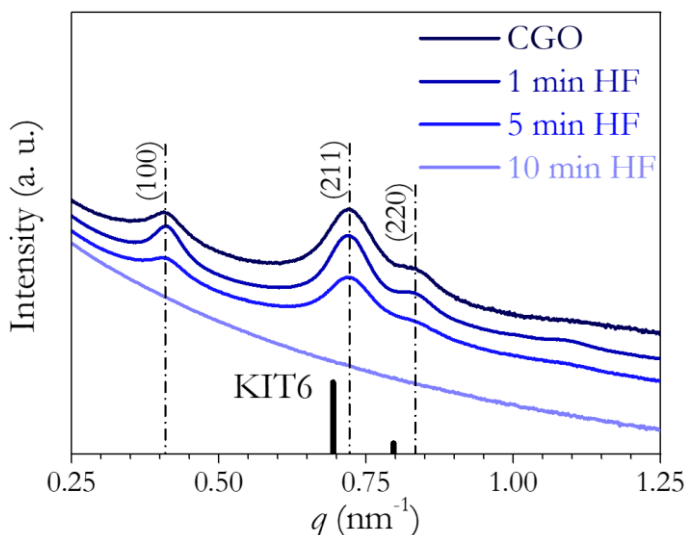Advanced strategies for Solid Oxide Electrolysis Cells

Figure 4.5: SAXS analysis on CGO powders after silica removal by NaOH and the additional etching with HF (1, 5, 10 mins exposure). The measurements (carried out by collaborators to the present work), made thanks to the ALBA synchrotron, showed that the periodicity of the mesoporous structure was maintained for etching times ≤ 5 min.

Figure 4.6 presents the BET analysis made on the powders, which showed the evolution of the pores on the structure. In particular, the peak pore width of the powders shifted from values around 4 nm for the mesoporous after cleaning by NaOH, to 6 and 8 nm after 1 and 5 minutes of HF etching, respectively. Correspondingly, the BET surface area increased with the etching time and reached a maximum of ≈118 $m^2 g^{-1}$ after 5 min, higher than the starting value (86 $m^2 g^{-1}$). This is due to the HF etching which increased the surface area available due to the SiO_2 contamination removal and the partial etching of the CGO. Instead, after 10 minutes of HF exposition, a drop of the incremental area was observed, with a measured BET area of 52 $m^2 g^{-1}$, confirming the worsening (due to the partial chemical instability) of the active area of the mesostructure as already suggested by the SAXS analysis of Figure 4.5.
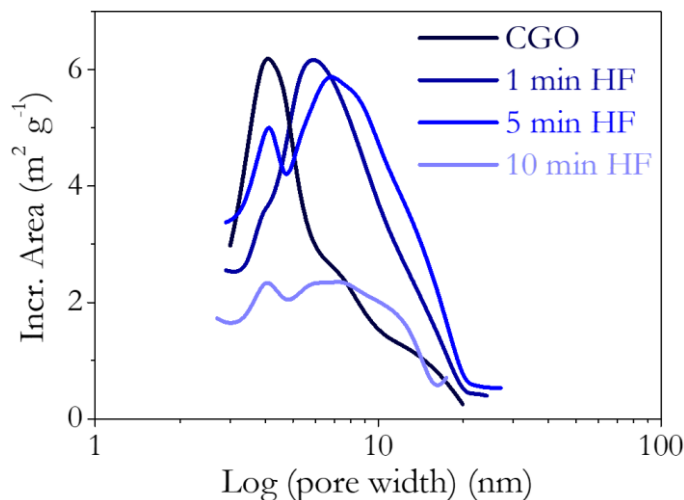
Figure 4.6: BET analysis of CGO powders after silica removal etching by NaOH and NaOH+HF (1, 5, 10 mins). The measurements revealed an increase of mesoporous area and an increase of the peak pore width for HF treatments up to 5 min.

SEM micrographs of the CGO powder after washing by NaOH confirmed the mesoporous structure and its periodicity (Figure 4.7a-c), as also pointed out by SAXS analysis (Figure 4.5). However, elongated particles and filaments observed on the powder (as highlighted in Figure 4.7d) were attributed to the incomplete removal of silica.
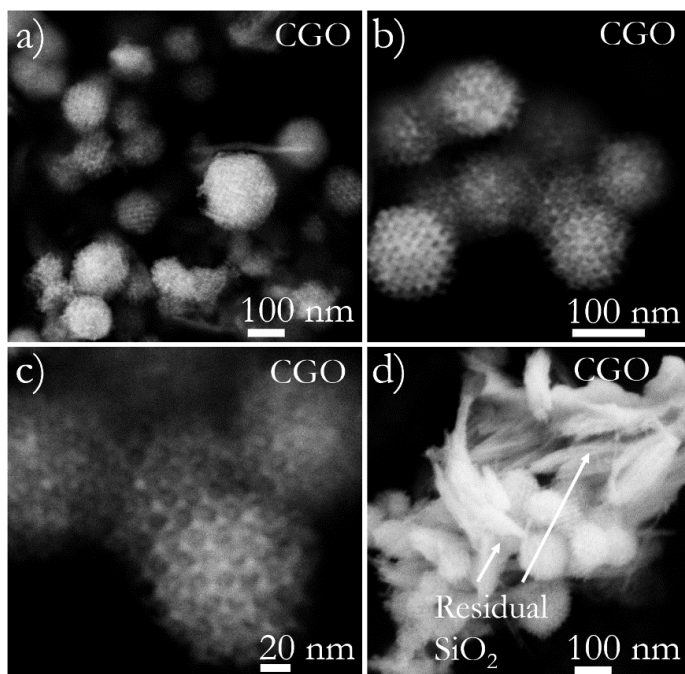
Figure 4.7: SEM micrographs of CGO after washing by NaOH (a, b, c and d). (d) represents a zone with an unusual high SiO_2 contamination.

Consistently with the above reported observations, SEM pictures of regions with impurities (Figure 4.8a-c) showed the progressive reduction of the size of the silica particles with increasing HF etching time. The collapse of the nanostructure after 10 minutes of exposition to HF is also evident. This confirms the previously mentioned reactivity of Ce and Gd with fluorine and the consequent CGO etching starting from the surfaces and the grain boundaries.
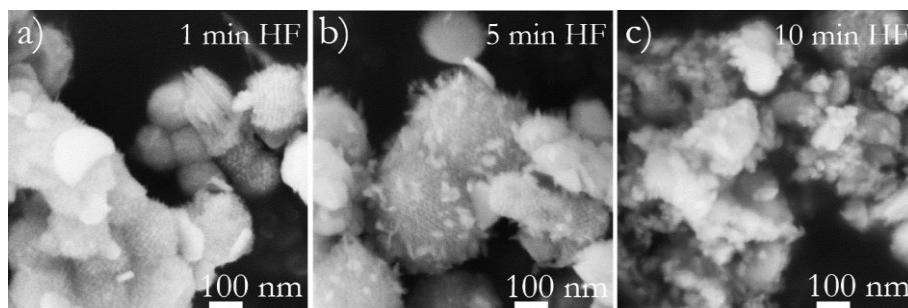
Figure 4.8: SEM micrographs of CGO mesoporous powders after washing by NaOH and etched by 2.5 %v/v HF for 1 min (a), 5 min (b), and 10 min (c).

TPR experiments under hydrogen atmosphere were carried out to investigate the HF etching effect on the redox activity of the mesoporous CGO powder. Figure 4.9 shows the TPR profiles of the NaOH-washed and HF-treated samples, revealing a much larger activity for the samples that had been etched by HF. The samples treated for 1, 5 and 10 min showed a strongly enhancement of the reduction peak centred at 600-700 °C. This indicates that the reduction of a higher fraction of doped-ceria was occurring in this particular temperature range. This is consistent with previous published studies about the catalytic activity of mesoporous doped-ceria.[36,37] A shift of the peak towards higher temperatures was detected according to the HF treatment duration increase, confirming the deleterious effect of HF treatment for long expositions (i.e. > 5 min).
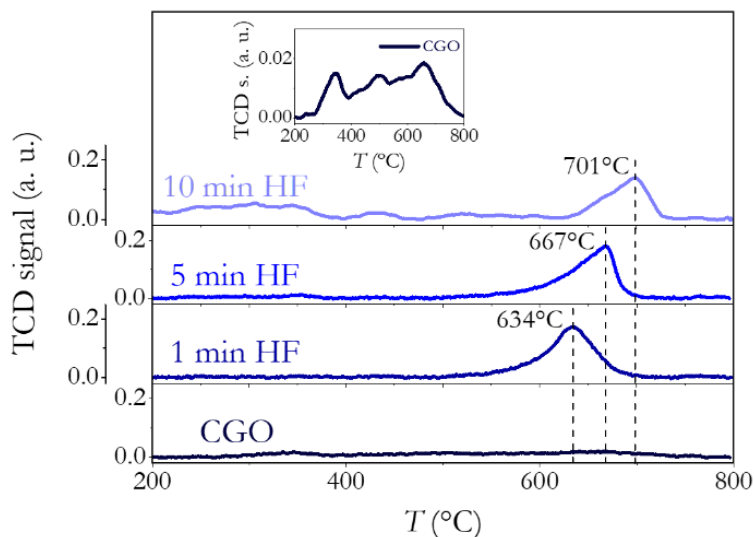
Figure 4.9: TPR analysis of the CGO mesoporous powder and HF-CGO after 1, 5 and 10 min of etching. In the inset, the TPR curve of CGO before HF etching is reported with magnified by a zoom of the TCD signal axis.

Considering the above described behaviour, the 5 min exposure, at 2.5 %v/v HF, was considered as the optimal treatment for the cleaning step on the fabrication process of the mesoporous CGO backbone. The selected treatment maximized the BET surface area ($\approx$118 m^2 g^{-1}) and the redox activity (cf. Figure 4.9). At the same time, the 5 min HF-CGO preserved the initial mesoporous ordered structure (cf. Figure 4.5) while strongly reduced the Si content (cf. Figure 4.2). Importantly, the analyses demonstrated that the fluorite impurities formed after 5 min etching (cf. Figure 4.4) did not affect the final properties of the material. Resulting BET surface area and TCD signal (key structural and functional parameter, respectively) exhibited strongly enhanced values that promoted an improvement on the electrochemical performance.

4.3   TEM analysis on mesoporous particles

TEM analysis on some rare-earth doped ceria mesoporous particles were conducted in collaboration with the Universitat de Barcelona (UB), with the aim to investigate the microstructure of the material.

In particular, in Figure 4.10, Figure **4.11**, Figure **4.12** andFigure **4.13** the analysis on a mesoporous particle with a similar composition to the one object of the study (of $Ce_{0.8}Gd_{0.1}Pr_{0.1}O_{1.9}$ (CGPO)) is reported. Please note that the material was prepared at IREC by the same hard-template method and that the total doping content is the same as in thee CGO discussed here (20%). Therefore, the TEM results obtained on CGPO can be reasonably extrapolated to CGO. The CGPO powders were analysed by TEM after the cleaning only with NaOH.

Figure 4.10a shows the Annular Dark-Field (ADF) image that was acquired at -70°, used for the electron tomography 3D reconstruction of Figure 4.10b, same case but at -30° for Figure 4.10c -Figure 4.10d and at 0° for Figure 4.10e -Figure 4.10f. One can notice the excellent agreement between the original particle analysed by ADF and the TWM3D reconstruction. In particular the hexagonal geometry presented in Figure 4.10e and in the corresponding reconstruction of the Figure 4.10f, which was expected for a replica of the KIT-6 template, is extremely clear.
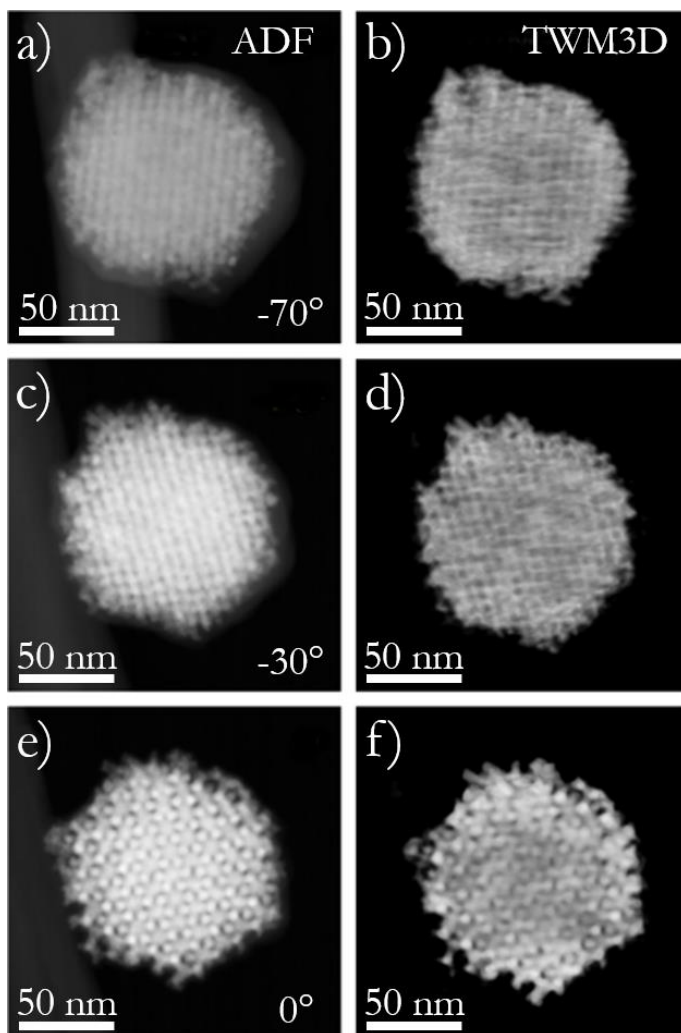
Advanced strategies for Solid Oxide Electrolysis Cells

Figure 4.10: TEM reconstruction reported with the permission of the Universitat de Barcelona. ADF image taken at -70° (a) with the corresponding ET 3D reconstruction (b), also at (c) and (d) -30° and (e) and (f) 0°.

Figure 4.11a shows the prospective of the volume rendering of the ET reconstruction with the orthogonal cuts marked with different colours. Figure 4.11b is therefore the lateral cut (yellow square) of Figure 4.11a, while Figure 4.11c and Figure 4.11d are respectively the top (red square) and the front (blue square) views. The slices at different angle obtained by the 3D reconstruction presented a zig-zag patter which can be clearly observed in Figure 4.11b and Figure 4.11c. This pattern was the result of the complete

filling of the replica during synthesis with the formation of the bi-continuous structure. The presence of the two channels can be observed from the front cut reported in Figure 4.11d.
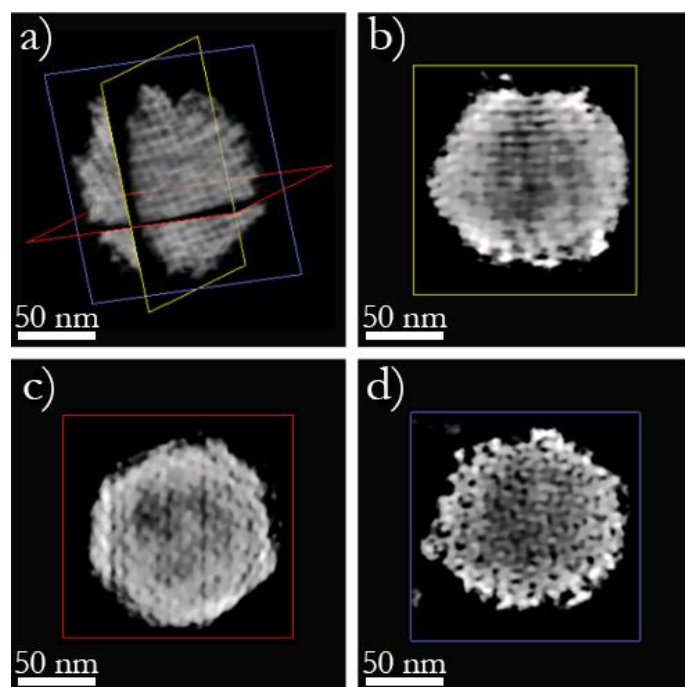

Figure 4.11: TEM reconstruction reported with the permission of the Universitat de Barcelona. Panel (a) shows the ET reconstruction of Figure 4.10 with indicated the planes of the different cuts of the volume rendering (b), (c) and (d). (b) is the lateral view in yellow, (c) the top view in red and eventually the (d) front view indicated in blue.

Figure 4.12 reports the Annular Dark-Field (ADF) reconstruction together with the Energy Dispersive X-Ray Spectroscopy (EDX) mapping of the same particle of $Ce_{0.8}Gd_{0.1}Pr_{0.1}O_{1.9}$ (CGPO) of Figure 4.10 and Figure 4.11. The image is here reported as representative of the mesoporous replica structure when both the bi-continuous channel of the KIT-6 template are filled (as described in Chapter II section 2.2.1). One can notice the high correspondence between the ADF image (Figure 4.12a) and the Ce signal from the TEM-EDX map (Figure 4.12b). The micrographs of the Pr (Figure

4.12c) and Gd (Figure 4.12d) signals shows that the dopants were distributed throughout the mesoporous particle; however in some zones the signal associated to such elements seemed to be more intense, revealing an higher concentration of the dopants.
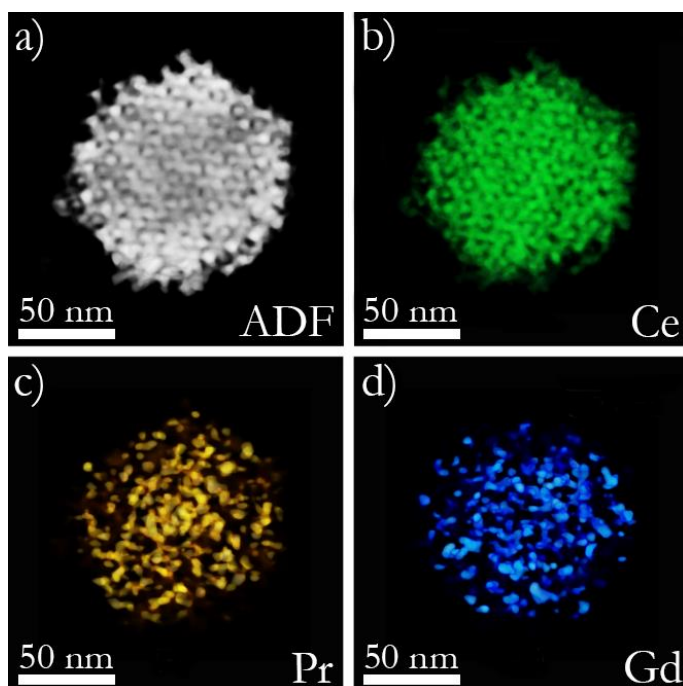

Figure 4.12: TEM reconstruction reported with the permission of the Universitat de Barcelona. The ADF image (a) of Figure 4.10 is compared with the TEM-EDX mapping of Ce (b), Pr (c) and Gd (d).

In order to further investigate the dopants distribution, slices of the reconstructed volume overlaying for both ADF (Figure 4.13a) and Ce TEM-EDX signal (Figure 4.13b) were over-plotted with Gd and Pr TEM-EDX signals. From these reconstructions one can conclude the trend of the dopants to be accumulated in clusters towards the particle necks (grain boundaries) of the ceria-based structure.
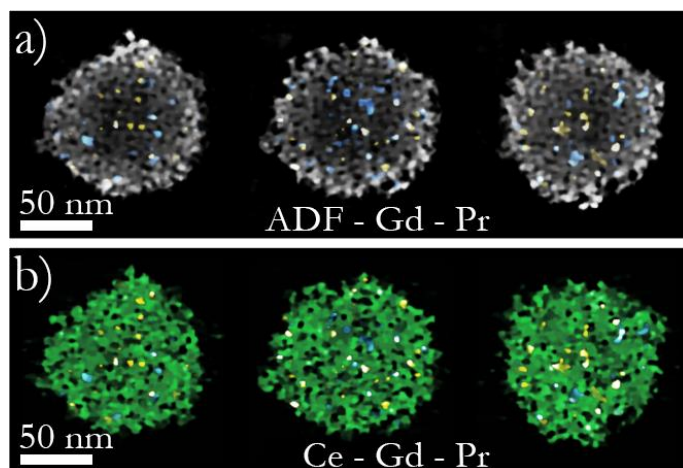
Figure 4.13: TEM reconstruction reported with the permission of the Universitat de Barcelona. Panels (a) and (b) represent respectivley the ADF image and the Ce signal with on both the Gd and Pr elemental signal.

The GB segregation of dopant cations in rare-earth doped ceria is a known issue which could considerably limit the conductivity of the material.[38,39] The localized amount of dopant creates domains with higher amount of oxygen vacancies respect to the bulk grain. These domains show a local order that limits oxygen vacancies mobility and blocks the ionic conductivity at the GB level.[40]

Further TEM analyses were conducted on the same CGO powders, before and after the etching by HF. Figure 4.14a shows an TEM picture of a particle after the washing by NaOH. This particle was analysed by electron energy loss spectroscopy (EELS) on a selected area. During the analysis, a careful tuning of the beam electron current was conducted, to avoid the reduction of the Ce^{3+} cations in Ce^{4+} under the electron beam. Figure 4.14b shows a colormap of the quantitative elements distribution obtained by clustering analysis while Figure 4.14c shows the reference points used. In a hyperdimensional space, clustering analysis aim to classify the p pixels with same attributes (represented by the c channels, characterized by different intensities). From the different intensities of these points it is possible to

Advanced strategies for Solid Oxide Electrolysis Cells

classify them as pertaining to one cluster or to another one. The spectrum image was therefore divided in zones with different chemical signature, each one indicated by a different color.[41] One can see in Figure 4.14c that two different clusters were identified, characterized by a very different ratio Gd/Ce obtained by the respective EELS signals (high energy, Gd ≈1200 eV, Ce ≈900 eV). As highlighted by Figure 4.14b, the highest Gd concentration (blue colour) was found at the grain surfaces. This confirmed the inhomogeneous distribution of the Gd dopant and in particular its accumulation at the GB level (blue spectral line in Figure 4.14c and blue pixels in Figure 4.14b).
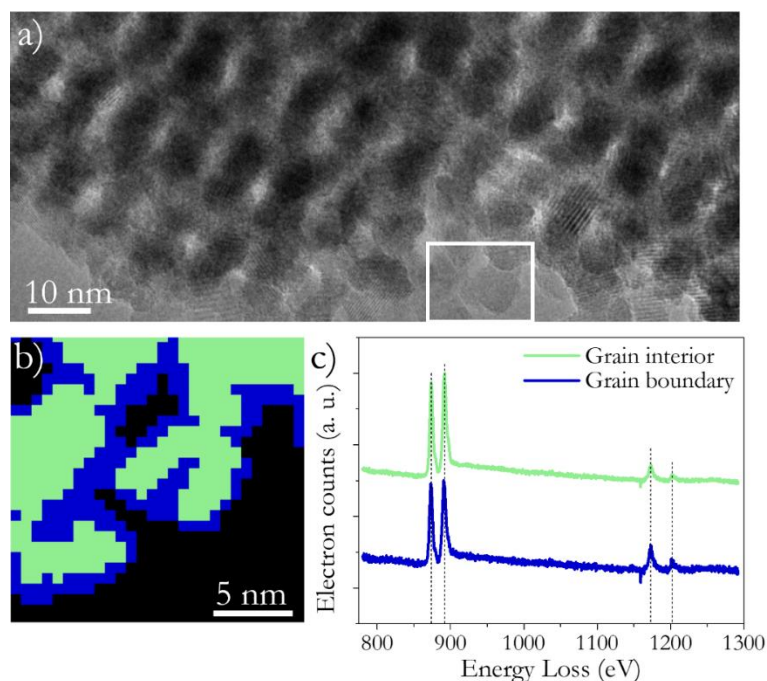

Figure 4.14: TEM analysis reported with the permission of the Universitat de Barcelona. TEM image of a large area of mesoporous CGO (a), with a white rectangel which rapresents the area of the EELS analysis. Cluster label mapping (b) obtained by the EELS analysis. Cluster centroids (c) for the distribution in b, with the EELS spectra of the inner (green) and outer (blue) zones.

The HAADF image acquired on the zone of the EELS analysis (Figure 4.15a) showed three grain boundaries. From the analysis it can be observed that only in the analysed bulk regions the Gd/Ce ratio was close to the nominal composition, while it grew across the grain boundaries (0.4 – 0.8).
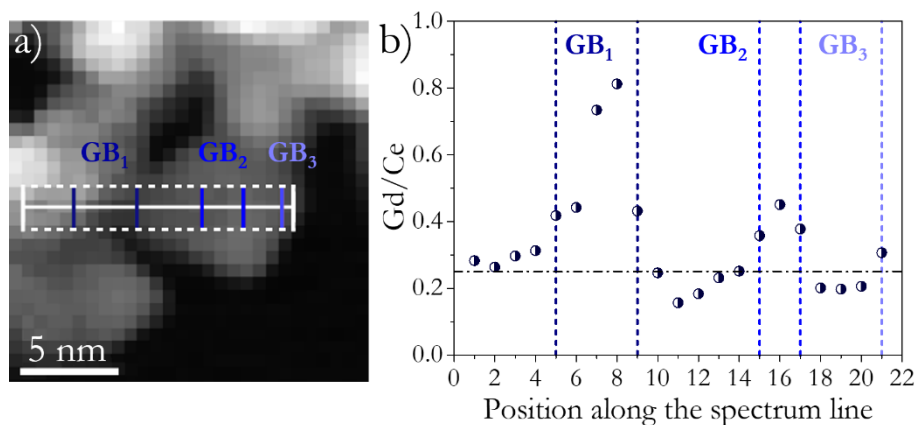
Figure 4.15: TEM analysis reported with the permission of the Universitat de Barcelona. HAADF image (a) of the area of the EELS-SI of Figure 4.14a with the lines that indicate the spectra summed for the spectrum line analysis. Gd/Ce ratio quantification (b) based on EELS along the line in (a).

Figure 4.16 shows the TEM analysis on CGO mesoporous powders after the etching by HF 2.5%v/v for 5 minutes. Figure 4.16a shows an HAADF image of the mesoporous CGO. In the image is indicated the region where Figure 4.16b and Figure 4.16c were acquired (white square). Figure 4.16b and Figure 4.16c are the HRTEM and HAADF images respectively of the analysed region. The grain boundaries are highlighted by yellow dashed lines.
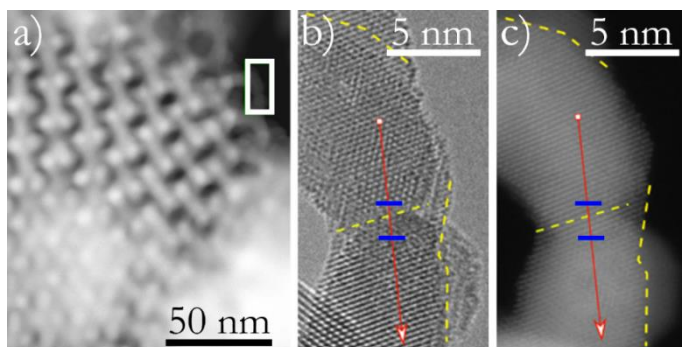
Advanced strategies for Solid Oxide Electrolysis Cells

Figure 4.16: TEM analysis reported with the permission of the Universitat de Barcelona. HAADF image of the mesoporous CGO after 5 min of HF exposure (a). In the white square is indicated the zone of the analysis. High-resolution TEM (b) and STEM-HAADF images (c) of the area where the EELS-SI was acquired, with graind boundaries highilted by dashed yellow lines. The red arrow indicate the direction of the spectrum line analysis.

Figure 4.17a shows the HAADF image co-acquired during the EELS analysis made across the red line and Figure 4.17b is the colour map of the Gd/Ce ratio. Figure 4.17c reports the result on the Gd/Ce ratio across the line of the EELS analysis. It can be noticed that there was no significant difference in composition between the bulk and the GB region. Considering these results, it is clear that HF treatment did not only etch the silica that contaminates the structure, but it was also able to remove the excess of Gd at the GB region.
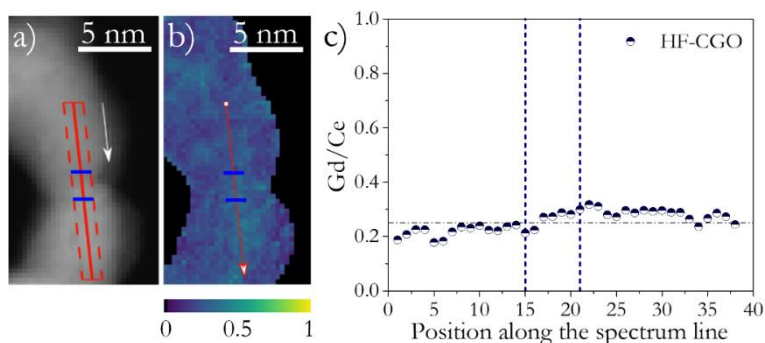
Figure 4.17: TEM analysis reported with the permission of the Universitat de Barcelona. HAADF image co-acquired with the EELS-SI (a) and map for the quantification of Gd/Ce (b). In (c) the quantification of the Gd/Ce ratio across the red line of panels a and b are shown. The dashed blue lines delimit the region of the grain boundary.

The presented results agree with what was highlighted by the complementary analysis of Figure 4.4. XRD showed some Gd and Ce fluorite phases on the pattern after the etching by HF. Moreover, the SAXS analysis of Figure 4.5 showed how the exposition to the hydrofluoric acid during a prolonged time could be deleterious for the mesoporous structure. TEM analysis demonstrated that HF etching affected mainly the GB of the CGO mesoporous structure. This caused the formation of the Gd and Ce fluorite and after long exposure the collapse of the structure. The tuning of the etching process revealed how such treatment could promote the removal of the unwanted dopant cluster and this explained the increment of surface area highlighted by BET analysis in Figure 4.6.

4.4 The use of sintering aid: reducing the attachment temperature.

4.4.1 Effect of the use of Co as sintering aid

With the aim of developing a process to optimise the attachment temperature of the scaffold to the electrolyte, Co oxide decorated CGO

Advanced strategies for Solid Oxide Electrolysis Cells

mesoporous powders were prepared. It is known that some metal oxides such as Cu, Co, Zn and Li,[42,43] added in small amounts as decorating agents, can act as sintering aids.[44,45] In particular, the effectiveness of Co oxide and its ability to activate the sintering process have been already proven in previous works.[46,47] The addition of small amounts of Co oxide (from 0.5 % mol up to 5 % mol) is able to lead to the densification of $Ce_{0.8}Gd_{0.2}O_{1.9}$ at temperatures as low as 850 ºC.[48]

Two different decoration concentrations (1 and 2 %mol) and two temperatures (825 and 850 °C) were considered. Pursuing this objective, CGO mesoporous powders were mixed in ethanol with $Co(NO_3)_2 \cdot 6H_2O$. Obtained suspension was stirred in ultrasound at room temperature for 30 min and then dried in oven at 120°C. The decorated powder was afterwards grinded in a mortar and calcined at 400 °C for 2 hours.[45]

Observing Figure 4.20a and 4.18b no particular difference was highlighted after sintering with respect to the amount of Co nitrate. Mesoporous powders presented surfaces areas $\approx$45.9 m^2 g^{-1} and $\approx$53.8 m^2 g^{-1} (after sintering at 825 °C) and $\approx$39.0 m^2 g^{-1} and $\approx$37.7 m^2 g^{-1} (after sintering at 850 °C) for 1 %mol and 2 %mol, respectively. Therefore, 1 %mol was chosen as preferred concentration to minimize the amount of Co oxide decorating the CGO scaffold. This was done with the aim to limit the function of Co oxide only to the sintering promotion, limiting the interaction with the electrochemical properties of the scaffold during operation. Furthermore, Co is a very costly material, due to its scarceness.

As a result of the performed characterization the process defined by 1 %mol of Co and 850 °C as Co attachment temperature showed the best final porosity. This combination was finally chosen for the decoration process ensuring the compatibility with the firing temperature of the current collector (LSCF - 850 ºC).
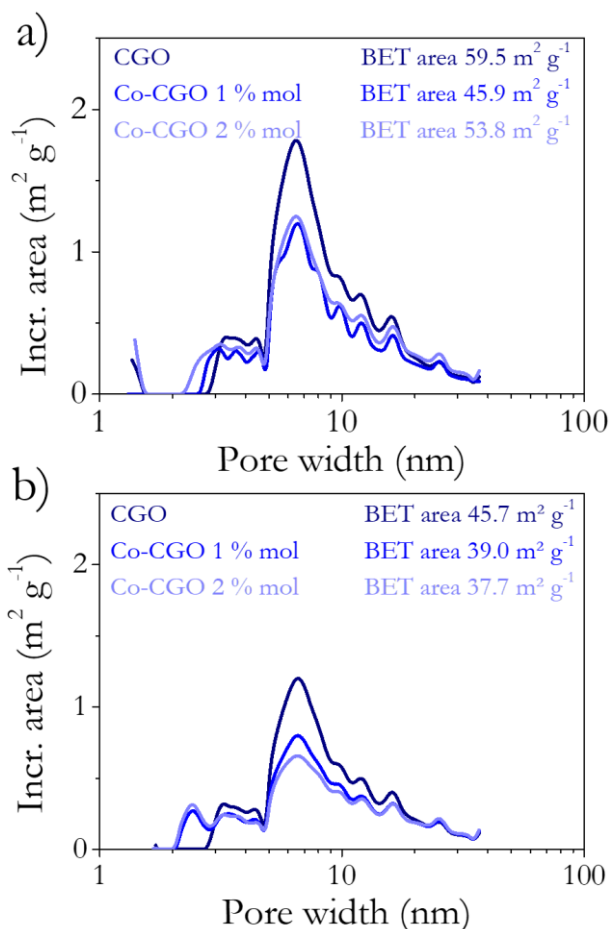
Figure 4.18: BET analysis on the CGO, Co-CGO 1 %mol and Co-CGO 2 %mol sintered at 825 °C (a) and 850 °C (b).

Figure 4.19a shows the comparison of BET areas between the CGO as synthetized powders, and after sintering at 850, 900 and 1100 °C. 900 and 1000 °C are the typical temperatures used for the firing of the undecorated mesoporous CGO. The results on the powders decorated with 1 %mol Co oxide sintered at 850 °C are also presented. In Figure 4.19a, the BET area values are displayed as a function of the sintering temperature while in Figure 4.19b the respective incremental area values are reported with respect to the pore width.

The effect of the sintering aid is clearly seen analysing the BET area results for the different temperatures and percentage of Co decoration. BET areas of 12.8 $m^2 g^{-1}$ were obtained for CGO powders sintered at 1100ºC, while areas of 39.0 $m^2 g^{-1}$ were measured for Co-CGO, which was fired at 850 ºC. This is expected to provide great advantages during operation in a real device in terms of gas diffusion inside the scaffold and available surface area for chemical reactions. 1100 ºC represents the typical temperature of choice for the attachment of the single phase material.[9,14,35] Notably, 850 ºC is the lowest possible attachment temperature for Co-CGO. This is because such a temperature is compatible with the processing of the other layers of the cell and with the final application (i.e. anode-supported SOEC operating at 750-850 ºC).
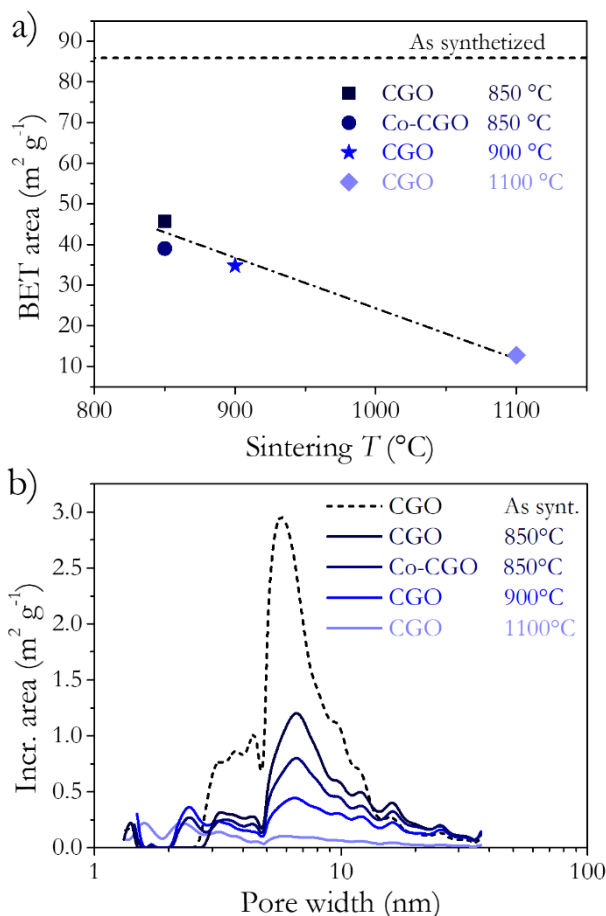
Figure 4.19: BET areas of the CGO mesoporous powders as synthetised and after sintering at 800, 900 and 1000 °C compared with a batch decorated with 1 %mol of cobalt as sintering aid (a). The dashed and dotted line must be considered only as guide for the eye. Incremental area vs. pore width of the same powders (b).

The mechanism by which Co acts as a sintering aid is extensively discussed in literature. According to Zhang *et al.*, Co oxide decoration activates sintering in the solid-state by promoting rapid diffusion of elements from the main phase and from the additive along the sinter bond.[49] German and Rabin explain that the addition of a second phase could work not only providing rapid diffusional transport at the interparticle contacts and therefore affecting the sintering kinetics, but also through liquid sintering, in which the dominant force is the surface tension of the liquid phase (Figure

4.20).[50] Jud and Gauckler explain that Co oxide addition can also lead to a viscous flow mechanism of material form high-stressed to low-stressed areas in the early sintering stage, influencing the overall process and so lowering the firing temperature.[51]

In the presented case, since 850 °C was the higher temperature used for the sintering of the decorated powders, both activated solid-state sintering and viscous flow are possible mechanisms.
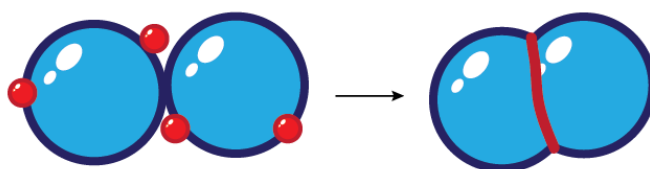
Figure 4.20: Scheme of the sintering process between two particles trigged by the sintering aid.

4.4.2 HF and Co-decoration combined effect

The higher values of specific area observed for Co-CGO after thermal treatment anticipate the observed improved behavior of Co_3O_4 decorated CGO. Incorporating the optimized HF etching process, the obtained BET area after thermal treatment (5 h, 850 ºC) was 14 m^2 g^{-1}. Te surface area was reduced if compared with the initial values of the same HF-Co-CGO (34 m^2 g^{-1}). Confirming this evolution, the SEM images of the as-synthesized and of thermally treated HF-Co-CGO are shown in Figure 4.21. The microstructural change from the as-synthesized HF-Co-CGO, to the one treated at high temperatures can be clearly observed. One can notice, in Figure 4.21a, that HF-Co-CGO before thermal treatment keeps the perfect ordered original mesoporous structure. On the other hand HF-Co-CGO after thermal treatment presented a partially sintered mesoporous structure

Advanced strategies for Solid Oxide Electrolysis Cells

with bigger grain size (Figure 4.21b).[2,34] As already mentioned above a certain degree of pososity was mantained after sintering and this is clearly showed in Figure 4.21b. The presence of residual porosity is a foundamental characteristic for the fabrication of the composite nanostrucuterd electrode.
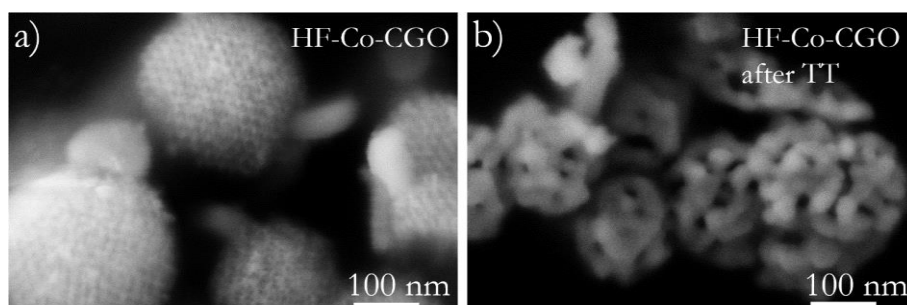
Figure 4.21: SEM images of the as synthesized HF-Co-CGO powder (a) and after thermal treatment at 850 °C for 5 hours (b).

4.5 Electrochemical characterization of symmetrical cells

Symmetric Au/CGO/YSZ cells, using four different types of CGO mesoporous scaffolds have been tested (Table 4.1):

Table 4.1: Characteristics of the scaffolds of the four symmetrical cell prepared for impedance spectroscopy measurements. CGO and HF-CGO cells were sintered at 1100 °C, while Co-CGO and HF-Co-CGO cells at 850 °C.

Cell ID	Mesoporous CGO scaffold	1% mol Co oxide	5 min HF
CGO	x		
Co-CGO	x	x	
HF-CGO	x		x
HF-Co-CGO	x	x	x

Starting with the analysis of the standard CGO symmetric cells, the representative Nyquist plot obtained at 770 °C and shown in Figure 4.22, exhibits a very depressed and slightly asymmetric arc. The fitting of this arc was performed by two different equivalent circuits; the *model (*4.1 and the

*model (*4.2. In these models L is an inductive contribution due to the setup, R_s is the serial resistance attributed to the electrical conductivity contributions (electronic from the current collection and ionic from the YSZ electrolyte and the CGO backbone), while ($R_{pi}Q_i$) refers to polarization impedance at the electrodes.

$$L \ - R_s \ - \ (R_p Q) \tag{4.1}$$

$$L \ - R_s \ - \ (R_{p1}Q_1) \ - \ (R_{p2}Q_2) \tag{4.2}$$

The bode plot of Figure 4.22b, highlighted the inaccuracy of the fitting obtained by *model (*4.1, while the asymmetry of the arc was perfectly fitted by circuit *model (*4.2. One can justify the presence of two arcs considering small microstructural differences between the two electrodes, which lead to a shift in the characteristic time response. This means that each of the impedance arcs should be assigned to the same electrode processes occurring at the top and bottom electrode, respectively. Alternatively, the two arcs could be correlated to different oxygen electrode reactions in the solid phase (e.g. reactions occurring at the Au/ceria/air TPBs and reactions on the ceria surface).[52,53] The impedance spectra of the four different cells were fitted by the proposed equivalent circuit $LR_s(R_{p1}Q_1)(R_{p2}Q_2)$ (inset Figure 4.22a and Figure 4.22b).
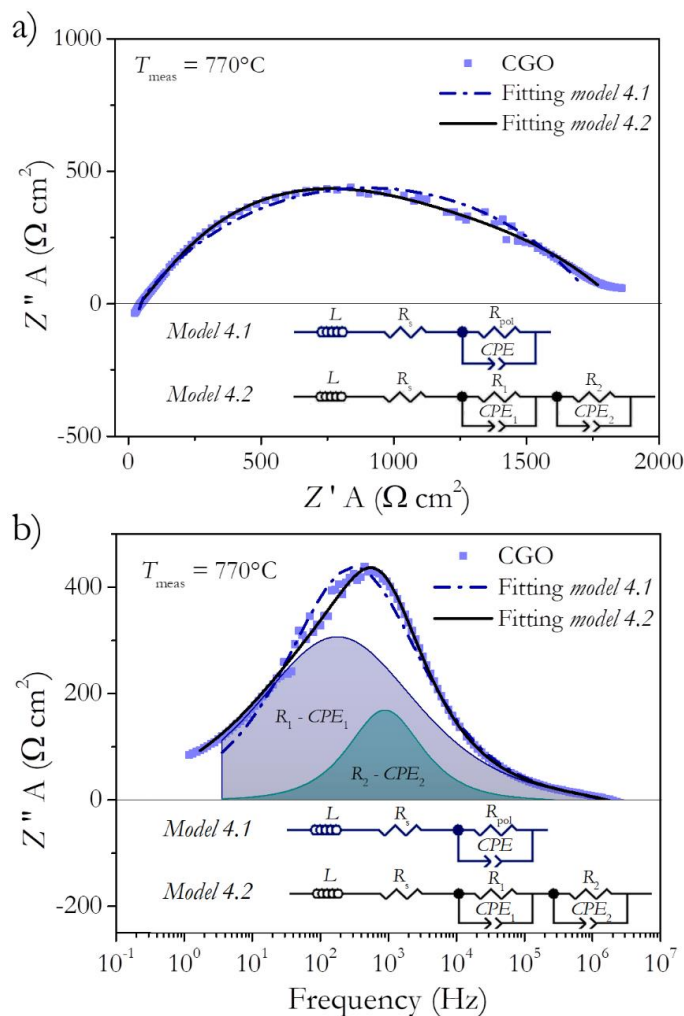
Figure 4.22: Nyquist plot (T =770 °C) of a Au/mesoporous CGO/YSZ tape cell (a) is shown with the equivalent circuits used for the fitting of the impedance spectra measured. Bode plot with the two different fitting models (b). The single R_i - CPE_i are highlighted.

The temperature dependence of the serial (ASR_s) area-specific resistance for the different tested symmetric cells is reported in Figure 4.23. By taking into account the measured electrolyte conductivity (YSZ tape), one can immediately observe that a significant increase of the ASR_s (up to two orders of magnitude at low temperatures) was present, owing to the ceria layer itself and to the ceria/YSZ interface. Such a resistive CGO contribution

Advanced strategies for Solid Oxide Electrolysis Cells

reached a maximum for the as-synthesized scaffold attached at 1100 °C (ASR_s^{CGO} = 54 Ω cm² at 750 °C and E_a = 1.29±0.02 eV) becoming substantially lower for the HF etched backbones ($ASR_s^{HF\text{-}CGO}$ = 38 Ω cm² at 750 °C and E_a = 1.11±0.02 eV). This can be directly associated to an improved ionic conduction within the ceria phase. Such improvement was likely localized at the GB level where Gd-rich clusters were detected by TEM analysis and where preferential segregation of SiO_2 is expected.[15,25,54] This effect can be explained by the twofold effect of HF etching on ceria GBs: scavenging of the siliceous phase and Gd cluster removal, which granted higher ion mobility. Suppression of the local ordering of oxygen vacancies, caused by the cluster formation can in fact increase ionic conductivity.[40] The measured activation energy values are compatible with ceria GB conductivity processes (whereas the typical activation energy range related to the bulk ionic conductivity in CGO is around 0.5 – 0.8 eV).[55,56] Such an observation is in agreement with the well-studied blocking boundary behaviour of nanocrystalline acceptor-doped ceria.[57]

As far as the CGO decoration by Co (II, III) oxide is concerned, a reduction of the ASR_s was observed for the symmetric cells ($ASR_s^{Co\text{-}CGO}$ = 27.2 Ω cm² at 750 °C and E_a = 1.14±0.02 eV)

The finding can be explained in the light of the expected beneficial influence of Co oxide decoration as sintering aid, which is extensively discussed in literature. According to Zhang et al., Co oxide decoration activates sintering in the solid-state by promoting the rapid diffusion of elements from the main phase and from the additive along the sinter bond.[49,50] Co oxide addition can also lead to a viscous flow mechanism in the early sintering stage, which influences the overall process reducing the firing temperature.[51] Both activated solid-state sintering and viscous flow are possible mechanisms for the behaviour observed here. Please also note that

such improved functionalities have been achieved by employing a strongly reduced sintering temperature treatment for the symmetric cells (850 °C vs 1100 °C for non-decorated powders), which leads to a net threefold increase of the residual porosity after sintering (39 $m^2 \cdot g^{-1}$ vs 12 $m^2 \cdot g^{-1}$ respectively).

HF-Co-CGO cell measurements highlighted an even higher decrease of the ASR_s compared to the one obtained by each individual approach. The resistance reduction is as large as one order of magnitude with respect to the CGO based cell ($ASR_s^{HF-Co-CGO}$ = 13.6 Ω cm^2 at 750 °C and E_a = 1.11±0.02 eV).

These results clearly prove the relevance of the synergistic approach of etching with HF for removing impurities and of decorating with Co (II, III) oxide for enhancing the quality of the attachment to the electrolyte as the sintering between the particles themselves.
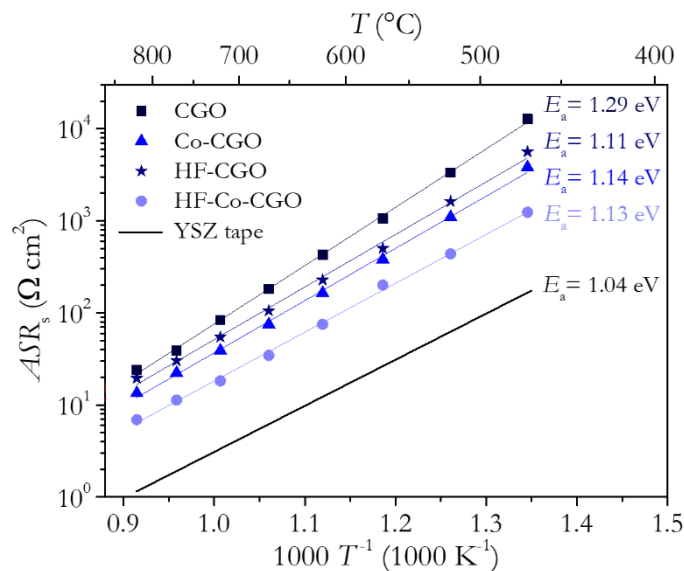

Figure 4.23: Arrhenius plots of area-specific serial (ASR_s) on CGO (T_{sint} = 1100 °C), Co-CGO (T_{sint} = 850 °C), HF-CGO (T_{sint} = 1100 °C) and HF-Co-CGO (T_{sint} = 850 °C) –based symmetric cells.

Advanced strategies for Solid Oxide Electrolysis Cells

Regarding the polarization resistance (Figure 4.24), taking as a reference the CGO-based cell, which featured $ASR_{pol}^{CGO} = 1.2 \cdot 10^3$ Ω cm^2 at 750 ºC and $E_a = 1.49 \pm 0.02$ eV, a very strong decrease of both the specific resistance ($ASR_{pol}^{HF\text{-}CGO} 1.3 \cdot 10^2$ Ω cm^2 at 750 °C) and the activation energy ($E_a = 1.32 \pm 0.02$ eV) due to the HF treatment was observed. This performance enhancement of the HF-CGO based cell is in great agreement with the TPR results previously shown (Figure 4.9): here, ASR_{pol} is mainly ascribed to the reaction at the gold/ceria/air, which is expected to be blocked by the presence of silica, which is a catalytic inhibitor. Both findings suggest an evolution of the active sites with the HF exposure probably due to the stabilization of surface oxygen vacancies via the generation of stable Ce^{3+} species.

Regarding Co oxide decoration the effect on the ASR_{pol} is marginal. In the case of HF and Co oxide decoration combined, the polarization resistance was reduced of more than one order of magnitude with respect to the CGO based cell ($ASR_{pol}^{HF\text{-}Co\text{-}CGO} = 2.2 \cdot 10^2$ Ω·cm^2 at 750 °C and E_a of 1.23 ± 0.01 eV).

The intrinsic properties of the acceptor-doped ceria under the experimental conditions (oxidizing atmosphere) of pure ionic conductor explain the high polarization resistance values measured reported in Figure 4.24. Moreover, in such a symmetric cell configuration the CGO electrodes are not infiltrated by any perovskite catalyst and a sluggish oxygen reaction kinetics is the consequence. Even taking into account the TPBs between mesoporous CGO (ionic conductor)/Au current collectors (electronic conductor)/air, a very poor activity is expected because of the strong oxygen binding energy of Au.[58] None of the potential reaction sites (ceria surface and TPBs) is expected to be highly active, and this explains the high polarization impedance of the test cells.

One can notice that the hydrofluoric acid etching had played the main role for the polarization resistance reduction. HF lowered ASR_{pol} of one order of magnitude also decreasing the activation energy. In any case Co oxide decoration had the merit of maintaining the good performances achieved by the HF etching despite the lower sintering temperature, which is crucial for the fabrication process of the mesoporous CGO scaffold. From this last consideration, the HF-Co-CGO scaffold is expected to present a better performance as functional layer of an SOC during operation. This because the achieved improvement on the intrinsic properties of the material, but also for the good gas diffusivity which is ensured by the higher final porosity of the backbone.
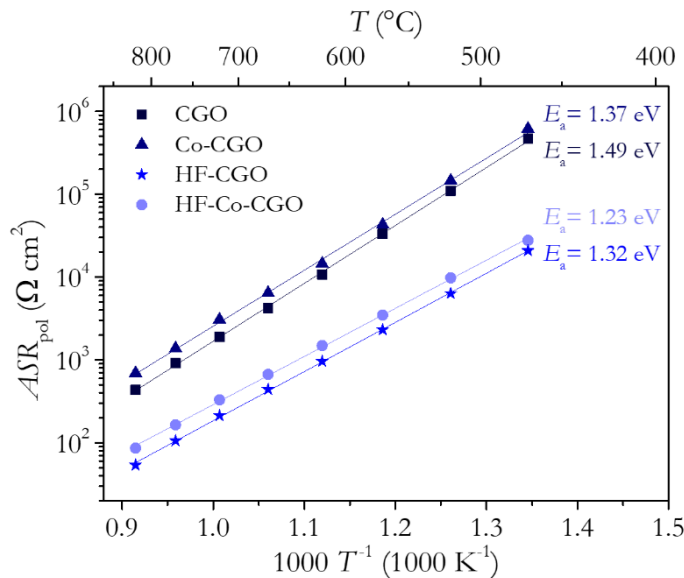
Figure 4.24: Arrhenius plots of area-specific polarization (ASR_{pol}) on CGO (T_{sint} = 1100 °C), Co-CGO (T_{sint} = 850 °C), HF-CGO (T_{sint} = 1100 °C) and HF-Co-CGO (T_{sint} = 850 °C) –based symmetric cells.

The results of the fittings, using the *model (*4.2 (Figure 4.22a and Figure 4.22b) of the Nyquist arcs obtained for the symmetric mesoporous CGO/YSZ cells are reported in Figure 4.25 and Figure 4.26. The two contributions are characterized by similar capacitances (10^{-7}-10^{-6} F cm^{-2},

184

Figure 4.25a and Figure 4.25b) and activation energies (1-1.5 eV, Figure 4.26c and Figure 4.26b) and should therefore be attributed to very similar phenomena arguably related to solid-gas reactions, i.e. the Au/ceria/gas TPB reaction and the oxygen exchange at the ceria surface.[59] Alternatively, a slight difference in the microstructural parameters (i.e. thickness and density) of the two electrodes may lead to the detected slight difference in the characteristic time response for each arc.
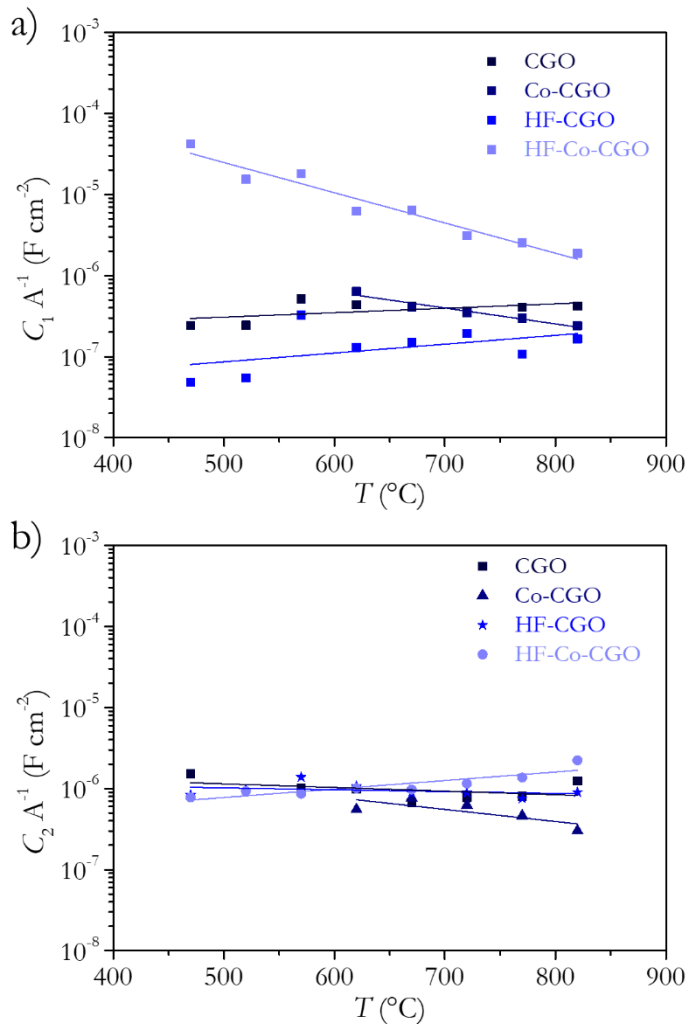
Figure 4.25: Resulting EIS fitting parameters for symmetric CGO/YSZ cells as a function of temperature. True capacitance values of the high (a) and low (b) frequency arcs.
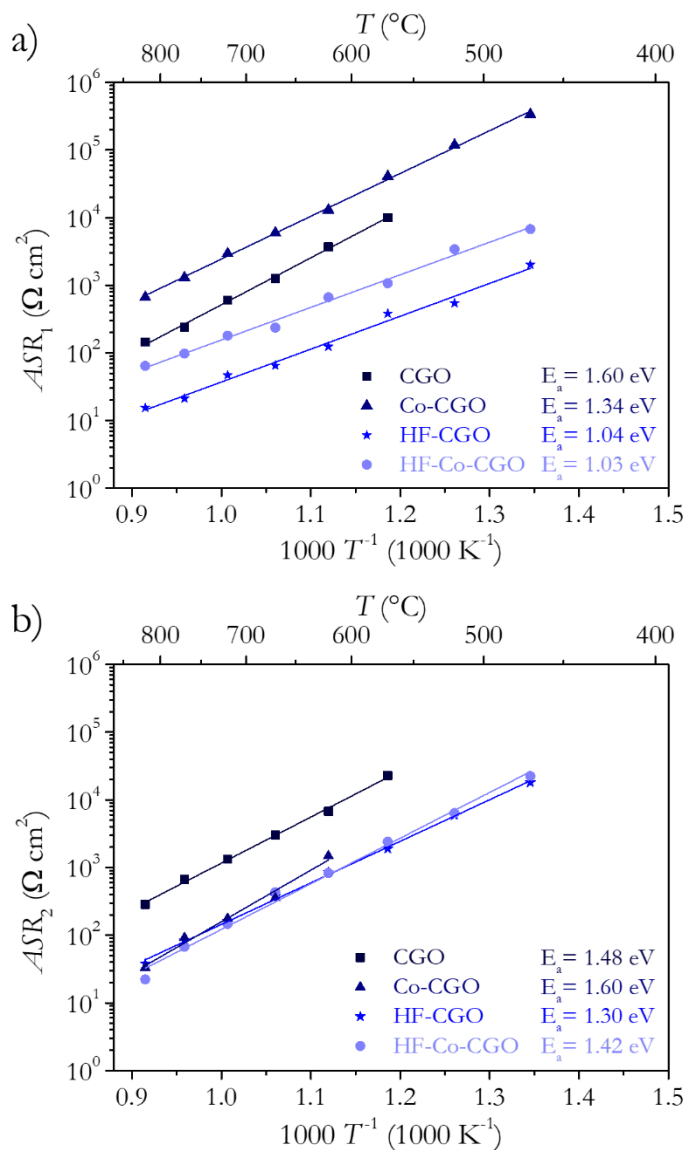
Figure 4.26: Resulting EIS fitting parameters for symmetric CGO/YSZ cells as a function of temperature. Polarization resistance values of the high (a) and low (b) frequency arcs.

In general, both serial and polarization ASR were reduced by one order of magnitude with respect to the CGO based cell. This study proved the effectiveness of HF for the removal of siliceous impurities and the suppression of the Gd-rich cluster formations. HF etching on mesoporous CGO effectively increased the ionic conductivity of the material. Co oxide

Advanced strategies for Solid Oxide Electrolysis Cells

decoration combined with silica removal demonstrated to improve the attachment of the material for a considerably lower temperature (850 °C).

4.6   Conclusion

CGO mesoporous materials has been successfully adapted as a scaffold for high performance oxygen electrode in SOC application. A twofold strategy was developed focused on the removal of SiO_2 contaminations coming from the synthesis process and on the lowering of the sintering temperature. ICP-MS measurements highlight that a contamination ≈0.9 %wt. of SiO_2 was still present within the powders after the standard NaOH alkaline etching. The additional developed etching process using hydrofluoric acid (2.5 %v/v) has been demonstrated effective to reduce the amount of silica to ≈0.2 %wt. Complementary structural analysis such as XRD, SAXS and BET demonstrate that after 5 min of HF etching the mesoporous powder maintains the ordered structure of the KIT-6 template. TPR analysis points also out that the activity of the powders increases as effect of the Si removal.

TEM clustering analysis highlights the beneficial effect of the HF etching at the GB level by removal of dopant segregates. The mesoporous powders treated by the hydrofluoric acid solution showed a uniform Gd/Ce ratio between the grain interior and the grain boundaries.

The improvement of the sintering process of the powders was achieved by the utilization of Co oxide as sintering aid. BET analysis demonstrates that at 850 °C the introduction of 1 %mol of Co oxide can effectively promote the interparticle sintering.

The electrochemical characterization clearly confirms the beneficial effects of the treatments developed in the present work. The etching by HF with the Gd cluster removal improved the ionic conductivity of the material,

with the ASR_s at 750°C which passes from 54 Ω cm^2 to 38 Ω cm^2 for CGO and HF-CGO symmetric cells (measured in an out-of-plane configuration), respectively. The reduction of silica contaminant has a positive effect on the polarization resistance, which passes from $1.2 \cdot 10^3$ Ω cm^2 (CGO) to $1.3 \cdot 10^2$ Ω cm^2 (HF-CGO), i.e. reduces one order of magnitude

The combined effect of the HF etching with the improved electrode-electrolyte interface, induced by Co_3O_4-decoration, decreased even more serial ASR achieving 13.6 Ω cm^2 at 750 °C for the HF-Co-CGO cell. Regarding the polarization resistance, the HF-Co-CGO cell maintains the good performance granted by the HF effect, but for a sintering temperature much lower (1100 °C vs. 850 °C) thanks to the Co oxide decoration. The scaffold maintained a higher relative porosity and this means larger surface area available for reactions.

The considered set of results in the present study demonstrates the effectiveness of the new fabrication route of CGO mesoporous scaffold for SOC application. The developed treatments which combined HF etching and Co oxide decoration had improved the properties of the material in terms of both ionic conductivity and catalytic activity. Furthermore, the sintering temperature of the materials was lowered of 250 °C, which supposes a great advantage for the fabrication process of the cell and the scalability of the process.

Advanced strategies for Solid Oxide Electrolysis Cells

4.7 Bibliography

1   L. Almar, T. Andreu, A. Morata and A. Tarancón, 2011, pp. 1647–1654.
2   L. Almar, A. Morata, M. Torrell, M. Gong, T. Andreu, M. Liu and A. Tarancón, *Electrochim. Acta*, 2017, **235**, 646–653.
3   S. C. Laha and R. Ryoo, *Chem. Commun.*, 2003, 2138–2139.
4   L. Almar, A. Morata, M. Torrell, M. Gong, M. Liu, T. Andreu and A. Tarancón, *J. Mater. Chem. A*, 2016, **4**, 7650–7657.
5   H. Yang and D. Zhao, *J. Mater. Chem.*, 2005, **15**, 1217–1231.
6   M. Mamak, N. Coombs and G. Ozin, *J. Am. Chem. Soc.*, 2000, **122**, 8932–8939.
7   M. Mamak, N. Coombs and G. A. Ozin, *Chem. Mater.*, 2001, **13**, 3564–3570.
8   J. M. Serra, S. Uhlenbruck, W. A. Meulenberg, H. P. Buchkremer and D. Stöver, *Top. Catal.*, 2006, **40**, 123–131.
9   L. Almar, T. Andreu, A. Morata, M. Torrell, L. Yedra, S. Estradé, F. Peiró and A. Tarancón, *J. Mater. Chem. A*, 2014, **2**, 3134–3141.
10   C. Sun, H. Li and L. Chen, *Energy Environ. Sci.*, 2012, **5**, 8475–8505.
11   C. Sun, J. Sun, G. Xiao, H. Zhang, X. Qiu, H. Li and L. Chen, *J. Phys. Chem. B*, 2006, **110**, 13445–13452.
12   C. Sun, H. Li and L. Chen, *J. Phys. Chem. Solids*, 2007, **68**, 1785–1790.
13   C. Sun, Z. Xie, C. Xia, H. Li and L. Chen, *Electrochem. commun.*, 2006, **8**, 833–838.
14   M. Torrell, L. Almar, A. Morata and A. Tarancón, *Faraday Discuss.*, 2015, **182**, 423–435.
15   L. Ge, Q. Ni, G. Cai, T. Sang and L. Guo, *J. Power Sources*, 2016, **324**, 582–588.
16   P.-S. Cho, Y. H. Cho, S.-Y. Park, S. B. Lee, D.-Y. Kim, H.-M. Park, G. Auchterlonie, J. Drennan and J.-H. Lee, *J. Electrochem. Soc.*, 2009, **156**, B339.
17   Y. H. Cho, P. S. Cho, G. Auchterlonie, D. K. Kim, J. H. Lee, D. Y. Kim, H. M. Park and J. Drennan, *Acta Mater.*, 2007, **55**, 4807–4815.
18   L. Almar Liante, University of Barcelona, 2014.
19   H. Yen, Y. Seo, S. Kaliaguine and F. Kleitz, *Angew. Chemie*, 2012, **124**, 12198–12201.
20   M. Torrell, S. García-Rodríguez, A. Morata, G. Penelas and A. Tarancón, *Faraday Discuss.*, 2015, **182**, 241–255.
21   V. Duraisamy, S. Palanivel, R. Thangamuthu and S. M. S. Kumar, *ChemistrySelect*, 2018, **3**, 11864–11874.
22   S. A. Ghom, C. Zamani, S. Nazarpour, T. Andreu and J. R. Morante, *Sensors Actuators, B Chem.*, 2009, **140**, 216–221.
23   W. Yue and W. Zhou, *Chem. Mater.*, 2007, **19**, 2359–2363.
24   J. W. Kury, Z. Z. Hugus and W. M. Latimer, *J. Phys. Chem.*, 1957, **61**, 1021–1021.
25   J. Bae, *Solid State Ionics*, 1998, **106**, 247–253.
26   J. S. Judge, *J. Electrochem. Soc.*, 1971, **118**, 1772.
27   P. A. M. van der Heide, M. J. Baan Hofman and H. J. Ronde, *J. Vac. Sci. Technol. A Vacuum, Surfaces, Film.*, 1989, **7**, 1719–1723.

28   J. L. M. Rupp, U. P. Muecke, P. C. Nalam and L. J. Gauckler, *J. Power Sources*, 2010, **195**, 2669–2676.

29   D. J. Monk, D. S. Soane and R. T. Howe, *Thin Solid Films*, 1993, **232**, 1–12.

30   Y. Doi, A. Takai, Y. Sakamoto, O. Terasaki, Y. Yamauchi and K. Kuroda, *Chem. Commun.*, 2010, **46**, 6365–6367.

31   T. Grewe, X. Deng and H. Tüysüz, *Chem. - A Eur. J.*, 2014, **20**, 7692–7697.

32   H. Liu, K. Tao, P. Zhang, W. Xu and S. Zhou, *New J. Chem.*, 2015, **39**, 7971–7978.

33   F. Kleitz, S. Hei Choi and R. Ryoo, *Chem. Commun.*, 2003, 2136.

34   L. Almar, B. Colldeforns, L. Yedra, S. Estradé, F. Peiró, A. Morata, T. Andreu and A. Tarancón, *J. Mater. Chem. A*, 2013, **1**, 4531–4538.

35   E. Hernández, F. Baiutti, A. Morata, M. Torrell and A. Tarancón, *J. Mater. Chem. A*, 2018, **6**, 9699–9707.

36   S. Liang, E. Broitman, Y. Wang, A. Cao and G. Veser, *J. Mater. Sci.*, 2011, **46**, 2928–2937.

37   M. Jin, J.-N. Park, J. K. Shon, Z. Li, M. Y. Yoon, H. J. Na, Y.-K. Park and J. M. Kim, *Res. Chem. Intermed.*, 2011, **37**, 1181–1192.

38   D. R. Ou, F. Ye and T. Mori, *Phys. Chem. Chem. Phys.*, 2011, **13**, 9554–9560.

39   Z. P. Li, T. Mori, G. J. Auchterlonie, J. Zou and J. Drennan, *Appl. Phys. Lett.*, 2011, **98**, 1–4.

40   F. Ye, T. Mori, D. R. Ou, J. Zou, G. Auchterlonie and J. Drennan, *Solid State Ionics*, 2008, **179**, 827–831.

41   P. Torruella, M. Estrader, A. López-Ortega, M. D. Baró, M. Varela, F. Peiró and S. Estradé, *Ultramicroscopy*, 2018, **185**, 42–48.

42   C. Nicollet, J. Waxin, T. Dupeyron, A. Flura, J. M. Heintz, J. P. Ouweltjes, P. Piccardo, A. Rougier, J. C. Grenier and J. M. Bassat, *J. Power Sources*, 2017, **372**, 157–165.

43   D. Pérez-Coll, P. Núñez, J. C. C. Abrantes, D. P. Fagg, V. V. Kharton and J. R. Frade, *Solid State Ionics*, 2005, **176**, 2799–2805.

44   R. I. Tomov, T. B. Mitchel-Williams, R. Maher, G. Kerherve, L. Cohen, D. J. Payne, R. V. Kumar and B. A. Glowacki, *J. Mater. Chem. A*, 2018, **6**, 5071–5081.

45   E. Jud, C. B. Huwiler and L. J. Gauckler, *J. Am. Ceram. Soc.*, 2005, **88**, 3013–3019.

46   E. Jud and L. J. Gauckler, *J. Electroceramics*, 2005, **15**, 159–166.

47   D. Pérez Coll, Universidad de La Laguna, 2005.

48   C. Kleinlogel and L. J. Gauckler, *Adv. Mater.*, 2001, **13**, 1081–1085.

49   X. Zhang, C. Decès-Petit, S. Yick, M. Robertson, O. Kesler, R. Maric and D. Ghosh, *J. Power Sources*, 2006, **162**, 480–485.

50   R. M. German and B. H. Rabin, *Powder Metall.*, 1985, **28**, 7–12.

51   E. Jud and L. J. Gauckler, *J. Electroceramics*, 2005, **14**, 247–253.

52   J. Koettgen, S. Grieshammer, P. Hein, B. O. H. Grope, M. Nakayama and M. Martin, *Phys. Chem. Chem. Phys.*, 2018, **20**, 14291–14321.

53   M. Mogensen, N. M. Sammes and G. A. Tompsett, 2000, **129**, 63–94.

54   K. Haga, S. Adachi, Y. Shiratori, K. Itoh and K. Sasaki, *Solid State Ionics*, 2008, **179**, 1427–1431.

55   K. R. Reddy and K. Karan, *J. Electroceramics*, 2005, **15**, 45–56.

56   X.-D. Zhou, W. Huebner, I. Kosacki and H. U. Anderson, *J. Am. Ceram. Soc.*, 2002, **85**, 1757–1762.

57   M. C. Göbel, G. Gregori, X. Guo and J. Maier, *Phys. Chem. Chem. Phys.*, 2010, **12**, 14351–14361.

58   Z. W. Seh, J. Kibsgaard, C. F. Dickens, I. Chorkendorff, J. K. Nørskov and T. F. Jaramillo, *Science (80-.).*, 2017, **355**, 1–12.

59   A. Flura, C. Nicollet, S. Fourcade, V. Vibhu, A. Rougier, J. M. Bassat and J. C. Grenier, *Electrochim. Acta*, 2015, **174**, 1030–1040.

Chapter V

Performance and durability of large area SOCs using improved mesoporous CGO

5.1 Chapter overview

The aim of this chapter is to present the results of the electrochemical characterisation of functionalized SOCs.

i. Electrochemical and microstructural characterization of a button cell (diameter ≈2 cm) with optimized mesoporous oxygen electrode is presented (section 5.2).

   a. The mesoporous used includes the improvements and optimizations already described in Chapter IV (HF etching, Co oxide decoration and optimized sintering temperatures).

   b. A commercial anode supported half-cell with composition NiO-YSZ/YSZ was utilized for the fabrication

ii. Results on the scale-up of mesoporous CGO oxygen electrode for large area cell (≈25 cm^2) are presented (section 5.3).

   a. *1st generation* mesoporous CGO (no HF cleaning and no Co oxide decoration) was utilized for the fabrication of the oxygen electrode. This facilitated the comparison with previous work of the group.[1,2]

   b. A commercial half-cell with composition YSZ/YSZ/ CGO$_{BL}$ was used to fabricate the cell.

Part of the results presented on large-area cell characterization are based on previous electrochemical measurements carried out by other researchers from IREC (E. Hernández, PhD thesis) in collaboration with the author.[3]

Button cell of section 5.2 and large area cells of section 5.3 were characterized structurally and electrochemically in SOFC, SOEC and COSOEC configuration, followed by a durability test and post-mortem characterization.

5.2   Studies on optimised full SOC button cells

In order to demonstrate the improvement promoted by the use of the optimized materials on the performance of SOC devices, a mesoporous oxygen electrode was deposited on a commercial anode supported button half-cell (NiO-YSZ/YSZ, d ≈2 cm – HF-Co-CGO cell in the rest of the chapter) produced by SOLIDpower SpA. The mesoporous materials were developed through the work discussed in Chapter IV.

Figure 5.1 shows representative SEM micrographs in which the structure of the cell cross-section is presented. One can notice in Figure 5.1a the NiO-YSZ fuel electrode (≈300 μm thick), the YSZ electrolyte (≈7 μm) and the CGO barrier layer, the latter deposited by PLD (≈1 μm). The oxygen electrode is formed by the HF-Co-CGO scaffold infiltrated by LSCF (≈10–15 μm). An additional LSCF layer (≈20–25 μm) was deposited on top of the functional layer, to improve the current collection of the electrode.

On Figure 5.1b a micrograph at high magnification of the electrolyte-full electrode interface is presented. In the picture, the good homogeneity of the oxygen electrode and its good attachment to the PLD barrier layer is showed. No signs of delamination were present after sintering, neither macro-voids in the microstructure of the electrode. Furthermore, the good adhesion of the PLD barrier layer to the YSZ electrolyte and its good density after sintering was observed.
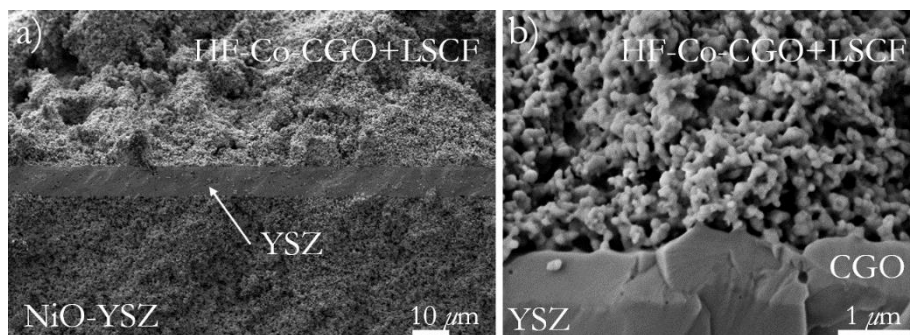
Advanced strategies for Solid Oxide Electrolysis Cells

Figure 5.1: SEM micrograph of the button cell with HF-Co-CGO+LSCF oxygen electrode (a) with highlighted, the YSZ electrolyte and the NiO-YSZ fuel electrode. Micrograph at higher magnification (b) where the CGO barrier layer deposited by PLD and the microstructure of the oxygen electrode are shown. In particular, the latter presents an electrode, with no presence of macro-voids and with a good attachment to the barrier layer.

5.2.1 Electrochemical characterization of the optimised SOC cells

The scheme of Figure 5.2 highlights the differences among the three cells discussed here. All the three of them were anode supported cells with same fuel electrode and electrolyte made by tape casting. Figure 5.2a and Figure 5.2b present two cell with CGO barrier layer made by PLD and mesoporous CGO infiltrated by LSCF perovskites as functional electrode. Lastly a layer of commercial LSCF was deposited on top to improve the current collection. The mesoporous and the commercial LSCF powders were deposited by automatic airbrushing, while the infiltration was made by hand. the HF-Co-CGO mesoporous (Figure 5.2a) is shown in orange with blue edges. The functional layer of the cell showed in Figure 5.2b is made of *1ˢᵗ generation* mesoporous CGO, i.e. the scaffold was etched only by NaOH to remove the silica template used for the synthesis and without Co oxide decoration. The mesoporous is indicated in orange with dark orange edges. The last cell of Figure 5.2c is a state-of-the-art fuel electrode-based cell with composition Ni-YSZ/YSZ/CGO/LSCF prepared using standard techniques (i.e. tape casting for the fuel electrode and the electrolyte and

screen printing for barrier layer and oxygen electrode) and with commercial powders.
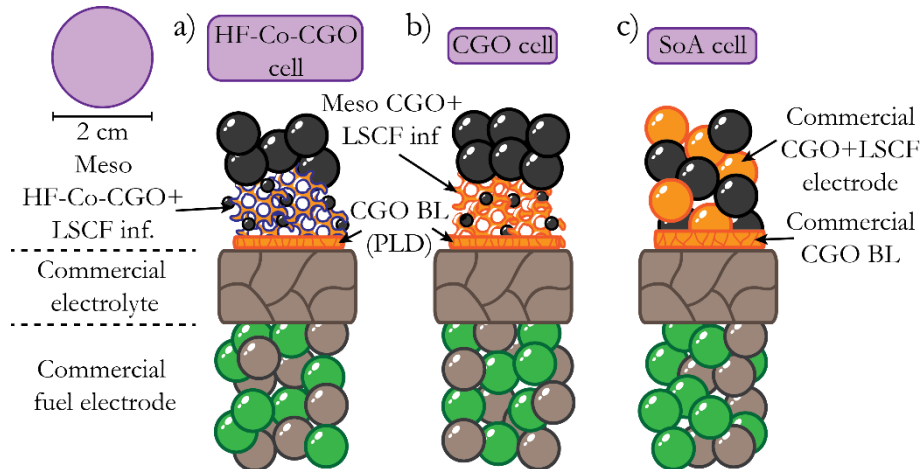

Figure 5.2: Structure of the three different cells measured. One can notice that the both the HF-Co-CGO (a) and the CGO (b) cells present a functional layer formed by a mesoporous scaffold infiltrated by LSCF perovskite. The SoA cell shows a commercial oxygen electrode made by screen printing (c).

Galvanostatic polarization I-V curve showed the performances of the studied cells in both SOFC and COSOEC mode at 750 °C compared with the CGO and the SoA button cells. Figure 5.3 shows the characterization in SOFC mode. The HF-Co-CGO cell presented a maximum power density of 1.35 W cm^{-2} at 0.7 V. This represents a strongly enhanced performance compared to the CGO-based (0.75 W cm^{-2} at 0.7 V) and the SoA (0.57 W cm^{-2} at 0.7 V) cells. Note that the HF-Co-CGO cell did not reach the decreasing slope of the power density curve in the plot.

The measured performances represent a remarkable result, among the best ever reported in literature for LSCF-based cells operating in fuel cell and co-electrolysis mode at 750 ºC.[4–9] Regarding operation in SOFC mode, a recent and comprehensive review of LSCF cells from Jiang[10] places our performance above optimized cells considering e.g. the reference work of Tietz *et al.*, which showed a power density at 0.7 V of 1.2 W cm^{-2} at 800 °C,[11]

or more advanced cells such as the ones recently published by Hong *et al.*[12] or He *et al.*[13] based on decorated LSCF-based oxygen electrodes, showing 0.8 W cm⁻² and 1.2 W cm⁻², respectively, at the same voltage and temperature.
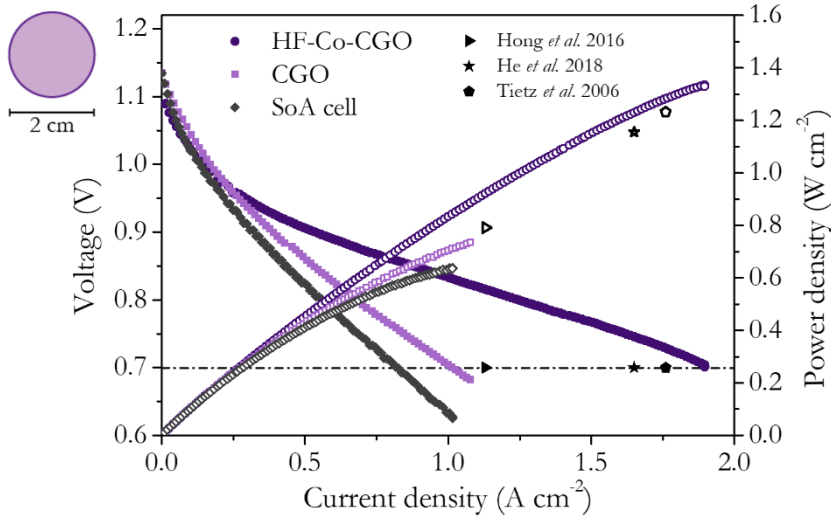

Figure 5.3: Comparison between SOFC-mode polarization curves at 750 °C for a series of fuel electrode-supported cell having different oxygen functional layers: infiltrated HF-Co-CGO and infiltrated CGO were employed for the fabrication of the oxygen electrode functional layer. The two mesoporous cells are compared with a SoA cell shown in the plot. Additionally current density and power values from literature are indicated in the figure.[11–13]

Under 65% H_2O + 25% CO_2 + 10% H_2 at the fuel electrode, excellent results were also obtained in COSOEC mode, as shown in Figure 5.4. The HF-Co-CGO cell reached a current density of 1.30 A cm⁻² at the thermoneutral voltage (1.3 V) (40% and 70% of enhancement compared to CGO and SoA cells, respectively). The performance obtained by the HF-Co-CGO cell under COSOEC mode is remarkably above other works for fuel electrode supported SOECs such as the one from Sun *et al.*,[14] which presented a current density of 0.68 A cm⁻² at 1.25 V at 750 °C. Rao *et al.*,[15] reported injected current densities of 1.01 A cm⁻² at 1.3 V and 750 °C for optimized Ni-YSZ/YSZ/CGO/LSCF-CGO cells. Rinaldi *et al.*,[16] measured 0.89 A cm⁻² of injected current density for similar cells at the same temperature and voltage.

Please note the relevance of such results in COSOEC with respect to the state of the art in the field. Moreover, this reported unprecedented results were obtained under relevant operation conditions for real applications in Power-to-Gas scenarios (750 °C with a flow of 22.22 Nml min^{-1} cm^{-2} and a gas composition of 65% H_2O, 25% CO_2 and 10% H_2).[17]
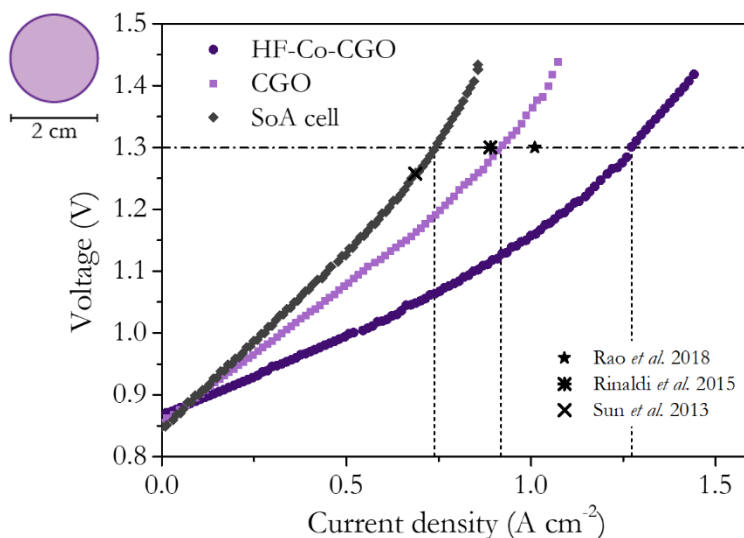
Figure 5.4: Polarization curves for HF-Co-CGO, CGO and SoA cells at 750 °C in COSOEC conditions (flow density of 22.22 Nml min^{-1} cm^{-2} and gas composition of 65% H_2O, 25% CO_2 and 10% H_2). Current density values from literature are included as special symbols for comparison.[14–16]

5.2.2 Durability test on the optimised SOC cells

In order to evaluate the stability of the HF-Co-CGO cell in operation conditions, a durability test of 1000 h in co-electrolysis was conducted and the results are reported in Figure 5.5. A degradation rate of 105 mV kh^{-1} has been obtained. Note that the first 300 h are normally considered as the typical stabilization time of the cell and are not considered in the calculations. Similar results are found on state-of-the-art cells reported in literature working under similar conditions.[7,18,19] Graves *et al.* presented a degradation rate of ≈140 mV kh^{-1} applying 0.5 A cm^2 at 850 °C.[7] Tietz *et al.* showed a degradation

Advanced strategies for Solid Oxide Electrolysis Cells

rate of $\approx$33 mV kh^{-1} at 778 °C with 1 A cm^2.[20] A large area cell with from Rao *et al.* presents 122 mV kh^{-1} applying 0.75 A cm^2 at 750 °C.[15]
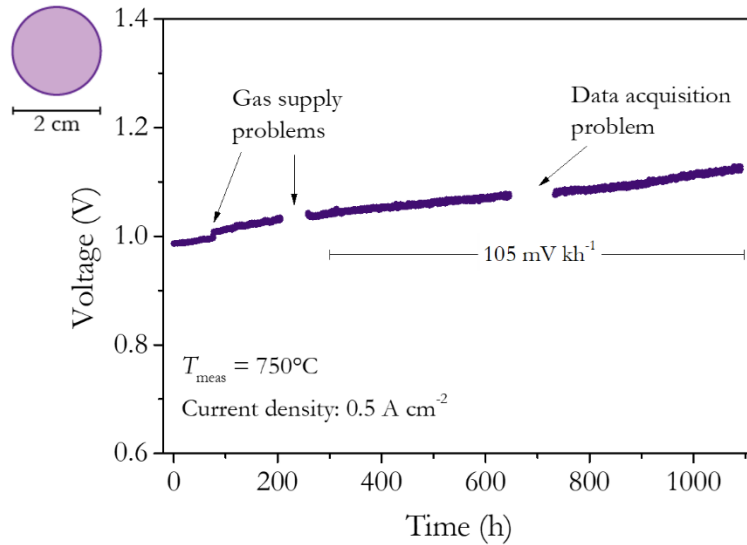
Figure 5.5: Long term durability test of the HF-Co-CGO cell, in COSOEC conditions of 1100 h presenting a degradation rate of 105 mV kh^{-1} for the last 800 h.

Electrochemical characterization by impedance spectroscopy is reported in Figure 5.6. EIS measurements were conducted at the OCV before (Figure 5.6a) and after (Figure 5.6b) the durability test. They were fitted by Zview program with an equivalent circuit shown as inset of both Figure 5.6a and Figure 5.6b. The circuit, selected as the simplest circuit able to fit the spectra, is composed by a L inductance, representing the contribution from the set-up, a R_s serial resistance, involving all the ohmic contributions (ion conduction through the electrolyte and current collection)[9,21] and two ZARC elements ($R_{pi}Q_i$), The two elements represent all the polarization contribution coming from the electrodes and from the electrodes/electrolyte interfaces. The true capacitance can be calculated as $C_p = Q_p^{(1/n)} \cdot R_{p1}^{(1-n)/n}$.

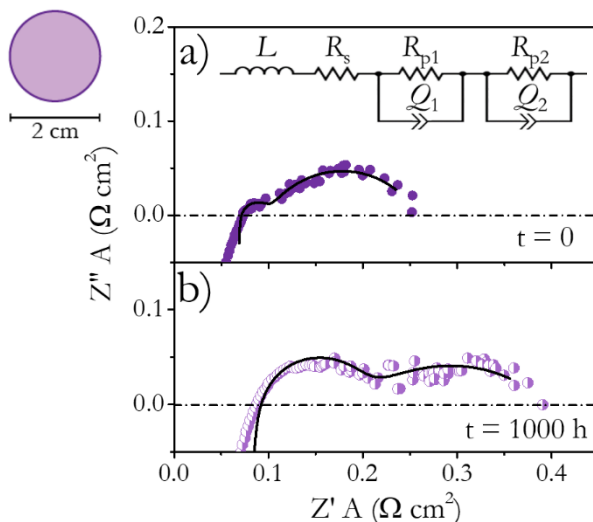**Figure 5.6:** EIS measurements were conducted at OCV before the durability process (a) and after 1000 h of testing (b). The fitting of the plots was made by the utilization of an equivalent circuit with 2 ZARC elements presented as inset of the figures. The two arcs are called $(R_{p1}Q_1)$ and $(R_{p2}Q_2)$ to indicate the button cell.

Results of the fitting are reported on Table 5.1 and present two different contribution with characteristic frequencies of ≈ 1000 Hz, defined as $(R_{p1}Q_1)$ and a second one at ≈ 1 Hz defined as $(R_{p2}Q_2)$. The higher frequency arc presents a capacitance value which passes from $5.9 \ 10^{-3}$ F cm^{-2} to $5.3 \ 10^{-4}$ F cm^{-2} during degradation. The characteristic frequencies and the capacitance values are typical for charge transfer phenomena happening at the composite electrodes.[9,22] On the other hand, the low frequency arc presents a capacitance which remains in both cases around 10^{-1} F cm^{-2}. Considering the characteristic frequency (≈ 1 Hz), the low frequency arc could be assigned to gas diffusion phenomena or gas conversion, processes usually dominated by the fuel electrode which is the thicker layer.[9,22,23]

One can notice that the high frequency arc $(R_{p1}Q_1)$ is the one that played the main role in the degradation of the HF-Co-CGO cell during the durability test. In Table 5.1 an increase of the R_{p1} resistance of almost one order of magnitude is highlighted, passing from $3.1 \ 10^{-2}$ Ω cm^2 to $1.1 \ 10^{-1}$ Ω

Advanced strategies for Solid Oxide Electrolysis Cells

cm². Considering the ASR_{tot}, the high frequency arc passes from the 12 % of the total resistance, to the 28 % after 1000 h of durability test.

Table 5.1: Results of the fitting on the impedance measurements of Figure 5.6. Here are reported the values of the inductance L, the serial resistance R_s, the polarization resistance R_{pi}, the true capacitances Q_i and the characteristic frequencies associated to the ZARC elements.

	t = 0	t = 1000 h
L (H)	1.1 10^{-7}	1.7 10^{-7}
R_s (Ω cm²)	6.8 10^{-2}	8.1 10^{-2}
R_{p1} (Ω cm²)	3.1 10^{-2}	1.1 10^{-1}
C_{p1} (F cm^{-2})	5.9 10^{-3}	5.3 10^{-4}
f_1 (Hz)	8.9 10^{2}	2.6 10^{3}
R_{p2} (Ω cm²)	1.6 10^{-1}	2.0 10^{-1}
C_{p2} (F cm^{-2})	5.3 10^{-1}	1.6 10^{-1}
f_2 (Hz)	1.9	4.9
ASR_{pol} (Ω cm²)	0.19	0.32
ASR_{tot} (Ω cm²)	0.26	0.40

The evolution of the cell during degradation can be attributed mainly to the high frequency arc. This arc seems related to charge transfer phenomena at the composite electrodes, therefore a certain microstructural evolution is expected from SEM characterization. Deactivation of one or both the electrodes could be the cause of such an evolution.

5.2.3 Post-test microstructural characterization

In order to gain further insights on the causes of cell evolution during operation, post-test SEM analysis on cell cross sections have been performed and are reported in Figure 5.7. Here, both the general structure of oxygen electrode (Figure 5.7a) and details of at high magnification (Figure 5.7b-d) are shown. One can appreciate the good adhesion between barrier layer and oxygen electrode. Furthermore, the oxygen electrode shows a quite homogeneous pore distribution. Remarkably, no apparent microstructural

evolution of the oxygen electrode can be appreciated (Figure 5.7c), i.e. the mesoporous backbone retains an excellent stability. This is due to the reliability of the mesoporous CGO synthetized following the route parameters developed and optimized on the present thesis. In particular, the Co oxide decoration improved the attachment of the scaffold, to the barrier layer and between the particles themselves despite the low sintering temperature (850 °C). The low firing temperature granted the stability of the mesoporous architecture as it is observed in Figure 5.7c.
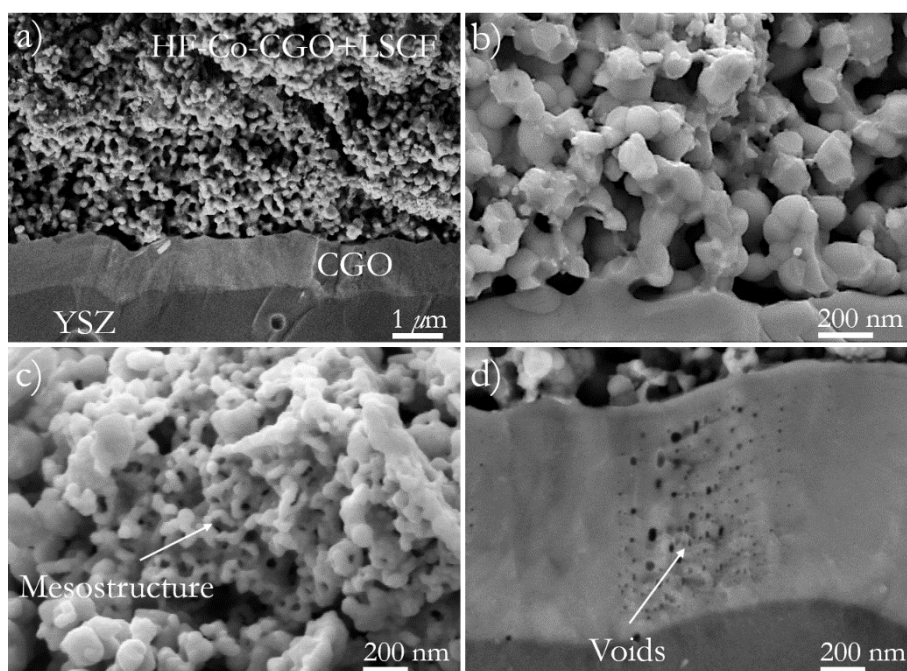
Figure 5.7: SEM micrograph showing the oxygen electrode (a). Picture at high magnification representing the interface oxygen electrode/barrier layer (b). Mesoporous scaffold after the durability test of 1000 h (c) and some nano sized pores that appeared on the barrier layer during the durability test of 1000 h (d).

The presence of nano sized pores in the barrier layer on the oxygen side (Figure 5.7d) was observed and becomes object of study. Such pores are one of the SoA reported causes for the SOEC degradation.[20,24] Tietz *et al.* describes similar voids in SOEC after a durability test of 9000 h and identifies

Advanced strategies for Solid Oxide Electrolysis Cells

them as Kirkendall voids.[20] In his paper, the void formation was attributed to the large pO_2 gradient across the electrolyte, which determined a strong driving force for mass transport.[24] From his description such porosities were likely formed at the interface electrolyte/oxygen electrode, being oriented with the grain boundary or in the direction of the potential applied. Virkar *et al.* described the formation of similar defects at the interface electrolyte/oxygen electrode.[25] Following this interpretation, the high internal pressure, caused by the abrupt change oxygen chemical potential at the interface, generated the voids. Such defects eventually cause the delamination of the oxygen electrode and the failure of the cell. Virkar *et al.* highlight that this is an intrinsic problem in SOEC because electronic and ionic currents move in the same direction. Furthermore he suggests to insert an intermediate ion conductive layer as mitigation strategy, to tailor the electronic transport through the cell and minimize the tendency for high pressure buildup.[25] Looking at Figure 5.7d, the CGO barrier layer deposited by PLD is probably acting also with this function, preventing the delamination of the cell.

Figure 5.8 shows two SEM micrographs of the Ni-YSZ fuel electrode obtained by secondary electrons (SE) and using a SEM in-lens detector acquiring at low voltage acceleration ($\approx$1 kV). In Figure 5.8b the bright zones represent the percolating metallic Ni, while the dark ones are the ensemble of YSZ and all the non-percolating Ni particles.[26,27] One can notice the depletion of percolating areas close to the interface with the electrolyte.
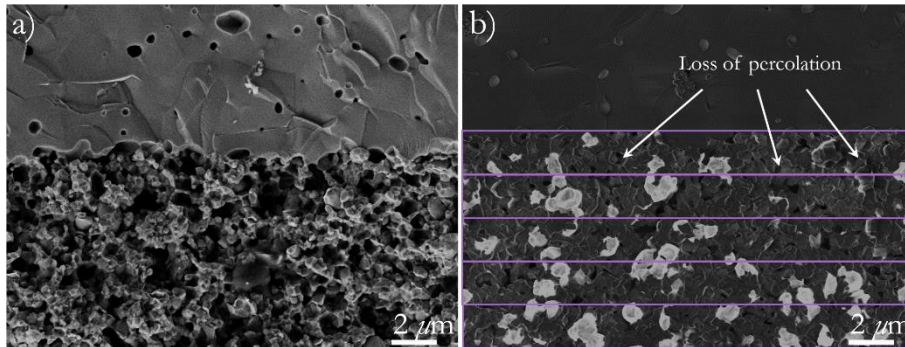
Figure 5.8: SEM micrograph of the fuel electrode after the degradation (a). Image acquired with in-lens detector at low acceleration voltage (b). In white the percolating Ni particles are shown.

These deactivation phenomena are extensively studied in literature and are mainly caused by coarsening of metallic Ni particles or by Ni evaporation from the electrode as shown in Figure 5.9.[28,29] A dedicated quantitative analysis of the percolating Ni particles is presented in greater detail in section 5.3.3 (Figure 5.22), in comparison with a reference fuel electrode before operation. Such study highlighted only a ≈6 % percolating metallic Ni close to the interface with the electrolyte. The same analysis on a fuel electrode before operation showed a percentage ≈25 %. This fact can explain the great evolution of the high frequency arc highlighted by impedance measurements, which was associated to charge transfer phenomena at the electrodes. The progressive deactivation of the fuel electrode can be therefore considered as the main cause of degradation of the cell.
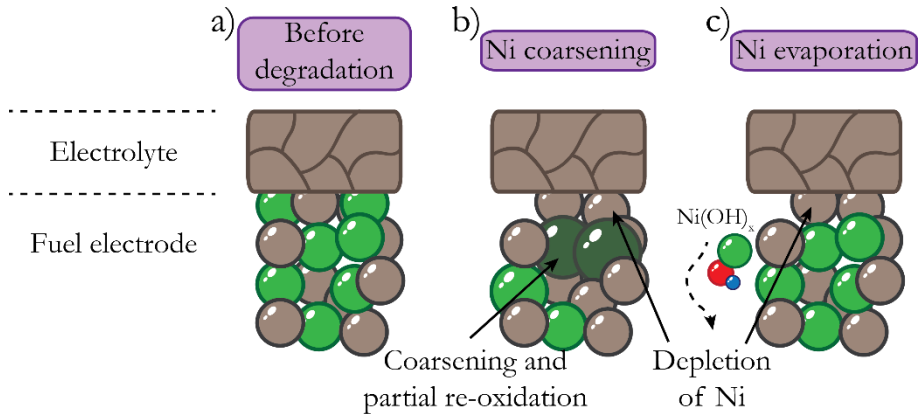
Advanced strategies for Solid Oxide Electrolysis Cells

Figure 5.9: Schematic representation of the degradation mechanism in fuel electrode. The ideal condition is the one represented in (a), in which the metallic Ni is distributed all around the electrode. The coarsening of the Ni and its reoxidation (b) cause the loss of the percolation close to the electrolyte. Same effect is obtained with the evaporation of Ni (c) from the electrode.

5.3   Studies on large area cells with mesoporous CGO

Mesoporous CGO scaffold infiltrated by LSCF was deposited on large area state-of-the-art planar half-cells of 25 cm^2 (HTCeramics). The aim of the study is to evaluate the scalability of the nanostructured electrode for its future employment in real stack devices. The commercial half cells were composed by a Ni-YSZ fuel electrode support, a Y_2O_3-ZrO_2 (YSZ) electrolyte and a CGO barrier layer (BL).[30] Figure 5.10 shows some SEM micrographs which present the microstructure of the fabricated cell. Looking at Figure 5.10a it is possible to observe the complete NiO-YSZ/YSZ/CGO$_{BL}$/CGO$_{meso}$-LSCF/LSCF cell, while Figure 5.10b and Figure 5.10c show a detail of the nanostructured oxygen electrode at different magnifications. On the pictures one can notice the porous Ni-YSZ electrode ($\approx$300 μm), the fully dense and gas tight YSZ electrolyte layer ($\approx$7 μm) and the diffusion barrier layer of ($\approx$3 μm) directly attached to the electrolyte to avoid insulating LZO phase formation.[30] The oxygen electrode, was deposited by 3-axis automated airbrushing on an area of 16 cm^2. Such

automated airbrush allowed the deposition of a uniform layer on areas of different dimensions. Figure 5.10b and Figure 5.10c show a good attachment of the CGO-LSCF nanocomposite. In addition, a highly porous microstructure that ensures the adequate gas diffusion is observed, while the mesoporous nature of the CGO scaffold is hidden by the infiltrated LSCF (Figure 5.10d).
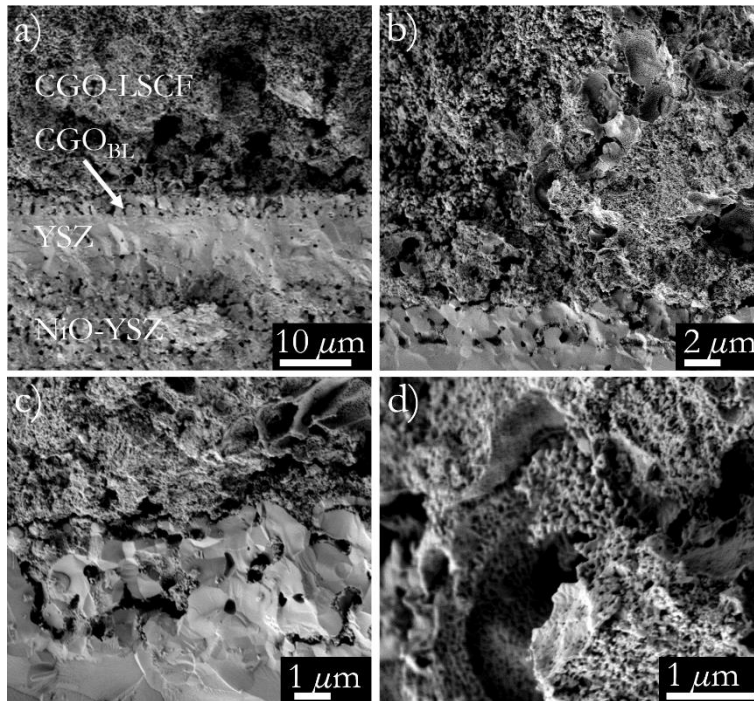
Figure 5.10: Representative SEM micrograph of the cell (a), showing the cross section with the NiO-YSZ fuel electrode, the YSZ electrolyte and the CGO-LSCF oxygen electrode. Micrographs (b) representing the oxygen electrode and a high magnification micrograph of the CGO barrier layer (c). Lastly, a high magnification micrograph (d) showing the small residual porosity after sintering and infiltration of the mesoporous CGO.

5.3.1 Electrochemical characterization of large area cell

Large area cells (≈ 25 cm^2 with active area ≈ 16 cm^2) were electrochemically characterized in SOEC and COSOEC mode, with a final

durability test in COSOEC of 600 h. The cells were placed between two alumina plates with channels to ensure a good gas distribution. A complete description of the setup could be found in Chapter II. The results are presented and compared with reference button cells (NiO-YSZ/YSZ /CGO$_{BL}$/CGO$_{meso}$-LSCF/LSCF; diameter ≈2 cm). Such reference cells were tested under the same conditions to highlight the reliability of the scale-up process on the final performance.

5.3.1.1 *Characterization of optimised cells in steam electrolysis mode (SOEC)*

Figure 5.11 shows the results of the measurements made in SOEC mode with 50% H$_2$O + 50% H$_2$ at the fuel electrode. Current densities as high as 11 A (0.69 A cm^{-2}) and 10.7 A (0.67 A cm^{-2}) under oxygen and synthetic air atmospheres, respectively, were reached at the thermoneutral voltage (V$_{th}$ = 1.3 V). These values overcame the measured performance of button reference cell (active area ≈2 cm^2) that reaches 0.63 A cm^{-2} under the same conditions. The observed difference was likely due to gas distribution limitation typically occurring in button cells experimental setups. The gas distribution in ProboStat stations could lead to such effects for high current densities. On the contrary the large areas setup allowed a better distribution of the gases mitigating such phenomenon. Figure 5.11 shows the injected current density as a function of the measured voltage for each gas composition.

As expected, the change on the oxygen electrode gas composition, from pure oxygen to synthetic air, induced slight variations (≈0.98 V to ≈0.95 V) of the measured Open Circuit Voltage (OCV). The two measured values were in agreement with the ones predicted by the Nernst equation,[31–34] namely 0.99 V and 0.96 V for oxygen and air, respectively, demonstrating the good sealing of the testing rig and the electrolyte gas tightness.
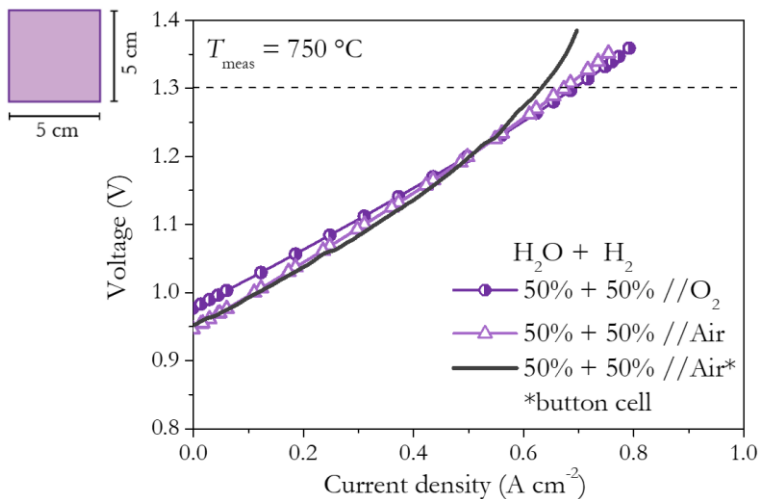
Figure 5.11: Polarization curves measured on the large area cell (active area ≈16 cm²) at 750 °C in SOEC mode. The gas composition at the fuel electrode was the same for the two measurements (50% H_2O + 50 H_2), while at the oxygen electrode pure oxygen and synthetic air were provided. The reference button cell (active area ≈2 cm²) was exposed to 50% H_2O + 50 H_2//Air.

Figure 5.12 shows the impedance measurements at OCV in pure oxygen and synthetic air atmospheres. The DRT analysis presented in Figure 5.12a was realized by the utilization of open source software *DRTtools*.[35] The regularization parameter used for the DRT calculations (10^{-3}) was arbitrarily chosen as the highest value which could provide a good fitting. From the analysis by DRT, four contributions were proposed at ≈10^4, 10^3, 10^2 and 10^1-10^0 Hz.

The fitting of the EIS spectra of Figure 5.12b results on an equivalent circuit composed by an inductance L, a serial resistance R_s which includes all the ohmic contributions (e.g. ionic conduction through the electrolyte and current collection)[9,21] and four ZARC elements ($R_{pi}Q_i$). The ZARC elements refer to the polarization electrochemical processes at the electrodes or at the electrolyte/electrode interfaces. The equivalent circuit is shown as an inset of Figure 5.12b and was designed after the distribution of relaxation times (DRT) analysis. The contribution of the constant phase elements Q accounts

Advanced strategies for Solid Oxide Electrolysis Cells

for a distribution of relaxation times represented by n ($0 \leq n \leq 1$); $n < 1$ results in a depression angle on the experimental impedance arcs and corresponds to wider peak on the DRT plot.[36,37] From Q, the true capacitance can be calculated as $C_p = Q_p^{(1/n)} \cdot R_{p1}^{(1-n)/n}$. The observed values of n are always above 0.8 for SOEC and above 0.6 in COSOEC, meaning that ZARC's behaviour is closer to the one of ideal capacitors.

Observing the variations of the different contributions, one can notice that the change in gas composition at the oxygen electrode from pure oxygen to synthetic air determined the increase of ($R_{p2}Q_2$). Therefore, this contribution was attributed to the oxygen electrode. ($R_{p2}Q_2$) passed from $3.0 \cdot 10^{-2}$ Ω cm^2 to $7.1 \cdot 10^{-2}$ Ω cm^2 and caused the increment of the ASR_{pol}, from 0.17 Ω cm^2 to 0.20 Ω cm^2.
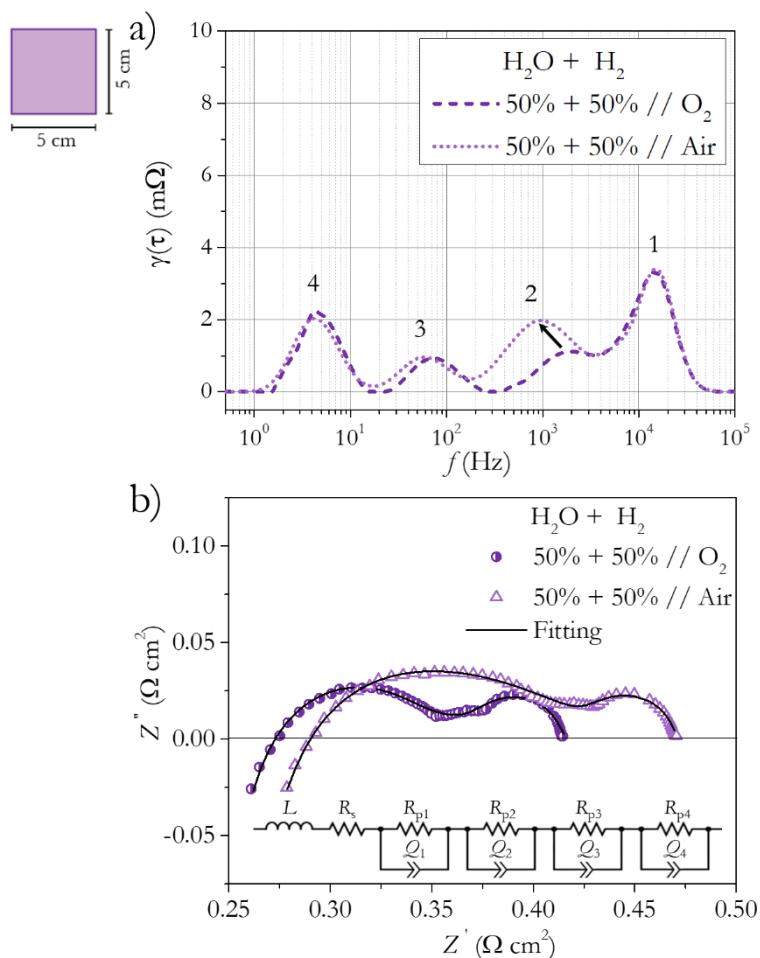
Figure 5.12: DRT analysis of the EIS spectra measured at OCV in SOEC mode, with oxygen and synthetic air at CGO-LSCF electrode (a). From the analysis four contribution were highlighted at $\approx 10^4$, 10^3, 10^2 and 10^1-10^0 Hz. Nyquist EIS plot of the EIS measurements are shown (b) with the fitting of the spectra. The equivalent circuit used for the fitting is sketched in the inset.

Table 5.2 reports the resistances, capacitances and frequencies obtained by fitting the spectra with the proposed equivalent circuit. The capacitance and frequency value of $(R_{p1}Q_1)$ $(C_1 \approx 10^{-4}$ F cm^{-2} and $f_1 \approx 10^4$Hz) is consistent with charge transfer processes happening at the fuel electrode.[9,38–40] Modifying the oxygen atmosphere (from air to pure oxygen) involved a remarkable change in the resistance of $(R_{p2}Q_2)$ $(C_2 \approx 10^{-3}$ F cm^{-2} and $f_2 \approx 500$-1000 Hz), which allow a direct assignment of these contributions to the

Advanced strategies for Solid Oxide Electrolysis Cells

oxygen electrode. Typically, at these frequencies, oxygen reactions and fuel and oxygen transport phenomena are present in both electrodes. The smallest polarization arc ($R_{p3}Q_3$), which appeared at ≈ 10 Hz, has a capacitance around 10^{-1} F cm^{-2} characteristic of non-charge transfer phenomena such as ions transfer through the composite electrodes (CGO in the case of the oxygen electrode and YSZ in the case of the fuel electrode). The lowest frequency arc ($R_{p4}Q_4$) with a characteristic frequency ≈ 1 Hz and an associated large capacitance (≈ 1 F cm^{-2}) was assigned to gas diffusion or gas conversion limitations, typically in the fuel electrode.[7,21,38,40] This interpretation is confirmed by these two low frequency arcs, being only marginally affected by the change in gas composition at the oxygen electrode side.

The area specific resistance considering all the polarization resistance contributions was 0.17 Ω cm^2 and 0.2 Ω cm^2 for the cells measured under oxygen and air, respectively.

Table 5.2: Results from fitting EIS data measured at OCV at 750 °C of the two SOEC experiments reported on Figure 5.12 (50% H$_2$O and 50% H$_2$ at the fuel electrode measured with both pure O$_2$ and synthetic air at the oxygen electrode). The fitting results in *n* values between 0.8 and 1 for all the *Q* elements.

	Gas composition at oxygen electrode	
Parameters	**Pure oxygen**	**Synthetic air**
L (H)	$1.4 \cdot 10^{-8}$	$1.6 \cdot 10^{-8}$
R_s (Ω cm^2)	$2.4 \cdot 10^{-1}$	$2.7 \cdot 10^{-1}$
R_{p1} (Ω cm^2)	$7.8 \cdot 10^{-2}$	$6.6 \cdot 10^{-2}$
C_{p1} (F cm^{-2})	$1.4 \cdot 10^{-4}$	$2.0 \cdot 10^{-4}$
f_1 (Hz)	$1.4 \cdot 10^{4}$	$1.2 \cdot 10^{4}$
R_{p2} (Ω cm^2)	$3.0 \cdot 10^{-2}$	$7.1 \cdot 10^{-2}$
C_{p2} (F cm^{-2})	$2.0 \cdot 10^{-3}$	$1.8 \cdot 10^{-3}$
f_2 (Hz)	$2.6 \cdot 10^{3}$	$1.2 \cdot 10^{3}$
R_{p3} (Ω cm^2)	$2.3 \cdot 10^{-2}$	$2.1 \cdot 10^{-2}$
C_{p3} (F cm^{-2})	$9.3 \cdot 10^{-2}$	$1.1 \cdot 10^{-1}$
f_3 (Hz)	74	67
R_{p4} (Ω cm^2)	$3.9 \cdot 10^{-2}$	$4.2 \cdot 10^{-2}$
C_{p4} (F cm^{-2})	$8.8 \cdot 10^{-1}$	$8.3 \cdot 10^{-1}$

f_4 (Hz)	4.5	4.6
ASR_{pol} (Ω cm^2)	0.17	0.20
ASR_{tot} (Ω cm^2)	0.41	0.47

5.3.1.2 *Characterization of large area cells under COSOEC mode*

Large area cells with infiltrated mesoporous functional layers were electrochemically characterized by galvanostatic polarization curves and EIS measurements in galvanostatic mode, under two different fuel electrode atmospheres (45% H_2O + 45% CO_2 + 10% H_2 and 65% H_2O + 25% CO_2 + 10% H_2) and two different oxygen electrode conditions (O_2 and synthetic air) at 750°C. The performance of a button cell counterpart (composition: Ni-YSZ/YSZ/CGO$_{BL}$/CGO$_{meso}$-LSCF/LSCF, active area ≈1.54 cm^2), tested under the same conditions, is plotted as a reference. Figure 5.13 shows the voltage as a function of the injected current density for each gas composition. Open Circuit Voltages (OCV) of 0.88 V and 0.87 V were obtained when using pure oxygen and air, respectively. This is in excellent agreement with the theoretical values (0.89 V for oxygen and 0.86 V for air).[31–34] This last consideration proves an excellent electrolyte gas tightness and a good sealing of the tested cells. Injected currents as high as 11.7 A (0.73 A cm^{-2}) and 11.4 A (0.71 A cm^{-2}) were reached at the thermoneutral voltage (V_{th}=1.3 V) under pure oxygen, while 10.9 A (0.68 A cm^{-2}) was measured in synthetic air atmosphere. The best performance was obtained for the cell measured under higher steam content (65 %) in the fuel mixture, in agreement with the predicted kinetics of the COSOEC and with other reported results in literature.[7,41,42] Different reasons can explain this effect. Zhan *et al.* in their work identify for example the higher diffusion rate in the electrode and the higher charge transfer reaction rate of steam and hydrogen compared with carbon dioxide. Furthermore, the possible H_2 production via water-gas shift reaction, due to the presence of a larger percentage of steam in the mixture,

Advanced strategies for Solid Oxide Electrolysis Cells

is another possible reason.[43] In comparison to the reference button cell, large area cell measurements showed slightly better results. Although the differences were very small, the lower performance at 1.3 V observed for the button cell ($\approx$0.63 A cm^{-2}, respect to $\approx$0.68 A cm^{-2} of the large area cell at the same conditions) was attributable to gas distribution limitations. Such limitations, observed also in SOEC mode, are typically occurring in button cells' experimental setup due to the gas distribution of the ProboStat station used for the measurements.
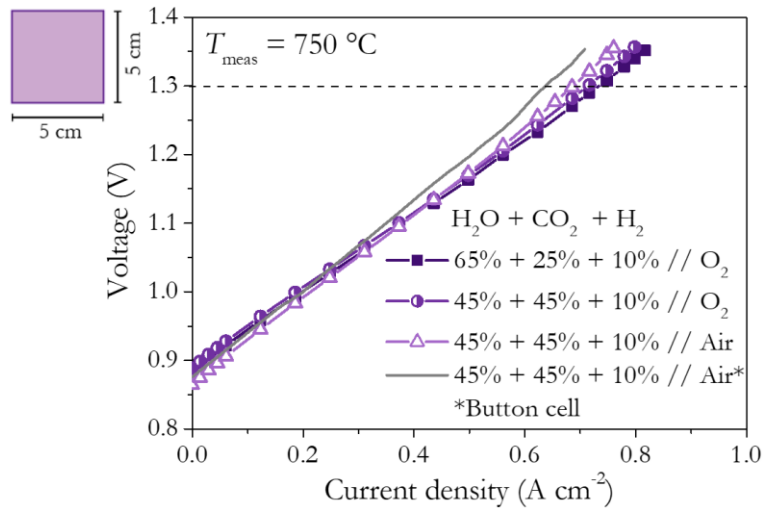

Figure 5.13: Polarization curves in COSOEC mode at 750 °C with different gas compositions (65% H_2O + 25% CO_2 + 10 H_2 // O_2, 45% H_2O + 45% CO_2 + 10 H_2 // O_2 and 45% H_2O + 45% CO_2 + 10 H_2 // Air). The polarization curves are compared with the performance of a button cell measured at the same temperature with gas composition 45% H_2O + 45% CO_2 + 10 H_2 // Air.

Impedance measurement at OCV are shown in Figure 5.14. The DRT analysis of Figure 5.14a had been used to determine the frequency ranges for the four contributions proposed in the equivalent circuit used the fitting of the obtained Nyquist arcs (Figure 5.14b). The chosen equivalent circuit is shown as inset of the figure.
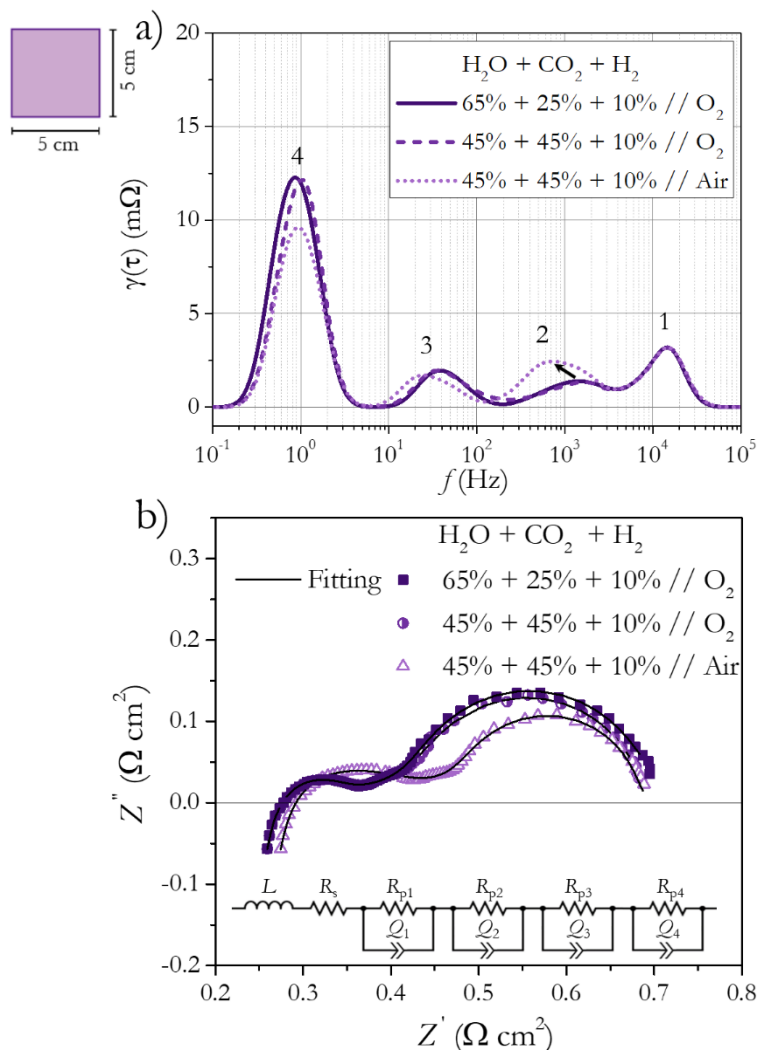
Figure 5.14: DRT analysis of the three EIS measured at OCV in COSEC mode (a). From such analysis four contribution where highlighted at $\approx 10^4$, 10^3, 10^2-10^1 and 10^0 Hz. Nyquist plot of the EIS measurements conducted at OCV (b). The equivalent circuit used for the fitting is presented as inset of (b).

At the light of the Nyquist fitting and DRT analysis four contributions were observed at $\approx 10^4$, 10^3, 10^2-10^1 and 10^0 Hz. One can notice that the large contribution to the resistance was coming from ($R_{p4}Q_4$), which was the process at the lowest frequency. Furthermore, the change in gas composition at the oxygen electrode determined the growth of the contribution ($R_{p2}Q_2$), as observed in SOEC mode.

Advanced strategies for Solid Oxide Electrolysis Cells

Table 5.3 reports the resistances, capacitances and frequencies obtained by fitting the obtained arcs for the 4 different contributions proposed by the equivalent circuit. The capacitance and frequency values of the high frequency arc ($R_{p1}Q_1$) ($C_1 \approx 10^{-4}$ F cm^{-2} for $f_1 \approx 10$ kHz) were ascribed as charge transfer processes at the fuel electrode (typically assigned to $f > 1$ kHz).[9,23,38–40] For the second contribution at relative lower frequency, ($R_{p2}Q_2$) the obtained values ($C_2 \approx 10^{-3}$ F cm^{-2} for $f_2 \approx 500$-1000 Hz) were characteristics of oxygen electrode reactions and also of fuel and oxygen electrode mass transport.[23] This hypothesis was completely in agreement with the observed resistance variation promoted by the changes from air to pure oxygen at the oxygen electrode gas composition. The smallest contribution ($R_{p3}Q_3$), observed at $f_3 \approx 30$ Hz, had a capacitance around $C_3 \approx 10^{-2}$ F cm^{-2}, which is representative of non-charge transfer phenomena such as ion transport through the composite electrodes (LSCF or CGO in the case of the oxygen electrode and YSZ in the case of the fuel electrode).[23] According to this interpretation, the change in resistance of this contribution should be only marginally affected by the change in gas composition at the oxygen electrode side, as indeed was observed in the presented results. Finally, the lowest frequency arc ($R_{p4}Q_4$) ($f_4 \approx 1$ Hz) presented an associated large capacitance of $C_4 \approx 1$ F cm^{-2}, related to gas conversion.[7,21,38,40] Gas conversion is typically contributing at this temperature, although gas diffusion limitations could occur due to the thickness of the fuel electrode.[44,45] The decrease of low frequency contribution passing from O_2 to synthetic air (0.24 Ω cm^2 and 0.20 Ω cm^2 respectively, as shown in Table 5.3 and Figure 5.14) could be justified by the presence of some small leaks or other experimental issues, despite the good observed OCV values.[46] The total area specific resistance (ASR), considering all the polarization resistance contributions, was 0.45 Ω cm^2 and 0.43 Ω cm^2 for the cells measured under oxygen and air, respectively.

Table 5.3: Results from fitting with $LR_s(R_{p1}Q_1)(R_{p2}Q_2)(R_{p3}Q_3)(R_{p4}Q_4)$ equivalent circuit of the EIS data recorded at OCV for a large area cell measured under COSOEC mode at 750 °C. Here R_s values are presented and C_p represents the true capacitance calculated as $C_p = Q_i^{(1/n)} R_{pi}^{(1-n)/n}$, where the values of the n parameter used for the fitting are between 0.6 and 1.

Parameters	Gas composition at oxygen electrode		
	45%+45%+10% //O$_2$	45%+45%+10% //Air	65%+25%+10% //O$_2$
L (H)	$1.4 \cdot 10^{-8}$	$1.4 \cdot 10^{-8}$	$1.5 \cdot 10^{-8}$
R_s (Ω cm^2)	$2.4 \cdot 10^{-1}$	$2.5 \cdot 10^{-1}$	$2.4 \cdot 10^{-1}$
R_{p1} (Ω cm^2)	$7.6 \cdot 10^{-2}$	$7.7 \cdot 10^{-2}$	$7.6 \cdot 10^{-2}$
C_{p1} (F cm^{-2})	$1.2 \cdot 10^{-4}$	$1.2 \cdot 10^{-4}$	$1.2 \cdot 10^{-4}$
f_1 (Hz)	$1.7 \cdot 10^4$	$1.9 \cdot 10^4$	$1.8 \cdot 10^4$
R_{p2} (Ω cm^2)	$3.3 \cdot 10^{-2}$	$7.7 \cdot 10^{-2}$	$3.4 \cdot 10^{-2}$
C_{p2} (F cm^{-2})	$1.8 \cdot 10^{-3}$	$1.4 \cdot 10^{-3}$	$1.9 \cdot 10^{-3}$
f_2 (Hz)	$2.6 \cdot 10^3$	$1.4 \cdot 10^3$	$2.5 \cdot 10^3$
R_{p3} (Ω cm^2)	$1.1 \cdot 10^{-1}$	$8.7 \cdot 10^{-2}$	$9.3 \cdot 10^{-2}$
C_{p3} (F cm^{-2})	$6.2 \cdot 10^{-2}$	$5.9 \cdot 10^{-2}$	$6.4 \cdot 10^{-2}$
f_3 (Hz)	$2.5 \cdot 10^1$	$3.1 \cdot 10^1$	$2.7 \cdot 10^1$
R_{p4} (Ω cm^2)	0.24	0.20	0.26
C_{p4} (F cm^{-2})	$7.6 \cdot 10^{-1}$	$8.0 \cdot 10^{-1}$	$7.5 \cdot 10^{-1}$
f_4 (Hz)	0.88	1.0	0.82
ASR_{pol} (Ω cm^2)	0.45	0.44	0.46
ASR_{tot} (Ω cm^2)	0.69	0.69	0.70

Figure 5.15 shows a summary graphical explanation of the impedance interpretations in SOEC and COSOEC configurations for large area cells. The four arcs are qualitatively represented and the frequencies related to defined processes are reported Figure 5.15a. $(R_{p1}Q_1)$ was assigned to charge transfer at the fuel electrode, $(R_{p2}Q_2)$ to oxygen reaction or to fuel and oxygen transport phenomena which could happen at both electrodes. $(R_{p3}Q_3)$ was attributed to oxygen ion transport at the fuel electrode and $(R_{p4}Q_4)$ to gas conversion at the fuel electrode. Figure 5.15b shows the scheme of an SOEC, where the position of the four processes are indicated.
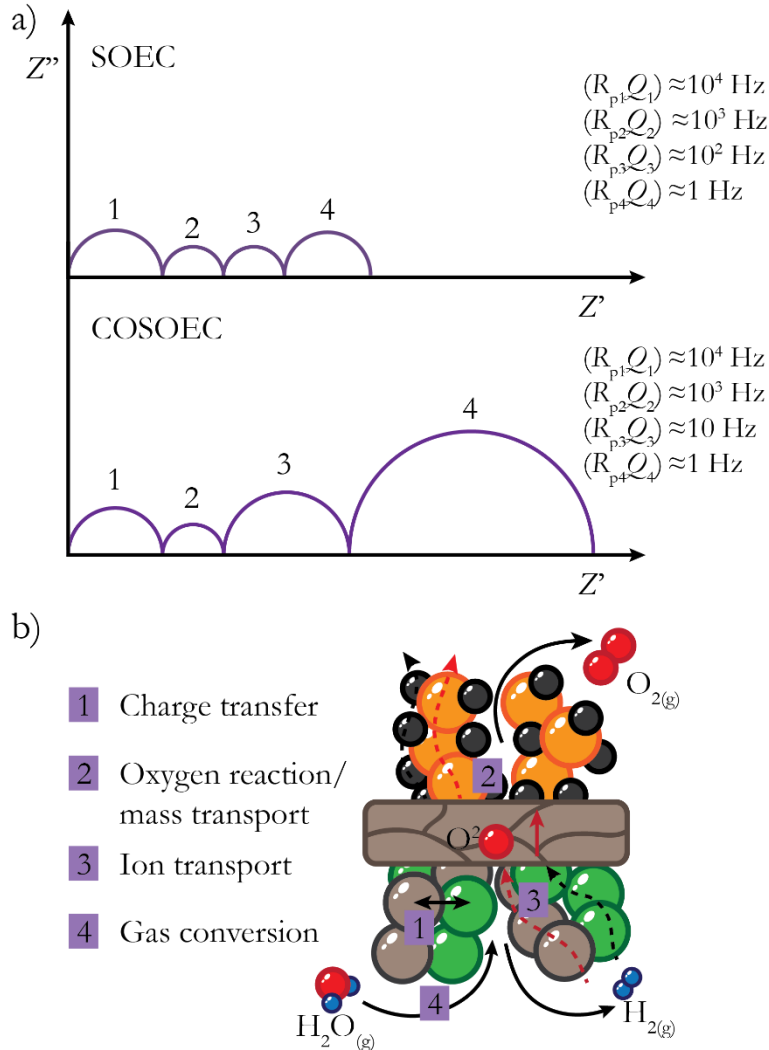
a)

b)

Figure 5.15: Schematic summary of the impedance measurements in SOEC and COSOEC conditions. The four arcs $(R_{p1}Q_1)(R_{p2}Q_2)(R_{p3}Q_3)(R_{p4}Q_4)$ are qualitative represented maintaining the proportion among them (a). The frequencies associated to the arcs are reported in figure for the two configurations. Schematic representation of the processes associated to the impedance arcs (b). 1 indicates charge transfer at the fuel electrode, 2 oxygen reaction or mass transport at the oxygen electrode, 3 ion transport at the fuel electrode and 4 gas conversion at the fuel electrode.

By comparing tables Table **5.2** and Table **5.3** one can notice that the two low frequency arcs are the ones which were affected the most by the change from SOEC to COSOEC mode. This is in agreement with the

assignment of such contributions to the fuel electrode, which seems to be the component of the cell that influenced the most the polarization resistance of the cell.

5.3.2 Durability test of the large area cell

With the aim of analysing the electrochemical processes of the cell during long-term operation, a durability test was performed in galvanostatic COSOEC mode (65% H_2O + 25% CO_2 + 10% H_2 // O_2) applying a total current of 8 A (j=0.5 A cm^{-2}) during 600 h (Figure 5.16). After the first 300 h (commonly considered a reasonable stabilization period), the degradation rate was ≈126 mV kh^{-1}.
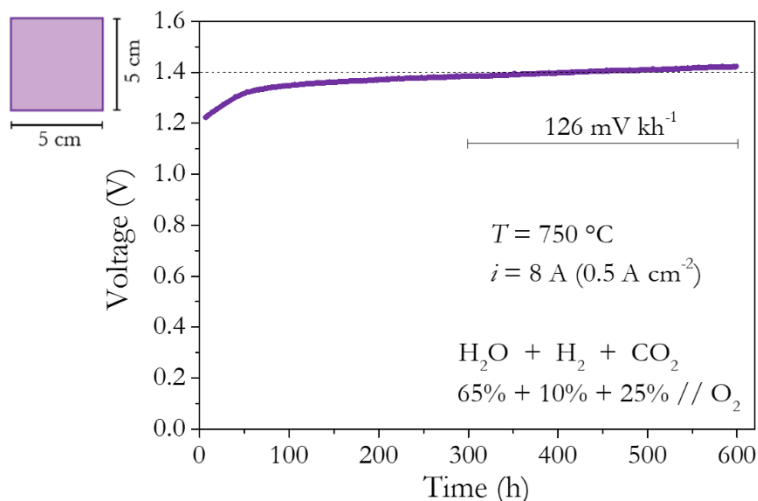

Figure 5.16: Degradation of the cell under COSOEC mode (65% H_2O + 25% CO_2 + 10% H_2 // O_2), injecting current density i = 8 A (j = 0.5 A cm^{-2}) at 750 °C and continuous operation for 600 h.

Impedance measurements were carried out at the beginning of the experiment and after 300 and 600 h of operation (Figure 5.17) at OCV. Figure 5.17 shows the DRT analysis and the Nyquist plot of the EIS measurements. The $LR_s(R_{p1}Q_1)(R_{p2}Q_2)(R_{p3}Q_3)(R_{p4}Q_4)$ equivalent circuit was maintained for the fitting and study of the obtained Nyquist plots. The results are compiled

Advanced strategies for Solid Oxide Electrolysis Cells

in Table 5.4. An evolution of the different impedance contributions during the continuous operation under COSOEC mode was detected. Furthermore, a certain increase of the serial resistance (R_s) was observed. The serial resistance passed from 0.24 Ω cm^2 to 0.30 Ω cm^2 after 600 h of durability test. However, it presented the typical values of tape-casted YSZ electrolytes and screen-printed CGO barrier layers, as reported in a previous work of the group.[47] Despite this fact, the overall ASR of the cell was mainly dominated by the polarization contribution.
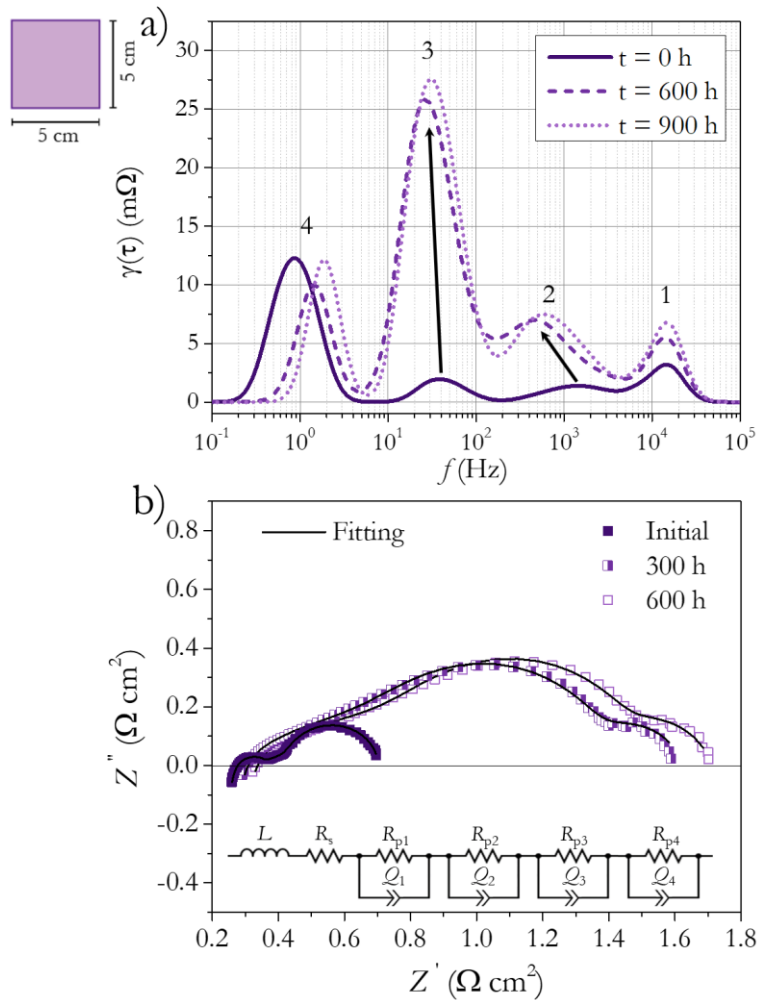

Figure 5.17: DRT calculation of EIS measurements (a) recorded at the beginning of the experiments and after 300 and 600 h of degradation. In figure is showed the

Advanced strategies for Solid Oxide Electrolysis Cells

evolution of the four arcs $(R_{p1}Q_1)(R_{p2}Q_2)(R_{p3}Q_3)(R_{p4}Q_4)$. Nyquist plots (b) of same EIS measurements. The equivalent circuit used for the fitting is presented as inset of the figure.

The DRT plot of Figure 5.17a shows the analysis at the beginning of the test and after 300 h and 600 h of durability test. As in the previous cases, the DRT analysis divided the polarization resistance in four different contributions at $\approx 10^4$, 10^3, 10^2-10^1 and 10^0 Hz. One can notice how the contributions related with the detected evolution due to the degradation were $(R_{p2}Q_2)$ and $(R_{p3}Q_3)$ (f=10^3 Hz and 10^2-10^1 Hz).

The high frequency arc $(R_{p1}Q_1)$, associated to the charge transfer at the fuel electrode, underwent a small increase during the degradation, while the two biggest contributions came from $(R_{p2}Q_2)$ and $(R_{p3}Q_3)$, which together represented more than 70% of the polarization resistance. Following the interpretation of the SOEC and COSOEC characterization, $(R_{p2}Q_2)$ (10^3 Hz) was most likely related to oxygen reaction or fuel and oxygen transport, which could take place at both electrodes.[23] Such process increased its contribution from $3.4 \cdot 10^{-2}$ Ω cm^2 to $3.0 \cdot 10^{-1}$ Ω cm^2. On the other side, $(R_{p3}Q_3)$ ($\approx 10^2$-10^1 Hz) was likely attributed to the oxygen ion diffusion within the fuel electrode. It continued growing during the entire degradation test, becoming the largest contribution to the overall polarization resistance (respectively $9.3 \cdot 10^{-2}$ Ω cm^2 and $7.1 \cdot 10^{-1}$ Ω cm^2 at the initial point and after 600 h of degradation). This interpretation is also consistent with the post-mortem microstructural analysis of the cell (presented in detail in the following section), which shows a consistent evolution of the fuel electrode microstructure. As far as $(R_{p4}Q_4)$ is concerned, its contribution, which is fully compatible with gas conversion/diffusion phenomena, had been quite constant during operation.[44,45]

Table 5.4: Results from fitting with an $LR_s(R_{p1}Q_1)(R_{p2}Q_2)(R_{p3}Q_3)(R_{p4}Q_4)$ equivalent circuit of the EIS data. The impedances were recorded at OCV at the beginning of the measurements and after 300 and 600 h in operation with 0.5 A cm⁻², for a large area cell measured by COSOEC mode (65% H_2O + 25% CO_2 + 10% H_2 // O_2) at 750 °C. Here R_s values are reported and C_p represents the true capacitance calculated as $C_p = Q_i^{(1/n)} R_{pi}^{(1-n)/n}$, where the values of the n parameter used for the fitting are between 0.6 and 1.

	Initial point	t = 300 h	t = 600 h
L (H)	$1.5 \cdot 10^{-8}$	$1.4 \cdot 10^{-8}$	$1.4 \cdot 10^{-8}$
R_s (Ω cm²)	$2.4 \cdot 10^{-1}$	$2.6 \cdot 10^{-1}$	$3.0 \cdot 10^{-1}$
R_{p1} (Ω cm²)	$7.6 \cdot 10^{-2}$	$1.4 \cdot 10^{-1}$	$1.8 \cdot 10^{-1}$
C_{p1} (F cm⁻²)	$1.2 \cdot 10^{-4}$	$9.2 \cdot 10^{-5}$	$1.0 \cdot 10^{-4}$
f_1 (Hz)	$1.8 \cdot 10^4$	$1.2 \cdot 10^4$	$8.9 \cdot 10^3$
R_{p2} (Ω cm²)	$3.4 \cdot 10^{-2}$	$2.9 \cdot 10^{-1}$	$3.0 \cdot 10^{-1}$
C_{p2} (F cm⁻²)	$1.9 \cdot 10^{-3}$	$1.1 \cdot 10^{-3}$	$1.2 \cdot 10^{-3}$
f_2 (Hz)	$2.5 \cdot 10^3$	$5.0 \cdot 10^2$	$4.2 \cdot 10^2$
R_{p3} (Ω cm²)	$9.3 \cdot 10^{-2}$	$7.0 \cdot 10^{-1}$	$7.1 \cdot 10^{-1}$
C_{p3} (F cm⁻²)	$6.4 \cdot 10^{-2}$	$7.0 \cdot 10^{-3}$	$7.2 \cdot 10^{-3}$
f_3 (Hz)	$2.7 \cdot 10^1$	$3.4 \cdot 10^1$	$3.1 \cdot 10^1$
R_{p4} (Ω cm²)	0.26	0.22	0.23
C_{p4} (F cm⁻²)	$7.5 \cdot 10^{-1}$	$6.1 \cdot 10^{-1}$	$5.5 \cdot 10^{-1}$
f_4 (Hz)	0.82	1.2	1.3
ASR_{pol} (Ω cm²)	0.46	1.3	1.4
ASR_{tot} (Ω cm²)	0.70	1.56	1.70

Figure 5.18 shows a summary of the evolution of each contribution to the overall resistance as a function of time. The equivalent circuit $(R_{p1}Q_1)(R_{p2}Q_2)(R_{p3}Q_3)(R_{p4}Q_4)$ with the four ZARCs elements is shown as inset. Observing the recap of Figure 5.18 it can be clearly concluded that oxygen ion diffusion, associated to $(R_{p3}Q_3)$ element, had dominated the degradation process of the cell compared to other processes. The evolution of the fuel electrode of the cell seems the main responsible for the drop in performances of the devices.
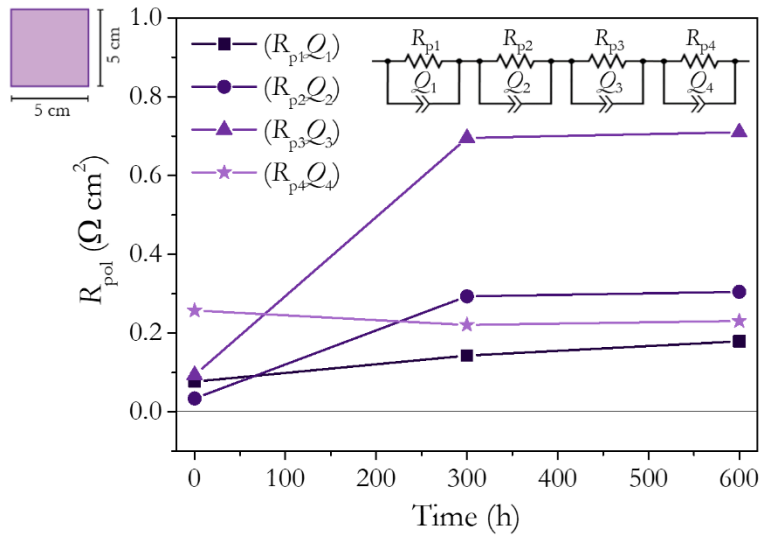
Figure 5.18: Evolution of the $(R_{p1}Q_1)(R_{p2}Q_2)(R_{p3}Q_3)(R_{p4}Q_4)$ arcs with time from the starting point and after 300 and 600 h of durability test in COSEC condition. The gas composition used for the experiment was 65% H_2O + 25% CO_2 + 10% H_2 // O_2. The impedance measurements were conducted at OCV and at 750 °C. The equivalent circuit is presented as inset of the figure.

5.3.3 Post-test microstructural characterization

The microstructure of the large area cell was characterized by SEM-EDX after 600 hours of operation in COSOEC mode for studying the evolution of the cell during operation. Cross-section micrographs of the oxygen electrode/electrolyte interface are shown in Figure 5.19a and in Figure 5.19b, where it is possible to distinguish a dense YSZ electrolyte and the CGO barrier layer. The latter showed a certain porosity because of its fabrication process by screen-printing. The mesoporous CGO scaffold infiltrated by LSCF perovskite can be observed in Figure 5.19b.
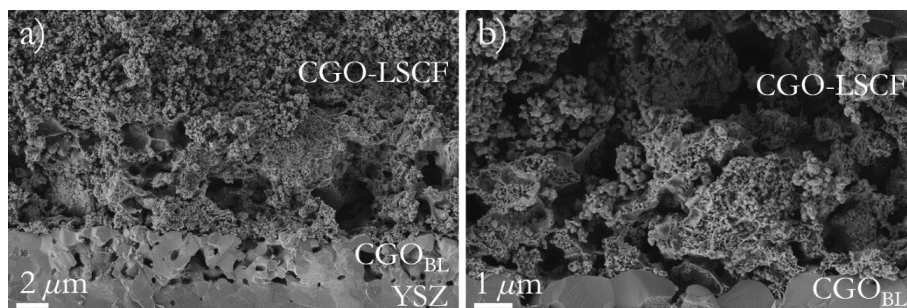
Figure 5.19: SEM cross-section micrograph of the oxygen electrode interface microstructure after 600 h of degradation in COSOEC mode (a). Micrograph showing a detail of the CGO-LSCF functional layer (b).

No apparent microstructural changes due to the long-term operation were observed on this side of the cell, indicating a great stability of the mesoporous-based structure and the interface. Such an excellent performance and stability were the base of the obtained results obtained in the here presented research line.[2,48,49] This finding is also confirmed by EDX analysis, presented in Figure 5.20, where part of the oxygen electrode (Figure 5.20a) was analysed. The overlay and coloured compositional elemental mapping of Figure 5.20b shows the spatial distribution of the main phases constituting the cell (Zr, for YSZ, Ce for CGO and La for LSCF). More in detail, one can observe a high lanthanum (La) signal localized on the upper part of the cell (which corresponds to the commercial LSCF layer deposited by airbrushing). Lanthanum signal was still present in the area of the mesoporous structure (cf. Ce signal), confirming that the mesoporous functional layer was still properly functionalized by the infiltrated perovskite after 600 h of operation. This means that the increase of ($R_{p2}Q_2$) observed was not directly related to the evolution of the oxygen electrode microstructure. Such contribution was originally assigned either to oxygen reactions or to fuel and oxygen transport phenomena at both electrodes. However considering the results of the microstructural analysis it should be

associated to more subtle changes such LSCF redistribution or, possibly, to the microstructural evolution of the fuel electrode.[49]
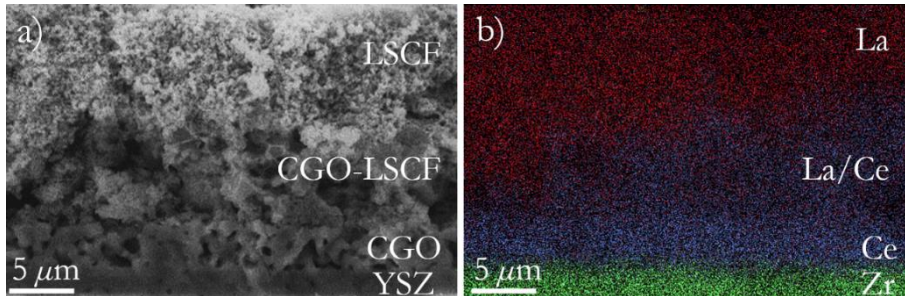

Figure 5.20: Zone of the oxygen electrode in which the SEM-EDX analysis was done (a) and distribution of the elements (b).

Figure 5.21 shows the SEM characterization of the fuel electrode by both secondary electrons (SE, Figure 5.21a and Figure 5.21b) and in-lens detectors (Figure 5.21c and Figure 5.21d). The SE micrographs present the microstructure of the fuel electrode before (performed on an equivalent reference cell) and after degradation, respectively, demonstrating a proper attachment to the electrolyte in both cases. The micrographs of the same zones of the cell obtained using the in-lens detector at low acceleration voltage (1 kV), allowed to highlight the contrast between the electronically percolating Ni (bright particles) and the non-percolating phases (dark particles, e.g. YSZ or isolated metallic Ni clusters).[26,27,29,50] Observing the SEM micrographs, a clear difference in the distribution of the percolating Ni particles can be observed before and after operation for 600 h. In-lens pictures were analysed by an image-processing program (ImageJ, see Ref.)[51] to estimate the percentage of percolating Ni for each subdivision (delimited by purple horizontal lines) as a function of the distance from the electrolyte/fuel electrode interface.
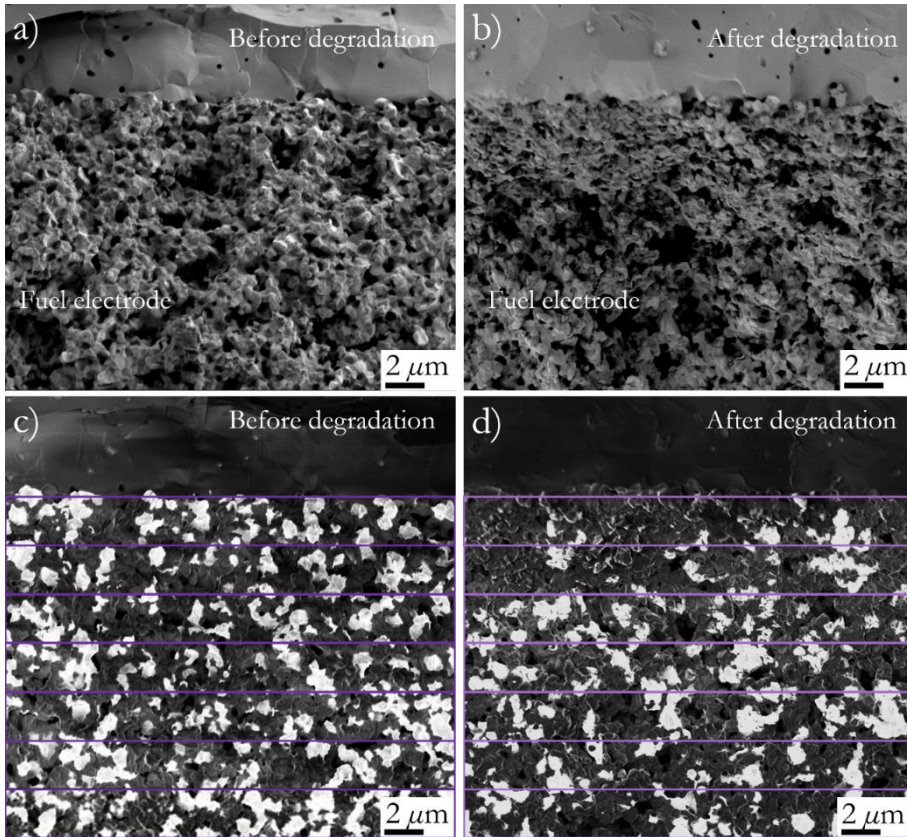
Advanced strategies for Solid Oxide Electrolysis Cells

Figure 5.21: SEM cross-section micrographs of the YSZ electrolyte/Ni-YSZ fuel electrode interface recorded employing SE2 (a, b) and low voltage and in-lens detectors (c, d). Fig. (a) and (c) refer to a reference cell before operation, whereas Fig. (b) and (d) are result of post-mortem analysis (600 h of degradation in COSOEC mode).

The quantification of the percentage of percolated nickel rich phase as a function of the distance from fuel electrode/electrolyte interface is presented in Figure 5.22. Here, the results obtained from the button HF-Co-CGO cell are also presented, for a better discussion of the detected phenomena. One can notice that, before the degradation, in all the analysed areas the percentage of percolating network remained around 25%, while after the 600 h at 750 °C and 0.5 A cm^{-2} this value decreased to ≈10 % almost linearly while approaching the electrolyte/fuel electrode interface. The percentage of percolated Ni particles for the button HF-Co-CGO cell

Advanced strategies for Solid Oxide Electrolysis Cells

decreased down to ≈6 % at the vicinity of the electrolyte/fuel electrode interface. Interestingly, both cells showed a very similar drop of percolation. Note that the durability tests of HF-Co-CGO button and of CGO large area cells were made with same gas composition at the fuel electrode (65% H_2O, 25% CO_2, 10% H_2), at the same temperature (750 °C) and while applying the same current density (0.5 A cm^{-2}). The main difference was the duration of the tests, 1100 h for the HF-Co-CGO cell and 600 h for the CGO large area cell. The fact of the observed microstructural evolution, together with similar degradation rates of the two type of cells (106 mV kh^{-1} for the HF-Co-CGO compared with 126 mV kh^{-1} for the CGO large area cell), reinforce the conclusion of a degradation process driven by the evolution of the fuel electrode.
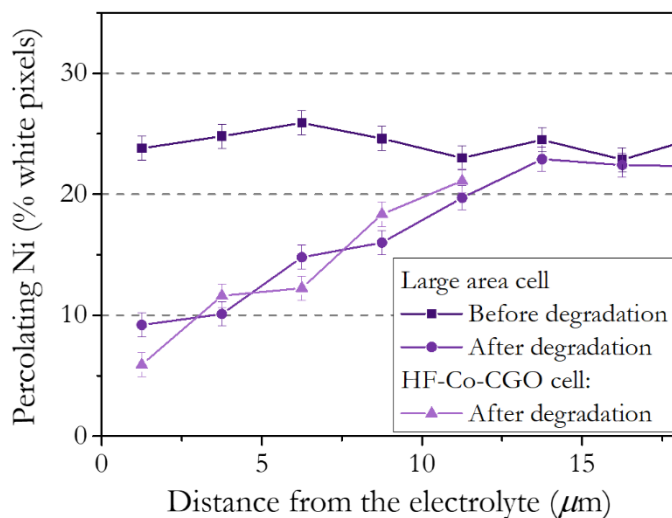

Figure 5.22: Quantification of percolating Ni areas from Figure 5.21c and Figure 5.21d. The amount of metallic Ni, which participates in the electronic pathway decreased in the direction of the electrolyte because of the degradation process. In the figure, also the quantification of the fuel electrode of the HF-Co-CGO cell shown in Figure 5.8 is represented. This button cell was observed at the SEM after 1100 h of durability test in the same condition.

Such a loss of percolation in the active region of the fuel electrode could largely explain the degradation behaviour observed via electrochemical

Advanced strategies for Solid Oxide Electrolysis Cells

characterization of the cell, at least for what concerns the lower frequency polarization elements. The increase of $(R_{p3}Q_3)$ (f =10 Hz), which was the main contribution to the impedance during the operation of the large area cell, was clearly related to the degradation of the fuel electrode. Such degradation consisted in the decrease of percolating volume, caused by Ni particles coarsening, which resulted in obstacles for the oxygen ion transport to TPBs (higher tortuosity) and charge transfer reaction within YSZ. This phenomenon, driven by surface energy minimization and by the high mobility of Ni at high temperature, often occurs when partial re-oxidation of the Ni metal takes place due to the inhomogeneity on the reduction atmosphere.[52] Such effect is possibly aggravated by Ni volatilization and leads to a decrease of the TPB areas close to the electrolyte.[28,29,49,53,54] The origin of this degradation was consistent with the one observed by Rao *et al.* on cells with the same combination of materials.[15]

Overall, the large area cells presented in this work showed remarkable performance proving that nanostructured oxygen electrodes are excellent candidates for upscaling. The observed degradation was dominated by the two middle frequencies elements $(R_{p2}Q_2)$ ($\approx$500-1000 Hz) and $(R_{p3}Q_3)$ (10 Hz) which were attributed to fuel and oxygen transport phenomena (possibly taking place at both electrodes) and to oxygen ion transport at the fuel electrode respectively. Their contributions passed from $3.4 \cdot 10^{-2}$ Ω cm^2 to $3 \cdot 10^{-1}$ Ω cm^2 for $(R_{p2}Q_2)$ and from $9.3 \cdot 10^{-2}$ Ω cm^2 to $7.1 \cdot 10^{-1}$ Ω cm^2 for $(R_{p3}Q_3)$. In particular, $(R_{p3}Q_3)$, which was associated to the degradation of the fuel electrode, represented half of the total contribution to the polarization resistance. Such results indicated the fuel electrode as the weakest element of the SOC cells, and that the association of improved fuel electrodes with the oxygen electrode developed in the present work may lead to strongly improved devices, able to fully utilize the potential of improved oxygen electrodes. However, it is known that the degradation rates reported by the

authors should be improve to achieve the valuers reported for other COSOEC tests under similar conditions, where degradation rates of less than 3 mV kh^{-1} for 800 h at 750 °C and 0.5 A cm^{-2} were achieved.[2]

All in all, the mesoporous CGO electrode infiltrated by LSCF perovskite on large area cells demonstrated its reliability for scale-up. The measurements in both SOEC and COSOEC conditions were equivalents to the ones obtained from the button cells counterparts. The durability test in COSOEC condition for 600 h highlighted a degradation of the fuel electrode, confirmed by the microstructural analysis by SEM. The CGO mesoporous electrode presented a high stability under operation at the working conditions.

5.4 Conclusion

Nano-composite oxygen electrode based on LSCF infiltrated on mesoporous $Ce_{0.8}Gd_{0.2}O_{1.9}$ scaffolds were successfully fabricated and tested in fuel cell, electrolysis and co-electrolysis mode at 750 °C.

Optimized oxygen electrode leaded to outstanding performance of complete NiO-YSZ/YSZ/CGO$_{BL}$/HF-Co-CGO$_{meso}$+LSCF/LSCF cells in SOFC, steam and co-electrolysis mode yielding power densities as high as 1.35 W cm^{-2} at 0.7 V and injected currents above 1.3 A cm^{-2} at 1.3 V, respectively, in the intermediate range of temperatures ($T = 750$ °C). Under the durability tests, the developed COSOEC has shown a degradation rate of 106 mV kh^{-1}.

The CGO nanostructure has demonstrated its potential as functional oxygen electrode, infiltrated by LSCF perovskite, for large area cells (25 cm^2 with 16 cm^2 of active area). A large area cell with composition NiO-YSZ/YSZ/CGO$_{BL}$/CGO$_{meso}$+LSCF/LSCF had been successfully fabricated and tested at 750 °C. The results showed that the performance obtained for

the button cells was maintained and even increased for high current densities in COSOEC 10.9 A (0.68 A cm^{-2}) mode, demonstrating the feasibility of the use of nanostructured composites in large scale cells. A durability test of 600 h, with an applied current of 8 A (0.5 A cm^{-2}), resulted in a degradation rate of 126 mV kh^{-1}, mainly due to fuel electrode microstructural evolution as derived the microstructural and electrochemical (DRT and EIS) analysis.

For both HF-Co-CGO button and CGO large area cells the microstructural analysis highlighted a remarkable loss of the percolation network of metallic Ni due to coarsening or Ni evaporation, close to the electrolyte interface in the post-mortem analysis. There was no evidence of significant evolution in the microstructure of the mesoporous-based oxygen electrode. For the large area cell, a minor evolution of the oxygen electrode was correlated to subtle changes such as LSCF redistribution or increase of the oxygen electrode tortuosity.

This work represented the successful implementation of next-generation nanostructured oxygen electrodes based on optimized mesoporous ceria in full SOC cells. An unprecedented improvement in the electrochemical activity and long-term stability of such cells was obtained, validating the relevance of such mesostructures for SOC application. Furthermore, one of the first examples of the scale-up of infiltrated nanostructured composites was presented, with the infiltrated mesoporous CGO implemented in large area solid oxide cells which was developed and presented in this chapter. These results showed the potential of nano-scaled materials in the following generations of SOFC/SOEC devices.

5.5   Bibliography

1   M. Torrell, L. Almar, A. Morata and A. Tarancón, *Faraday Discuss.*, 2015, **182**, 423–435.

2   E. Hernández, F. Baiutti, A. Morata, M. Torrell and A. Tarancón, *J. Mater. Chem. A*, 2018, **6**, 9699–9707.

3   E. M. Hernández Rodríguez, University of Barcelona, 2018.

4   J. Hong, C. Balamurugan, H.-N. Im, S.-Y. Jeon, Y.-S. Yoo and S.-J. Song, *J. Electrochem. Soc.*, 2018, **165**, F132–F141.

5   J. Laurencin, M. Hubert, D. F. Sanchez, S. Pylypko, M. Morales, A. Morata, B. Morel, D. Montinaro, F. Lefebvre-Joud and E. Siebert, *Electrochim. Acta*, 2017, **241**, 459–476.

6   H. Zheng, Y. Tian, L. Zhang, B. Chi, J. Pu and L. Jian, *J. Power Sources*, 2018, **383**, 93–101.

7   C. Graves, S. D. Ebbesen and M. Mogensen, *Solid State Ionics*, 2011, **192**, 398–403.

8   H. Fan, Y. Zhang and M. Han, *J. Alloys Compd.*, 2017, **723**, 620–626.

9   H. Fan, M. Keane, N. Li, D. Tang, P. Singh and M. Han, *Int. J. Hydrogen Energy*, 2014, **39**, 14071–14078.

10   S. P. Jiang, *Int. J. Hydrogen Energy*, 2019, **44**, 7448–7493.

11   F. Tietz, V. A. C. Haanappel, A. Mai, J. Mertens and D. Stöver, *J. Power Sources*, 2006, **156**, 20–22.

12   T. Hong, K. S. Brinkman and C. Xia, *ChemElectroChem*, 2016, **3**, 805–813.

13   S. He, Q. Zhang, G. Maurizio, L. Catellani, K. Chen, Q. Chang, M. Santarelli and S. P. Jiang, *ACS Appl. Mater. Interfaces*, 2018, **10**, 40549–40559.

14   X. Sun, M. Chen, Y.-L. Liu, P. Hjalmarsson, S. D. Ebbesen, S. H. Jensen, M. B. Mogensen and P. V. Hendriksen, *J. Electrochem. Soc.*, 2013, **160**, F1074–F1080.

15   M. Rao, X. Sun and A. Hagen, *J. Electrochem. Soc.*, 2018, **165**, F748–F755.

16   G. Rinaldi, S. Diethelm and J. Van herle, *ECS Trans.*, 2015, **68**, 3395–3406.

17   Efficient Co-Electrolyser for Efficient Renewable Energy Storage: ECo Project (ref. 699892). Webpage consulted the 7-8-2020, http://www.eco-soec-project.eu/.

18   P. Hjalmarsson, X. Sun, Y. L. Liu and M. Chen, *J. Power Sources*, 2013, **223**, 349–357.

19   Y. Zheng, J. Wang, B. Yu, W. Zhang, J. Chen, J. Qiao and J. Zhang, *Chem. Soc. Rev.*, 2017, **46**, 1427–1463.

20   F. Tietz, D. Sebold, A. Brisse and J. Schefold, *J. Power Sources*, 2013, **223**, 129–135.

21   A. Nechache, M. Cassir and A. Ringuedé, *J. Power Sources*, 2014, **258**, 164–181.

22   E. Perry Murray, M. J. Sever and S. A. Barnett, *Solid State Ionics*, 2002, **148**, 27–34.

23   P. Caliandro, A. Nakajo, S. Diethelm and J. Van herle, *J. Power Sources*, 2019, **436**, 226838.

24   D. The, S. Grieshammer, M. Schroeder, M. Martin, M. Al Daroukh, F. Tietz,

Advanced strategies for Solid Oxide Electrolysis Cells

J. Schefold and A. Brisse, *J. Power Sources*, 2015, **275**, 901–911.

25 A. V. Virkar, *Int J Hydrog. Energ*, 2010, **35**, 9527–9543.

26 K. Thydén, Y. L. Liu and J. B. Bilde-Sørensen, *Solid State Ionics*, 2008, **178**, 1984–1989.

27 M. H. Pihlatie, A. Kaiser, M. Mogensen and M. Chen, *Solid State Ionics*, 2011, **189**, 82–90.

28 P. Tanasini, M. Cannarozzo, P. Costamagna, A. Faes, J. Van Herle, A. Hessler-Wyser and C. Comninellis, *Fuel Cells*, 2009, **9**, 740–752.

29 M. Hubert, J. Laurencin, P. Cloetens, B. Morel, D. Montinaro and F. Lefebvre-Joud, *J. Power Sources*, 2018, **397**, 240–251.

30 M. Morales, V. Miguel-Pérez, A. Tarancón, A. Slodczyk, M. Torrell, B. Ballesteros, J. P. Ouweltjes, J. M. Bassat, D. Montinaro and A. Morata, *J. Power Sources*, 2017, **344**, 141–151.

31 L. Bernadet, J. Laurencin, G. Roux, D. Montinaro, F. Mauvy and M. Reytier, *Electrochim. Acta*, 2017, **253**, 114–127.

32 J. P. Stempien, Q. Liu, M. Ni, Q. Sun and S. H. Chan, *Electrochim. Acta*, 2014, **147**, 490–497.

33 M. Ni, M. K. H. Leung and D. Y. C. Leung, *Int. J. Hydrogen Energy*, 2007, **32**, 2305–2313.

34 M. Ni, *J. Power Sources*, 2012, **202**, 209–216.

35 T. H. Wan, M. Saccoccio, C. Chen and F. Ciucci, *Electrochim. Acta*, 2015, **184**, 483–499.

36 A. Leonide, V. Sonn, A. Weber and E. Ivers-Tiffée, *J. Electrochem. Soc.*, 2007, **155**, B36.

37 M. R. Shoar Abouzari, F. Berkemeier, G. Schmitz and D. Wilmer, *Solid State Ionics*, 2009, **180**, 922–927.

38 R. Barfod, M. Mogensen, T. Klemensø, A. Hagen, Y.-L. Liu and P. Vang Hendriksen, *J. Electrochem. Soc.*, 2007, **154**, B371–B378.

39 M. Shah and S. A. Barnett, *Solid State Ionics*, 2008, **179**, 2059–2064.

40 L. dos Santos.Gómez, J. M. Porras-Vázquez, E. . Losilla, F. Martín, J. R. Ramos-Barrado and D. Marrero-López, *J. Power Sources*, 2017, **347**, 178–185.

41 S. D. Ebbesen and M. Mogensen, *J. Power Sources*, 2009, **193**, 349–358.

42 S. D. Ebbesen, C. Graves and M. Mogensen, *Int. J. Green Energy*, 2009, **6**, 646–660.

43 Z. Zhan, W. Kobsiriphat, J. R. Wilson, M. Pillai, I. Kim and S. A. Barnett, *Energy and Fuels*, 2009, **23**, 3089–3096.

44 M. Mogensen, S. Primdahl, M. J. Jørgensen and C. Bagger, *J. Electroceramics*, 2000, **5**, 141–152.

45 W. Zhou, R. Ran, Z. Shao, W. Jin and N. Xu, *J. Power Sources*, 2008, **182**, 24–31.

46 M. Rao, S. H. Jensen, X. Sun, A. Hagen and M. B. Mogensen, 2019, **13**, 208–214.

47 M. Morales, A. Pesce, A. Slodczyk, M. Torrell, P. Piccardo, D. Montinaro, A. Tarancón and A. Morata, *ACS Appl. Energy Mater.*, 2018, **1**, 1955–1964.

48 S. Anelli, F. Baiutti, A. Hornés, L. Bernadet, M. Torrell and A. Tarancón, *J. Mater. Chem. A*, 2019, **3**, 10031–10037.

49 L. Almar, A. Morata, M. Torrell, M. Gong, T. Andreu, M. Liu and A.

Tarancón, *Electrochim. Acta*, 2017, **235**, 646–653.

50   A. Hauch, P. S. Jørgensen, K. Brodersen and M. Mogensen, *J. Power Sources*, 2011, **196**, 8931–8941.

51   C. T. Rueden, J. Schindelin, M. C. Hiner, B. E. DeZonia, A. E. Walter, E. T. Arena and K. W. Eliceiri, *BMC Bioinformatics*, 2017, **18**, 1–26.

52   M. Torrell, A. Morata, P. Kayser, M. Kendall, K. Kendall and A. Tarancón, *J. Power Sources*, 2015, **285**, 439–448.

53   S. B. Adler, *Chem. Rev.*, 2004, **104**, 4791–4843.

54   A. Nakajo, G. Rinaldi, P. Caliandro, G. Jeanmonod, L. Navratilova, M. Cantoni and J. Van herle, *J. Electrochem. Energy Convers. Storage*, 2020, **17**, 1–13.

Chapter VI

Solid Oxide Cells for partial oxidation of methane

6.1   Chapter overview

i.   The goal of this Chapter is to present the results obtained by exploring the fabrication of a solid oxide electrocatalytic device for the direct production of syngas by electrochemical assisted partial oxidation of methane (POM).

    a.   The principles of operation are reported as a summary (section 6.2).

    b.   The results of the simulations made using an open source chemical process program (DWSIM - Open Source Process Simulator, 2015) are presented (section 6.3).

    c.   The fabrication of the devices and the characterization of the used materials are described (sections 6.4 and 6.5).

    d.   Electrochemical performance of the fabricated cell through current-voltage polarization curves are showed. Together with the electrochemical performance, the characterization of the outlet gases during operation obtained by gas chromatography is presented (section 6.6).

6.2 Principles of operation

As commented in Chapter I, the coupling of POM with the typical co-electrolysis process could be extremely advantageous because of the moderately exothermic nature of the POM reaction. In fact the enthalpy of the POM reaction is $\Delta H^o_{298K} = $ -802 kJ mol^{-1}, and therefore can compensate the energetic demand for co-electrolysis.[1–3]

Figure 6.1 shows the schematic representation of the cell used for this experiment. One can notice the NiO-YSZ electrode, the YSZ electrolyte and the CGO infiltrated by Ni and Cu catalysts. The chemical reaction at NiO-YSZ electrode is the one of water electrolysis, where water is split to obtain hydrogen and oxygen. Oxygen ions move through the electrolyte and react with methane, producing hydrogen and carbon monoxide, also known as syngas. This process can also be used under co-electrolysis of water and carbon dioxide at the NiO-YSZ electrode. In this case, it would be possible to produce syngas from both electrodes.
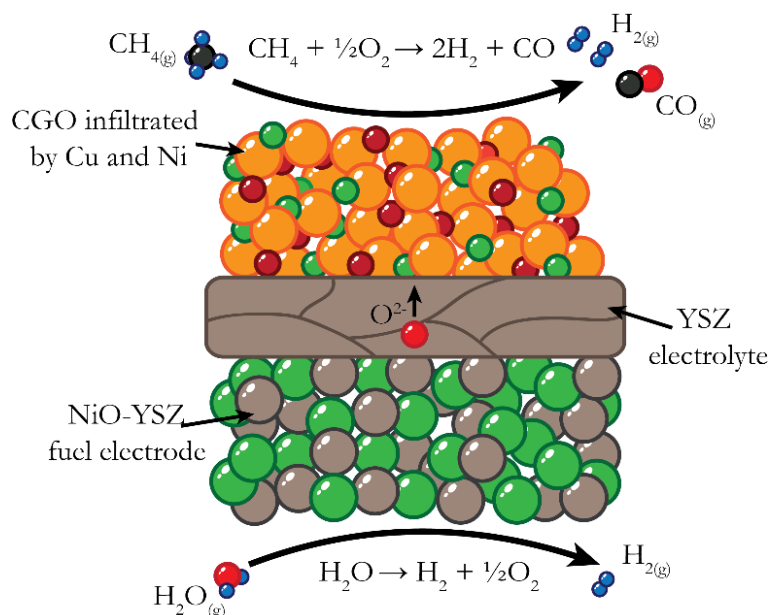
Figure 6.1: Schematic representation of the cell fabricated for electrochemical assisted partial oxidation of methane. It is possible to notice the Ni-YSZ electrode, the YSZ electrolyte and the Ni-Cu-CGO electrode. At the Ni-YSZ side, water splits in hydrogen and oxygen. Oxygen ions are driven to the Ni-Cu-CGO electrode where they react with methane. From methane and oxygen reaction, hydrogen and carbon monoxide are produced.

6.3   Simulation of the POM process on the developed cells

6.3.1   Description of the simulation flowsheet

Before the experimental validation of the developed POM cells, a set of simulated experiments were performed with the aim of defining the best conditions for the POM experiments with real cells. These simulations were conducted to predict the products of the chosen reactions at different temperatures and with different reactant ratios, i.e. methane and oxygen. The experiments of section 6.6 were conducted taking in consideration these simulations and other studies found in literature.[4,5] Presented simulations were made by utilization of an open source chemical process program (DWSIM - Open Source Process Simulator, 2015). DWSIM can simulate

239

steady-state, vapor–liquid, vapor–liquid-liquid, solid–liquid and aqueous electrolyte equilibrium processes.

The minimization method used was the *Direct Gibbs Energy Minimization*, while Peng-Robinson equation of state was chosen, suitable for hydrocarbon compounds.[6] Figure 6.2 shows the flowsheet used for the simulation, where the Gibbs reactor used for the study is indicated by *G*.

The starting species considered where only oxygen and methane, with different proportion (4:1, 2:1 and 1:1 of CH_4 and O_2 respectively) from 300 °C to 1000 °C.

Methane and oxygen inlets can be observed in Figure 6.2, which were mixed and heated by a "mixer" and an "heater" elements. Then, the gases moved to the Gibbs reactor where they were converted into products. Two outlets streams were defined from the Gibbs reactor. This is a feature of the DWSIM program to make test on reactors characterized by different efficiencies. To make the simulation simpler, the efficiency of the reactor was considered close to ≈100%. This means that no species came out from the "waste" outlet. Lastly, the gases were cooled down after the "outlet reactor" and the results were read in the "Product" element of the flowsheet.

From this simulation, the molar ratio of the produced species and the conversion efficiency of the process were calculated.
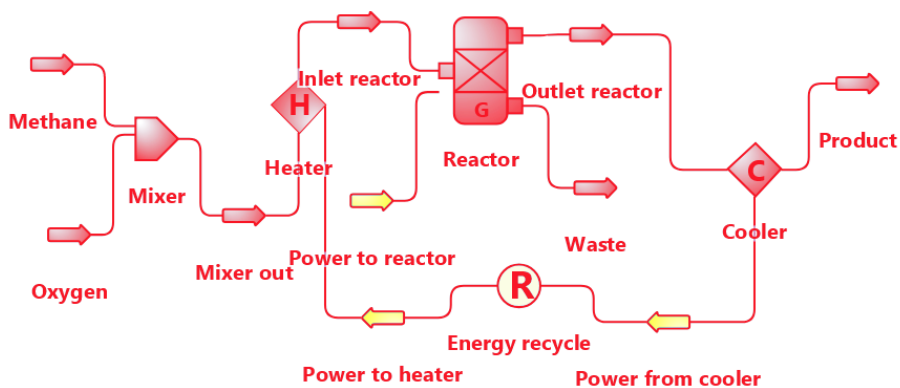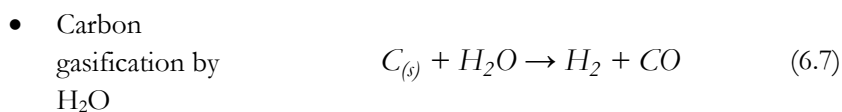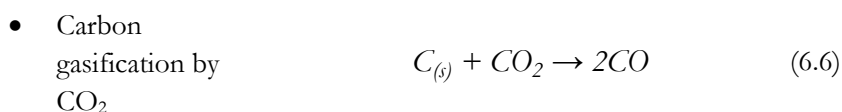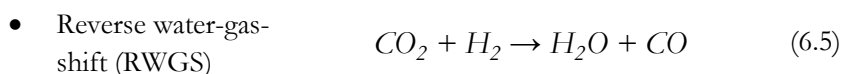
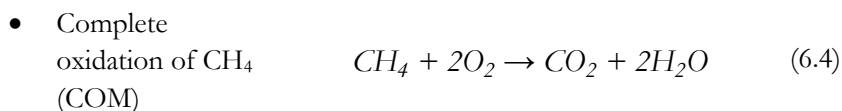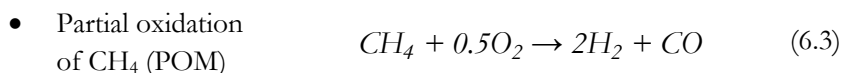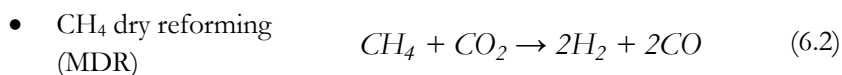Advanced strategies for Solid Oxide Electrolysis Cells

Figure 6.2: Flowsheet made with DWSIM to simulate the CH_4 conversion at different temperatures with O_2. One can notice the inlets of methane and oxygen, which are mixed in the "mixer" element; subsequently they pass through the "heater" to reach the reactor. In the reactor, calculations are made based on the chosen parameters. The products are cooled down in the "cooler" and they can be read in the "product" outlet.

Generally, quite a large number of reactions compete during these processes but depending on the choice of the parameters (e.g. temperature, type of catalyst, etc.), some could be promoted. The simultaneous occurrence of several reactions could be problematic for the final composition of the outcome gas. Such reactions can lead to the production of unwanted species, such as water and carbon dioxide, which would alter typical ratios H_2/CO (=2) of the POM reaction. Furthermore, the generation of unwanted products such CO_2, H_2O or CH_4 dilutes the produced syngas, requiring additional processes for its purification while the carbon deposition caused by Bouduard reaction or by methane decomposition, could be extremely deleterious for the electrode. Considering the temperature range in which usually SOC devices work (600 °C – 900 °C)[7], the possible reactions which could proceed concurrently are listed below:[5]

- CH_4 steam reforming (MSR)

$$CH_4 + H_2O \rightarrow 3H_2 + CO \qquad (6.1)$$

- CH$_4$ dry reforming (MDR)

$$CH_4 + CO_2 \rightarrow 2H_2 + 2CO \qquad (6.2)$$

- Partial oxidation of CH$_4$ (POM)

$$CH_4 + 0.5O_2 \rightarrow 2H_2 + CO \qquad (6.3)$$

- Complete oxidation of CH$_4$ (COM)

$$CH_4 + 2O_2 \rightarrow CO_2 + 2H_2O \qquad (6.4)$$

- Reverse water-gas-shift (RWGS)

$$CO_2 + H_2 \rightarrow H_2O + CO \qquad (6.5)$$

- Carbon gasification by CO$_2$

$$C_{(s)} + CO_2 \rightarrow 2CO \qquad (6.6)$$

- Carbon gasification by H$_2$O

$$C_{(s)} + H_2O \rightarrow H_2 + CO \qquad (6.7)$$

- Boudouard reaction

$$2CO \rightarrow C_{(s)} + CO_2 \qquad (6.8)$$

- CH$_4$ Decomposition

$$CH_4 \rightarrow C_{(s)} + 2H_2 \qquad (6.9)$$

The Gibbs reactor did not allow to simulate the effect of catalyst, therefore the final consideration from such simulation are only related to the thermodynamics of the process. Moreover, all the reactions involving solid carbon were excluded, because the Gibbs reactor cannot simulate heterogeneous reactions with solid species.

During the simulation the following reactions, which are promoted by low temperatures (200 - 400 °C), were also considered.[5]

- CO$_2$ methanation

$$4H_2 + CO_2 \rightarrow CH_4 + 2H_2O \qquad (6.10)$$

- CO methanation

$$3H_2 + CO \rightarrow CH_4 + H_2O \qquad (6.11)$$

Advanced strategies for Solid Oxide Electrolysis Cells
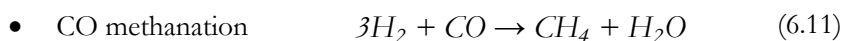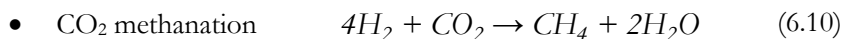
- Water-Gas Shift $\qquad H_2O + CO \rightarrow CO_2 + H_2 \qquad$ (6.12)

6.3.2   Results of the simulation

Figure 6.3, Figure **6.4** and Figure **6.5** summarize the results of the different simulation processes considering 4:1, 2:1 and 1:1 of methane and oxygen, respectively.

As expected, a 4:1 methane/oxygen ratio leaded to an incomplete conversion of the methane, which remained around the 50 %. In this case, the amount of oxygen was the limiting factor, due to its total conversion to other products such as CO and CO_2. It is already reported that in these conditions a certain amount of carbon deposition is expected even at high temperatures.[4] The quantification of the solid carbon amount was difficult without taking into consideration the corresponding Boudouard (6.8) and methane decomposition (6.9) reactions in the simulation. Such reactions cannot be inserted in the Gibbs reactor, which does not support heterogeneous reaction with solid products. However in a similar study from Siang *et al.* for different $CH_4:O_2$ ratios (5:1 and 3:1) the carbon yield considered at 800 °C was between 60% and 35%.[5] Therefore, looking at the case presented in Figure 6.3, a similar amount of solid carbon could be expected.
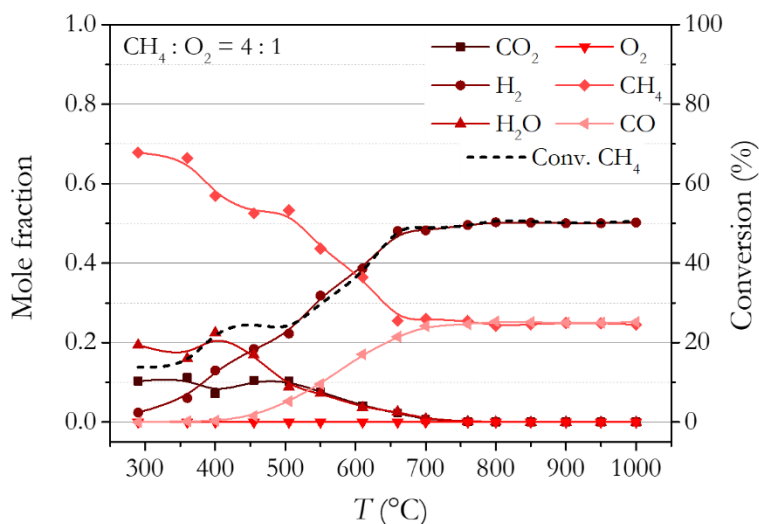
Figure 6.3: Simulations made using the DWSIM programs with CH_4:O_2 ratio 4:1. In this condition both POM, COM, carbon decomposition and Boudouard reaction are dominating the process. The CH_4 conversion % is presented with a black dotted line.

Figure 6.4 shows the simulation made considering the inlet CH_4:O_2 ratio equal to 2:1. In this case, POM was the preferred reaction because the O_2 molar content was exactly half with respect to CH_4.[2,4] It can be noticed that for the high temperature range (800 – 1000 °C) the expected products were only H_2 and CO. Despite the high conversion rate of methane, represented by the dotted line in Figure 6.4 some deposition of solid carbon probably occurs even at high temperature. However, coke deposition above 600 °C is expected to be very low, indeed it should be less than 10% of the total methane consumption.[5]
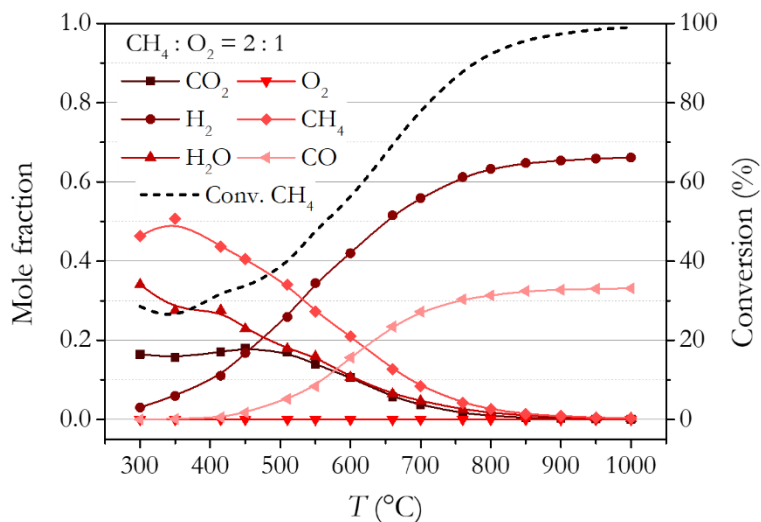
Advanced strategies for Solid Oxide Electrolysis Cells

Figure 6.4: Simulations made using the DWSIM programs with $CH_4:O_2$ ratio 2:1. In this condition both POM is dominating the process. The CH_4 conversion % is presented as black dotted line.

Figure 6.5 shows the simulation made with $CH_4:O_2$ ratio 1:1. In this case the expected reactions which should had contributed to CH_4 consumption were POM (6.3) and COM (6.4). All methane was consumed after 750 °C, so no carbon deposition was expected above this temperature. The main products were CO, H_2, CO_2 and H_2O.
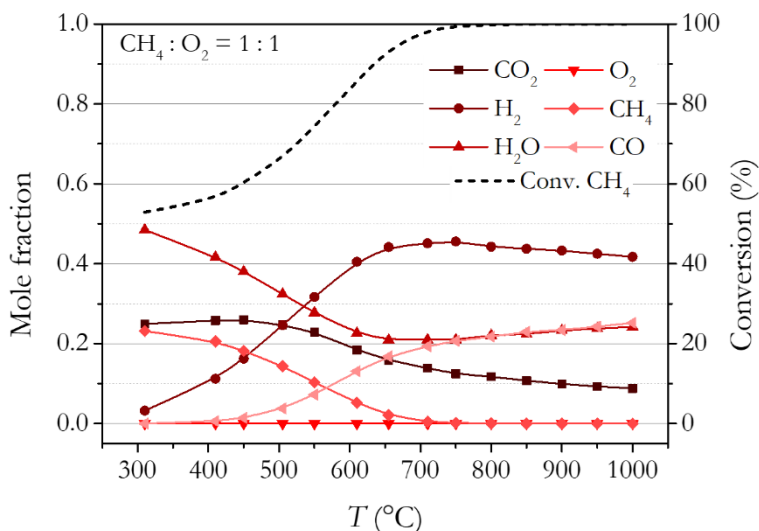
Figure 6.5: Simulations made using the DWSIM program with $CH_4:O_2$ ratio 1:1. In this condition, both POM and COM are dominating the process even if RWGS is expected at high temperature. The CH_4 conversion % is presented as black dotted line.

The calculated molar ratios, for all the methane/oxygen ratios under considerations, are reported on Table 6.1 at two different temperatures (750 °C and 800 °C). POM is expected to be promoted for temperatures above 600 °C[5] and 750 °C and 800 °C are typical operation temperatures for SOECs and also for devices which use methane as fuel. These two temperatures were considered as the best options for the experiment in a real device. One can notice that for both 750 °C and 800 °C, the simulations made with $CH_4:O_2$ ratios 4:1 and 2:1 presented molar ratio values coherent with POM reactions. In fact, the amount of hydrogen was exactly the double with respect to CO values for all those cases.

Regarding the 1:1 case, if only POM and COM are considered as possible reactions inside the reactor, the ratios H_2/CO and H_2O/CO_2 should be both =2. Looking at the number of Table 6.1 one can notice that the H_2/CO was ≈2.2 and H_2O/CO_2 ≈1.75. This could be explained only taking

Advanced strategies for Solid Oxide Electrolysis Cells

in consideration RWGS reaction. Therefore, 1:1 scenario and others, where O_2 amount is higher compared with CH_4, should be avoided.

Table 6.1: Molar factions of the obtained species at 750 °C and 800 °C for the different CH_4:O_2 ratios (4:1, 2:1, 1:1). The calculation was made using the DWSIM program and applying the *Direct Gibbs Energy Minimization* as minimization method.

T (°C)	CH_4:O_2	H_2	CO_2	CO	CH_4	H_2O
	4:1	0.50	$1.2 \ 10^{-3}$	0.25	0.25	$2.0 \ 10^{-3}$
750 °C	2:1	0.60	$1.6 \ 10^{-2}$	0.30	$4.2 \ 10^{-2}$	$2.6 \ 10^{-2}$
	1:1	0.46	0.12	0.21	$2.0 \ 10^{-3}$	0.21
	4:1	0.50	$3.8 \ 10^{-4}$	0.25	0.24	$7.1 \ 10^{-4}$
800 °C	2:1	0.63	$9.6 \ 10^{-3}$	0.31	$2.6 \ 10^{-2}$	$1.8 \ 10^{-2}$
	1:1	0.44	0.12	0.22	$5.1 \ 10^{-4}$	0.22

Figure 6.6 shows the diagram of the results presented in Table 6.1 as recap for the two temperature chosen for the experiment.

Despite a small amount of CH_4 still present in the products, which is expected to be consumed and cause coke deposition, the 2:1 ratio of CH_4 and O_2 should produce syngas with minimum amounts of water and CO_2. Increasing the temperature to 800 °C improved the methane consumption through POM reaction, decreasing the deposition of carbon. This should prevent the deactivation of the electrode and reduce the possibility for COM reaction to generate water and carbon dioxide.
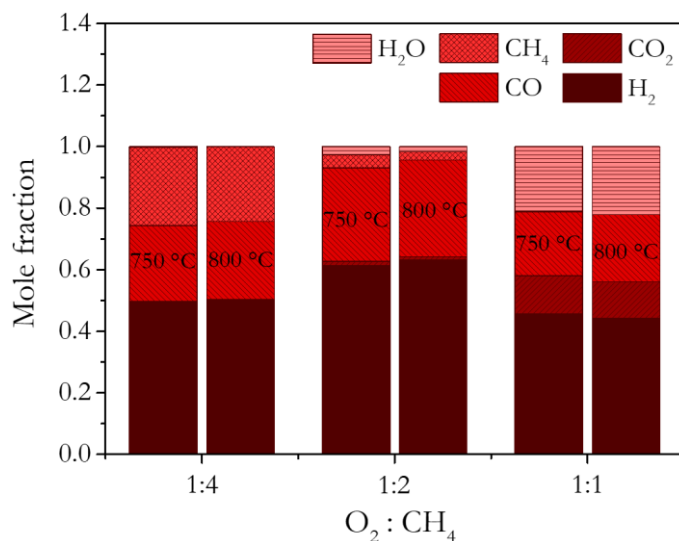
Figure 6.6: Diagram of the calculated molar factions 750 °C and 800 °C for the different CH$_4$:O$_2$ ratios. The calculation was made using the DWSIM program and applying the *Direct Gibbs Energy Minimization* as minimization method.

6.4 Cells fabrication

Fuel electrode supported half-cells (NiO-YSZ as fuel electrode and YSZ as electrolyte) prepared by tape casting (SOLIDpower S.p.A.) were used as a substrate to develop POM devices. CGO commercial powder was deposited by airbrushing on top of the dense electrolyte. The CGO backbone was sintered at 1250 °C and then it was infiltrated by an ethanol-based solution of Ni and Cu nitrates. The cells were infiltrated in a three-step process, followed by thermal calcination.

Finally, two cells were selected for the experiment, infiltrated with two different molar precursor concentration, 0.1 M and 1.3 M. The 0.1 M solution was prepared with the aim of facilitate the infiltration process due to the low concentration of cations. The calculated amount in weight % of Ni and Cu cations for this solution was ≈2 %wt. However, in most of the cases reported in literature the catalyst concentration is above the 5 %wt.[8–11] Therefore the 1.3 M solution was prepared with the aim of reach ≈10 %wt.

of Ni and Cu cations inside the CGO scaffold. The two cells were characterized and studied together to investigate the distribution of the infiltrated solution in the scaffold and the activities of the catalysts. Because of the concentration solutions, the cells were named 0.1-cell and 1.3-cell respectively.

Figure 6.7 shows a picture of the 1.3-cell after the sintering of the CGO scaffold (Figure 6.7a) and after the calcination of the infiltrated solution (Figure 6.7b).
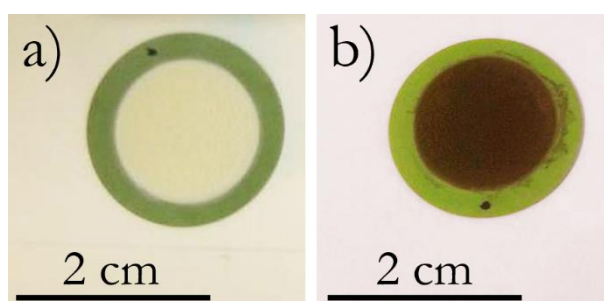

Figure 6.7: 1.3-cell after the sintering of the ceramic scaffold at 1250 °C (a) and after the infiltration and calcination process at 500 °C (b).

6.4.1 Characterization of the catalyst

Two samples of commercial CGO powder (100 mg each) were decorated with Ni and Cu oxides, using the same two solutions used for the infiltration of the cells. Such samples were prepared with the aim of evaluating the amount of catalyst necessary for the reaction with methane. The volume of the impregnation solutions (0.5 ml for each) was calculated to reproduce the same infiltration features existing in the sintered CGO scaffold of the final cells.

6.4.1.1 *SEM-EDX of functionalized powders*

The two samples impregnated by the Ni and Cu nitrate solutions with concentration 0.1 M and 1.3 M were analysed by SEM-EDX after calcination

at 500 °C for 2 h. Figure 6.8 shows the Ni and Cu amount which was around the 10 %wt. each for the 1.3 M solution. Regarding the 0.1 M one, the signal of Ni and Cu could not be detected by the instrument because it was below the limit of the SEM-EDX detector.
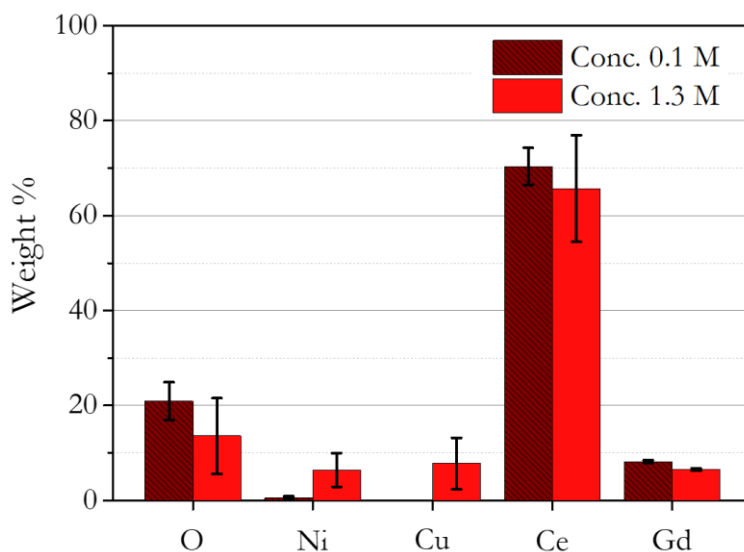

Figure 6.8: Atomic % obtained by SEM-EDX analysis of the two sets of powders impregnated by the Ni and Cu precursor solutions with concentration 0.1 M and the 1.3 M, respectively.

6.4.1.2   Characterization of catalytic activity

The powders were analysed by Thermal Programmed Reduction (TPR) using a gas mixture with 45 ml min^{-1} of N_2 and 15 ml min^{-1} of CH_4. The graph of Figure 6.9 highlights the higher signal of reduced catalysts for the powders impregnated with 1.3 M solution. The area of the reaction peak of the powder with such a solution was the 70% larger than the ones decorated with 0.1 M solution.
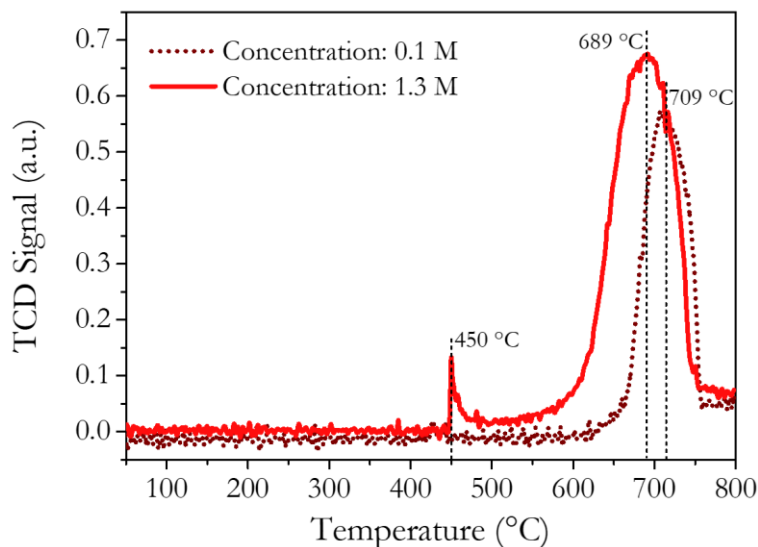
Figure 6.9: TPR analysis using a mixture of N_2 and CH_4 to test the behaviour of the different amount of catalysts exposed to methane. The gas mixture was composed by 45 ml min^{-1} of N_2 and 15 ml min^{-1} of CH_4.

The powder decorated with 0.1 M solution showed just one peak at ≈709 °C while the other sample, decorated with the solution 1.3 M, showed two peaks: a small one around ≈450 °C and a large one at ≈689 °C.[12,13] The peak at 450 °C is most likely related to Copper oxidation, which is known to happen around this temperature.[14,15] One can notice that this peak was not detected for the sample impregnated by the 0.1 M solution. The SEM-EDX analysis on such powders revealed that Cu was below the detection limit of the instrument. Furthermore, the activity of metallic copper for methane decomposition is rather poor.[13] This means that copper oxidation cannot be detected by CH_4-TPR analyses for small amount of Cu.

Both samples presented two peaks at the typical temperature for Ni oxidation.[16] Hornes *et al.* reported peaks at ≈600 °C and ≈650 °C for Ni-Cu-CGO and Ni-Cu-Ce$_2$O$_3$ catalysts.[13]

The sample decorated with 1.3 M solution showed a larger peak related to catalysts reduction, as expected by the different amount of catalyst decorating the CGO powders. The catalytic activity of samples impregnated

by such solution is expected to be larger. From the CH$_4$-TPR analysis it was highlighted that the operation temperature of devices decorated by such Ni-Cu metallic particles should be > 700 °C.

6.5   Structural characterization of the final POM cells

SEM-EDX analysis were made on the cross section of the two cells to have more information about the distribution of the elements inside the backbones. The 1.3-cell was characterized by SEM analysis, however the elemental mapping by EDX was made on a test-cell prepared on top of an YSZ tape (160 μm thickness). The CGO scaffold and the infiltration process were conducted at the same time and with the same procedure of the 1.3-cell, therefore the microstructure of the test cell can be considered as representative.

6.5.1   Microstructural analysis of scaffold infiltrated by 0.1 M solution

Figure 6.10 shows some SEM micrographs of the cell infiltrated by the precursor solution of Ni and Cu with concentration 0.1 M (0.1-cell). The CGO scaffold forming the Ni-Cu-CGO electrode can be clearly observed in Figure 6.10a, showing a continuous layer of ≈100 μm. Moreover, the infiltrated nanoparticles appeared well distributed around the area of the backbone (Figure 6.10b).

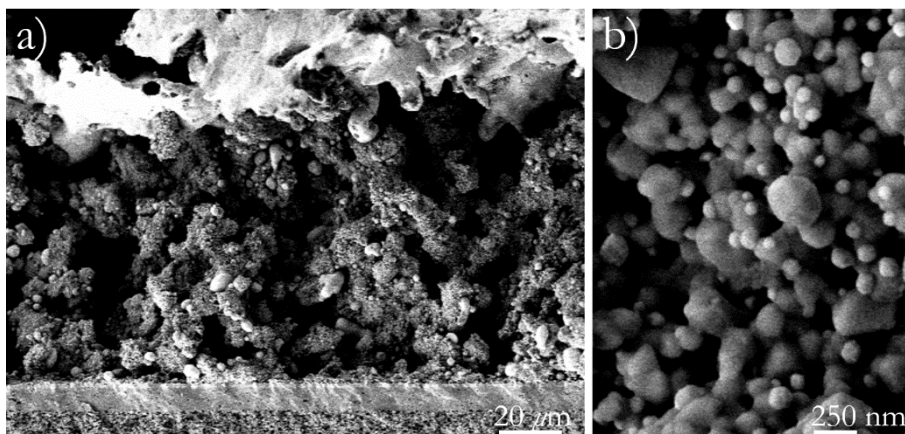Advanced strategies for Solid Oxide Electrolysis Cells

Figure 6.10: SEM micrograph of the CGO scaffold of the 0.1-cell (a). The scaffold was sintered at 1250 °C, while the infiltration with the precursor solution (0.1 M) was made in three steps with a final calcination at 500 °C. High magnification micrograph (b) which shows the infiltrated nanoparticles of Ni and Cu.

Figure 6.11 shows the SEM-EDX analysis map made on the 0.1-cell. Figure 6.11a presents the zone of the analysis, while in Figure 6.11b the elemental distribution map can be observed. Zr (blue) and Ce (white) were chosen as trace elements to identify YSZ and CGO layers, respectively. Observing Figure 6.11b one can notice blue areas, corresponding to Zr signal, located on top and inside the scaffold, while Zr signal was expected to be revealed only at the electrolyte and at the NiO-YSZ fuel electrode. Such effect can be explained as an artifact due to the overlapping between the X-ray signal of the Au M-family with the one of the Zr L-family.[17] Gold paste was deposited on top of the electrodes as current collector before assembling the cell in the measuring setup. Some gold particles penetrated inside the backbone because of its porosity and were detected from EDX analysis as Zr signal, due to the aforementioned overlap. It is reported in literature positive catalytic effects of gold nano-particles for POM reaction. Furthermore, they should reduce the carbon deposition and therefore prevent the electrode deactivation.[18] However, due to the micrometric dimension of the observed

gold particles, no considerable effects are expected on the catalytic activity of the electrode.

Ni and Cu signals are indicated by green and red colours in Figure 6.11b. They seem generally well distributed all around the structure. However, looking Ni signal seems more intense and distributed on the edges of the CGO scaffold.
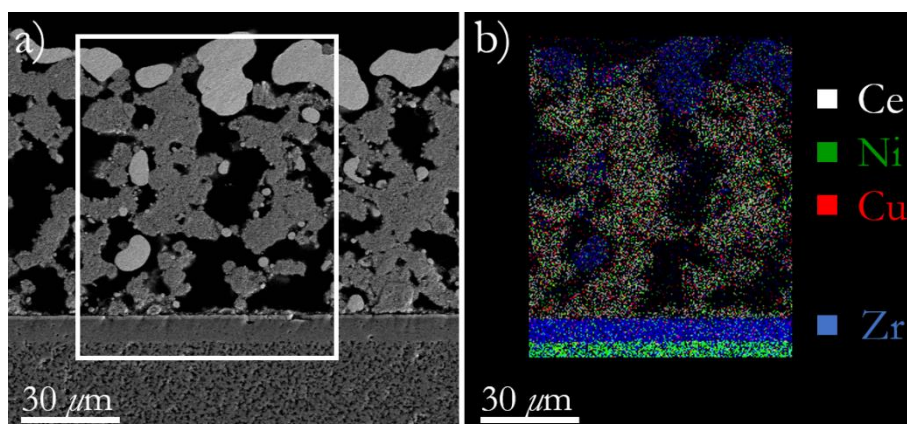

Figure 6.11: SEM micrograph of the 0.1 cell (a) presenting the area in which the EDX map was made (b). The YSZ is indicated by Zr (white), the CGO by Ce (blue). The white areas inside and on top the electrode are Au particles, which signal is overlapped with the one of Zr. Ni and Cu are indicated with green and red, respectively.

Figure 6.12 presents a line scan analysis made to quantify the Ni and Cu amounts in the scaffold of the 0.1-cell. The analysis were made on the points indicated in Figure 6.12a and the results showed in Figure 6.12b highlighted the presence of a high amount of Ni (around the 10 %at.), and a very low signal (sometimes under the detection limit) for Cu.
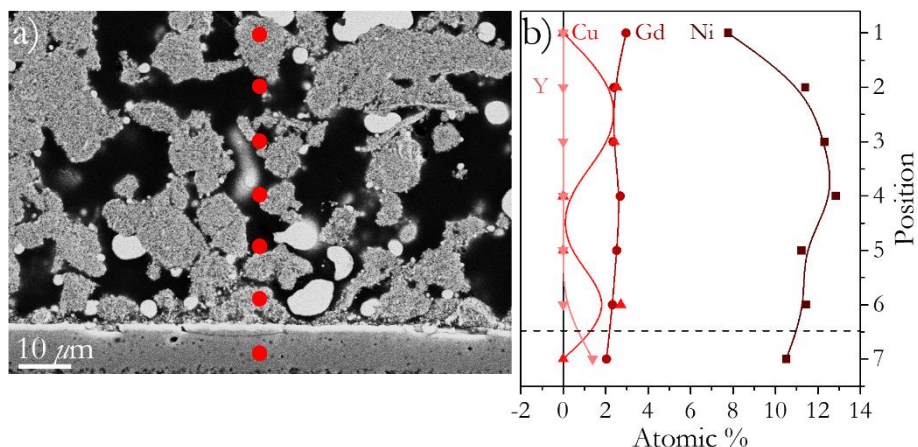
Figure 6.12: SEM micrograph (a) of the 0.1-cell, indicating the zone of the sample were the EDX line scan was made. Results of the EDX line scan (b) form the top of the electrode to the electrolyte. The interface electrode/electrolyte is indicated by a dotted line in figure.

6.5.2 Microstructural analysis of scaffold infiltrated by 1.3 M solution

The Ni-Cu-CGO electrode of the 1.3-cell presented a microstructure similar to the one of the 0.1-cell. Observing Figure 6.13 one can notice that nanoparticles were homogenously distributed around the scaffold. The presence of such particles ensures the functionalization of the CGO backbone. The picture shows a uniform layer with thickness ≈100 μm. Some big particles were revealed inside the scaffold. These particles are probably made of gold coming from the current collector hand painted on top of the cell, as in the case of the 0.1-cell. Au particles did probably not have any catalytic effect on the activity of the electrode. As already mentioned, gold nanoparticles should improve the catalytic activity with methane, but because of the dimension of the observed particles no effects were expected in this sense.
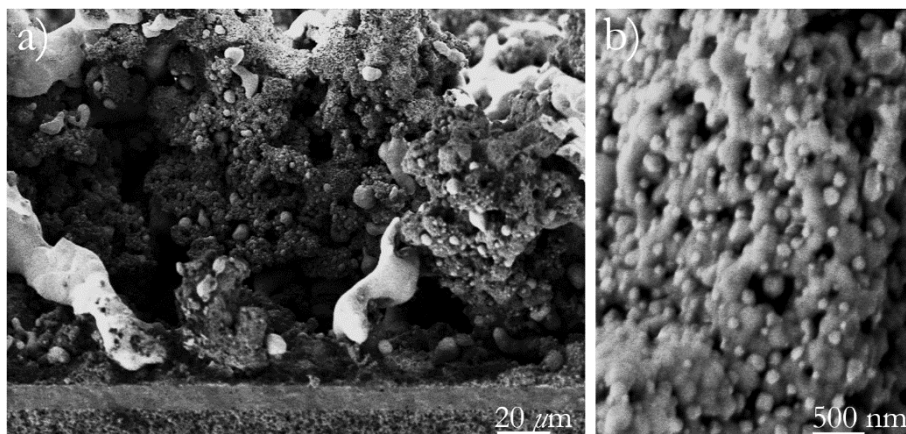
Figure 6.13: SEM micrograph of the CGO scaffold of the 1.3-cell (a). The scaffold was sintered at 1250 °C while the infiltration took place in three steps with a final calcination at 500 °C. High magnification micrograph (b) showing the infiltrated nanoparticles of Ni and Cu.

As already mentioned, the elemental analysis for the 1.3-cell was made on a test cell where the CGO scaffold was deposited directly on a YSZ tape. The scaffold was prepared and infiltrated in the same way as the 1.3-cell. Figure 6.14a shows the region of the sample where the map of Figure 6.14b was made. As in the case of the 0.1-cell, Zr (blue) and Ce (white) were chosen as marker elements for YSZ and CGO, respectively. Ni and Cu are represented by green and red dots. In this case, the scaffold showed a different elemental distribution compared with the 0.1-cell. Ni and Cu signals were present all around the scaffold, uniformly distributed. This is particularly important to ensure the catalytic functionalization of the electrode.
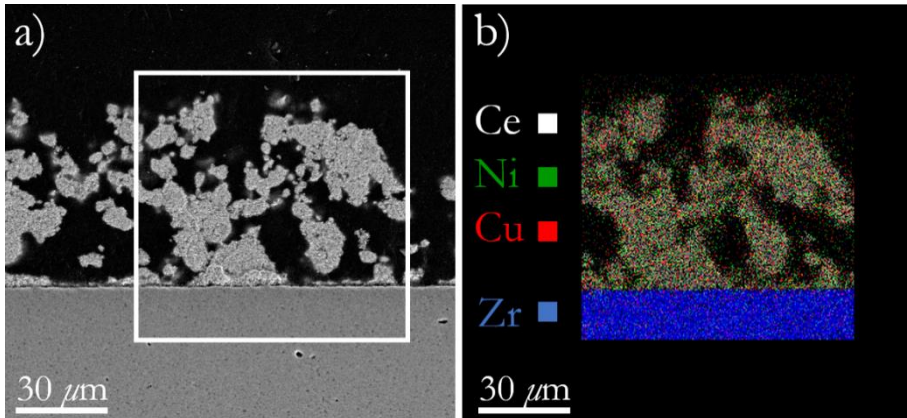
Figure 6.14: SEM micrograph of the 1.3-cell copy (a), presenting the region of the analysis. EDX map (b), where YSZ is indicated by Zr (blue), CGO by Ce (white). Ni and Cu are indicated in green and red, respectively.

Figure 6.15a shows a SEM-EDX line scan crossing from the top of the electrode to the electrolyte. The values presented in Figure 6.15b revealed a Cu and Ni amount between 3.5-5 %at for each. From such observation, it was clearly demonstrated by the micrograph and elemental microanalysis that the 1.3-cell presented a better catalysts distribution compared to the 0.1-cell.
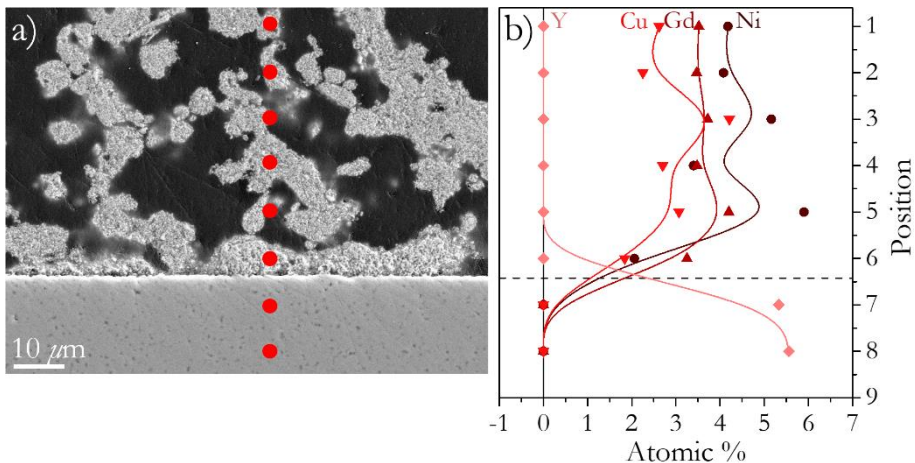

Figure 6.15: SEM micrograph (a) of the 1.3-cell copy, indicating the zone of the sample were the EDX line scan was made. Results of the EDX line scan (b) from the top of the electrode to the electrolyte. The interface electrode/electrolyte is indicated by a dotted line in figure.

6.6   Electrochemical performance

After the simulation presented in section 6.3, the devices were experimentally characterized. The performance of the 0.1-cell and of the 1.3-cell were analysed by current density-voltage polarization curves (i-V). The gas composition of the Ni-YSZ electrode was kept constant during all the experiments (50 ml min^{-1}, with 50 % H_2O and 50% H_2). The gas composition of the Ni-Cu-CGO was changed for the different tests. However, the flow was always maintained at 50 ml min^{-1}.

Together with the current density-voltage polarization curves, the characterization of the gas outlet from the measured cells is reported. The aim of this part of the work was to determine the methane consumption and try to detect the presence of hydrogen produced by POM reaction. Analysis of the gas composition was made using an Agilent 490 Micro Gas Chromatographer.

6.6.1   Preliminary test with synthetic air

The performance of the 0.1-cell and the 1.3-cell were firstly analysed at 750 °C with 50% H_2O and 50% H_2 at the fuel electrode and synthetic air at the Ni-Cu-CGO electrode as shown in Figure 6.16. This first test was made with the aim of verifying the gas tightness of the cells during the measurements. Both cells presented an OCV value ≈0.95 V. From Nernst equation (1.15) the theoretical OCV value can be calculated:[19]

$$V_{eq} = V^0 + \frac{RT}{nF} ln \left(\frac{p_{H_2} p_{O_2}^{1/2}}{p_{H_2O}} \right) \qquad (6.13)$$

Advanced strategies for Solid Oxide Electrolysis Cells

With V^0 (6.14) the standard reversible cell potential, R the ideal gas constant (R = 8.314 J mol^{-1} K^{-1}), T the temperature in K, F the Faraday constant, n the number of electrons involved and p the gas partial pressure.

$$V^0 = \frac{\Delta G^0}{nF} = \frac{\Delta H^0 - T\Delta S^0}{nF}$$
(6.14)

Where ΔG^0, ΔH^0 and $T\Delta S^0$ are respectively the electrical, total and heat energy demand at the standard state. Such values can be obtained from literature.[20] Considering the gas composition of the two electrodes, p_{H_2} and p_{H_2O} are =0.5 and p_{O_2} is =0.21. The calculated theoretical OCV was =0.96 V.[21–23] This first values confirmed the reliability of the system, which presented a good gas tightness.
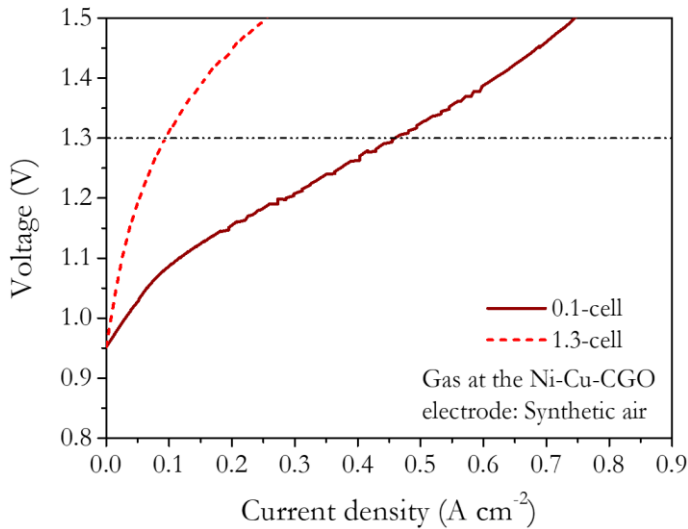

Figure 6.16: Current-voltage curve of the 0.1-cell and 1.3-cell at 750 °C. The measurements were conducted with 50% H_2O and 50% H_2 at the Ni-YSZ electrode and synthetic air at the Ni-Cu-CGO electrode to test the gas tightness of the cell.

At 1.3 V the 0.1-cell presented 0.46 A cm^{-2}, while the 1.3-cell showed only 0.1 A cm^{-2}. This values can be explained due to the lack of a percolating electronic pathway in the Ni-Cu-CGO electrode, oxygen evolution reactions

are expected to be promoted only at the Au/ceria/air TPB or on the ceria surface.[24,25]

6.6.2   Electrochemical assisted POM using H_2 as safe gas

The Ni-Cu-CGO electrodes of the 0.1-cell and the 1.3-cell were reduced and tested again at 750 °C. The 1.3-cell was tested also at 800 °C. The gas composition at the Ni-YSZ electrode was 50% H_2O and 50% H_2. For this experiment the gas composition at the Ni-Cu-CGO electrode was 82% N_2, 12% CH_4 and 6% H_2. The 6% of H_2 was used as safe gas, to avoid re-oxidation phenomena. Furthermore, the presence of H_2 moved the equilibrium of the CH_4 decomposition reaction (6.9) to the reactants, decreasing the risk of coke deposition. The results of the measurements are presented in Figure 6.17: note that for these measurements OCVs presented negative values. This is due to the presence of methane and hydrogen at the Ni-Cu-CGO electrode. The measured OCV values at 750 °C were ≈-0.15 V for the 0.1-cell and ≈-0.14 V for the 1.3-cell. At 800 °C the OCV of the 1.3-cell was -0.17 V. This fact is correlated with the negative ΔG that POM reaction presents for temperatures above 650 °C. At high temperature POM can occur spontaneously and that makes electrochemical assisted POM much more convenient compared to conventional electrolysis processes.[1]
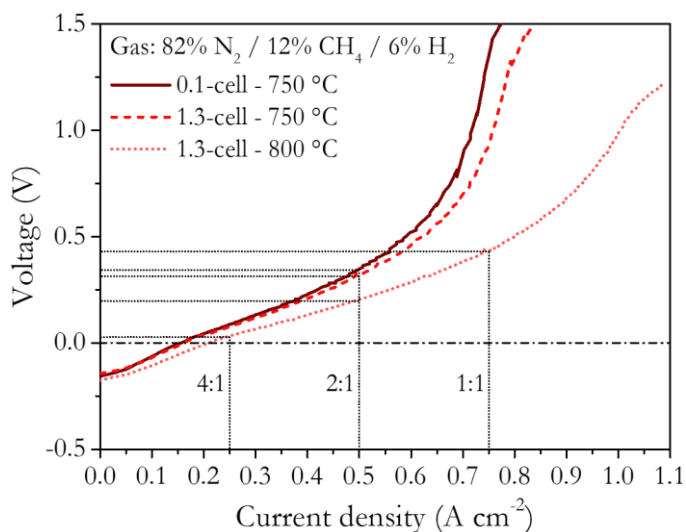
Advanced strategies for Solid Oxide Electrolysis Cells

Figure 6.17: *i*-V curves of the 0.1-Cell at 750°C and of 1.3-Cell at 750 and 800 °C. The measurements were made with 50% H_2O/50% H_2 at the Ni-YSZ electrode and 82% N_2/12% CH_4/6% H_2 at the Ni-Cu-CGO electrode. The dotted lines in figure indicate the current densities used for the experiments and the corresponding CH_4:O_2 ratio is reported. At 750 °C the 0.1-cell and the 1.3-cell were tested applying 0.5 A cm^{-2}, while at 800 °C the 1.3-cell was measured at 0.25 A cm^{-2}, 0.5 A cm^{-2} and 0.75 A cm^{-2}.

At 750 °C, the performance of the 1.3-cell appeared to be slightly better compared to the 0.1-cell, with 0.63 A cm^2 compared to 0.6 A cm^2 at 0.5 V (end of the linear part of the curve). As expected, increasing the temperature up to 800 °C improved the performance of the 1.3-cell, which reached 0.8 A cm^{-2} at 0.5 V.

As shown by the simulation presented above, the best condition to produce syngas by POM was satisfied when the molar ratio between CH_4:O_2 was 2:1.[4] The desired CH_4 flow during all the experiments was maintained at ≈5.8 ml min^{-1}. If the flow is normalized for the area of the cell (≈1.54 cm^2), the value become ≈3.8 ml min^{-1} cm^{-2}. Assuming that reactants and products behave like ideal gases, the molar flow of methane ($n_{CH_4}^{flow}$) can be calculated by equation (6.15):

$$n^{flow} = \frac{flow}{V_{mol}} \tag{6.15}$$

Where V_{mol} is the molar volume of a gas ($22.4 \; 10^3$ ml mol^{-1}). Therefore, $n^{flow}_{CH_4} = 1.7 \; 10^{-4}$ mol min^{-1} cm^{-2} and considering the mentioned ratio 2:1 between CH$_4$ and O$_2$, the necessary oxygen flow to promote POM reaction is the half, i.e. $n^{flow}_{O_2} = 1.9 \; 10^{-5}$ mol min^{-1} cm^{-2}.

In an SOEC the oxygen that is driven to the anode through the electrolyte is proportional to the applied current. In the case of the electrochemically assisted POM the same principle is applied. The current density j was found using (6.16):

$$j = n^{flow}_{O_2} \; z \, F \tag{6.16}$$

Where z is the number of electrons involved (for O$_2$ z = 4), F the Faraday constant. The resulting current density for POM is $j = 0.5$ A cm^{-2}.

At such a current density the two cells presented small voltage values, which were 0.32 V (0.1-cell at 750 °C), 0.35 V (1.3-cell at 750 °C) and 0.21 V (1.3-cell at 800 °C). This demonstrated that for the gas composition used both cells were suitable for the POM experiment. One can notice that at 800 °C the linear part of the i-V curve reached ≈0.9 A cm^{-2}. This means that, at such temperature and gas composition, higher currents can be safely used. In particular 0.75 A cm^{-2}, which corresponds to the CH$_4$:O$_2$=1:1 situation presented in the simulation section. For such current both POM and COM should be promoted, and no carbon deposition is supposed to occur.

6.6.2.1 *Gas outlet characterization of the measurements with safe gas*

Figure 6.18 shows the results of the μGC analysis made on the two cells (0.1-cell and 1.3-cell) at 750 °C. The experiment was conducted applying a current density of 0.5 A cm^2, which was demonstrated to provide the

necessary amount of oxygen for POM reaction. The two measurements were conducted providing 2.9 ml min^{-1} of H_2 as a safe gas (gas composition: 82% N_2, 12% CH_4, 6% H_2).

The data presented in Figure 6.18 are the percentage of methane consumed, together with the flows in ml min^{-1} measured by the μGC. The N_2 flows (41.3 ml min^{-1} and 44.2 ml min^{-1} for measurements with and without safe gas respectively) were considered constant during the experiments. Such flows, not reported in the plots, were used as reference, to convert the μGC output in flow units.

The methane consumed was the 38 % for the 0.1-cell measured with H_2 as a safe gas. In the case of the 1.3-cell the consumption percentage was around 19 %.

Regarding the products, as mentioned the values for the unconsumed methane and for the N_2 reference are not shown. The three species considered were H_2, CO and CO_2. Such compounds are the three products which can give some indication about the type of reaction that took place in the cell.

The most reliable indicator for POM reaction was CO. For the first two measurements made on the 0.1-cell and the 1.3-cell the measured CO was ≈0.29 ml min^{-1} and ≈0.36 ml min^{-1}, respectively. From this analysis the 1.3-cell seemed the best candidate for the electrochemically assisted POM, despite the lower percentage of methane consumed. In the case of the 1.3-cell a small amount of CO_2 (≈0.20 ml min^{-1}) was also detected, probably caused by the occurrence of COM reaction.

Quantification of relevant products such as H_2 were affected by possible leakages and instrumental limitation (impossibility to measure H_2O formed), respectively. Moreover, hydrogen can react with oxygen to produce water, altering its amount in the final composition of the gas outlet.

The poorer selectivity of the 0.1-cell towards POM reaction can be explained by the catalyst distribution highlighted by SEM-EDX analysis. Ni accumulation around certain zones of the CGO scaffold was highlighted and it was probably connected with the infiltration process. This distribution issue was probably caused by the low concentration of the solution and de-wetting phenomena. Such results confirmed the necessity of larger infiltration volumes or the utilization of solutions with higher concentration.
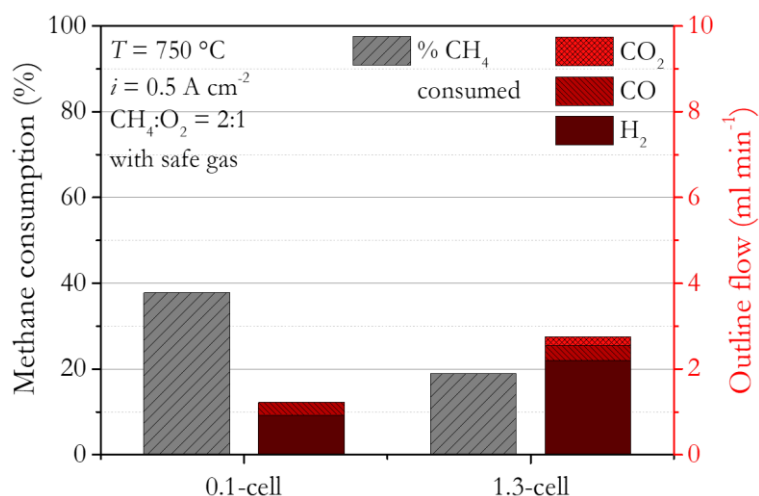

Figure 6.18: Measurements of the outlet gas composition during the tests made on the 0.1-cell and 1.3-cell with 0.5 A cm^{-2} applied. Considering this current density, the CH$_4$:O$_2$ ratio should correspond to 2:1. The gas composition at the Ni-YSZ electrode was in all cases 50 ml min^{-1} with 50% H$_2$O/50% H$_2$. At the Ni-Cu-CGO electrode a flow of 50 ml min^{-1} was supplied. The gas compositions used were 82% N$_2$/12% CH$_4$/6% H$_2$.

Figure 6.19 shows the measurements at 800 °C with safe gas applying different currents, 0.25 A cm^{-2}, 0.5 A cm^{-2} and 0.75 A cm^{-2}. On both electrodes 50 ml min^{-1} were supplied. The gas composition at the Ni-YSZ electrode was 50% H$_2$O/50% H$_2$, while at the Ni-Cu-CGO it was 82% N$_2$/12% CH$_4$/6% H$_2$. The initial amount of CH$_4$ was ≈5.8 ml min^{-1}. Considering the relation between the current and the amount of oxygen

moved to the Ni-Cu-CGO electrode, the three measurements should correspond to the simulated ratios of $CH_4:O_2$, which are 4:1, 2:1 and 1:1.

The CH_4 consumed during the three measurements was $\approx 26\%$, $\approx 27\%$ and $\approx 28\%$. Looking at the production of CO and CO_2 during the experiments one can notice that carbon monoxide decreased with the current, while carbon dioxide increased. Considering 0.25 A cm^{-2}, 0.5 A cm^{-2} and 0.75 A cm^{-2} applied currents, the measured values for CO were ≈ 0.6 ml min^{-1}, ≈ 0.5 ml min^{-1} and ≈ 0.4 ml min^{-1}, while the CO_2 measured was ≈ 0.2 ml min^{-1}, ≈ 0.3 ml min^{-1} and ≈ 0.4 ml min^{-1}. Looking at the simulations made in section 6.3, no CO_2 should have been produced for 0.25 A cm^{-2}. Furthermore, for the measurement where 0.5 A cm^{-2} was applied, much less CO_2 should have been produced compared with the CO flow.

As in the case of the previous measurements, the percentage of consumed methane can be revealing. The oxygen electrochemically driven was in all the cases in excess in comparison to the consumed methane. In fact, by the reduction of the current, the CO production increased, while CO_2 decreased. This means that the ideal condition for POM reaction was approached by decreasing the oxygen provided. However, this was not the main goal of the experiment, which was the consumption of almost all the methane to produce syngas. Oxygen was never detected by the gas chromatographer, highlighting that it reacted in some way.

One hypothesis can be that only a part of the methane entered in contact with the oxygen driven to the Ni-Cu-CGO electrode by the current. This could happen because methane did not diffuse properly inside the electrode or because most of the oxygen was consumed fast. This oxygen consumption could have been provoked by hydrogen to form water or by the reoxidation of part of the Ni and Cu catalysts. This is in agreement with the amounts of hydrogen measured and reported in Figure 6.19. One can notice that hydrogen amount dropped with the increase of the current (i.e.

oxygen), although these values can have been influenced by leakages (as mentioned before).
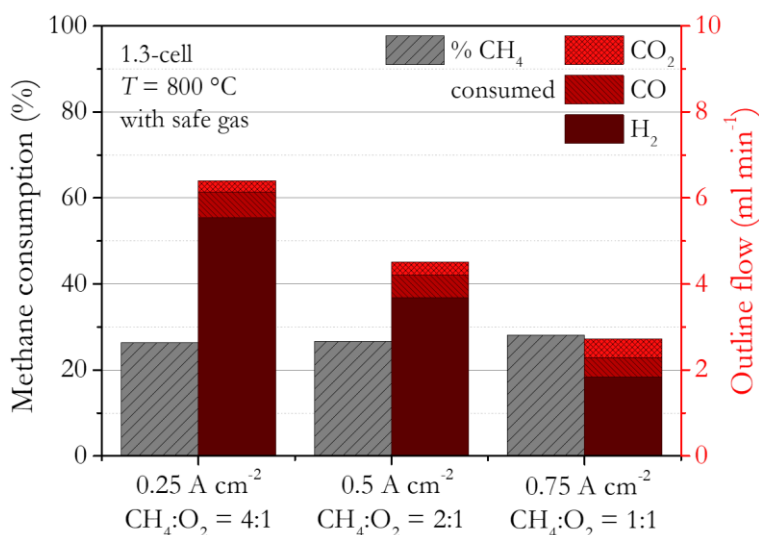

Figure 6.19: Results of the μGC analysis on the 1.3-cell. The cell was measured 800 °C with different current applied: 0.25 A cm^{-2}, 0.5 A cm^{-2} and 0.75 A cm^{-2}, corresponding to $CH_4:O_2$ ratios 4:1, 2:1 and 1:1, respectively. The gas composition at the Ni-YSZ electrode was in all cases 50 ml min^{-1} with 50% H_2O/50% H_2. At the Ni-Cu-CGO electrode a flow of 50 ml min^{-1} was supplied. The gas compositions used was 82% N_2/12% CH_4/6% H_2.

6.6.3   Electrochemical assisted POM without safe gas

Some other experiments were conducted on the 1.3-cell at 750 °C and 800 °C. In this case the gas composition at the Ni-Cu-CGO electrode was 50 ml min^{-1} 88 % N_2/12 % CH_4, therefore no safe gas was utilized. i-V measurements at the two temperature are showed in Figure 6.20.

One can notice that the two curves were quite similar in performances, with 0.45 A cm^{-2} and 0.47 A cm^{-2} at 0.5 V for the measurements at 750 °C and 800 °C, respectively.

Observing the plot, the device showed a reasonable performance at 800 °C, which demonstrated the availability for POM experiments applying

Advanced strategies for Solid Oxide Electrolysis Cells

0.5 A cm^{-2}. The oxygen supplied at such current corresponded to half of the CH$_4$, which is the ideal condition to promote POM towards other reactions.
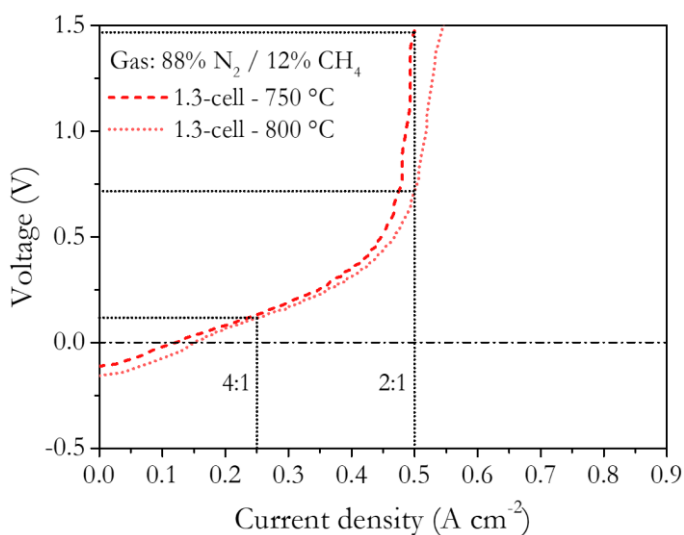

Figure 6.20: *i*-V curves of the 1.3-Cell at 750 °C and 800 °C. The gas composition at the Ni-Cu-electrode is 88.4% of N$_2$ and 11.6 % of CH$_4$. The dotted lines in figure indicate the current densities used for the experiments and the corresponding CH$_4$:O$_2$ ratio is reported. At 750 °C the 1.3-cell was tested applying 0.5 A cm^{-2}, while at 800 °C it was measured at 0.25 A cm^{-2} and 0.5 A cm^{-2}.

6.6.3.1   Gas outlet characterization of the measurements without safe gas

The 1.3-Cell gas outlet was measured at 750 °C applying 0.5 A cm^{-2} and 800 °C, applying 0.25 and 0.5 A cm^{-2}. The three measurements are presented in Figure 6.21. The methane consumed was ≈28 % at 750 °C, while at 800 °C was ≈27 % for 0.25 A cm^{-2} and ≈29 % for 0.5 A cm^{-2}. The performances were quite similar among them in terms of methane consumption.

The two measurements conducted applying 0.5 A cm^{-2} presented in both cases a certain amount of CO$_2$: 0.8 ml min^{-1} and 0.7 ml min^{-1} at 750 °C and 800 °C. These results could be explained taking in consideration that not all the methane was converted. The oxygen amount provided by the current was calculated starting from the CH$_4$ supplied at the Ni-Cu-CGO. This

267

means that the oxygen was in excess compared with the methane that reacted. Looking at the simulations presented above and to the literature,[2] it is possible to conclude that these conditions promoted COM reaction instead of POM.

Considering the two measurements at 800 °C with 0.25 A cm^{-2} and 0.5 A cm^{-2}, one can notice that, as in the case of the previous sections, where safe gas was used, CO decreased with the current and CO_2 increased. For 0.25 A cm^{-2} and 0.5 A cm^{-2} the CO flows measured were ≈0.6 ml min^{-1} and ≈0.3 ml min^{-1}, while the CO_2 flows were ≈0.4 ml min^{-1} and ≈0.7 ml min^{-1}. Interestingly, the measurements using 0.25 A cm^{-2} was the only measurements made without safe gas in which hydrogen was revealed by the μGC.

The CO_2 production with low current was not expected and could mean that only part of the oxygen provided by the current was able to reach the methane supplied. The rest of the oxygen reacted with some other component present in the gas mixture, likely hydrogen to form water. In this case no hydrogen was supplied as safe gas, therefore the oxygen in excess should react only with the one produced by POM or methane decomposition. Also, some leakages could have been present and hydrogen from the Ni-YSZ could have been passed to the Ni-Cu-CGO during the experiments. Another possibility is that oxygen reacted with the Ni and Cu catalysts and this could have caused a reoxidation of the catalysts which also influenced the performance of the device.
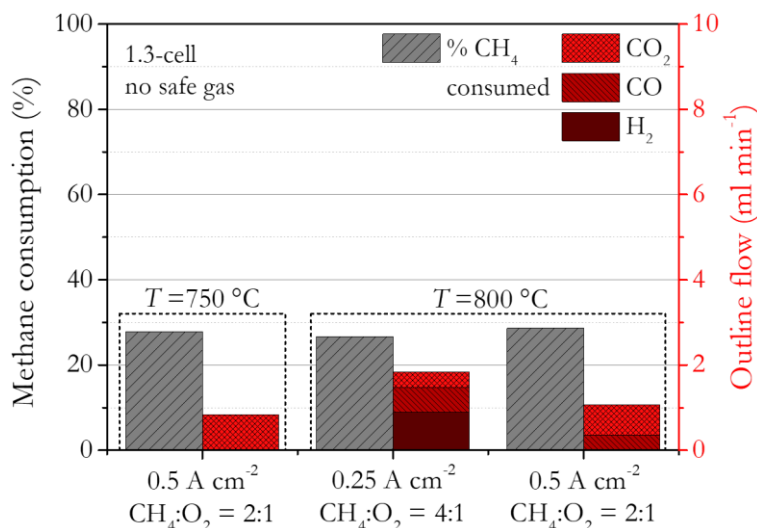
Figure 6.21: Results of the *μ*GC analysis on the 1.3-cell. The cell was measured at 750 °C and 800 °C with different current applied: 0.25 A cm^{-2} and 0.5 A cm^{-2}. The gas composition at the Ni-YSZ electrode was in all cases 50 ml min^{-1} with 50% H_2O/50% H_2. At the Ni-Cu-CGO electrode a flow of 50 ml min^{-1} was supplied. The gas compositions used was 88.4 N_2/11.6% CH_4.

Supposing that the main reactions that acted in this process were POM, COM, methane decomposition and water formation, it is possible to do some further consideration. Some calculations were made to predict the H_2 amount considering the CO and CO_2 values measured and the CH_4 consumed. The results are reported in Table 6.2 for the measurements at 800 °C.

The methane consumed was calculated by the difference between the one supplied at the inlet (≈5.8 ml min^{-1}), minus the values measured by chromatography analysis. CO and CO_2 measured values were considered the reference to determine the amount of CH_4 consumed by POM and COM, respectively. The rest of the methane was supposed to be consumed by CH_4 decomposition reaction, to produce hydrogen. Therefore, it is possible to determine the theoretical value of H_2 produced. The O_2 flows were calculated from the current applied. CO and CO_2 measured amounts were also used to determine the amount of oxygen consumed by POM and COM reactions.

The calculated hydrogen produced by POM and by CH_4 decomposition was 1.94 ml min^{-1}(0.25 A cm^{-2}) and 2.62 ml min^{-1}(0.5 A cm^{-2}). Taking into consideration the water formation reaction between the hydrogen produced and the oxygen remaining 1.5 ml min^{-1} and 0 ml min^{-1} were calculated for 0.25 A cm^{-2} and 0.5 A cm^{-2} current densities. Furthermore, 0.35 ml min^{-1} of O_2 should have been measured for 0.5 A cm^{-2}.

From the results presented in Table 6.2 the measured hydrogen amount was ≈0.9 ml min^{-1} and ≈0 ml min^{-1} for 0.25 A cm^{-2} and 0.5 A cm^{-2}. No oxygen was detected during both measurements. It is possible that some leakages supplied additional H_2 from the Ni-YSZ electrode, this could explain the larger amount of hydrogen measured for 0.25 A cm^{-2} and the complete oxygen consumption observed for 0.5 A cm^{-2}.

Table 6.2: Results of the calculation of H_2 theoretical values expected considering POM, COM, CH_4 decomposition and formation of water as the only reactions. The calculations are made starting from the CH_4 consumed (the injected values minus the measured one) and using the measured CO and CO_2 values as reference for POM and COM reactions.

	i = 0.25 A cm^{-2}	i = 0.5 A cm^{-2}
CH_4 consumed	1.55 ml min^{-1}	1.66 ml min^{-1}
CH_4 consumed by POM/COM	0.94 ml min^{-1}	1.06 ml min^{-1}
CH_4 consumed by CH_4 dec.	0.60 ml min^{-1}	0.60 ml min^{-1}
H_2 produced by POM	0.73 ml min^{-1}	1.41 ml min^{-1}
H_2 produced by CH_4 dec.	1.21 ml min^{-1}	1.21 ml min^{-1}
H_2 Tot	1.94 ml min^{-1}	2.62 ml min^{-1}
O_2 from current	1.45 ml min^{-1}	2.90 ml min^{-1}
O_2 remaining after POM/COM	0.43 ml min^{-1}	1.31 ml min^{-1}
O_2 remaining	0.00 ml min^{-1}	0.35 ml min^{-1}
H_2 remaining after H_2O formation	1.51 ml min^{-1}	0.00 ml min^{-1}

Looking at the results of the different experiments made, the main problem seemed related to the permeability of methane inside the electrode. Most of the methane did not react with the oxygen provided by the

electrolysis reaction. This could be connected with the microstructure of the electrode, e.g. thickness too large, porosity not sufficiently opened, infiltration which obstructs the gases permeability.

The utilization of functional electrode made of mesoporous materials as backbones can be a possible solution for this problem. The open porosity of mesoporous materials (> 100 $m^2 g^{-1}$) should improve the permeability of the gases inside the electrode.[26,27] Furthermore, the utilization of functional layers with thickness in the range 10-20 μm, should promote the reaction between methane and oxygen.

Ni and Cu reoxidation is another possible reason for the low methane consumption rate and it would explain why no oxygen was measured during the experiments. A possible solution to prevent catalyst reoxidation is the utilization of perovskites instead of bimetallic materials. It has been demonstrated that B-site doping of typical catalyst elements (e.g. Ni, Ru, Fe, etc…) in perovskites can effectively promote POM reaction and the stability of the catalyst during operation.[28,29]

6.7   Conclusion

Electrochemically enhanced POM for production of syngas was studied in this chapter. Two cells with NiO-YSZ/YSZ/Ni-Cu-CGO composition were fabricated for electrochemical assisted partial oxidation of methane to produce syngas.

Simulations were made to determine the best condition for promoting POM reaction. Such simulations highlighted the molar ratio 2:1 of CH_4 and O_2 as the best option for syngas production. Furthermore 800 °C was found as the best temperature to maximize the production of H_2 and CO and reduce the possible coke deposition.

The infiltrated cells were microstructurally and compositionally characterized. Moreover, they were electrochemically tested at two temperatures (750 °C and 800 °C) and using two different atmospheres at the Ni-Cu-CGO electrode (82.6% N_2/11.6% CH_4/5.8% H_2 and 88.4% N_2/11.6% CH_4).

From the analysis of the gases outline the maximum methane consumption reached was ≈38 % for the cell with CGO scaffold infiltrated by 1-3 %wt of Ni and Cu catalysts. The measurement was conducted at 750 °C and with safe gas. This value is far from the simulated values that predicted ≈85% of methane consumption. Other measurements on the cell with catalysts amount ≈10%wt, showed consumption percentages around 20-30 %. For this cell, the measurements at 800 °C presented the best results, with methane consumption values ≈30 %. In almost all the measurements, CO_2 was also detected in disagreement with the results obtained from simulations. In fact, CO_2 produced by COM reactions was expected for CH_4:O_2 ratios higher than 2. Considering the initial methane flow supplied, which was ≈5.8 ml min^{-1}, such condition was respected for all the current densities ≤0.5 A cm^2.

From such considerations is possible to conclude that the incomplete methane conversion was mainly due to poor permeability of the gas inside the electrode or because the oxygen coming from the electrolyte reacted with the catalysts. These considerations mean that part of the methane did not enter in contact with the oxygen or that the catalysts, partially re-oxidated, did not effectively promoted POM reaction.

Gas permeability problems can be easily solved by the utilization of porous nanostructure like mesoporous scaffolds, characterized by high open porosities which can greatly improve the performance of the device. Regarding the catalyst reoxidation, the utilization of perovskite catalysts,

Advanced strategies for Solid Oxide Electrolysis Cells

which can be very selective for POM reaction and present good stability during operation is a possible solution.

Despite these considerations, the working principles of the electrochemically assisted POM were demonstrated. The production of CO, which is directly correlated to the POM reaction, was detected in all the experiments. Considering the tests made applying 0.25 A cm^{-2} a CO flow of ≈0.6 ml min^{-1} was measured with and without the utilization of H_2 as safe gas. Starting from this study it will be possible to further improve the CH_4 consumption and the direct syngas production by means of electrochemically assisted partial oxidation of methane. If optimized, this method can represent an alternative to the current steam reforming increasing the production of syngas and simplifying the process.

6.8 Bibliography

1   Y. Wang, T. Liu, S. Fang, G. Xiao, H. Wang and F. Chen, *J. Power Sources*, 2015, **277**, 261–267.

2   T. M. Gür, *Prog. Energy Combust. Sci.*, 2016, **54**, 1–64.

3   Y. Zheng, J. Wang, B. Yu, W. Zhang, J. Chen, J. Qiao and J. Zhang, *Chem. Soc. Rev.*, 2017, **46**, 1427–1463.

4   J.-H. Koh, B.-S. Kang, H. C. Lim and Y.-S. Yoo, *Electrochem. Solid-State Lett.*, 2002, **4**, A12–A15.

5   T. J. Siang, A. A. Jalil, A. A. Abdulrasheed, H. U. Hambali and W. Nabgan, *Energy*, 2020, **198**, 1–14.

6   K. Tangsriwong, P. Lapchit, T. Kittijungjit, T. Klamrassamee, Y. Sukjai and Y. Laoonual, *IOP Conf. Ser. Earth Environ. Sci.*, 2020, **463**, 012057.

7   M. Reytier, S. Di Iorio, A. Chatroux, M. Petitjean, J. Cren, M. De Saint Jean, J. Aicart and J. Mougin, *Int. J. Hydrogen Energy*, 2015, **40**, 11370–11377.

8   A. Hornés, D. Gamarra, G. Munuera, J. C. Conesa and A. Martínez-Arias, *J. Power Sources*, 2007, **169**, 9–16.

9   B. Christian Enger, R. Lødeng and A. Holmen, *Appl. Catal. A Gen.*, 2008, **346**, 1–27.

10   A. Hornés, M. J. Escudero, L. Daza and A. Martínez-Arias, *J. Power Sources*, 2014, **249**, 520–526.

11   J. Lu, C. Zhu, C. Pan, W. Lin, J. P. Lemmon, F. Chen, C. Li and K. Xie, *Sci. Adv.*, 2018, **4**, 1–8.

12   J. Juan-Juan, M. C. Román-Martínez and M. J. Illán-Gómez, *Appl. Catal. A Gen.*, 2009, **355**, 27–32.

13   A. Hornés, P. Bera, M. Fernández-García, A. Guerrero-Ruiz and A. Martínez-Arias, *Appl. Catal. B Environ.*, 2012, **111–112**, 96–105.

14   L. Kundakovic and M. Flytzani-Stephanopoulos, *Appl. Catal. A Gen.*, 1998, **171**, 13–29.

15   G. Águila, F. Gracia, J. Cortés and P. Araya, *Appl. Catal. B Environ.*, 2008, **77**, 325–338.

16   O. Dewaele and G. F. Froment, *J. Catal.*, 1999, **184**, 499–513.

17   D. E. Newbury and N. W. M. Ritchie, *J. Mater. Sci.*, 2014, **50**, 493–518.

18   T. P. Maniecki, K. Bawolak, D. Gebauer, P. Mierczynski and W. K. Jozwiak, *Kinet. Catal.*, 2009, **50**, 138–144.

19   E. M. Hernández Rodríguez, University of Barcelona, 2018.

20   M. W. Chase, *NIST-JANAF Thermochemical Tables*, 1998, vol. 9.

21   M. Ni, M. K. H. Leung and D. Y. C. Leung, *Int. J. Hydrogen Energy*, 2007, **32**, 2305–2313.

22   J. P. Stempien, Q. Liu, M. Ni, Q. Sun and S. H. Chan, *Electrochim. Acta*, 2014, **147**, 490–497.

23   L. Bernadet, J. Laurencin, G. Roux, D. Montinaro, F. Mauvy and M. Reytier, *Electrochim. Acta*, 2017, **253**, 114–127.

24   M. Mogensen, N. M. Sammes and G. A. Tompsett, 2000, **129**, 63–94.

25   J. Koettgen, S. Grieshammer, P. Hein, B. O. H. Grope, M. Nakayama and M. Martin, *Phys. Chem. Chem. Phys.*, 2018, **20**, 14291–14321.

Advanced strategies for Solid Oxide Electrolysis Cells

26   M. Torrell, L. Almar, A. Morata and A. Tarancón, *Faraday Discuss.*, 2015, **182**, 423–435.

27   L. Almar, A. Morata, M. Torrell, M. Gong, M. Liu, T. Andreu and A. Tarancón, *J. Mater. Chem. A*, 2016, **4**, 7650–7657.

28   S. McIntosh and M. Van Den Bossche, *Solid State Ionics*, 2011, **192**, 453–457.

29   A. H. Elbadawi, L. Ge, Z. Li, S. Liu, S. Wang and Z. Zhu, *Catal. Rev. - Sci. Eng.*, 2020, **00**, 1–67.

Chapter VII

Conclusion

7.1 Conclusion

The present thesis was devoted to the exploration of new concepts for advanced solid oxide electrolysis devices. The thesis was focused on three main topics: i) the hybrid printing of SOC devices by means of additive manufacturing techniques, i.e. inkjet printing and robocasting; ii) the synthesis of mesoporous CGO materials for the fabrication of nanocomposite oxygen electrode for SOC devices; iii) the fabrication of cells based on nanocomposite electrodes and their long term characterization in real operation conditions; iv) the study of a novel electrochemically assisted partial oxidation of methane as an alternative strategy for syngas production. More specifically, the conclusions of this thesis can be summarized by topics as follows:

- **Automatic infiltration of functional electrodes by inkjet printing and fabrication of fully 3D printed cells by hybrid inkjet and robocasting printing.**
  - Automatic infiltration by means of inkjet printing demonstrated to be an excellent alternative for electrode functionalization. Electrochemical performances of YSZ/CGO+LSCF symmetrical cells automatically infiltrated by inkjet printing were tested at 750 °C. Good electrical percolation of the electrode and extension of the TPB were obtained due to the adjustment of the printing parameters. Furthermore, the utilization of ordered mesoporous materials as ceramic scaffold demonstrated to be particularly effective to improve the distribution of the infiltration solution. ASR_s and ASR_{pol} passed from 2.7 Ω cm^2 and 1.3 Ω cm^2, for a reference cell without infiltration, to 0.8 Ω cm^2 and 0.1 Ω cm^2 for

Advanced strategies for Solid Oxide Electrolysis Cells

a cell characterized by mesoporous CGO scaffold automatically filtrated by inkjet printing with LSCF perovskite.

o Fully printed symmetrical cells were fabricated obtaining dense inkjet-printed YSZ electrolyte (thickness $\approx 3\,\mu$m) and porous robocasted LSM-YSZ electrodes. The formulated inks demonstrate a good compatibility in terms of mechanical properties and showed electrochemical behaviour compatible with SoA cells of the same composition ($\approx 0.9\ \Omega\ cm^2$ at 750°C). These results demonstrated the potential of robocasting and inkjet printing as fabrication techniques for fully 3D-printed SOC.

- **CGO mesoporous properties were studied and a new synthesis route was presented in order to solve previously observed issues related to this material.**

  o The studied optimized synthesis route allowed the reduction of the SiO_2 contamination coming from the template from ≈ 0.9 %wt to ≈ 0.2 %wt. Furthermore, the sintering temperature was successfully reduced to 850 °C thanks to Co oxide decoration.

  o TEM analysis has highlighted dopant clusters all around the mesoporous interfaces. These zones with high concentration of Gd were effectively removed by HF etching.

  o Ionic conductivity and catalytic activity of these materials were improved. This was effectively demonstrated by the electrochemical measurements of the YSZ/CGO_{meso} symmetrical cell. At 750°C ASR_s and ASR_{pol} passed from 54.4 $\Omega\ cm^2$ and $1.2 \cdot 10^3\ \Omega\ cm^2$, for a mesoporous CGO scaffold fabricated without the presented optimized route, to 13.6 $\Omega\ cm^2$ and $2.2 \cdot 10^2\ \Omega\ cm^2$, for a cell with mesoporous CGO scaffold after etching by HF and Co oxide decoration.

Advanced strategies for Solid Oxide Electrolysis Cells

- **CGO mesoporous materials have been successfully adapted as scaffold for high performance oxygen electrode in SOC applications.**
  - A complete SOC was fabricated with oxygen electrode made of mesoporous CGO etched by HF and decorated by Co oxide, infiltrated by LSCF. The button cell was tested in SOFC at, steam and co-electrolysis mode 750 °C, yielding power densities as high as 1.35 W cm^{-2} at 0.7 V and injected currents above 1.3 A cm^{-2} at 1.3 V, respectively. To the best of the author's knowledge, the performance measured in COSOEC mode was the best result ever measured for a co-electrolysis device operating at these conditions (H$_2$O 65%, CO$_2$ 25%, H$_2$ 10%, 750 °C). The durability test under co-electrolysis was conducted for more than 1100 hours and highlighted a degradation rate of 106 mV kh^{-1}.
  - Large area cell (25 cm^2) with oxygen electrode made of mesoporous CGO infiltrated by LSCF perovskite were electrochemically tested at 750 °C in SOEC and COSOEC modes. The scalability of the process for mesostructured scaffold was successfully demonstrated. Under co-electrolysis currents of 10.9 A (0.68 A cm^{-2}) were reached. A durability test of 600 h with an applied current of 8 A (0.5 A cm^{-2}) was conducted, measuring a drop of voltage of 126 mV kh^{-1}.
  - For both cells the main cause of degradation was found on the fuel electrode evolution under co-electrolysis. A remarkable loss of the percolation network of metallic Ni due to coarsening or Ni evaporation, close to the electrolyte interface in the post-mortem analysis was highlighted. No evidence of significant evolution in the microstructure of the mesoporous-based oxygen electrode was found.

- **Electrochemically enhanced POM for production of syngas was simulated and analysed in a real device.**
  - o Simulations were made to determine the best condition for promoting POM reaction. Such simulations highlighted the molar ratio 2:1 of CH_4 and O_2 as the best option for syngas production.
  - o Complete devices with CGO scaffold infiltrated by Ni and Cu precursors were fabricated and tested.
  - o Incomplete methane conversion was detected. In particular, at 800 °C applying a current density of 0.5 A cm^{-2}, the methane consumption rate measured was ≈30 %. The reasons of the incomplete methane conversion were found in the poor permeability of the electrode to the gas or in the reoxidation of the catalysts.
  - o The detection of produced CO (detected by μGC analysis) in all the experiments proved that POM reaction occurred in all the measurements, demonstrating the success of this proof of concepts. In any case further improvements are needed in this direction.

Appendix I

Deposition of structural ceramics on metal substrates

A1.1 Motivation of presented work

The results presented in this appendix were performed on the frame of an industrial project in collaboration with AMES group. The main goal of the collaboration was the production of nanostructured Yttria-stabilized Zirconia (YSZ) ceramic membranes to be applied as hydrogen purification membranes deposited on top of porous metal substrates fabricated by powder metallurgy (PM). Derived from this goal, the deposition of half SOC (NI-YSZ fuel electrode and YSZ electrolyte) was also studied. AMES is a powder metallurgy company that fabricated by this technique porous and dense pieces mainly for the automobilism sector. However, AMES is also involved in different I+D projects in other applications such as high temperature fuel cells and electrolysers, gas purification membranes, etc…

A1.2 Overview of the presented results

In order to obtain a gas purification membrane able to work with hydrogen mixtures, the obtained membranes have to present a high density with small porosity restricted to the nanoscale. Techniques such as PLD can produce layers characterized by small, interconnected porosity (pore diameters ≈5 nm). However, to consent the PLD deposition, intermediate layers, as the ones developed in the present work, need to be fabricated on top of the porous metal substrate to gradually reduce the porosity.

i.   Screen printing or robocasting (RC) (Figure A1.1a), were used to deposit the first intermediate layer and inkjet printing (IJP) for the deposition of another coating with very small porosity (Figure A1.1b).

ii.   Porous layers of YSZ were deposited on top of the metal substrates for Gas membrane production (Figure A1.1c).

A1. Deposition of structural ceramics on metal substrates

iii. Due to the versatility of the AM deposition techniques and the materials used, part of the work was also dedicated to the fabrication of functional ceramics on top of the metal substrates for the application is the Solid Oxide Cell (SOC) field

    a. NiO-YSZ was deposited on top of the metal substrates as fuel electrode and an additional YSZ dense layer was deposited to be used as electrolyte (Figure A1.1d).

The YSZ and NiO-YSZ layers shown were deposited using the BioX robocasting produced by CellInk. The results presented are part of a stage at the DTU Energy (Denmark). Part of the work was done in collaboration with DTU researchers.
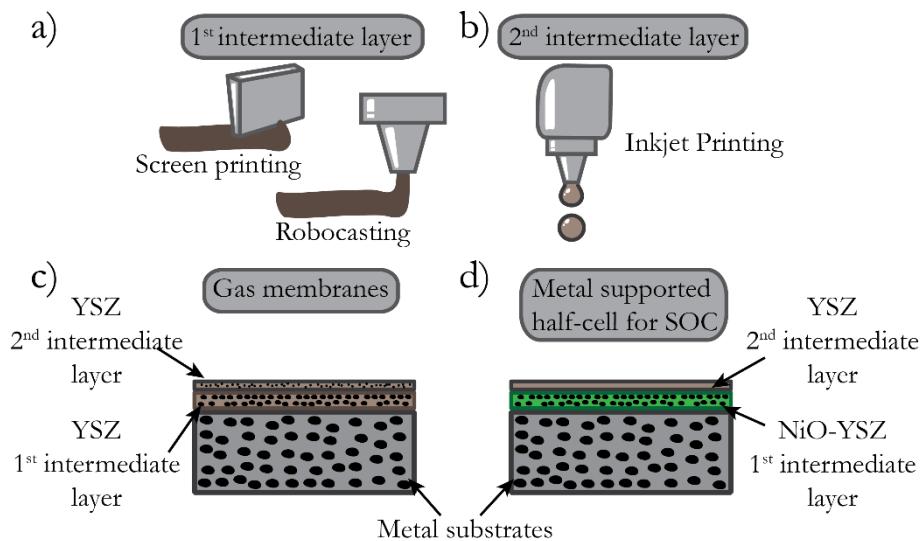
Figure A1.1: Techniques and materials used for the production of gas membranes: deposition of the first intermediate layer by screen printing or robocasting (a) and of the second coating by IJP (b). Schematic representation of the prepared samples, for gas separation membrane application (c) and as functional ceramic layers for metal supported SOC (d).

Advanced strategies for Solid Oxide Electrolysis Cells

A1.3 Metal substrates

The metal substrates made of AISI 316L, discs of diameter ≈2 cm and thickness ≈0.5 cm (Figure A1.2a), were provided by AMES groups and produced by powder metallurgy technology. A representative picture of the substrates is shown in Figure A1.2b.
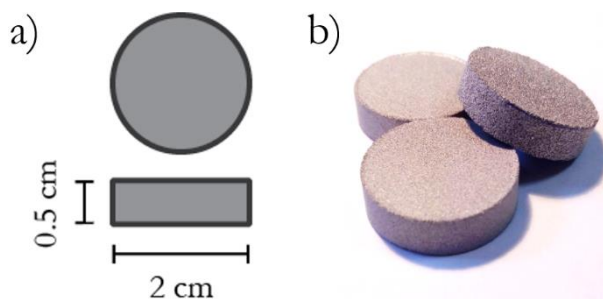
Figure A1.2: Scheme of the metal substrate (a) and representative picture (b).

The composition of the 316L stainless steel and some of the general characteristics of the material are reported in Table A1.1, the information were obtained from AMES website page.[1]
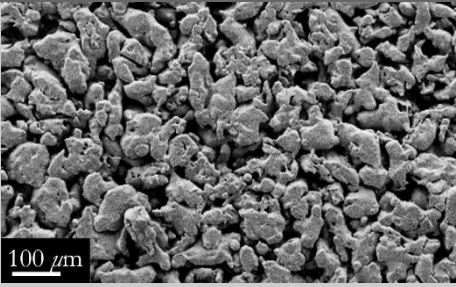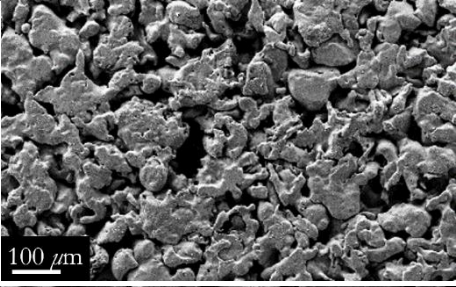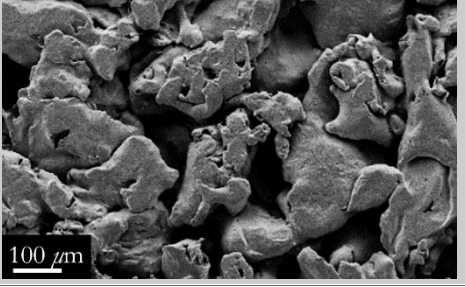
Table A1.1: Composition of the 361L stainless steel and general characteristics from AMES webpage.[1]

Composition		General characteristics	
Cr:	16-18%	Max. working T	600 °C ox atm.
Ni:	11-14%		850°C red atm
Mo:	2-3%	Coeff. linear expansion	$12 \cdot 10^{-6}$ K^{-1}
C:	< 0,03%		
Others:	2% max.		
Fe:	Rest		

Three types of metal substrates were provided by AMES, with same composition but different characteristics in terms of particle size. Representative SEM micrographs of the metal substrates are shown in Table A1.2. were the different particle sizes are indicated.

Advanced strategies for Solid Oxide Electrolysis Cells

Table A1.2: SEM micrographs representing the microstructure of the 3 substrates provided by AMES. The 316L_1 (particle size 45-75 μm), 316L_2, (particle size 75-150 μm) and 316L_3 (particle size 180-300 μm).

Substrate ID and particle size	SEM picture
316L_1 Particle size: 45-75 μm	100 μm
316L_2 Particle size: 75-150 μm	100 μm
316L_3 Particle size: 180-300 μm	100 μm

A1.4 Fabrication of YSZ membranes

A1.4.1 YSZ layer deposited by screen printing

A first attempt of deposit a ceramic coating on top of the metal substrates was made by screen printing deposition as shown in Figure A1.3. YSZ commercial powder (Kceracell) were mixed with a commercial medium (Fuelcellmaterials, a Nexceris company), with solid loading ≈20 %v/v.

Observing Figure A1.3, one can immediately observe the inhomogeneity which characterized the obtained layer. Deposition problems

Advanced strategies for Solid Oxide Electrolysis Cells

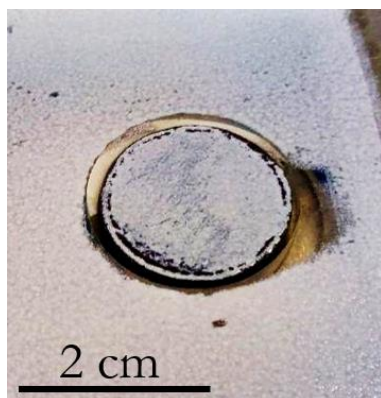were mainly caused by the irregular surface of the metal substrate due to the high porosity.

Figure A1.3: 316L_1 substrate after deposition of 1 layer of YSZ by screen printing.

After a first deposition on 316L_1 substrate, with the aim to determine the thickness of the screen-printed layers, 316L_1 and 316L_2 substrates were chosen for the deposition of the layers due to their smaller particle size. On top of 316L_1 substrate only one deposition was made, while two layers were screen printed on the 316L_2 sample. The ceramic layers were sintered at 1200 °C for 5 h and reducing atmosphere (H_2 5% + N_2 95%) to prevent the oxidation of the metal substrates. Figure A1.4 shows top view SEM micrographs of the two layers after sintering. One can notice that the coatings were cracked in multiple parts. The layer on top of 316L_2 (Figure A1.4b), was characterized by less and smaller cracks, because of the deposition in two steps.
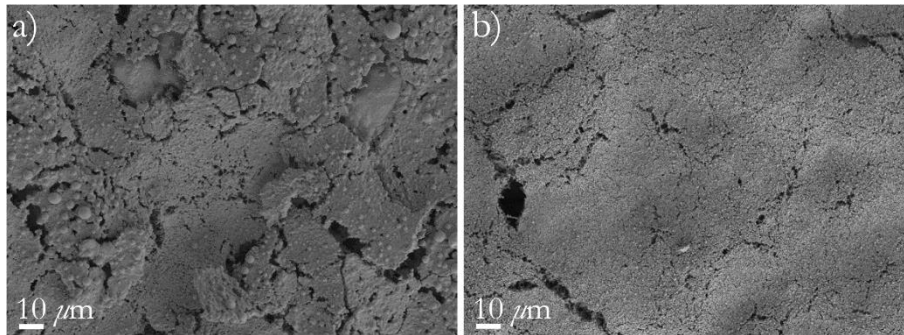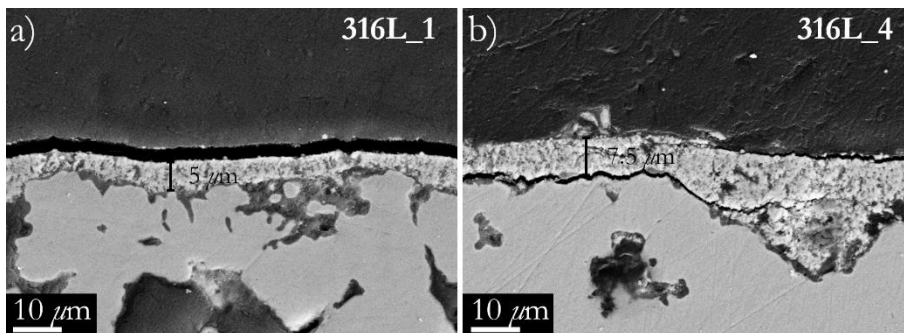
Figure A1.4: Top view SEM micrographs of YSZ coating deposited on top of the 316L_1 (a) and 316L_2 (b). One layer was deposited on top of 316L_1 and two on top of 316L_2. The samples were sintered at 1200 °C for 5h and reducing atmosphere (H_2 5% + N_2 95%).

Figure A1.5 presents SEM micrographs of the 316L_1 (a) and 316L_2 with YSZ deposited by screen printing. 316L_1 samples after one deposition presented a layer of ≈5 μm (Figure A1.5a) while for 316L_2 the layer thickness was ≈7.5 μm (Figure A1.5b).

Figure A1.5: Cross section SEM micrographs of YSZ coating deposited on top of the 316L_1 (a) and 316L_2 (b). One layer was deposited on top of 316L_1 and two on top of 316L_2. The samples were sintered at 1200 °C for 5 h and reducing atmosphere (H_2 5% + N_2 95%).

## A1.5 Robocasting/inkjet printing deposition of YSZ layers

RC was used because of its versatility to perform good coatings on rough and porous substrates. A slurry for RC deposition with YSZ as ceramic loading with a total solid loading ≈27 %v/v was prepared. The deposition of

Advanced strategies for Solid Oxide Electrolysis Cells

this slurry was made by RC on top of a 316L_2 and a 316L_3 metal substrates. The samples were additionally coated with YSZ by IJP. The YSZ ink was a water-based suspension with a ceramic loading ≈1%v/v.

All the samples were sintered at 1200 °C for 5 h and with H_2 5% + N_2 95 % atmosphere. The layer presented multiple cracks, but no delamination was observed as it can be seen in the images of the table A1.3.

Table A1.3: YSZ with pore formers and solid loading ≈27 %v/v robocasted on top of 316L_2 and 316L_3 before and after sintering using reducing conditions. On top of the robocasted layers, YSZ by inkjet printing was deposited.

	Robocasting deposition	Inkjet deposition	Sintering at 1200 °C 5% H_2
316L_2			
316L_3			
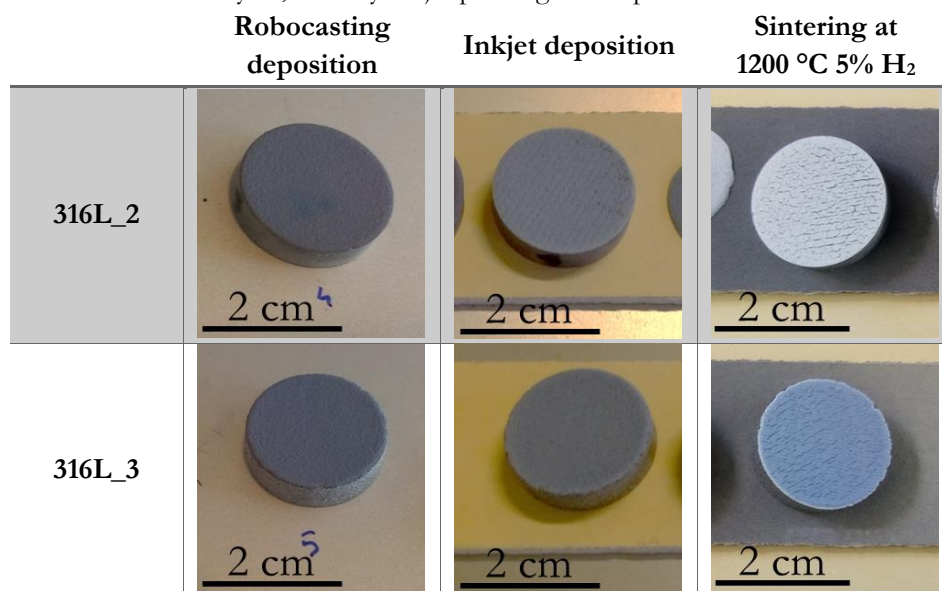
The delamination of the layers was probably caused by the difference of thermal expansion coefficient between 316L and YSZ ($12 \cdot 10^{-6}$ K^{-1} and $10.5 \cdot 10^{-6}$ K^{-1}, respectively. Other websites, like ESMAT web page, report higher values for 316L alloy, which are around $16 \cdot 10^{-6}$ K^{-1}.),[2–4] which caused the cracking of the layers during sintering.

The utilization of sintering aids should be considered in the future to lower the firing temperature reducing the issue related to TEC.

A1.6 Fabrication of functional ceramic layers by RC deposition combined with inkjet printing

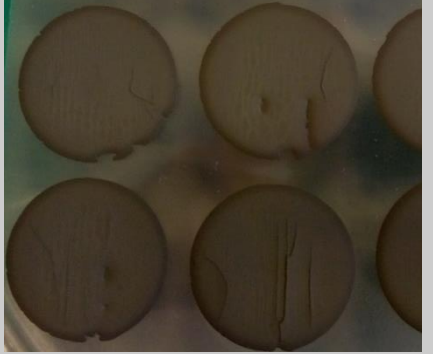### A1.6.1 Printability test of and YSZ layers

RC slurries based on NiO-YSZ were prepared with different solid loading concentrations. PMMA and graphite were used as pore former to provide a good interconnect porosity inside the ceramic layer. PVP K30 (molecular weight = 45,000-58,000 g mol^{-1}) and PVP K90 (molecular weight = 1,000,000-1,700,000 g mol^{-1}) were used as dispersant and binder, respectively. Their amount was always maintained around 1.5-2 %v/v for PVP K30 and 1-1.5 %v/v for PVP K90. Table A1.4 shows the results of the printing of different slurries after drying for 15 mins at 90 °C.

The first attempt was made preparing a slurry without any pore former with ≈40 %v/v of solid loading (≈20 %v/v of YSZ and ≈20 %v/v of NiO). After drying the samples immediately cracked in different parts.

Three more slurries adding PMMA and graphite as pore formers and reducing the solid loading were prepared. The concentrations of the slurries were ≈37 %v/v, ≈28 %v/v and ≈27 %v/v. The last formulation presented layers with small or no cracks after drying and demonstrated to be a good candidate as support for YSZ coatings deposition by IJP.

Table A1.4: Robocasted slurries with different solid loading. NiO-YSZ without pore formers and 40 %v/v, and then NiO-YSZ with pore formers and solid loading at 37 %v/v, 28 %v/v, 27 %v/v.

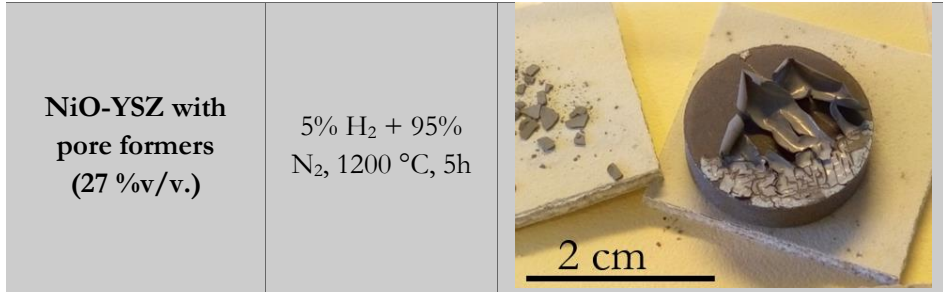| Composition	Solid loading	
NiO-YSZ no pore formers	≈40 %v/v.	
NiO-YSZ with pore formers	≈37 %v/v.	
NiO-YSZ with pore formers	≈28 %v/v.	
NiO-YSZ with pore formers	≈27 %v/v.	
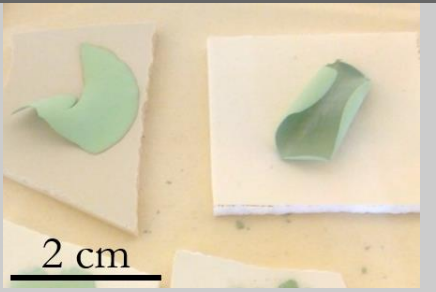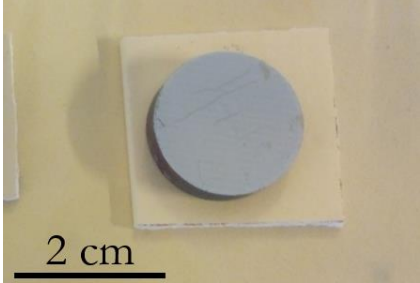
A1.6.2 Sintering in air and in reducing atmosphere

A RC layer prepared with NiO-YSZ and pore formers, with solid loading ≈27 %v/v was deposited on top of one of the metal substrates. A YSZ layer was printed by IJP on top of the layer. The sample was co-sintered at 1200 °C for 2 h in reducing conditions (5% H_2). Another Ni-YSZ/YSZ free-standing sample prepared by RC and IJP was sintered at the same temperature in air, as comparison.

In both cases the robocasted layers presented strong deformation, probably due to the higher shrinkage rate of the YSZ layer by IJP respect to the NiO-YSZ layers. In the case of the sample sintered in reducing atmosphere the constrain represented by the metal substrate caused the complete delamination of the layer, which broke in different parts.

Table A1.5: NiO-YSZ with pore formers and solid loading 27 %v/v after sintering in air and in reducing conditions. The layer sintered in reducing condition was deposited on top of a 316L_2 substrate.

Composition	Treatment	
NiO-YSZ with pore formers (27 %v/v.)	Synitetich air, 1200 °C, 5h	
NiO-YSZ with pore formers (27 %v/v.)	Before treatment	

Advanced strategies for Solid Oxide Electrolysis Cells

| NiO-YSZ with pore formers (27 %v/v.) | 5% H$_2$ + 95% N$_2$, 1200 °C, 5h | |

A1.6.3 Microstructural characterization

The samples were observed by SEM on top view, the results are shown in Figure A1.6. After the sintering in reducing condition (Figure A1.6a) the YSZ layer deposited by IJP presented a porous microstructure with small grains. Conversely, after the sintering in air a dense layer with only small porosity were present (Figure A1.6a).
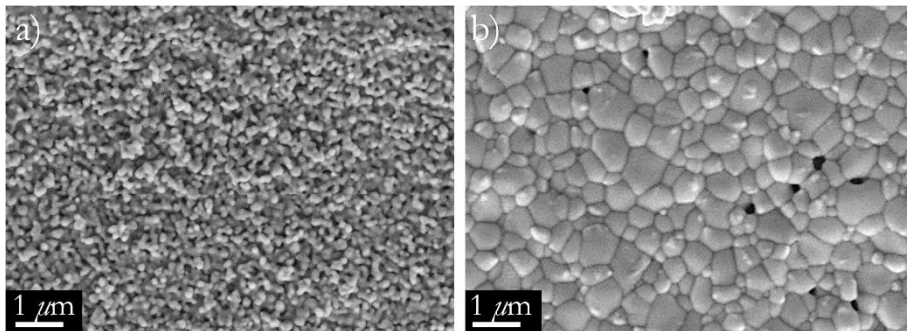

Figure A1.6: SEM micrographs of IJP YSZ layers, deposited on top of the robocasted layers presented in Table A1.5. after sintering at 1200 °C, 5 h with H$_2$ 5% (a) and 1200 °C, 5 h in air (b).

The samples were also observed in cross section as shown in Figure A1.7. The sample sintered upon reducing conditions (Figure A1.7a) presented a microstructure characterized by small pores, while a dense film was obtained by the sintering in air (Figure A1.7b).
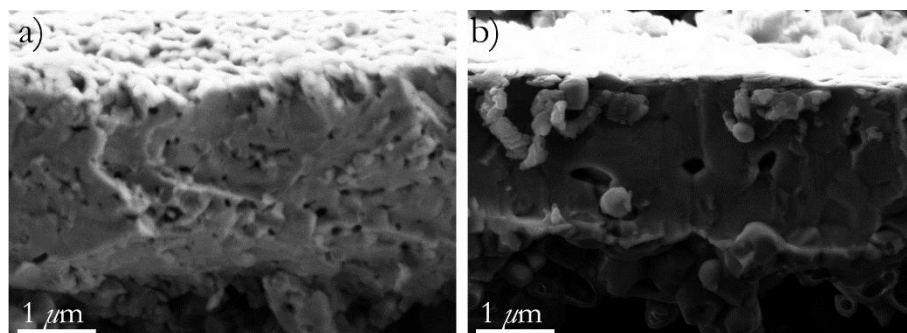
Figure A1.7: Cross section SEM micrographs of IJP YSZ layers, deposited on top of the robocasted layers presented in Table A1.5. after sintering at 1200 °C, 5 h with H_2 5% (a) and 1200 °C, 5 h in air (b).

Figure A1.8 shows some additional cross section images of the robocasted layer NiO-YSZ with the YSZ deposited by IJP sintered in air. The sample was embedded in epoxy resin, polished and observed by SEM. A dense YSZ layer is presented in the pictures, with a thickness around ≈1.5 μm.
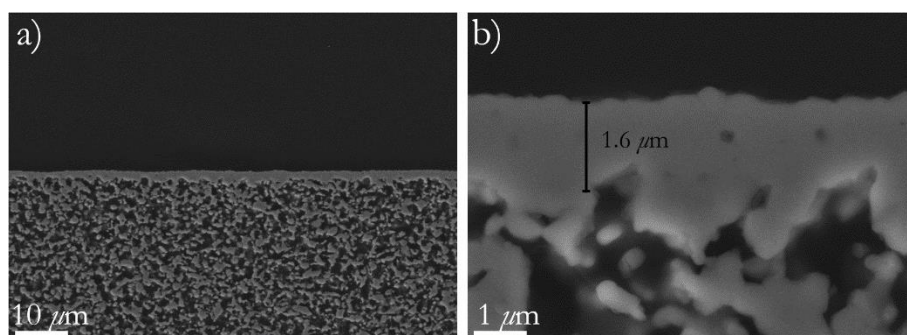

Figure A1.8: Cross section SEM micrographs of IJP YSZ film, deposited on top of the robocasted layer after embedding and polishing. The sample was sintered at 1200 °C, 5 h in air.

As in the case of YSZ deposition the delamination of the layers was mainly caused by the difference of TEC between 316L and NiO-YSZ layers. Furthermore, a certain difference in shrinkage after sintering between NiO-YSZ and YSZ film by IJP could be the cause of the delamination. The large shrinkage rate of the YSZ ink could explain the deformation observed.

Advanced strategies for Solid Oxide Electrolysis Cells

A1.7 Conclusion

YSZ coatings were deposited by screen printing, RC and IJP for the fabrication of gas purification membranes.

Due to the porosity of the substrates, the screen-printed layers presented several cracks and therefore RC was preferred as deposition technique. RC and IJP were used for the fabrication of layers with the aim of reducing the porosity of the metal substrate. YSZ layers were successfully printed on top of the robocasted layers, but they cracked after sintering at 1200 °C in reducing conditions. This was caused by the TEC difference between YSZ and the 316L substrates.

NiO-YSZ slurries were formulated to consent the deposition of functional ceramics for SOC application on top of the metal substrates. 27 %v/v was found as the preferred concentration to obtain layers without cracks.

YSZ layers were deposited on top of the Ni-YSZ robocasted layers. After sintering the layer cracked. In this case the difference in shrinkage after sintering between NiO-YSZ and YSZ had worsen the phenomenon.

RC demonstrated to be the best choice for the deposition of intermediate layers on top of irregular surfaces, due to its versatility. Better results could be obtained in the future with the utilization of metal substrates with TEC similar to YSZ and with sintering aids, in order to reduce the sintering temperature of the ceramic layers.

A1.8 Bibliography

1   AMES Group, AMES webpage, amespore.com. Consulted the 08-10-2020.
2   H. Hayashi, T. Saitou, N. Maruyama, H. Inaba, K. Kawamura and M. Mori, *Solid State Ionics*, 2005, **176**, 613–619.
3   J. Johnson and J. Qu, *J. Power Sources*, 2008, **181**, 85–92.
4   ESMAT, *ESA esmat webpage, www.esmat.esa.int. Consulted the 10-10-2020*, 2020.

Scientific contributions

Peer-reviewed scientific journals

Improved mesostructured oxygen electrodes for highly performing solid oxide cells for co- electrolysis of steam and carbon dioxide. S. Anelli, F. Baiutti, A. Hornés, L. Bernadet, M. Torrell, A. Tarancón. J. Mater. Chem. A, 2019,7, 27458-27468.

Co-electrolysis of steam and carbon dioxide in large area solid oxide cells based on infiltrated mesoporous oxygen electrodes. S. Anelli, E. Hernández, L. Bernadet, X. Sun, A. Hagen, F. Baiutti, M. Torrell, A. Tarancón. J. Power Sources, 2020, 478, 228774.

Conferences‡

Fundamental studies on mesoporous cerium oxide for oxide cell applications. S. Anelli, <u>F. Baiutti</u>, E. Hernandez, A. Morata, M. Torrell, A. Tarancón. E-MRS Spring meeting, 2018. Poster.

Synthesis and application of ceramic periodic mesoporous materials applied in high temperature solid oxide electrolysis cells. <u>M.Torrell</u>, S. Anelli, F. Baiutti, A. Tarancón. International Conference on High-Performance Ceramics (CICC), 2019 Oral presentation.

New generation mesoporous oxygen electrode for solid oxide cell application. <u>F Baiutti</u>, S Anelli, M Torrell, J Blanco Portals, L López-Conesa, S Estradé, F Peiró and A Tarancón. Solid State Ionics, 2019. Poster

Improved mesoporous oxygen electrode for Solid Oxide Electrolyser Cells application. <u>F Baiutti</u>, S Anelli, M Torrell, J Blanco Portals, L López-Conesa, S Estradé, F Peiró and A Tarancón. International Conference on Electroceramics, 2019. Oral.

Improved mesoporous oxygen electrode for Solid Oxide Electrolyser Cells application. <u>S. Anelli</u>, F. Baiutti, A. Hornes, L. Bernadet, M. Torrell, A. Tarancón. International Conference on Electrolysis (ICE), 2019. Poster. The poster was awarded the 1st prize.

---

‡ In this section, the underlining specifies the presenting author.

Advanced strategies for Solid Oxide Electrolysis Cells

A1. Deposition of structural ceramics on metal substrates

Improved mesoporous scaffolds for composite electrodes in solid oxide devices for direct hydrogen production. <u>Simone Anelli</u>, Federico Baiutti, Aitor Hornés, Lucile Bernadet, Marc Torrell, Albert Tarancón. 14th European SOFC & SOE Forum 2020. Oral presentation.

Advanced strategies for Solid Oxide Electrolysis Cells